Portal interactions within leptogenesis and precision observables

– and –

Quantum theory of orbitally-degenerate impurities in superconductors

by

Matthias Le Dall

Licence, Université Aix-Marseille III, France, 2008

M.Sc., Imperial College London, UK, 2009

A Dissertation Submitted in Partial Fulfillment of the

Requirements for the Degree of

DOCTOR OF PHILOSOPHY

in the Department of Physics and Astronomy

© Matthias Le Dall, 2017

University of Victoria

Portal interactions within leptogenesis and precision observables

– and –

Quantum theory of orbitally-degenerate impurities in superconductors

by

Matthias Le Dall

Licence, Université Aix-Marseille III, France, 2008

M.Sc., Imperial College London, UK, 2009

Supervisory Committee

_____

Dr. A. Ritz, Supervisor

(Department of Physics and Astronomy)

_____

Dr. R. de Sousa, Supervisor

(Department of Physics and Astronomy)

_____

Dr. M. Pospelov, Departmental Member

(Department of Physics and Astronomy)

_____

Dr. A. Monahan, Outside Member

(Department of Earth and Ocean Sciences)

Supervisory Committee

Dr. A. Ritz, Supervisor
(Department of Physics and Astronomy)

Dr. R. de Sousa, Supervisor
(Department of Physics and Astronomy)

Dr. M. Pospelov, Departmental Member
(Department of Physics and Astronomy)

Dr. A. Monahan, Outside Member
(Department of Earth and Ocean Sciences)

ABSTRACT

In the first part of the thesis, the need for physics beyond the Standard Model, as attested to by the evidence of dark matter, motivates us to study the effects of introducing into the standard theory of Leptogenesis a hidden sector scalar coupled to the Standard Model through the Higgs portal. We find that the new interactions are not constrained by the Davidson-Ibarra bound, thus allowing us to lower the mass scale of Leptogenesis into the TeV range, accessible to experiments. We then consider a broader class of new physics models below the electroweak scale, and classify precision observables according to whether or not deviations from the Standard Model at current levels of sensitivity can be explained purely in terms of new light degrees of freedom. We find that hadronic precision observables, e.g. those that test fundamental symmetries such as electric dipole moments, are unambiguous pointers to new UV physics.

In the second part of the thesis, motivated by recent measurements of the spatial structure of impurities embedded in superconductors (SC), we study the effect of su-

perconductivity on impurity states by generalizing the Anderson model of a quantum s-wave impurity to include orbital degeneracy. We find that the proximity effect induces an electron-electron attractive potential on the impurity site that mirrors the BCS pairing mechanism, resulting in the appearance of atomic Cooper pairs within the superconducting energy gap, called Yu-Shiba-Rusinov (YSR) states. We find that electron orbital degeneracy allows YSR states to have non-trivial orbital quantum numbers thus opening the possibility for optical transitions among YSR states. We enumerate the one-photon selection rules that apply to YSR states, unveiling transitions to the vacuum state that are forbidden in the normal state.

Contents

List of Tables

List of Figures

ACKNOWLEDGEMENTS

DEDICATION

I dedicate this thesis to my Parents, Brothers and Sister, who have relentlessly encouraged me and supported me. I would not be here without their trust.

I also dedicate this thesis to my Uncle who, with his playful and inquisitive mind, planted the seed of science in me.

"The scientist has a lot of experience with ignorance and doubt and uncertainty, and this experience is of very great importance, I think. [...] We have found of paramount importance that in order to progress we must recognize the ignorance and leave room for doubt. Scientific knowledge is a body of statements of varying degrees of certainty some most unsure, some nearly sure, none *absolutely* certain.

Now, we scientist are used to this, and we take it for granted that it is perfectly consistent to be unsure - that it is possible to live and *not* know. But I don't know whether everyone realizes that this is true. Our freedom to doubt was born of a struggle against authority in the early days of science. It was a very deep and strong struggle. Permit us to question - to doubt, that's all - not to be sure. And I think it is important that we do not forget the importance of this struggle and thus perhaps lose what we have gained. Here lies a responsibility to society."

Richard Feynman, "The pleasure of finding things out, The value of science"

Prologue

The Standard Model has proven to be a remarkably successful model of subatomic physics, tested to high precision over the past four decades, and predicting several new particles, including the Higgs boson discovered in 2012. At its core, is the concept of gauge symmetry and of spontaneous gauge symmetry breaking. Below a critical temperature, the Higgs field forms a condensate which causes the spontaneous breaking of local gauge symmetries, which is responsible for the generation of the masses of all fundamental particles.

Spontaneous symmetry breaking is not a concept specific to particle physics, but is pervasive throughout nature. In fact, analogous to the Higgs mechanism, the phenomenon of superconductivity is also a consequence of local gauge symmetry breaking. There, it is the condensation of conduction electrons into bound pairs, the so-called Cooper pairs, that breaks the symmetry and results in electromagnetic fields being unable to penetrate the bulk of the superconductor, a phenomenon called the Meissner effect.

Fascinated by this connection, I felt a desire to explore it further, and to use my knowledge of quantum field theory to help me better understand superconductivity.

Part I

Particle Physics

Chapter 1

Introduction

The idea that nature is made of microscopic indivisible elements dates back to the ancient Greeks, a concept they called *atomos*. The groundbreaking discovery is not so much that nature can be broken down into *atoms*, but rather that everything in the universe can be broken down into the *same* atoms. Nowadays, the atoms are classified in one single chart, the Periodic table of the elements. The same question has driven particle physicists towards searching for the *atoms of atoms*. This quest has resulted in the modern picture of particle physics, concisely organized in what is known as the Standard Model of particle physics, and is the crowning achievement combining quantum field theory and group theory. Its great predictive power was again demonstrated in 2012, with the discovery of the Higgs boson [1, 2].

In spite of its incredible precision, the Standard Model (SM) suffers from a few shortcomings. There is the issue of the neutrino masses. Indeed, the original formulation of the SM was designed with massless neutrinos [3, 4, 5], which was perfectly consistent with the precision of experiments at the time [6]. However, solar and atmospheric neutrino experiments detected a discrepancy between the expected flux of neutrinos coming from the Sun, and the flux measured on Earth [7]. Called the solar and atmospheric neutrino anomalies, they are resolved by postulating that neutrinos come in three flavors that oscillate as they travel. Theoretically, it is well established that neutrinos can oscillate if and only if they have non-zero masses [8, 9, 10], a prediction that has been confirmed experimentally by the measurement of two non-zero neutrino mass squared differences [11, 12, 13, 14].

Since massless particles have only one chirality, and that the weak interactions maximally break parity by interacting with left-handed chiralities, there is no right-handed field on the Standard Model. Naively, the simplest mechanism to account for

neutrino masses is by including the right-handed component to the neutrino fields. By coupling the left-handed to the right-handed via the Higgs doublet $\sim \lambda \nu_R \nu_L \cdot H$, akin to the charged lepton sector, in principle should allow for the generation of the neutrino masses upon the Higgs doublet acquiring a vacuum expectation value $m_\nu \sim \lambda \langle H \rangle$. Neutrino experiments point towards neutrino masses that are at least six orders of magnitude smaller than the charged lepton masses. Explaining this hierarchy poses a challenge: either this points towards a great deal of arbitrary fine-tuning of the dimensionless coupling parameter λ, or this is the sign of a novel mass-generating mechanism.

The right-handed component of the neutrino field is unlike any other fermion of the SM, being electrically neutral it is a singlet under electromagnetism, being right-handed it is a singlet under the weak interactions, and being a lepton it is a singlet under the strong interactions. Its pure singlet nature allows for the so-called Majorana mass term, $M \bar{\nu}_R \nu_R$, where the mass scale M is unconstrained, and could in principle be of a much higher scale than any other mass scale of the SM. This fact is utilized by the type-I see-saw mechanism [15, 16, 17, 18], which places $M \sim 10^{11}$GeV and the light neutrino masses of the order of $\sim \lambda \langle H \rangle^2 / M$, suppressed by the large scale. Although satisfying, this mass scale has not been observed. The Majorana mass term does not conserve lepton number, which has been observed to be a good quantum number. Lepton number violation is sought after in experiments trying to detect double beta decay for instance [19, 20, 21, 22, 23, 24].

Drawing an analogy with the quark sector, neutrino masses ought to lead to CP-violation in the lepton sector. In the quark sector, the three flavors of quarks are not the same as the mass eigenstates, but the two are related via a unitary rotation containing real angles and complex phases manifesting through the Cabbibo-Kobayashi-Maskawa (CKM) matrix [25, 26]. With three flavors of massive quarks, only one combination of those phases is physical. This one phase is in part responsible for CP-violation in the quark sector, contributing to the phenomena like Kaons and B mesons oscillations [27, 28, 29], or contributing to fundamental electric dipole moments (EDMs) [30].

The fact that neutrino flavors oscillate is a clear sign that the three mass eigenstates and the three flavor eigenstates are not the same, but can be related via a unitary rotation called the Pontecorvo-Maki-Nakagawa-Sakata (PMNS) matrix [31]. At first sight, the structure of the neutrino sector is analogous to the quark sector, except that the neutrino may either be Dirac or Majorana. A neutrino could be Dirac

if it carried a lepton charge, like all other leptons of the SM. In this case, no Majorana mass term is allowed and the rephasing of the PMNS matrix is the same as that of the CKM matrix, leaving one physical CP-phase. On the other hand, because the neutrino has no electric charge, it is possible that it be its own antiparticle in which case it would be a Majorana particle and lepton number would not be a conserved charge. If the neutrino is Majorana, it is not possible to remove as many phases as in the Dirac case, leaving one physical Dirac phase and two physical Majorana phases [32], for a total of three phases.

CP-violation of the neutrino sector feeds into the second issue of the SM that we are going to mention, that is the baryon asymmetry of the universe. It is clear that Earth and the solar system are made out of matter. Measurements of cosmic rays demonstrate that the amount of matter is dominant compared to the amount of antimatter [33, 34, 35].

The abundance of light elements, Hydrogen, Helium, Deuterium, etc, as predicted by ΛCDM [36] during the phase of Big Bang Nucleosynthesis (BBN) [37], depends on the baryon-to-photon ratio, $\eta_B = n_B/n_\gamma$. Independent measurements of the abundance of light elements in the universe [38] allow to constrain the ratio to the value,

$$\eta_B = (6.2 \pm 0.4) \cdot 10^{-10}. \tag{1.1}$$

Independent measurements of this ratio also come from the Planck satellite [39]. The generation of the baryon asymmetry in the universe is referred to as baryogenesis, and successful baryogenesis theories must contain three ingredients, first enumerated by Sakharov [40]. Charge conjugation flips the electric charge of particles into their opposite, that is transforms the matter particles into their antimatter counterparts. It is obvious that charge conjugation must be broken in order to generate a matter-antimatter asymmetric universe. However, charge alone is not sufficient because in principle the charge asymmetry generated in the left-handed sector could be compensated by an opposite charge asymmetry in the right-handed sector, with an overall charge asymmetry vanishing. As a result, we must impose that charge conjugation and parity transformation be broken simultaneously. This is why one of Sakharov's first criteria is that of C- and CP-violation.

As we mentioned, the SM is known to contain CP-violation in the quark sector. Studies of baryogenesis theories have shown that the amount of CP-violation in the quark sector is not sufficient to generate the right amount of asymmetry in

the universe [41, 42], because of the small CP-asymmetry suppressed by the small quark masses [43, 44]. If quark CP-violation was the only source of CP-violation, new physics would be required. The neutrino sector is believed to contain CP-violation also. Theories that attempt to explain the baryon asymmetry in the universe using the CP-asymmetry in the lepton sector are referred to as leptogenesis, because they generate a lepton asymmetry first, which later gets converted into a baryon asymmetry [45]. Leptogenesis studies show that if CP-violation is sufficiently strong, it could explain the baryon asymmetry in the universe [46, 47, 48, 49]. The lepton sector CP-phase is not precisely measured, however, and the mechanism to generate it is not known either.

The third shortcoming we are going to mention, is that of the dark matter in the universe, and we have several clues for its presence coming from independent sources. Its first signs came from measurements of galaxy rotations. By measuring the amount of luminous matter in galaxies (contained in stars mostly), we can infer the amount of visible mass and galaxy rotation speeds based on general relativity. However, this procedure constantly predicts speeds slower than the measured speeds [50, 51, 52]. This suggests that more matter is present in galaxies than what is seen, hence the name dark matter. Signs that dark matter clumps in big halos around galaxy clusters come from gravitational lensing, which show that light bends more than it would if all matter contained in the cluster was in the luminous form [53]. Again, this implies a large amount of mass than what is seen. Further clues come from astrophysical simulations of big scale structure, i.e. the scale of cluster and above. Simulations of the universe's evolution leads to a structure which matches with current observations, provided dark matter is included in the simulation [54, 55, 56]. The picture being that the large amount of dark matter provide the gravitational potential needed for baryonic matter to collapse and form the structure we see today.

That being said, the strongest signal for dark matter comes from measurements of the CMB anisotropies. The Planck satellite mission has measured the CMB power spectrum and provided the most precisely measured energy budget of the universe to be 4.9% in the form of brayonic matter, 26.6% in dark matter, and 68.5% in dark energy [39].

The particle nature of dark matter is unknown. We know it has mass, since it attracts gravitationally, but we do not know how it interacts with the SM. We know that it is neutral under electromagnetism since it is dark. Collider experiments trying to produce it have come up empty handed so far, suggesting dark matter is

also weakly interacting with the weak interactions. In principle, dark matter could be very complex, containing various particles and forces, in analogy to the visible sector which contains several generations of fermions, and forces mediated by bosons, and scalar fields generating masses. This general structure is referred to as the hidden sector.

There are various ways to couple a hidden sector to the visible sector, but a systematic organizing principle is in terms of relevant, marginal, and irrelevant operators. We can write down a general operator of the Lagrangian in the form,

$$\mathcal{L} = \sum_d \frac{g_d}{\Lambda^{d-4}} \mathcal{O}_d. \tag{1.2}$$

The dimension d of the operator counts the number of energy dimensions, Λ and energy scale and g_d a dimensionless coupling. For a given process taking place at energy E involving particles in the above operator, it is natural to expect the energy dependence as $g_d(E/\Lambda)^{d-4}$. The effect of operators of dimensions $d > 4$ will become irrelevant at low energies $E \ll \Lambda$, those operators are called *irrelevant*. On the other hand, the effect of operators of dimension $d < 4$ become relevant at low scale, and the operators are called *relevant*. Lastly, for operators such that $d = 4$ are constant as the energy varies, those operators are called *marginal*.

We do not know how new physics will appear first in experiment since, by definition, it is unknown. However, at collider experiments, the lowest energy degrees of freedom of the new theory will show up first. That is to say, operators that are most likely to describe physics at low energy are relevant or marginal operators. Among those, a class of operators called *portals* is of special interest [57, 58]. The simplest way to weakly couple the hidden sector to the SM is to assume the hidden sector is neutral under the SM, expressed by the Lagrangian,

$$\mathcal{L} = \sum_{d_1} \sum_{d_2} \frac{g_d}{\Lambda^{d_1+d_2-4}} \mathcal{O}_{d_1}^{SM} \mathcal{O}_{d_2}^{NP}, \quad d_1 + d_2 \leqslant 4. \tag{1.3}$$

The operator $\mathcal{O}_{d_1}^{SM}$ involves only SM fields, while $\mathcal{O}_{d_2}^{NP}$ involves only hidden sector fields such that $d_1 + d_2 \leqslant 4$ such that we focus on relevant or marginal operators. The power of this method is that the number of operators we can write down is very limited. In fact, we can enumerate three kinds of portals: the vector, the Higgs, and

the neutrino portals,

$$\mathcal{L}_{\text{vector}} = \kappa B^{\mu\nu} V_{\mu\nu}$$
$$\mathcal{L}_{\text{Higgs}} = -H^\dagger H (\beta S + \gamma S^2) \tag{1.4}$$
$$\mathcal{L}_{\text{Neutrino}} = -\lambda L H N,$$

where $V_{\mu\nu}$ is the field strength of a hidden sector vector gauge boson mediating a $U(1)_{NP}$ force and κ is the kinetic mixing parameter. The A and λ are the trilinear and quadratic Higgs portal couplings, with the singlet scalar S. Finally, a right-handed neutrino field N enters the neutrino portal with Yukawa coupling matrix Y_N.

The theme of this thesis is two-fold. First, we are going to modify the simplest theory of leptogenesis by including the Higgs portals, in an attempt to lower the typical mass scale of leptogenesis. We will prove that it is possible to do so, bringing the theory of leptogenesis in the TeV range, which is accessible by current collider experiments. The second theme is a follow up question. Given portal interactions that involve light new degrees of freedom, what are the experimental constraints that can be put on those models? The mechanism responsible for the baryon asymmetry in the universe is not known, since there is no unique way to do so. Therefore, even though portal interactions can be constrained within a given leptogenesis or baryogenesis model, it does not provide a strong general constraint on the portal class of operators. Instead, we are going to estimate the contributions of portal operators to observables that are extremely well measured, the so-called precision observables.

In Chapter 2 we will introduce in details the question of the baryon asymmetry, and review some of the simplest models, a particular emphasis is put on the specific theory called leptogenesis. In chapter 3, we will introduce our model and analyze in details the Sakharov's ingredients and its dynamics. In chapter 4, we will enumerate a number of precision observables which we will use to put constraints on all portals interactions.

Chapter 2

Review of Baryogenesis

What are the initial conditions of the early universe, and what was the initial matter-antimatter asymmetry? Indeed there is no reason, a priori, that the big bang would have created an asymmetric universe, since neither matter nor antimatter have a special role, what is defined as matter or antimatter is nothing but a convention. Besides, even if the universe did start out as an asymmetric universe, the period of inflation would have diluted away remnants of asymmetry due to the overwhelming expansion rate.

Below, we are going to describe a set of three conditions, called the Sakharov conditions [40], that are necessary (and sufficient) for a baryogenesis theory to generate a lasting baryon asymmetry. The conditions are baryon number violation, C- and CP-violation, and out-of-equilibrium interactions.

2.1   Sakharov's criteria

Baryon number violation

In order to arrive at a baryon-asymmetric universe from a baryon-symmetric universe, it is necessary to have processes that break baryon number conservation. To be more specific, we can consider a toy model where a particle, X, decays along two decay channels, $X \to F_1$, and $X \to F_2$, where the final states F_1, F_2 have respective baryon numbers B_1 and B_2. Of course, we also have the antiparticle decays $\overline{X} \to \overline{F}_{1,2}$. The

total baryon number generated out of X and $\overline{X}$ decays are [59, 60]

$$\begin{aligned}
B_X^T &= \mathrm{Br}(X \to F_1)\,(B_1 - B_X) + \mathrm{Br}(X \to F_2)\,(B_2 - B_X), \\
B_{\overline{X}}^T &= \mathrm{Br}(\overline{X} \to \overline{F}_1)\,(-B_1 + B_X) + \mathrm{Br}(\overline{X} \to \overline{F}_2)\,(-B_2 + B_X),
\end{aligned} \tag{2.1}$$

where the branching ratio is such that $\mathrm{Br}(X \to F_1) + \mathrm{Br}(X \to F_2) = 1$ lead to the net baryon number,

$$B^T = B_X^T + B_{\overline{X}}^T = \left[\mathrm{Br}(X \to F_1) - \mathrm{Br}(\overline{X} \to \overline{F}_1)\right](B_1 - B_2). \tag{2.2}$$

It is clear that we need $B_1 \neq B_2$ to get a non-zero net baryon number. We could set the baryon number of X such that the first channel conserves baryon number $B_X = B_1$, but if the second channel is such that $B_2 \neq B_1$, then automatically the second channel violates baryon number $B_2 \neq B_X$. In conclusion, baryon number violation is satisfied if there exist at least two channels with different baryon-number final states.

C- and CP-violation

As the net baryon number in Eq. (2.2) shows, besides baryon number violation, charge violation, C, is also necessary in order to generate a non-zero baryon asymmetry. Though C-violation alone is not sufficient, as CP-violation is simultaneously required. The reason has to do with chirality. Indeed, if X can decay into both the left- and right-handed components $F_{1L,R}$ of F_1, then the effect of charge conjugation is

$$\begin{aligned}
\Gamma(X \to F_{1L}) &\xrightarrow{C} \Gamma(\overline{X} \to \overline{F}_{1L}), \\
\Gamma(X \to F_{1R}) &\xrightarrow{C} \Gamma(\overline{X} \to \overline{F}_{1R}),
\end{aligned} \tag{2.3}$$

while the effect of CP-transformation also changes the chiralities,

$$\begin{aligned}
\Gamma(X \to F_{1L}) &\xrightarrow{CP} \Gamma(\overline{X} \to \overline{F}_{1R}), \\
\Gamma(X \to F_{1R}) &\xrightarrow{CP} \Gamma(\overline{X} \to \overline{F}_{1L}).
\end{aligned} \tag{2.4}$$

Therefore, even in a scenario where C-symmetry is broken but where CP-symmetry is preserved the decay of the particles and the decays of the antiparticles remain equal,

$$\Gamma(X \to F_{1L}) + \Gamma(X \to F_{1R}) = \Gamma(\overline{X} \to \overline{F}_{1L}) + \Gamma(\overline{X} \to \overline{F}_{1R}) \tag{2.5}$$

This is the reason why both C and CP symmetries must be broken.

Loss of equilibrium

The out-of-equilibrium condition is satisfied dynamically. In order to understand the need for out-of-equilibrium dynamics, let's first analyze the problem of baryogenesis in equilibrium.

Assuming baryon matter is in equilibrium throughout the universe's history, the baryon density is obtained from the Fermi-Dirac phase space densities,

$$
\begin{aligned}
n_B &= g \int \frac{d^3 p}{(2\pi)^3} \frac{1}{1 + e^{(E - \mu_B)/T}} \quad , \quad E = \sqrt{|\vec{p}|^2 + m^2}, \\
n_{\overline{B}} &= g \int \frac{d^3 p}{(2\pi)^3} \frac{1}{1 + e^{(\overline{E} - \overline{\mu}_B)/T}}, \quad \overline{E} = \sqrt{|\vec{p}|^2 + \overline{m}^2}.
\end{aligned}
\tag{2.6}
$$

where CPT-symmetry imposes that the particle and antiparticle masses are equal, $m = \overline{m}$. When interactions are in chemical equilibrium, the parameter μ_B is called the chemical potential and is conserved during chemical reactions. In particular, matter and antimatter particles can annihilate into two photons, $B + \overline{B} \to 2\gamma$, which imposes the condition $\mu_B + \mu_{\overline{B}} = 2\mu_\gamma = 0$, where the photon chemical potential vanishes because the number of photons is not conserved, due to absorption and emission. The existence of baryon number violating interactions open the possibility for interactions such as,

$$
B + B \to \overline{B} + \overline{B}.
\tag{2.7}
$$

If the rate of such an interaction is fast, the baryon violating interactions are in equilibrium and the chemical potentials satisfy the constraint,

$$
2\mu_B = 2\mu_{\overline{B}} = -2\mu_B \implies \mu_B = \overline{\mu}_B = 0.
\tag{2.8}
$$

This automatically guarantees that $n_B - n_{\overline{B}} = 0$. To summarize, the conditions of CPT symmetry and of thermal equilibrium lead to a zero baryon asymmetry. Keeping CPT symmetry as a symmetry of nature, then a non-zero asymmetry can be generated if there is departure from chemical equilibrium, i.e. if there is an asymmetry between the baryon and antibaryon chemical potentials. A way to achieve this, is for the interactions $2B \to 2\overline{B}$ to go out-of-equilibrium, $\mu_B \neq \mu_{\overline{B}}$.

In fact, as noted by [60], even if baryon-number-violating interactions were in chemical equilibrium, $\mu_B = 0$, a residual non-zero relic baryon and antibaryon number

density due to freeze-out in an expanding universe at the level of

$$\frac{n_B}{n_\gamma} = \frac{n_{\overline{B}}}{n_\gamma} \approx 10^{-20}, \tag{2.9}$$

is possible. This number raises two conceptual issues though. Firstly, it does not solve the question of the measurement of the baryon-to-photon ratio $\eta_B \sim 10^{-10}$, ten orders of magnitude larger. Secondly, this result would suggest a baryon-symmetric universe. However, equal amounts of baryon and antibaryon in the universe would generate a large amount of energetic gamma rays emanating from baryon-antibaryon annihilation, which we would be able to detect. The lack of such observations on the scale of the observable universe would imply the separation of matter and antimatter into patches on a very large scale. The problem then becomes that of finding the mechanism that generates such a large scale separation.

Given that those two problems are significant and demand conceptually unnatural solutions, it seems more natural to assume interactions processes simply go out of equilibrium.

2.2   Boltzmann Equations

Unlike CP-violation and baryon number violation, which are *static* conditions implemented at the level of the Lagrangian, departure from equilibrium is an intrinsic *dynamical* condition. To predict the baryon asymmetry it is necessary to precisely track the number density of each species of particles, which is done using a set of Boltzmann equations [61]. In the following, we are going to describe the general approach to develop Boltzmann equations for number densities in an expanding universe.

In general, probability densities can be functions of $t, \vec{x}, \vec{p}$, and their time evolution given by the total time derivative df/dt, with the total derivative,

$$\frac{d}{dt} = \frac{\partial}{\partial t} + \frac{1}{m}\vec{p} \cdot \vec{\nabla}_x + \vec{F} \cdot \vec{\nabla}_p. \tag{2.10}$$

The Liouville theorem [61], which can be formally proven using Hamilton's equations of motion, asserts the conservation of the phase space density,

$$\frac{d}{dt} f(t, \vec{x}, \vec{p}) = 0. \tag{2.11}$$

The generalization of the Liouville theorem to curved space-time coordinates $(t, \vec{x}) = x^\mu$, and energy-momentum coordinates $(E, \vec{p}) = p^\nu$, asserts the conservation of the number of particles along a geodesic characterized by the proper time τ, [62],

$$\frac{d}{d\tau} f(x^\mu, p^\nu) = \left[\frac{dx^\mu}{d\tau} \frac{\partial}{\partial x^\mu} + \frac{dp^\nu}{d\tau} \frac{\partial}{\partial p^\nu} \right] f(x^\mu, p^\nu) = 0, \tag{2.12}$$

This equation is general, and in cases where there is no external force with no external force, the particles are subject to the free geodesic equation,

$$\frac{dp^\nu}{d\tau} = -\Gamma^\nu_{\alpha\beta} p^\alpha p^\beta, \quad \frac{dx^\mu}{d\tau} = p^\mu, \tag{2.13}$$

where the $\Gamma^\mu_{\alpha\beta}$ coefficients are the connection Christoffel symbols associated to the spacetime metric $g_{\mu\nu}$,

$$\Gamma^\mu_{\alpha\beta} = \frac{1}{2} g^{\mu\nu} \left[\frac{\partial g_{\alpha\nu}}{\partial x^\beta} + \frac{\partial g_{\beta\nu}}{\partial x^\alpha} - \frac{\partial g_{\alpha\beta}}{\partial x^\nu} \right]. \tag{2.14}$$

For an isotropic and homogeneous universe, the spatial dependence $\vec{x}$ of the phase space density drops out, and only the magnitude of the 3-momentum $|\vec{p}|$ is relevant,

$$\frac{d}{d\tau} f(t, |\vec{p}|) = \left[E \frac{\partial}{\partial t} - \Gamma^i_{\alpha\beta} p^\alpha p^\beta \frac{\partial}{\partial p^i} \right] f(t, |\vec{p}|) \quad , \quad E = \sqrt{|\vec{p}|^2 + m^2}. \tag{2.15}$$

For a flat, expanding universe, the metric can be taken to be Friedman-Lemaître-Robertson-Walker [63],

$$ds^2 = -dt^2 + a(t) \left[dr^2 + r^2 d\Omega^2 \right], \tag{2.16}$$

where the scale factor $a(t)$ characterizes the expansion of the universe. The expansion rate is measured by the Hubble rate, $H(t) = \dot{a}(t)/a(t)$. In this metric, the only non-zero spatial Christoffel symbols are

$$\Gamma^0_{ij} = \delta_{ij} a^2 H \quad , \Gamma^i_{0j} = \Gamma^i_{j0} = \delta^i_j H, \tag{2.17}$$

leading to the relativistic Boltzmann equation in an expanding universe,

$$E \frac{\partial f(t, |\vec{p}|)}{\partial t} - H |\vec{p}|^2 \frac{\partial f(t, |\vec{p}|)}{\partial E} = 0. \tag{2.18}$$

with the Hubble rate $H = \sqrt{\rho\, 8\pi G/3}$, where ρ is the energy density and G is Newton's constant. The early universe was dominated by relativistic (massless) particles whose energy density is $\rho = g_* T^4 \pi^2/30$, with g_* the effective number of degrees of freedom in the plasma, and the temperature dependence of the Hubble rate,

$$H(T) = T^2 \sqrt{\frac{8\pi^3 g_*}{90 M_p^2}}, \tag{2.19}$$

with the Planck mass $M_p = 1/\sqrt{G}$. The Maxwell-Boltzmann, Fermi-Dirac, and Bose-Einstein equilibrium densities for massless particles are all examples of densities that satisfy the conservation equation, Eq. (2.18). Deviations from the conservation of the equilibrium densities are caused either by the mass of particles, or by collisions. Collisions are included by adding the collision term $C[f]$,

$$E\frac{\partial f(t, |\vec{p}|)}{\partial t} - H|\vec{p}|^2 \frac{\partial f(t, |\vec{p}|)}{\partial E} = C[f]. \tag{2.20}$$

Dividing both sides by E, and integrating over the phase space gives the integrated Boltzmann equation [64],

$$\frac{\partial n(t)}{\partial t} + 3H n(t) = g\int \frac{d^3 p}{(2\pi^3)^3 E} C(f), \quad n(t) = g\int \frac{d^3 p}{(2\pi)^3} f(t, |\vec{p}|). \tag{2.21}$$

where g counts the number of degrees of freedom of the particle. Integration by parts has been used in order to obtain the factor $3H$ on the left hand side. In particular, the Maxwel-Boltzmann distributions lead to the equilibrium number densities for a particle of mass m and for photons,

$$n^{eq} = \frac{gm^3}{2\pi^2}\frac{T}{m}K_2\left(\frac{m}{T}\right), \qquad n_\gamma^{eq} = \frac{g_\gamma}{\pi^2}T^3. \tag{2.22}$$

Boltzmann expressed the collision term in the integrated Boltzmann equation, Eq. (2.21) via the *Stosszahlansatz* (collision number hypothesis) [61],

$$\gamma_i = -\sum_{m,n}\left(\gamma_{i\to mn} - \gamma_{mn\to i}\right) - \sum_a \sum_{m,n}\left(\gamma_{ia\to mn} - \gamma_{mn\to ia}\right) + \cdots, \tag{2.23}$$

where the $\gamma_{ia\to mn\cdots}$ are thermal averaged cross sections, related to the interaction

amplitude in the following way,

$$\gamma_{ia\to mn\cdots} = \int d\Pi_{ia} d\tilde{\Pi}_{mn\cdots} |i\mathcal{M}_{ia\to mn\cdots}|^2 f_i f_a (1 \pm f_m)(1 \pm f_n)\cdots \tag{2.24}$$

where $i\mathcal{M}_{ia\to mn\cdots}$ is an S-matrix element, and the phase space integrals are

$$\int d\Pi_{ia} \equiv g_i g_a \int \frac{d^3 p_i}{(2\pi)^3 2E_i} \frac{d^3 p_a}{(2\pi)^3 2E_a},$$
$$\int d\tilde{\Pi}_{mn\cdots} \equiv \int \frac{d^3 p_m}{(2\pi)^3 2E_m} \frac{d^3 p_n}{(2\pi)^3 2E_n} \cdots (2\pi)^4 \delta(p_i + p_a - p_m - p_n - \cdots). \tag{2.25}$$

The '+' sign in $(1 \pm f)$ is for bosons, and the '-' for fermions. These are the induced emission and Pauli blocking factors respectively [65]. We will assume that the gas of particles is dilute enough to use the classical Maxwell-Boltzmann approximation, $1 \pm f \approx 1$. For the particle species 'i', the phase space and number densities are,

$$f_i = e^{(\mu_i - E)/T}, \quad n_i = e^{\mu_i/T} g_i \int \frac{d^3 p}{(2\pi)^3} e^{-E/T} = e^{\mu_i/T} n_i^{eq}. \tag{2.26}$$

In other words we have the relation $e^{\mu_i/T} = n_i/n_i^{eq} = f_i/f_i^{eq}$, where f^{eq} refers to the Maxwell-Boltzmann distribution at $\mu = 0$. In thermal equilibrium, μ_i is the chemical potential and is conserved in the interaction. Away from chemical equilibrium, though, μ_i will be determined through the Boltzmann equation. We can thus make the following approximation,

$$f_i f_a (1 \pm f_m)(1 \pm f_n)\cdots \approx e^{(-E_i - E_a)/T} e^{(\mu_i + \mu_a)/T} = f_i^{eq} f_a^{eq} \frac{n_i}{n_i^{eq}} \frac{n_a}{n_a^{eq}}, \tag{2.27}$$

and,

$$\gamma_{ia\to mn} = \frac{n_i}{n_i^{eq}} \frac{n_a}{n_a^{eq}} \gamma_{ij\to mn}^{eq}, \tag{2.28}$$

where γ^{eq} is given for $f_i = f_i^{eq}$. For decays and $2-2$ scatterings, the thermal cross sections take the form,

$$\gamma_{i\to mn}^{eq}(T) = n_i^{eq} \Gamma_{i\to mn} \left\langle \frac{M_i}{E} \right\rangle = n_i^{eq} \frac{K_1(z_i)}{K_2(z_i)} \Gamma_{i\to mn},$$
$$\gamma_{ia\to mn}^{eq}(T) = n_i^{eq} n_a^{eq} \langle v\sigma_{ia\to mn\cdots} \rangle = g_i g_a \frac{T^4}{32\pi^4} \int_{w_{min}}^{\infty} dw \sqrt{w} K_1\left(\sqrt{w}\right) \hat{\sigma}_{ij\to mn}\left(w\frac{m_i^2}{z_i^2}\right), \tag{2.29}$$

where $z_i = m_i/T$, $w = s/T^2$, and $K_{1,2}(z)$ are the modified Bessel functions of the second kind. The decay rate $\Gamma_{i \to mn}$ is calculated in the center of mass frame of particle 'i', the ratio $\langle m_i/E_i \rangle = K_1(z_i)/K_2(z_i)$ is the thermal average of the Lorentz factor between the center of mass frame and any other frame [66, 64, 67]. We have defined the reduced cross section,

$$\hat{\sigma}_{ia \to mn}(s) = \frac{1}{s} \delta \left(s, m_i^2, m_a^2 \right) \sigma_{ia \to mn}(s), \qquad \delta(a, b, c) = (a - b - c)^2 - 4bc. \quad (2.30)$$

It is convenient to switch to the comoving system of variables,

$$Y_i = \frac{n_i}{n_\gamma^{eq}},$$
$$Y_i^{eq} = \frac{n_i^{eq}}{n_\gamma^{eq}} = \frac{g_i}{2g_\gamma} z_i^2 K_2(z_i). \quad (2.31)$$

With these variables, the left-hand side of the Boltzmann equation, Eq. (2.21), transforms to $n_\gamma^{eq} z_i H \partial Y_i / \partial z_i$, and the full equation now reads

$$n_\gamma^{eq} z_i H \frac{\partial Y_i}{\partial z_i} = - \sum_{m,n} \left(\frac{Y_i}{Y_i^{eq}} \gamma_{i \to mn}^{eq} - \frac{Y_m}{Y_m^{eq}} \frac{Y_n}{Y_n^{eq}} \gamma_{mn \to i}^{eq} \right)$$
$$- \sum_a \sum_{m,n} \left(\frac{Y_i}{Y_i^{eq}} \frac{Y_a}{Y_a^{eq}} \gamma_{ia \to mn}^{eq} - \frac{Y_m}{Y_m^{eq}} \frac{Y_n}{Y_n^{eq}} \gamma_{mn \to ia}^{eq} \right), \quad (2.32)$$

In addition, we can define the decay and scattering functions [66],

$$D_{i \to mn} \equiv \frac{\gamma_{i \to mn}^{eq}}{n_\gamma^{eq} H} = z_i^2 Y_i^{eq} \frac{K_1(z_i)}{K_2(z_i)} K_{i \to mn}, \qquad K_{i \to mn} \equiv \frac{\Gamma_{i \to mn}}{H_i},$$
$$S_{ia \to mn} \equiv \frac{\gamma_{ia \to mn}^{eq}}{n_\gamma^{eq} H} = \frac{g_i g_a}{g_\gamma} \frac{m_i}{H_i} \frac{1}{32\pi^2} z_i \int_{w_{min}}^{\infty} dw \sqrt{w} K_1 \left(\sqrt{w} \right) \hat{\sigma}_{ij \to mn} \left(w \frac{m_i^2}{z_i^2} \right). \quad (2.33)$$

The Hubble rate $H_i = H(T = m_i)$. Through the Hubble time $t_i = 1/H_i$, we have a notion of the time scale before the equilibrium density of the massive particle 'i' is Boltzmann suppressed. This is to be compared with the natural time scale set by the particle lifetime $\tau_i = 1/\Gamma_{i \to mn}$. If the lifetime is larger than the Hubble time, $\tau_i > t_i$, we anticipate a number density excess relative to equilibrium. Thus the *equilibrium parameter* $K_{i \to mn} \equiv \Gamma_{i \to mn}/H_i$, as defined above, characterizes Sakharov's non-equilibrium condition. We follow the literature by using the notation K for the equilibrium parameters, to be distinguished from the modified Bessel function $K_i(z)$.
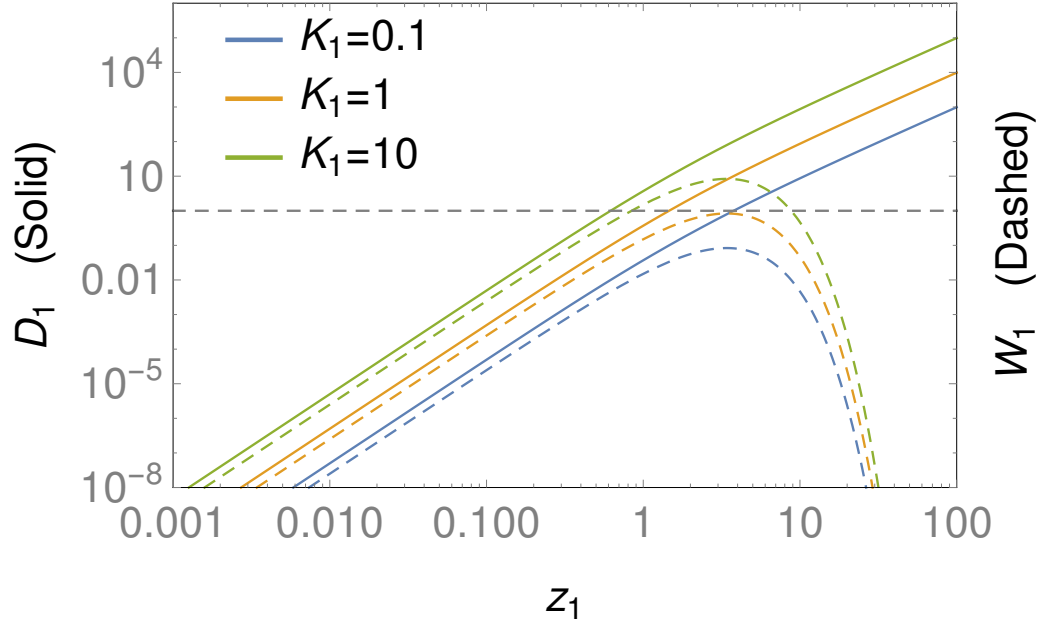
Figure 2.1: Thermal averaged decays (solid) and inverse decays (dashed) as a function of M_1/T, for various values of the equilibrium parameter $K_1 = \Gamma_{N_1}/H_1$.

The equilibrium parameter is used to quantify the strength of decays and inverse decays, but cannot be used to assess the equilibrium conditions because it compares the zero-temperature decay rate to the Hubble rate. Instead, a careful equilibrium assessment ought to compare the thermally averaged rates to the Hubble rate. For decays, this ratio is measured by the function $D_{i \to mn}$, and for decays this ratio is given by $S_{ia \to mn}$. Therefore, decays and scatterings are in equilibrium if

$$D_{i \to mn} > 1, \quad S_{ia \to mn} > 1. \tag{2.34}$$

A plot of the decay functions for various equilibrium parameters is shown in Fig. 2.1.

Before closing this section, it is important to note the shortcomings of this approach. Most notably, the Boltzmann equations are based on a classical treatment of the densities, and fail to account for quantum kinetic effects. Moreover, the decay rates and scattering cross section are calculated using zero temperature quantum field theory, which are then embedded in the Boltzmann equations which do capture thermal effects.

In spite of the shortcomings, the thermal classical Boltzmann equations using zero-temperature quantum field theory captures the essential dynamics of a model. Therefore, this approach is acceptable when the question posed is about the main

features of a theory, rather than precise predictions, which is our case.

2.3 Theories of Baryogenesis

In this section we are going to introduce some popular theories of baryogenesis, highlight their advantage as well as their shortcomings.

2.3.1 GUT Baryogenesis

Grand Unified Theories (GUTs) attempt to unify bosons and leptons into the same fundamental multiplet, [42, 68, 69] by enbedding the Standard Model gauge group $SU(3) \times SU(2)_L \times U(1)_Y$ into a larger gauge group, e.g. $SU(5)$ or $SO(10)$. Fundamental representations are mixtures of leptons and quarks. The interaction between the gauge field and the matter multiplets induces couplings between leptons and quarks, and opens up interaction channels that break lepton and baryon number. The consequence is that GUT theories naturally contain baryon and lepton number violation, as well as many more physical CP-phases than in the Standard Model. The energy scale of the symmetry breaking of the GUT groups, $M_{\mathrm{GUT}} = 10^{15}\mathrm{GeV}$, provides the natural scale for the GUT gauge bosons, $m \sim M_{\mathrm{GUT}}$. As the universe cools down below such energies, the theory will automatically provide massive particles decaying out-of-equilibrium. Thus, GUT theories naturally contain all three ingredients for a successful theory of baryogenesis. However, there are several issues with this kind of theories. One is the issue of testability due to the very high energy scales that may never be probed in any colliders, present or future. Another issue is linked with inflation, reheating and ultimately Big Bang Nucleosynthesis (BBN) [70]. As the current picture goes, the phase of inflation [71] would be driven by the inflaton field, and ends when the inlfaton decays and populates the universe with particles, during a phase called reheating. If GUT baryogenesis theories are to be viable, the reheating temperature must be high enough to produce the heavy states, i.e. one needs $T_{\mathrm{reheating}} \sim M_{\mathrm{GUT}}$. It has been theorized that at these energies, theories beyond the Standard Model can produce a large number of particle states, and the ones that interact only weakly will be out of equilibrium and stay in over abundance. This can be an issue if those particles decay late, as they can potentially impact the Big Bang Nucleosynthesis and modify the prediction of the production of light elements such as Hydrogen, Helium, Deuterium. One famous example of such particle is the Gravitino

within Supersymmetry, [72].

2.3.2   Electroweak baryogenesis

Electroweak baryogenesis generates the baryon asymmetry at the scale of the Electroweak phase transition, i.e. with a critical temperature $T_{EW} \sim 10^2 \text{GeV}$, [73, 74]. Above the critical temperature, the SM group $SU(3)_c \times SU(2)_L \times U(1)_Y$ is unbroken, and below the group is broken down to $SU(3)_c \times U(1)_{em}$. The theory hypothesizes that the transition occurs via bubble nucleation, i.e. that the transition is a first order phase transition. The broken phase is inside the bubbles, that is the phase we live in, meanwhile the outside phase is the symmetric phase. As the bubbles grow, they fill up the universe until the whole universe is in the broken phase. The generation of baryons happens during the transition. As we are going to see in Section 2.4, baryon violation is provided by the sphaleron processes of the Standard Model, which are in equilibrium and fast outside the bubbles, but their rates plunges inside the bubble. The particles outside the bubbles interact with the bubble walls to enter the new phase, and this interaction breaks CP. Thus, as the bubble wall sweeps the universe, it filters particles and leave the inside phase with a baryon asymmetry. Out-of-equilibrium is controlled by the strength of the phase transition. A strong first order transition is required for the sphalerons to be efficiently suppressed inside the bubble wall, and prevent the washout of the baryon asymmetry. The combination of these three factors creates a lasting baryon asymmetry inside the bubble, i.e. creates us. Nevertheless, the theory does have issues. The main one coming from the first order phase transition itself, its strength is measured by the ratio v_{EW}/T_{EW} of the vev and the temperature at the critical temperature. Besides, inside the bubble wall, the rate of the sphalerons is related to it via

$$\Gamma_{sphaleron} \sim e^{-E_{sphaleron}/T} \qquad , \qquad \frac{E_{sphaleron}}{T} \propto \frac{v}{T} \quad . \qquad (2.35)$$

Therefore, in order for the baryon asymmetry not to be washed out by the sphalerons inside the bubble, we require $\Gamma_{sphaleron}$ to be small, in other words, we need at least $v_{EW}/T_{EW} > 1$. In turn, that bound turns into a bound on the Higgs mass $m_H \lesssim 75 \text{GeV}$ [42]. This is in contradiction with the experimental measurements of the Higgs mass, $m_H = 125 \text{GeV}$ [1, 2, 38]. In other words, the Standard Model alone does not go through a strongly first order phase transition. In order for that it requires theories beyond the Standard Model, like supersymmetric theories for example.
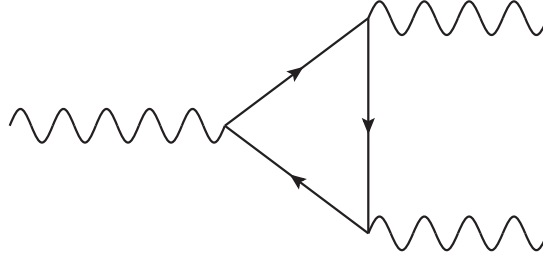
Figure 2.2: Triangle diagrams responsible for the chiral anomaly.

2.4 Baryogenesis via Leptogenesis

In the previous section we described two examples of baryogenesis models. This section introduces a third class of models, referred to as Leptogenesis. The main premise of leptogenesis is to generate an asymmetry in the lepton sector, which gets processed into the baryon asymmetry η_B [45]. Before going into the details of leptogenesis dynamics, though, the following section introduces SM processes called sphalerons that are able to efficiently convert the lepton asymmetry.

2.4.1 Anomalies and sphalerons

Anomalies refer to symmetries which are symmetries of the classical theory, but break down as the theory is quantized [75]. More specifically, if a Lagrangian $\mathcal{L}(\phi, \partial_\mu \phi)$ is symmetric under a symmetry group G, then the field transformations, $\phi' = U\phi$, $U \in G$ leave the lagrangian unchanged $\mathcal{L}(\phi, \partial_\mu \phi) = \mathcal{L}(\phi', \partial_\mu \phi')$, up to a total derivative which has no effect on the action. To that symmetry corresponds a Noether current, j^μ, which is a conserved current of the classical theory in the sense that, $\partial_\mu j^\mu = 0$. There exist symmetries which are conserved at the classical level but that are broken at the quantum level due to loop corrections, thus giving rise to an *anomaly*

$$\partial_\mu j^\mu \neq 0. \tag{2.36}$$

Anomalies of local gauge symmetries point to an inconsistency in the quantum field theory and must be avoided. Indeed, local gauge symmetries are redundancies in the physical description of matter-gauge interactions, and a breakdown of the redundancies is a sign of a pathological theory [76].

Let's first illustrate the situation with a gauge theory coupling massless fields, ψ, to an abelian gauge field, A_μ. The ensuing theory is Quantum Electrodynamics with

the lagrangian,

$$\mathcal{L} = \overline{\psi}\gamma^\mu \partial_\mu \psi - \frac{1}{4}F_{\mu\nu}F^{\mu\nu}. \tag{2.37}$$

with the abelian field strength $F_{\mu\nu} = \partial_\mu A_\nu - \partial_\nu A_\mu$. This lagrangian is symmetric under the global symmetry,

$$\psi \to e^{i\alpha}\psi, \quad j^\mu = \overline{\psi}\gamma^\mu\psi. \tag{2.38}$$

where j^μ is the associated Noether current. Because the fermion is massless, the lagrangian is also symmetric under the global symmetry, called the chiral symmetry

$$\psi \to e^{i\beta\gamma_5}\psi, \quad j_5^\mu = \overline{\psi}\gamma^\mu\gamma^5\psi \tag{2.39}$$

with j_5^μ the associated Noether chiral current. At the classical level, the chiral symmetry can only be broken by non-zero fermion masses. At the quantum level, we can show that the current conservation equation to take the form [77],

$$\partial_\mu j_5^\mu = -\frac{g^2}{16\pi^2}\epsilon_{\mu\nu\rho\sigma}F^{\mu\nu}F^{\rho\sigma} = -\frac{g^2}{16\pi^2}\tilde{F}_{\mu\nu}F^{\mu\nu}. \tag{2.40}$$

This is known as the Adler-Bell-Jackiw anomaly [78, 79, 80], whose dominant diagrams are the so-called *triangle* diagrams, shown in Fig. 2.2. It turns out those diagrams are the only contributions to the anomaly, the one-loop result is exact. The sum of the anomalies of all chiral currents are required to vanish in order for a theory to be anomaly free.

Here, we are interested in the global baryon and lepton B and L symmetries, which are conserved in the classical Standard Model, with associated Noether currents,

$$j_B^\mu = \frac{1}{3}\sum_i \left(\overline{Q}_{Li}\gamma^\mu Q_{Li} - \overline{u}_{Ri}\gamma^\mu u_{Ri} - \overline{d}_{Ri}\gamma^\mu d_{Ri}\right),$$
$$j_L^\mu = \sum_i \left(\overline{L}_{Li}\gamma^\mu L_{Li} - \overline{e}_{Ri}\gamma^\mu e_{Ri}\right), \tag{2.41}$$

where Q_L, L_L are the quark and lepton left-handed doublets, and u_R, d_R, e_R are the up, down, and electron right-handed singlets. The baryon number of a left-handed quark is $B(Q_L) = 1/3$ and that of a right-handed quark is $B(u_R) = B(d_R) = -1/3$, because left- and right-handed representations are conjugate of each other. The sum over quarks involves the sum over all flavors and all colors, while the sum over leptons
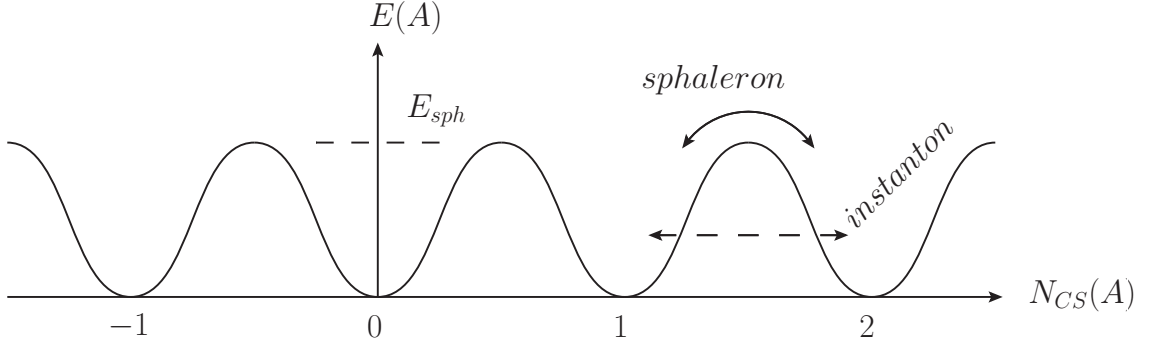
Figure 2.3: Sketch of the energy of a gauge field configuration A_μ as a function of the Chern-Simons number $N_{CS}(A)$ associated to that configuration.

only involve the sum over flavors. Note that those currents have specific chiralities which are enforced with projectors $P_{L,R} = (1 \pm \gamma_5)/2$. Therefore, the lepton and baryon currents are anomalous due to the anomalous chiral currents, whose anomalies receive contributions from the triangular diagrams calculated to be,

$$\partial_\mu j_B^\mu = \partial_\mu j_L^\mu = \frac{N_F}{32\pi^2} \left(g^2 \epsilon^{\mu\nu\rho\sigma} W_{\mu\nu}^a W_{\rho\sigma}^a - (g')^2 \epsilon^{\mu\nu\rho\sigma} B_{\mu\nu} B_{\rho\sigma} \right), \qquad (2.42)$$

where $W_{\mu\nu}^a$ are the three $SU(2)_L$ gauge fields, $a = 1, 2, 3$, $B_{\mu\nu}$ is the $U(1)_Y$ gauge field and where the N_F is the number of generations, $N_F = 3$ in the Standard Model. This result shows that, while the charge $B - L$ remains conserved, the charges B, L and $B + L$ are anomalous.

We might think that, being a divergence term, the anomaly would have no effect on the action, since the space-time integral of a divergence involves integrating the fields that vanish at infinity. However, the non-abelian character of the gauge group implies a non-trivial gauge field configuration, and the space-time integral of $\partial_\mu j^\mu$ may not vanish. In fact, the baryon and lepton anomalies are related to the total derivative of the Chern-Simons current K^μ,

$$\partial_\mu j_B^\mu = \partial_\mu j_L^\mu = N_F \partial_\mu K^\mu. \qquad (2.43)$$

The integral of the time component of the Chern-Simons number gives the Chern-Simons which characterizes different vacuum configurations,

$$\int d^3x K^0 = N_{CS}, \qquad (2.44)$$

resulting from the non-trivial vacuum configuration of the gauge group. Non-abelian gauge group have several degenerate ground states characterized by a Chern-Simons number and separated by energy barriers. A sketch of the gauge field configuration is shown in Fig. 2.3. Thus, integrating the baryon anomaly over space and time shows that

$$\int_{t_i}^{t_f} d^3x \ \partial_\mu j_B^\mu = B(t_f) - B(t_i) = N_F \left[N_{CS}(t_f) - N_{CS}(t_i) \right], \qquad (2.45)$$

and similarly for the lepton $L(t_f) - L(t_i) = N_F \left[N_{CS}(t_f) - N_{CS}(t_i) \right]$. There exist two processes which allow the gauge theory to change the vacuum's Chern-Simons number, $N_{CS}(t_f) - N_{CS}(t_i) = \pm 1$: the sphaleron which hops over the barrier, and the instanton [81] which tunnels through the barrier (see [82, 83, 84] for detailed reviews). Each of those processes change the baryon and lepton numbers by

$$\Delta B = \Delta L = \pm N_F. \qquad (2.46)$$

In the Standard Model the number of families is $N_F = 3$, so the Standard Model sphalerons and instantons violate the baryon and lepton numbers by 3, *viz* they create 9 quarks and 3 leptons.

The instanton rate is always suppressed by virtue of being a tunneling process. However, while suppressed at low temperature, the sphaleron process is enhanced above a certain threshold thanks to thermal fluctuations [85]. The sphaleron rates above and below the electroweak critical temperature are, [86, 87, 88, 89]

$$\begin{aligned} \frac{\Gamma_{sphaleron}}{V} &\sim e^{-E_{sphaleron}/T}, \quad T < T_{EW} \\ \frac{\Gamma_{sphaleron}}{V} &\sim \alpha_w^5 T^4 \sim 10^{-6} T^4, \quad T > T_{EW} \end{aligned} \qquad (2.47)$$

with $\alpha_w = g^2/4\pi$, and the sphaleron energy is related to the electroweak symmetry breaking scale,

$$E_{sphaleron} \approx \frac{8\pi v}{g}, \qquad (2.48)$$

where $v = 174\text{GeV}$ is Higgs vacuum expectation value. The fast high temperature sphaleron rate provides an efficient mechanism to break baryon/lepton number conservation.

It turns out, that sphaleron processes also relate baryon and lepton numbers. The

equilibrium number densities are obtained from equilibrium phase space densities. In particular, for massless particles, the asymmetry between particle and antiparticle densities are given by their chemical potential [90],

$$n - \overline{n} \approx \frac{gT^2}{\pi^2} 2\mu\zeta(2) \quad \text{(bosons)},$$
$$n - \overline{n} \approx \frac{gT^2}{\pi^2} \mu\zeta(2) \quad \text{(fermions)},$$

(2.49)

with the Zeta function $\zeta(2) = \pi^2/6$. Since the SM particles are massless above the electroweak phase transition, it is possible to determine chemical potentials and obtain number densities from the above equations. As introduced earlier, the chemical potentials are conserved in chemical reactions that are in equilibrium. At high temperatures, fast Yukawa and gauge interactions maintain the gauge bosons, leptons, and baryons in equilibrium. Among all those interactions, only the sphaleron violates baryon and lepton number conservation [91]. This implies a host of constraints among the chemical potentials.

Using all those conditions, the baryon number B, the lepton number L, the electric charge Q and the hypercharge I can be calculated and related to the baryon and lepton number to the $B - L$ charge. Especially important to leptogenesis, the baryon and lepton charges are related via,

$$B = \frac{8N + 4m}{22N + 13m} (B - L), \quad L = -\frac{14N + 9m}{22N + 13m} (B - L),$$

(2.50)

and,

$$B = -L \frac{8N + 4m}{14N + 9m}.$$

(2.51)

For $N = 3$ flavors, and $m = 1$ Higgs doublet, we find

$$B = -L \frac{28}{51}.$$

(2.52)

Normalize the baryon and lepton numbers with the photon number densities, this relation relates the baryon asymmetry to the lepton asymmetry $\eta_L \simeq -\eta_B 51/28 \simeq -1.09 \cdot 10^{-9}$. The sign of the asymmetry is ultimately controlled by the sign of the CP-asymmetry, which is a function of the CP-phases. Therefore, in subsequent calculations we will look at the magnitude of the asymmetry, $|L|$.

2.5 Vanilla Leptogenesis

The simplest model of baryogenesis via leptogenesis is referred to as vanilla leptogenesis [45]. It makes use of the CP-violation, lepton number and flavor ingredients of the minimal model of neutrinos beyond the Standard Model. The premise of the model relies on the type-I see-saw mechanism whereby three massive right-handed neutrino fields are introduced to give a mass to the neutrino via a Yukawa coupling.

The dynamical processes by which vanilla leptogenesis generates a lepton asymmetry is inspired from GUT baryogenesis, whereby a heavy particle decays in the early universe CP-asymmetrically and lepton-number-asymmetrically. In vanilla leptogenesis, N_1 plays the role of the heavy particle decaying asymmetrically into leptons and antileptons. For that reason, this model is also called N_1-leptogenesis.

2.5.1 Lepton number violation and neutrino masses

Type-I see-saw mechanism generates the neutrino mass by coupling the left-handed neutrino ν_L to the right-handed neutrinos N_R, via a Yukawa coupling with the Higgs doublet,

$$\mathcal{L}_{Yuk} = -\lambda_{ij}\overline{N}_R^i P_L L^j \cdot H + h.c \longrightarrow \mathcal{L}_m = -m_{Dij}\overline{N}_R^i \nu_L^j + h.c \tag{2.53}$$

where the Dirac neutrino mass term develops after the Higgs acquires a vacuum expectation value, $m_{Dij} = \lambda_{ij} \langle H \rangle$. The lepton doublet is $L^j = (\nu_L^j, e_L^j)^T$, the Higgs doublet is $H = (H_+, H_0)^T$. In this notation, the scalar product stands for $L^j \cdot H = \epsilon_{\alpha\beta}L^{j\alpha}H^\beta$ with $\alpha, \beta = 1, 2$ the SU(2) indices, and $\epsilon_{\alpha\beta}$ the SU(2) invariant tensor. Because there are three left-handed neutrinos, it is simplest to postulate three right-handed neutrinos.

Since the neutrino has no electric charge and since right-handed fields are singlets under $SU(2)_L$, the right-handed neutrino is a singlet under the SM group, allowing the Majorana mass term,

$$\mathcal{L}_{\mathrm{Maj}} = -\frac{M_{ij}}{2}\overline{N}_R^{iC} N_R^j. \tag{2.54}$$

We use rotation freedom to go into the basis which diagonalises the Majorana mass term, and combining it with Yukawa-sourced mass term, we obtain the neutrino mass matrix,

$$\mathcal{L}_{\nu\ \mathrm{mass}} = -\frac{1}{2}\begin{pmatrix} \overline{\nu}_L & \overline{N}_R^C \end{pmatrix}\begin{pmatrix} 0 & m_D^\dagger \\ m_D & M \end{pmatrix}\begin{pmatrix} \nu_L \\ N_R \end{pmatrix} + h.c. \tag{2.55}$$

Each of the blocks are of dimension 3×3 in flavor space. This matrix can be diagonalised via a unitary transformation U relating the flavor states to the mass eigenstates [92, 93],

$$
\begin{pmatrix} \nu_L \\ N_R \end{pmatrix} = U \begin{pmatrix} \nu_L^m \\ N_R^m \end{pmatrix}, \quad U = \begin{pmatrix} -U_L & -m_D^\dagger M^{-1} U_R \\ M^{-1} m_D U_L & U_R \end{pmatrix}, \tag{2.56}
$$

Where $U_{L,R}$ are unitary matrices that diagonalize the left- and right-handed flavor sectors separately. Taking the characteristic scale of matrix elements such that $M \gg m_D$ leads us into the see-saw regime. Ignoring the subdominant corrections, the diagonalisation process leads to the diagonal block mass matrix

$$
\mathcal{L}_{\text{mass}} = -\frac{1}{2} \begin{pmatrix} \overline{\nu}_L^m & \overline{N}_R^m \end{pmatrix} \begin{pmatrix} U_L^\dagger m_D^\dagger M^{-1} m_D U_L & 0 \\ 0 & U_R^\dagger M U_R \end{pmatrix} \begin{pmatrix} \nu_L^m \\ N_R^m \end{pmatrix} + h.c. + \mathcal{O}\left(m_D^2 M^{-2}\right) \tag{2.57}
$$

In other words, this procedure gives rise to light and heavy mass eigenstates whose masses parametrically scale as $M_{\text{light}} \sim m_D^2/M$, and $M_{\text{heavy}} \sim M$, respectively. The associated states are,

$$
\nu_L^m \sim -U_L \nu_L, \quad N_R^m \sim U_R N_R. \tag{2.58}
$$

The lightest mass eigenstate is mostly left-handed which we identify with the SM neutrinos. The heaviest mass eigenstate mostly contains right-handed components and are beyond the SM. From now on, the latter ones are referred to as the Right-Handed Neutrinos (RHNs).

The lepton field has lepton number one, $L(L) = 1$, while the Higgs field has zero lepton charge $L(H) = 0$. Assuming that the Yukawa interaction conserves lepton number, forces the charge assignment $L(N) = L(L) = 1$, and leads to the lepton content of the Majorana mass term to be $L(\mathcal{L}_{\text{Maj}}) = 2L(N) = 2$. Conversely, deciding that $L(N) = 0$ such that the Majorana mass term conserves lepton number, forces the charge assignment of the Yukawa to be $L(\mathcal{L}_{\text{Yuk}}) = -L(N) + L(L) = 1$. The bottom line is that, although the lepton charge assignment is arbitrary, only those physical observables that involve both $\{\lambda, M\}$ parameters are susceptible to generate a lepton asymmetry.
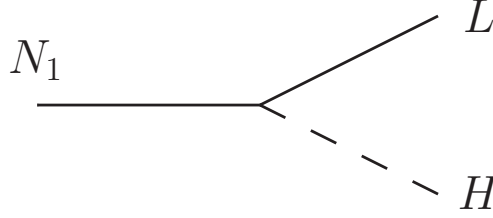
Figure 2.4: Tree level diagram for the N_1 decay process.

2.5.2 Vanilla CP-violation and Cutkosky rules

We now turn to the CP-phases of the RHN sector above. The coupling λ is a generic complex matrix, containing 9 real parameters, and 9 phases. By redefining the left-handed lepton doublet L, we can phase away 3 of the phases, leaving 6 physical phases in λ. Because of the real and diagonal Majorana mass terms, M_i, it is not possible to redefine the neutrino fields without affecting M_i, which would otherwise have allowed to remove two more phases from λ.

The decay-sourced CP-violation is a measure of the difference between the decay rate into leptons and the decay rate into antileptons. It is measured through the dimensionless ratio,

$$\epsilon_1 \equiv \frac{\Gamma(N_1 \to LH) - \Gamma(N_1 \to \overline{LH})}{\Gamma(N_1)}, \tag{2.59}$$

where the total decay rate $\Gamma(N_1) = \Gamma(N_1 \to LH) + \Gamma(N_1 \to \overline{LH})$. If we schematically write the decay probability amplitude for the decay into particle as $i\mathcal{M} = \gamma_0 + \gamma_1 I$, with some combination of coupling constants at tree level, γ_0, and at loop level, γ_1, and a loop function I which captures the loop kinematics, then the amplitude for the decay into antileptons is given by $i\overline{\mathcal{M}} = \gamma_0^* + \gamma_1^* I$. Since the final phase space integrals for two-body decay rates are trivial, the rates are proportional to the magnitude squared of the amplitudes, $\Gamma(N_1 \to LH) \propto |i\mathcal{M}|^2 = |\gamma_0|^2 + 2\mathrm{Re}\{\gamma_0\gamma_1^* I^*\}$, and $\Gamma(N_1 \to \overline{LH}) \propto |i\overline{\mathcal{M}}|^2 = |\gamma_0|^2 + 2\mathrm{Re}\{\gamma_0^*\gamma_1 I^*\}$, where the two-loop order has been ignored. Because the final phase space integrals account for kinematics only, they are the same for particles and antiparticles alike, and cancel out in the ratio for the CP-asymmetry giving,

$$\epsilon_1 = \frac{4 \ \mathrm{Im}\{I\} \ \mathrm{Im}\{\gamma_0\gamma_1^*\}}{2|\gamma_0|^2} + \mathcal{O}(\gamma_1^2). \tag{2.60}$$

This is showing that to lowest order, the decay-sourced CP-violation arises from the
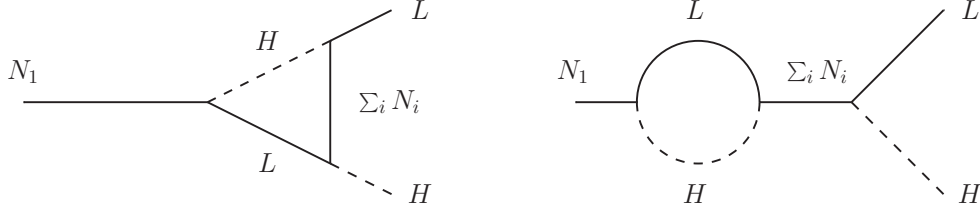
Figure 2.5: The one-loop vertex (left) and wave function (right) corrections to the RHN decay process. The interference of those loop diagrams with the tree level diagram leads to the CP-asymmetry.

interference between the tree level decay process and their one-loop level corrections.

The amplitudes of the tree level, $i\mathcal{M}_{tree}$, is shown in Fig. 2.4, and the vertex and wave function corrections, $i\mathcal{M}_{vertex}$ and $i\mathcal{M}_{wave}$, are shown in Fig. 2.5. The amplitudes take the form,

$$
\begin{aligned}
i\mathcal{M}_{tree} &= -i\epsilon_{\alpha\beta}\lambda_{ki}^*\overline{u}(k)P_R u(p), \\
i\mathcal{M}_{vertex} &= -i\epsilon_{\alpha\beta}\sum_j(\lambda^\dagger\lambda)_{ji}\lambda_{kj}^*\overline{u}(k)P_R\mathcal{J}_{vertex}u(p), \\
i\mathcal{M}_{wave} &= -i\epsilon_{\alpha\beta}\sum_j(\lambda^\dagger\lambda)_{ji}\lambda_{kj}^*\overline{u}(k)P_R\mathcal{J}_{wave}u(p),
\end{aligned}
\tag{2.61}
$$

where

$$
\begin{aligned}
\mathcal{J}_{vertex} &= iM_i\sqrt{r_{ji}}\int\frac{d^4l}{(2\pi)^4}\frac{\slashed{l}+\slashed{p}-\slashed{k}}{(l^2-M_j^2+i\epsilon)((p+l-k)^2+i\epsilon)((l-k)^2+i\epsilon)}, \\
\mathcal{J}_{wave} &= \frac{i}{M_i}\frac{2\sqrt{r_{ji}}}{1-r_{ji}}\int\frac{d^4l}{(2\pi)^4}\frac{\slashed{l}}{(l^2+i\epsilon)((l-p)^2+i\epsilon)},
\end{aligned}
\tag{2.62}
$$

with the momenta p and k being those of the external RHN and lepton respectively, while l is the momentum of the internal RHN, flowing "upwards".

The first step, is to calculate the decay rate, which is done as follows. First, we write down explicitly the amplitude square, and then to sum over the outgoing spins, and average over the incoming spins. This quantity is denoted X. In our case, there

is only 2 outgoing spins and two incoming spins, so that

$$X = \frac{1}{2} \sum_{k,\alpha,\beta} \sum_{spins} |i\mathcal{M}_{tree} + i\mathcal{M}_{vertex} + i\mathcal{M}_{wave}|^2$$

$$= (\lambda^\dagger\lambda)_{ii} M_i^2 + 2\text{Re}\left\{ \sum_j (\lambda^\dagger\lambda)_{ij}^2 \text{Tr}\left[P_R \mathcal{J}(\not{p} + M_i)\not{k} \right] \right\}. \tag{2.63}$$

where $\mathcal{J}$ can stand for either $\mathcal{J}_{\text{vertex}}$ or $\mathcal{J}_{\text{wave}}$, as expressed in Eq. (2.61). The traces simplify to $2\text{Tr}\{P_R \mathcal{J}(\not{p} + M_i)\not{k}\} = M_i \text{Tr}\{\mathcal{J}\not{k}\}$ because the trace of an odd number of γ^μ matrices vanishes. The phase space integrals for two-body decay processes is trivial, $\Gamma(N_i \to LH) = (|\vec{k}|/8\pi M_i^2)X$, and in the center of mass frame where $\vec{p} = 0$ and $|\vec{k}| = M_i/2$ we get the decay rate,

$$\Gamma_i \equiv \Gamma(N_i \to LH) + \Gamma(N_i \to \overline{LH}) = \frac{(\lambda^\dagger\lambda)_{ii}}{8\pi} M_i, \tag{2.64}$$

and giving the CP-asymmetry to be,

$$\epsilon_1 = \frac{1}{(\lambda^\dagger\lambda)_{ii}^2 M_i} \sum_j \text{Im}\left\{(\lambda^\dagger\lambda)_{ij}^2\right\} \text{Im}\left\{\text{Tr}\{\mathcal{J}\not{k}\}\right\}. \tag{2.65}$$

The calculation of the imaginary part can be done using the Cutkosky rules [94]. This technique relies on the fact that an imaginary part arises every time one of the internal lines is on-shell. Consider the integral

$$A(k) \equiv \int \frac{d^4q}{(2\pi)^4} \frac{iP(q,k)}{(p_1^2 - M_1^2 + i\epsilon)(p_2^2 - M_2^2 + i\epsilon)(p_3^2 - M_3 + i\epsilon)}, \tag{2.66}$$

where q represents an internal momentum, and k an external momentum and p_1, p_2, p_3 are functions of the external and internal momenta, and where $P(q,k)$ is a real function. Because $\epsilon \to 0^+$, each propagator factor is written using the identity $1/(a + i\epsilon) = \mathcal{P}1/a - i\pi\delta(a)$. For the sake of the argument, say p_1, p_2 are on-shell, $p_1^2 = M_1^2$ and $p_2^2 = M_2^2$, then the imaginary $2i\text{Im}\{A\}$ is obtained by retaining the

following terms,

$$\frac{1}{p_1^2 - M_1^2 + i\epsilon} \quad \longrightarrow \quad 2\pi i \delta(p_1^2 - M_1^2)\theta(p_1^0) \quad ,$$
$$\frac{1}{p_2^2 - M_2^2 + i\epsilon} \quad \longrightarrow \quad 2\pi i \delta(p_2^2 - M_2^2)\theta(p_2^0), \tag{2.67}$$
$$\frac{1}{p_3^2 - M_3^2 + i\epsilon} \quad \longrightarrow \quad \mathcal{P}\frac{1}{p_3^2 - M_3^2}.$$

Because of the delta functions the internal lines p_1, p_2 that are normally virtual become real, we obtain

$$\text{Im}\{A\} = -\frac{1}{8\pi^2}\int d^4q \frac{P(q,k)}{p_3^2 - M_3^2}\delta(p_1^2 - M_1^2)\delta(p_2^2 - M_2^2), \tag{2.68}$$

where we have omitted the step functions. Forcing the on-shell condition along internal in such way is called *cutting* the diagram. The Cutkosky rules consist in identifying all possible *cuts*, and adding their respective contributions to obtain the imaginary part. Applying the Cutkosky rules to the loop functions in Eq. (2.62) leads,

$$\text{Im}\{\text{Tr}\left[\mathcal{J}_{vertex}\slashed{k}\right]\} = -\frac{M_i\sqrt{r_{ji}}}{8\pi}\left[1 - (1 + r_{ji})\log\left(\frac{1 + r_{ji}}{r_{ji}}\right)\right],$$
$$\text{Im}\{\text{Tr}\left[\mathcal{J}_{wave}\slashed{k}\right]\} = -\frac{M_i\sqrt{r_{ji}}}{8\pi(1 - r_{ji})}. \tag{2.69}$$

and finally,

$$\epsilon_i = \sum_{j\neq i}\frac{\text{Im}\{(\lambda^\dagger\lambda)_{ji}^2\}}{8\pi(\lambda^\dagger\lambda)_{ii}}\sqrt{r_{ji}}\left[\frac{2 - r_{ji}}{1 - r_{ji}} - (1 + r_{ji})\log\left(\frac{1 + r_{ji}}{r_{ji}}\right)\right]. \tag{2.70}$$

2.5.3 Boltzmann equations for vanilla leptogenesis

Now that we have analyzed Sakharov's conditions of lepton, baryon number violation, and CP-violation, we are going to analyze in detail the condition of loss of equilibrium.

The final lepton asymmetry is a result of the competition between the CP-asymmetric RHN decays $N_1 \rightarrow LH$ ($\overline{LH}$) which generate to the lepton asymmetry, and the CP-asymmetric inverse decays LH ($\overline{LH}$) $\rightarrow N_1$ which wash-out the lepton asymmetry. We can distinguish two cases: the strong and weak washout regimes [66], measured

by the ratio of the decay rate to the Hubble rate in the temperature regime, $T \sim M_1$,

$$K_1 = \frac{\Gamma_{N_1}}{H(T = M_1)}. \tag{2.71}$$

In the strong washout, $K_1 \gg 1$, the decays and inverse decays are both fast and in equilibrium around $T \simeq M_1$. While the decays remain in equilibrium at lower temperatures, inverse decays go out of equilibrium due to the decreasing RHN abundance. In the weak washout, while the decays come in equilibrium around $T \sim M_1$, the inverse decays are always out of equilibrium.

In order to scheme the dynamics, we are going to assume a thermal right-handed neutrino initial abundance and a strong washout regime. The dynamics can be broken down in three phases:

- **Phase I**

$$T \gtrsim M_1 \tag{2.72}$$

  In this phase, the Boltzmann factor $e^{-M_1/T}$ reduces the equilibrium neutrino abundance, in turn causing the neutrino abundance to be thrown out of equilibrium. The consequence is that decays $N \to LH$ become dominant compared to the inverse decays $LH \to N_1$ in an attempt to restore equilibrium. Since the decays are dominant, a large lepton asymmetry is produced in this phase.

- **Phase II**

$$T \lesssim M_1 \tag{2.73}$$

  We have assumed a strong washout regime, $K_1 \gg 1$, meaning the decay rate is large enough to restore equilibrium. Since equilibrium is restored, the inverse decay rates are equal to the decay rates, resulting is a substantial washing out of the lepton asymmetry.

- **Phase III**

$$T \ll M_1 \tag{2.74}$$

  In this phase, the neutrino abundance is vanishingly small due to the exponential Boltzmann factor, thus freezing out all dynamics; there is not enough thermal energy for inverse decays $LH \to N_1$ to produce neutrinos, and the density of neutrinos is too small for decays $N_1 \to LH$ to have any effect. The result is that the lepton asymmetry freezes out, thus reaching its final abundance.

These dynamics differ slightly for different initial conditions and value of K_1. For a weak washout regime, the inverse decay processes never come into equilibrium, and the phase II is effectively inexistent. For a vanishing initial RHN abundance, the low RHN density suppresses the decays in Phase I, and the inverse decays have the effect of both increasing the RHN abundance and create a negative lepton asymmetry.

Vanilla leptogenesis without scattering processes

Here, we apply the Boltzmann equations developed in Sec. 2.2 to N_1-leptogenesis. Specifically, we adapt the equations for the neutrino N_1 abundance, Y_{N_1}, as well as two equations for the lepton and antilepton abundances, Y_L, $Y_{\overline{L}}$, from which we obtain the lepton asymmetry $Y_{L-\overline{L}} = Y_L - Y_{\overline{L}}$. We begin with equation of motion for the neutrino abundance, and then turn onto the lepton asymmetry.

As a first step, we ignore the scattering processes, thus the only processes affecting the neutrino abundance are the decays and inverse decays at tree level. As a direct application of Eq. (2.32), the Boltzmann equation for N_1 abundance Y_1 in response to one-to-two decays and inverse decays reads,

$$n_\gamma^{eq} z_1 H \frac{\partial Y_1}{\partial z_1}\bigg|_{1\leftrightarrow 2} = -\frac{Y_1}{Y_1^{eq}}\left[\gamma_{N_1 \to LH}^{eq} + \gamma_{N_1 \to \overline{LH}}^{eq}\right] + \frac{Y_H}{Y_H^{eq}}\left[\frac{Y_L}{Y_L^{eq}}\gamma_{LH \to N_1}^{eq} + \frac{Y_{\overline{L}}}{Y_{\overline{L}}^{eq}}\gamma_{\overline{LH} \to N_1}^{eq}\right].$$

$$(2.75)$$

The CPT theorem guarantees the equality $\Gamma(N_1 \to LH) = \Gamma(\overline{LH} \to \overline{N}_1)$, combined with the Majorana nature of $N_1 = \overline{N}_1$,

$$\Gamma(N_1 \to \overline{LH}) = \Gamma(LH \to N_1). \qquad (2.76)$$

The γ^{eq} functions as defined in Eq. (2.29) are related to the decay rate at zero temperature and the number densities of incoming particles, e.g. $\gamma_{N_1 \to \overline{LH}}^{eq} \sim n_{N_1}^{eq}\Gamma(N_1 \to \overline{LH})$. Because we have assumed the number densities to follow Maxwell-Boltzmann distributions, and because of energy conservation during the decay process, we can write $n_{N_1}^{eq} = n_L^{eq} n_H^{eq}$. In turn, we can write the thermal averaged inverse decay rate $\gamma_{LH \to N_1}^{eq} = \gamma_{N_1 \to \overline{LH}}^{eq}$ [95]. Furthermore, as described in the previous section, the decay CP-asymmetry in decays gives the relations

$$\Gamma(N_1 \to LH) = \frac{1 + \epsilon_1}{2}\Gamma(N_1), \quad \Gamma(N_1 \to \overline{LH}) = \frac{1 - \epsilon_1}{2}\Gamma(N_1) \qquad (2.77)$$

with the total decay rate $\Gamma(N_1) = \Gamma(N_1 \to LH) + \Gamma(N_1 \to \overline{LH})$. Those relations readily translate in the γ^{eq} functions, $\gamma^{eq}_{N_1 \to LH} = \gamma^{eq}_{N_1}(1 + \epsilon_1)/2$ and $\gamma^{eq}_{N_1 \to \overline{LH}} = \gamma^{eq}_{N_1}(1 - \epsilon_1)/2$. It follows that,

$$\frac{Y_L}{Y_L^{eq}} \gamma^{eq}_{LH \to N_1} + \frac{Y_{\overline{L}}}{Y_{\overline{L}}^{eq}} \gamma^{eq}_{\overline{LH} \to N_1} = -\frac{1}{2}\left(\frac{Y_L}{Y_L^{eq}} - \frac{Y_{\overline{L}}}{Y_{\overline{L}}^{eq}}\right)\epsilon_1 \gamma_1^{eq} + \frac{1}{2}\left(\frac{Y_L}{Y_L^{eq}} + \frac{Y_{\overline{L}}}{Y_{\overline{L}}^{eq}}\right)\gamma_1^{eq}. \tag{2.78}$$

Assuming the Higgs and light lepton abundances are close to equilibrium, we can approximate $(Y_L/Y_L^{eq} - Y_{\overline{L}}/Y_{\overline{L}}^{eq})\epsilon_1 \sim 0 + \mathcal{O}(\epsilon_1^2)$, and $(Y_L/Y_L^{eq} + Y_{\overline{L}}/Y_{\overline{L}}^{eq}) \sim 2 + \mathcal{O}(\epsilon_1^2)$, up to small corrections of order ϵ_1^2. We obtain the neutrino abundance equation,

$$n_\gamma^{eq} z_1 H \frac{\partial Y_1}{\partial z_1}\bigg|_{1 \leftrightarrow 2} = -\gamma_1^{eq}\left(\frac{Y_1}{Y_1^{eq}} - 1\right). \tag{2.79}$$

Turning into the lepton asymmetry Boltzmann equations, we proceed first by writing the equation for Y_L then for $Y_{\overline{L}}$. Including the $1 \leftrightarrow 2$ processes gives the equation,

$$\begin{aligned}
n_\gamma^{eq} z_1 H \frac{\partial Y_L}{\partial z_1}\bigg|_{1 \leftrightarrow 2} &= \frac{Y_1}{Y_1^{eq}} \gamma^{eq}_{N_1 \to LH} - \frac{Y_L}{Y_L^{eq}} \gamma^{eq}_{LH \to N_1}, \\
n_\gamma^{eq} z_1 H \frac{\partial Y_{\overline{L}}}{\partial z_1}\bigg|_{1 \leftrightarrow 2} &= \frac{Y_1}{Y_1^{eq}} \gamma^{eq}_{N_1 \to \overline{LH}} - \frac{Y_{\overline{L}}}{Y_{\overline{L}}^{eq}} \gamma^{eq}_{\overline{LH} \to N_1},
\end{aligned} \tag{2.80}$$

from which the equation for the asymmetry, $Y_{L-\overline{L}} = Y_L - Y_{\overline{L}}$ easily follows,

$$n_\gamma^{eq} z_1 H \frac{\partial Y_{L-\overline{L}}}{\partial z_1}\bigg|_{1 \leftrightarrow 2} = \epsilon_1 \gamma^{eq}_{N_1}\left(\frac{Y_1}{Y_1^{eq}} + 1\right) - \frac{Y_{L-\overline{L}}}{2Y_L^{eq}} \gamma^{eq}_{N_1}. \tag{2.81}$$

where again the assumption that $Y_L^{eq} = Y_{\overline{L}}^{eq}$ has been made under the premise that the equilibrium lepton chemical potential at high temperature is very small.

It is well known that this procedure leads to a pathological equation as it does not satisfy Sakharov's condition, since it generates a lepton asymmetry, $\partial Y_{L-\overline{L}}/\partial z_1 \neq 0$ even if $Y_1 = Y_1^{eq}$ [95]. The reason for this is that not all CP-violating processes occurring at $\mathcal{O}(\epsilon_1)$ have been taken into account. The solution to this problem is to include the s-channel scattering processes shown in Fig. 2.6, that violate lepton number by two units, $\Delta L = 2$. Because the mediator is more massive than the ingoing and outgoing particles, there exist a part of the parameters space where
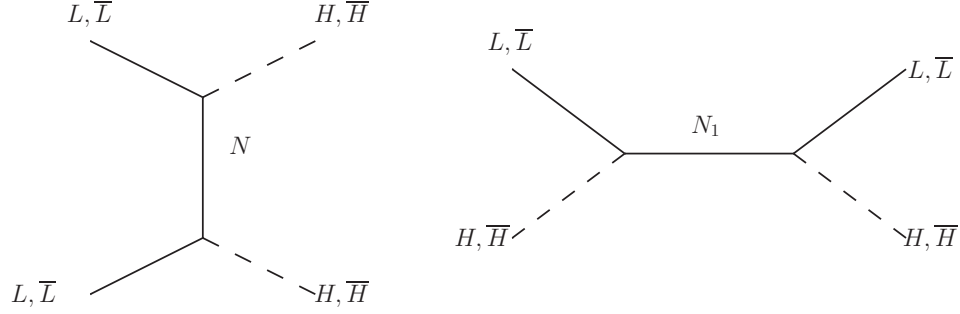
Figure 2.6: Set of $\Delta L = 2$ scattering processes that correct the double counting in the decay and inverse decay sector.

the mediator is created on-shell, at which point the scattering process is the chain of inverse decay followed by a decay [90], $LH \rightarrow N_1 \rightarrow \overline{LH}$, with cross section $\sigma^{\text{on-shell}}(LH \rightarrow \overline{LH}) = \Gamma(LH \rightarrow N_1)\text{Br}(N_1 \rightarrow \overline{LH})$. This on-shell contribution is CP-asymmetric at the level of $\sim \epsilon_1$,

$$\sigma^{\text{on-shell}}(LH \rightarrow \overline{LH}) = \left(\frac{1 - \epsilon_1}{2}\right)^2 \Gamma(N_1) \approx \frac{1 - 2\epsilon_1}{4}\Gamma(N_1). \tag{2.82}$$

Meanwhile the total cross section is CP-symmetric $\sigma(LH \rightarrow \overline{LH}) = \sigma(\overline{LH} \rightarrow LH)$. This can be seen since unitarity demands conservation of probabilities, $\sum_j \sigma(i \rightarrow j) = \sum_j \sigma(j \rightarrow i)$, which leads to the constraint,

$$\sigma(LH \rightarrow \overline{LH}) + \sigma(LH \rightarrow LH) = \sigma(\overline{LH} \rightarrow LH) + \sigma(LH \rightarrow LH). \tag{2.83}$$

This implies that the off-shell part of the scattering, $\sigma^{off-shell} = \sigma - \sigma^{on-shell}$ has the same symmetry as the on-shell part, which is the same as the decay CP-asymmetry. Since the on-shell part of the scattering has already been included indirectly via decays and inverse decays, we must include the off-shell scattering, which has not been included. Doing so gives the $\Delta L = 2$ equation

$$n_\gamma^{eq} z_1 H \frac{\partial Y_{L-\overline{L}}}{\partial z_1}\bigg|_{2\leftrightarrow 2,\Delta L=2} = -2\epsilon_1 \gamma_{N_1}^{eq} - \frac{Y_{L-\overline{L}}}{2Y_L^{eq}} 4 \left(\gamma_{LH\rightarrow\overline{LH}}^{eq} - \frac{1}{4}\gamma_{N_1}^{eq}\right). \tag{2.84}$$

Finally, the subtracted rate $\gamma_{LH\rightarrow\overline{LH}}^{eq} - \frac{1}{4}\gamma_{N_1}^{eq}$ is small and leads to a negligible contribution to the asymmetry since it is multiplied by a $Y_{L-\overline{L}}$. The combination of the

(a) Thermal initial abundance

(b) Vanishing initial abundance
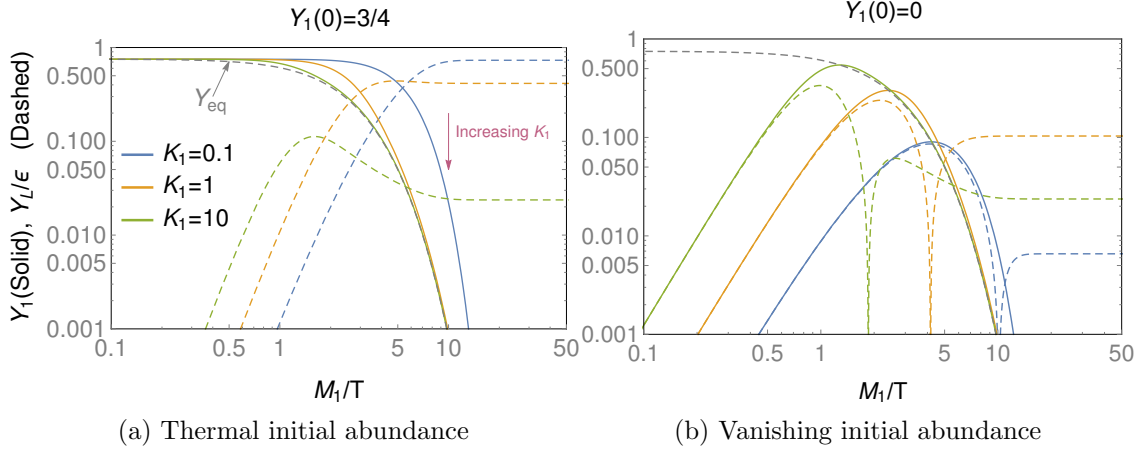
Figure 2.7: Numerical solutions to the vanilla leptogenesis Boltzmann equations with no scattering, showing the thermal evolution of the neutrino abundance (plain) and lepton asymmetry (dashed) for three equilibrium parameters $K = 0.1, 1, 10$ in blue, orange, green respectively.

$1 \leftrightarrow 2$ and $2 \leftrightarrow 2$ lepton asymmetry equations give us the equation,

$$n_\gamma^{eq} z_1 H \frac{\partial Y_{L-\bar{L}}}{\partial z_1} = \epsilon_1 \gamma_{N_1}^{eq} \left(\frac{Y_1}{Y_1^{eq}} - 1 \right) - \frac{Y_{L-\bar{L}}}{2Y_L^{eq}} \gamma_{N_1}^{eq}. \tag{2.85}$$

Vanilla plots   The lepton asymmetry and neutrino abundance equations, Eq. (2.85) and Eq. (2.79), are what constitute the vanilla leptogenesis dynamics. We rewrite the equations in terms of the decay functions introduced in Sec. 2.2 [66],

$$\begin{aligned}
z_1 \frac{\partial Y_1}{\partial z_1} &= -D_1 \left(\frac{Y_1}{Y_1^{eq}} - 1 \right), \\
z_1 \frac{\partial Y_{L-\bar{L}}}{\partial z_1} &= \epsilon_1 D_1 \left(\frac{Y_1}{Y_1^{eq}} - 1 \right) - \frac{Y_{L-\bar{L}}}{2Y_L^{eq}} D_1.
\end{aligned} \tag{2.86}$$

The numerical solutions are shown in Fig. 2.7. In Figs. 2.7a and Figs. 2.7b, we plotted the solutions for the neutrino abundance and the lepton asymmetry as a log log plot as a function of $z_1 = M_1/T$, for a thermal and vanishing initial neutrino abundance. We plotted the solutions for three cases, weak washout $K = 0.1$, strong washout $K = 10$ and intermediate washout $K = 1$. The three phases enumerated at the beginning of this section are most apparent in the strong washout, and are less prominent in the weak and intermediate washout regimes, though present.
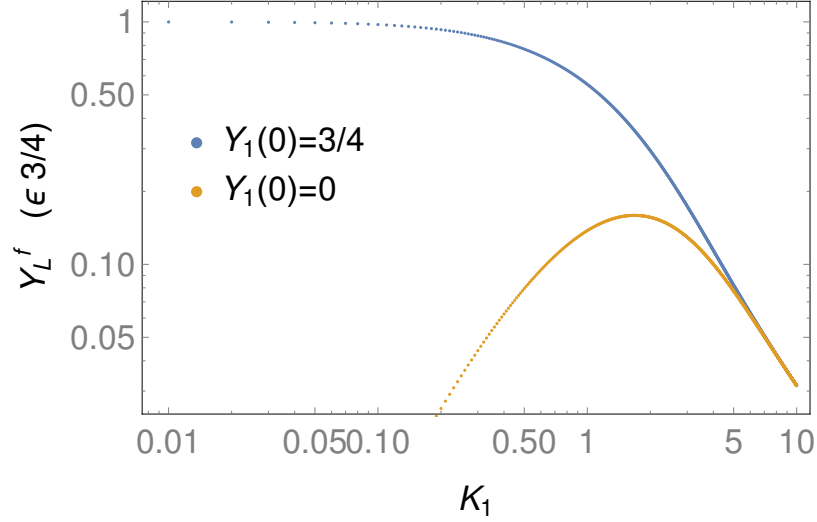
Figure 2.8: Efficiency factor $\kappa = Y^f_{L-\overline{L}}/\epsilon_1$, for a thermal initial RHN abundance (blue) and vanishing initial abundance (orange).

Inserting the neutrino abundance equation into the lepton asymmetry equation, we conveniently obtain the compact equation,

$$\frac{\partial Y_{L-\overline{L}}}{\partial z_1} = -\epsilon_1 \frac{\partial Y_1}{\partial z_1} - \frac{Y_{L-\overline{L}}}{2Y^{eq}_L} \frac{D_1}{z_1}, \tag{2.87}$$

The final asymmetry is formally obtained by integrating out the above equation, and can be parametrized with the efficiency factor, κ_1,

$$Y^f_{L-\overline{L}} = \epsilon_1 \kappa_1 \ Y^{eq}_1(0) \tag{2.88}$$

where the efficiency factor is,

$$\kappa_1 = -\frac{1}{Y^{eq}_1(0)} \int_0^\infty dz_1 \frac{\partial Y_1}{\partial z_1} \exp\left\{ -\int_{z_1}^\infty dz' \frac{D_1(z')}{2Y^{eq}_L z'} \right\}. \tag{2.89}$$

A numerical integration of the efficiency factor is shown in Fig. 2.8.

Inclusion of scattering processes

The scattering processes that affect the RHN abundance are shown in Fig. 2.9. The application of Eq. (2.32) readily leads to the scattering part of the Boltzmann equation
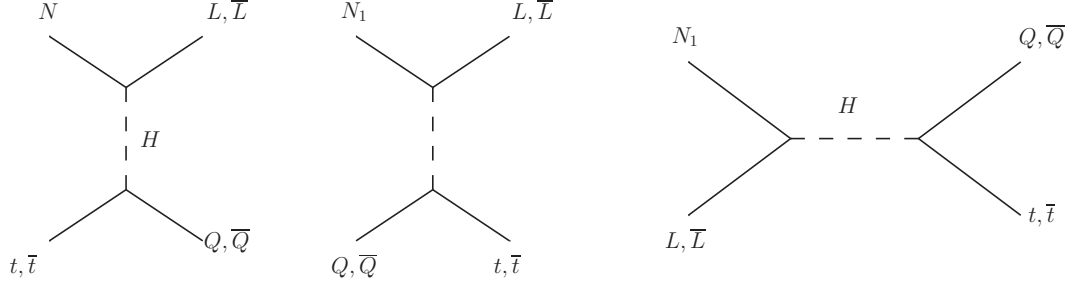
Figure 2.9: Set of scattering processes that affect the neutrino abundance; the $\Delta L = 1$ scattering processes that affect the neutrino abundance and lepton asymmetry

[65, 66, 90],

$$
\begin{aligned}
n_\gamma^{eq} z_1 H \frac{\partial Y_1}{\partial z_1}\bigg|_{2\leftrightarrow 2} = & -\frac{Y_1}{Y_1^{eq}} \left[\gamma_{N_1 t \to LQ}^{eq} + \gamma_{N_1 \bar{t} \to \overline{LQ}}^{eq} + \gamma_{N_1 Q \to Lt}^{eq} + \gamma_{N_1 \overline{Q} \to \overline{Lt}}^{eq} \right] \\
& + \frac{Y_L}{Y_L^{eq}} \left[\gamma_{LQ \to N_1 t}^{eq} + \gamma_{Lt \to N_1 Q}^{eq} \right] + \frac{Y_{\overline{L}}}{Y_{\overline{L}}^{eq}} \left[\gamma_{\overline{LQ} \to N_1 \bar{t}}^{eq} + \gamma_{\overline{Lt} \to N_1 \overline{Q}}^{eq} \right] \\
& - \frac{Y_1}{Y_1^{eq}} \left[\frac{Y_L}{Y_L^{eq}} \gamma_{N_1 L \to Qt}^{eq} + \frac{Y_{\overline{L}}}{Y_{\overline{L}}^{eq}} \gamma_{N_1 \overline{L} \to \overline{Qt}}^{eq} \right] + \gamma_{Qt \to N_1 L}^{eq} + \gamma_{\overline{Qt} \to N_1 \overline{L}}^{eq}
\end{aligned}
$$

$$(2.90)$$

Making use of discrete CP- and CPT-symmetries, we are able to simplify this equation. Firstly, CPT symmetry guarantees $\sigma(i \to j) = \sigma(\bar{j} \to \bar{i})$, while the approximation of CP-symmetric scattering rates gives $\sigma(i \to j) = \sigma(\bar{i} \to \bar{j})$. Those symmetries translate into symmetries of the thermal rates,

$$
\gamma_{i \to j}^{eq} = \gamma_{\bar{j} \to \bar{i}}^{eq}, \quad \gamma_{i \to j}^{eq} = \gamma_{\bar{i} \to \bar{j}}^{eq}.
\tag{2.91}
$$

Because we are in the large N_1 mass regime where the lepton and quark masses are approximated to zero, $M_1 \gg m_L, m_Q, m_H \sim 0$, the t-channels where we invert the incoming and outgoing quark lines are equal, e.g. $\gamma_{N_1 t \to LQ}^{eq} = \gamma_{N_1 Q \to Lt}^{eq}$. The tree level scattering rate in the s- and t-channel is written as $\gamma_{s,t}^{eq}$.

Combining CPT-symmetry, CP-asymmetry and masslessness of Standard Model
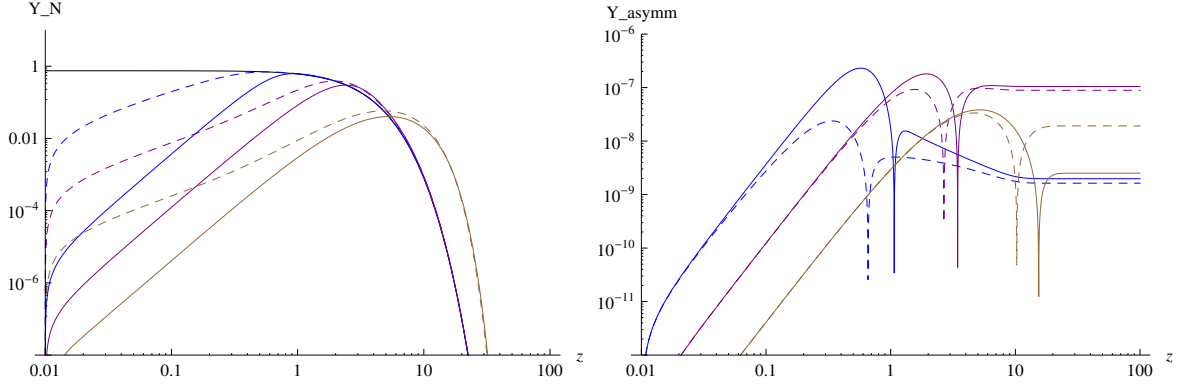
Figure 2.10: Effects of the $2 \leftrightarrow 2$ scattering processes on the neutrino abundance (left) and lepton asymmetry (right). Solid lines are solutions of the Boltzmann equations with no scattering, and the dashed lines are those with scattering. The color coding is $K = 30$ (blue), $K = 1$ (purple), $K = 1/30$ (brown).

quarks and leptons allows us to simplify the Boltzmann equations,

$$
\begin{aligned}
\frac{Y_L}{Y_L^{eq}} \left[\gamma_{LQ \to N_1 t}^{eq} + \gamma_{Lt \to N_1 Q}^{eq} \right] + \frac{Y_{\overline{L}}}{Y_{\overline{L}}^{eq}} \left[\gamma_{\overline{LQ} \to N_1 \bar{t}}^{eq} + \gamma_{\overline{Lt} \to N_1 \overline{Q}}^{eq} \right] &= 4\gamma_t^{eq} \\
\frac{Y_L}{Y_L^{eq}} \gamma_{N_1 L \to Qt}^{eq} + \frac{Y_{\overline{L}}}{Y_{\overline{L}}^{eq}} \gamma_{N_1 \overline{L} \to \overline{Qt}}^{eq} &= 2\gamma_s^{eq} \\
\gamma_{Qt \to N_1 L}^{eq} + \gamma_{\overline{Qt} \to N_1 \overline{L}}^{eq} &= 2\gamma_s^{eq}.
\end{aligned}
\tag{2.92}
$$

The neutrino abundance equation thus becomes,

$$
\begin{aligned}
n_\gamma^{eq} z_1 H \frac{\partial Y_1}{\partial z_1} = &- \gamma_{N_1}^{eq} \left(\frac{Y_1}{Y_1^{eq}} - 1 \right) - 4\gamma_t^{eq} \left(\frac{Y_1}{Y_1^{eq}} - 1 \right) - 2\gamma_s^{eq} \left(\frac{Y_1}{Y_1^{eq}} - 1 \right) \\
&- \epsilon_1 \frac{Y_{L-\overline{L}}}{2Y_L^{eq}} \left(\gamma_{N_1}^{eq} + 4\gamma_t^{eq} + \frac{Y_1}{Y_1^{eq}} 2\gamma_s^{eq} \right),
\end{aligned}
\tag{2.93}
$$

where we again used the approximation $Y_{L+\overline{L}}/2Y_L^{eq} = 1$, ignoring subdominant terms of order $\sim \epsilon_1^2$. Since CP-asymmetry has been ignored in the scattering sector, the $2 \leftrightarrow 2$ processes do not contribute to the lepton-asymmetry. The effects of the scattering processes on the neutrino abundance and lepton asymmetry is shown in Fig. 2.10. Since CP-asymmetry has been ignored in scattering processes, they only affect the neutrino abundance. In turn, the neutrino abundances affects the lepton asymmetry. Scattering processes add more ways for the neutrino abundance to keep up with the expansion and maintain equilibrium, and consequently contributes to

increased lepton asymmetry washout.

2.5.4   Shortcomings and alternative theory

Before moving on to the next part, this section highlights some of the shortcomings of vanilla leptogenesis, and alternative theories.

Flavor effects   Vanilla leptogenesis treats all lepton flavors equally and predicts the asymmetry in the total lepton number, $L = L_e + L_\mu + L_\tau$. However, the flavor is a lot richer than that due to the non-trivial structure of the Yukawa matrices. It is possible to improve the model of leptogenesis by treating each flavor separately, by introducing 3 CP-asymmetries, $\epsilon_{e,\mu,\tau}$, and by developing a set of three Boltzmann equations for each of the three lepton flavors [96, 97, 98, 99, 100, 101].

Gravitino problem   One attractive feature of vanilla leptogenesis is its ability to explain light neutrino masses by the use of the RHN with mass $M \sim 10^8 \text{GeV}$, which also sets the magnitude of the CP-asymmetry allowing the correct final lepton asymmetry. However, this high mass is in conflict with BBN through the reheating problem, in the same way as GUT baryogenesis. If we assume the RHN is thermally produced, then the temperature at the time of reheating must be at least as large as the mass of the lightest RHN, $T_{\text{reheating}} \sim M_1$, and the simplest vanilla leptogenesis model demands $M_1 \gtrsim 10^8 \text{GeV}$. The problem is that large reheating temperatures will also lead to an large abundance of light stable particles, such as the particles that exist in supersymmetric models with R-parity, e.g. gravitino or neutralino [102, 103, 104]. Since they are stable and have interactions with the Standard Model, they have the potential to affect Big Bang Nucleosynthesis [105]. This tension is referred to as the gravitino problem. In order to avoid spoiling BBN, it would seem more natural to have lower reheating temperatures, which then would come in contradiction with the prediction of the simplest leptogenesis model.

   This point is the so-called gravitino problem. However, there are many ways around this problem, since it relies on several assumptions. Supersymmetric theories have not been experimentally confirmed, neither have the existence of R-parity and of light stable particles such as the gravitino and the neutralino. Besides, there are possible ways for vanilla leptogenesis to generate a lepton asymmetry even if the initial RHN abundance is not thermal, that is to say, the RHN does not have to be

thermally produced, which weakens the requirement $T_{\text{reheating}} \sim M_1$.

Resonant leptogenesis   It is possible to be in a resonant regime where the scales of the RHN mass and of the CP-asymmetry are disconnected, allowing for successful leptogenesis with lower masses. In the resonant regime, the two lightest RHN neutrinos are almost degenerate, $|M_1 - M_2| < \Gamma_1$ [106, 107]. In that regime, the wave function correction to the CP-asymmetry is dominant, and receives an enhancement of the order of $1/|M_1 - M_2|$. It is therefore possible to attain small masses, yet keep a sizable CP-asymmetry.

The validity of Weinberg's theorem and its limitation   It was proven by Nanopoulos and Weinberg [108], that the vertex correction that contributes to CP-violation of baryon (lepton) violating decays ought to be calculated at the second order in the baryon number B (lepton number L) violating coupling. This is true if the only available decay channel happens through that vertex. Vanilla leptogenesis is an example of this theory, where the only available $N_1 \to LH$ decay channel is through the Yukawa coupling λ that mediates lepton number violation. Because the Yukawa sets the scale of the light neutrino masses, this dependence also sets the small magnitude of the CP-violation.

However, if additional decay channels that conserve B (L) are available, then it is possible to have a non-vanishing CP-violation calculated at the first order in the B (L) breaking coupling [109]. The model we are going to introduce in Chapter 3 is an example of such model. Indeed, as we will see, it is precisely that which allows us to lower the scale of the CP-asymmetry. Higgs Portal Leptogenesis is an example of theory allowing for low RHN mass scale.

2.6   Summary

To summarize, this section has introduced and discussed the three Sakharov criteria: baryon number violation, C- and CP-violation, and out-of-equilibrium dynamics, which a theory must satisfy in order to reproduce the baryon asymmetry of the universe. As examples, we have introduced the models of GUT baryogenesis and Electroweak baryogenesis. We have also introduced a third class of models, referred to as Baryogenesis via Leptogenesis, the premise of which is to generate a lepton asymmetry in the universe which is processed by the non-perturbative sphaleron processes of

the Standard Model into a baryon asymmetry.

In particular, vanilla leptogenesis is historically the first example of a baryogenesis-via-leptogenesis model. To generate the lepton asymmetry, it makes use of the heavy right-handed neutrino which decays in the early universe into leptons and antileptons in a CP-asymmetric fashion. This model is already well established to explain the scale of the light-neutrino masses, playing a role in its attractiveness.

Vanilla leptogenesis presents some limitations, however. The mass scale of leptogenesis is at least $\sim 10^8 \text{GeV}$, which makes it impossible to observe in particle or cosmological experiments nowadays. Moreover, the only available decay channels violates lepton number. Because of a theorem first proven by Nanopoulos and Weinberg, it is necessary to calculate the loop correction to second order in that coupling, making the CP-asymmetry a fourth order quantity. The coupling scale is set by the light neutrino masses, which is very small. As a consequence, the CP-asymmetry is very small.

It is possible to avoid this scale locking if additional lepton-number conserving decay channels are available, which would allow to calculate the loop correction to first order in the lepton number violating coupling. In the next chapter, we are going to analyze a model which implements such a modification, and we will show how it allows to enhance the CP-asymmetry scale, yet reduce the right-handed neutrino mass.

Chapter 3

Higgs Portal Leptogenesis

As we saw in the previous chapter, vanilla leptogenesis is a minimal model that concisely reconciles two puzzles of modern physics: the light neutrino masses, and the baryon asymmetry of the universe. It relies on the existence of at least two new right-handed neutrinos that couple to their left-handed counterparts via a Yukawa-like interaction, λNLH, and that have a Majorana mass term, MNN, by virtue of being singlet under the SM group. The model invokes the type-I seesaw mechanism to generate left-handed neutrino masses, $m_\nu \sim \lambda^2 \langle H \rangle^2 / M$, which can be put at the order of the centi-eV by a combination of couplings $\lambda \sim 10^{-2}$ and masses $M \sim 10^{11}$GeV. Furthermore, the baryon asymmetry is derived from the generation of lepton asymmetry thanks to the existence of physical CP-phases in the coupling matrices λ.

In spite of its simplicity, the model does have setbacks. Firstly, testability is an issue, since the large masses M make it difficult to be tested in current direct or indirect experiments. That being said, the Majorana nature of the neutrinos can potentially be tested in neutrinoless double beta decay experiments, though the experiments have so far yielded no positive signal. Secondly, there is mounting evidence that dark matter constitutes a large part of the energy budget of the universe, which is not included in the vanilla leptogenesis environment. It is therefore desirable both to lower the mass scale of the minimal model, and to extend the field content to include a dark sector.

Portal operators offer a minimal way to couple a dark sector to the SM particle content. By virtue of being dimension 4 or below, and by imposing that the dark sector be neutral under the SM group, portal interactions are a powerful organizing principle, constraining the available interactions to three: the Neutrino, Higgs, and

Vector portals,

$$\mathcal{L}_{\text{vector}} = \kappa B^{\mu\nu} V_{\mu\nu}$$
$$\mathcal{L}_{\text{Higgs}} = -H^\dagger H(\beta S + \gamma S^2) \tag{3.1}$$
$$\mathcal{L}_{\text{Neutrino}} = -\lambda LHN,$$

as were introduced in the Introduction. Being renormalizable operators, the portal interactions do not involve UV degrees of freedom, and as such are a natural place to look for new light new physics. Vanilla leptogenesis already makes use of the Neutrino portal. The aim of this research, is to further include the Higgs portals in an attempt to lower the scale of leptogenesis, a model we call *Higgs Portal Leptogenesis* (HPL).

We find that the presence of both the Higgs and Neutrino singlets, S, N allows for a purely-hidden-sector coupling, $\alpha_{ij} S N_i N_j$, where α_{ij} is a coupling matrix that contain new physical CP-phases. The combination of this operator with the Higgs and Neutrino portals opens up a new CP-asymmetry that scales as $\alpha\beta/M$. The β/M factor is suppressed in the vanilla leptogenesis mass regime, but becomes advantageous in HPL since it allows an enhancement of the CP-asymmetry in the low mass regime, $\beta/M \sim \mathcal{O}(1)$. Our model relies on the fact that in this regime the hidden sector CP-asymmetry channel is dominant, thus generating the CP-asymmetry almost entirely via the hidden sector.

The particularity of the hidden-sector CP-asymmetry channel, is that it cannot be generated by the lightest neutrino flavor, and as such the model does require at least two RHN flavors to decay in order to take advantage of the β/M enhancement. In our model, we limit ourselves to two RHN flavors, and we enumerate the set of scattering and decay processes relevant to leptogenesis, and develop a set of Boltzmann equations to keep track of the lepton number asymmetry. We numerically solve the set of Boltzmann equations, and explore the parameter space of couplings and mass ratio M_2/M_1 between the two RHN flavors, unveiling a two-stage lepton evolution that display a rich dynamics. We find that in the low mass regime, the CP-asymmetry generated from the lightest N_1 neutrino is turned off. In this regime, the lepton asymmetry is entirely generated by N_2 decays, leaving the freedom to put N_1 around the electroweak scale.

In Section 3.1 we introduce the model Lagrangian and calculate the new source of CP-asymmetry. In Section 3.2, we develop a system of Boltzmann equations that include decay and scattering processes that the hidden sector takes part of. We also

give analytical approximations for the two-stage Boltzmann equations in a simple approximation where the scattering processes are ignored. In Section 3.3, we numerically resolve the full set of Boltzmann equations, and prove that the model is able to generate the observed baryon asymmetry in the RHN mass range, $\sim \mathcal{O}(\text{TeV})$. Finally, we summarize our findings in the Summary section.

3.1   Higgs Portal and the CP-asymmetry

3.1.1   The Model

Our focus in this thesis is a minimal extension of conventional leptogenesis, which adds a scalar singlet S along with the right-handed singlet neutrinos N_i. This opens up the Higgs and neutrino portals

$$\mathcal{L}_{\text{portals}} = -\lambda_{ji}\overline{N}_i P_L L_j \cdot H - \beta S H^\dagger H - \left(\frac{1}{2}M_i\delta_{ij} + \alpha_{ij}S\right)\overline{N}_i^c P_L N_j + h.c. + \cdots \quad (3.2)$$

The Higgs portal coupling β is one part of the full scalar potential $V(H, S)$, and breaks the $S \to -S$ symmetry. Thus, determining the vacuum structure requires a separate analysis incorporating thermal corrections. This potential has been studied in detail elsewhere [110, 111, 112], and here we simply assume that the parameters are chosen to ensure viable electroweak symmetry breaking, and importantly that $\langle S \rangle = 0$. The possibility of a more complex behaviour of $\langle S \rangle$, which modifies the effective RHN mass is nonetheless interesting, and will be discussed further in the concluding section.

In minimal leptogenesis, the Yukawa couplings λ determine both the light neutrino mass spectrum and the CP-asymmetry generated in RH neutrino decays [113, 114, 115, 116]. Opening the Higgs portal allows these two physical phenomena to be decoupled, with the Majoron coupling α_{ij} providing a new CP-odd source that is unconstrained (for $\langle S \rangle = 0$) by the light neutrino mass spectrum. In the Lagrangian (3.2), a unitary rotation has been used to diagonalize the RH neutrino mass matrix $M_{ij} \to M_i\delta_{ij}$. The Majorana nature of $N_i = N_i^c$ ensures that M_{ij} is symmetric, and for n flavors the diagonalization leaves M_i as n real mass eigenvalues [92, 93]. In general, the corresponding rotation simply rearranges the $n(n+1)/2$ phases in the symmetric matrix α_{ij}, which is thus a physical CP-odd source in addition to the

neutrino Yukawa λ_{ij}.[1]

3.1.2 CP Asymmetry

The CP-asymmetry arising from RH neutrino (RHN) decays to leptons and antileptons is measured by ϵ_i,

$$\epsilon_i \equiv \frac{\Gamma(N_i \to LH) - \Gamma(N_i \to \overline{LH})}{\Gamma_i}. \tag{3.3}$$

The total decay rate Γ_i, in the denominator, is calculated at tree level,

$$\Gamma_i \equiv \sum_{k,\alpha,\beta} \left(\Gamma(N_i \to L_k^\alpha H^\beta) + \Gamma(N_i \to \overline{L_k^\alpha H^\beta}) \right) = \frac{(\lambda^\dagger \lambda)_{ii}}{8\pi} M_i, \tag{3.4}$$

where the lepton family index, $k = 1, 2, 3$ stands for the electron, muon and tau families respectively. The $\alpha, \beta = 1, 2$ indices denote the components of the SU(2) lepton and Higgs doublets $L = (\nu_l \quad e_l)^T$ and $H = (H^+ \quad H^0)^T$. If we schematically write the decay amplitude as $i\mathcal{M} = \gamma_0 + \gamma_1 I$, with $\gamma_{0,1}$ the tree and loop level combinations of coupling constants, and I the loop function, then the decay amplitude for the antiparticle is $i\overline{\mathcal{M}} = \gamma_0^* + \gamma_1^* I$, while the decay rates $\Gamma(N_i \to LH)$ and $\Gamma(N_i \to \overline{LH})$ are proportional to $|i\mathcal{M}|^2$ and $|i\overline{\mathcal{M}}|^2$ respectively. At tree level, the difference vanishes, but at the loop level, the CP-asymmetry takes the schematic form

$$\epsilon_i \sim 2\frac{\text{Im}\{\gamma_0 \gamma_1^*\}}{|\gamma_0|^2}\text{Im}\{I\}. \tag{3.5}$$

Thus, CP-asymmetry from two-body decays requires at least one loop and a phase in the loop function. In standard leptogenesis, only the Yukawa λ_{ij} allows for this decay channel, and can accommodate CP-violation. In Higgs Portal Leptogenesis, additional lepton number violating and CP-violating sources are present in the theory, specifically the α_{ij} coupling as discussed above. As a result, additional loop-induced decay channels open up, as displayed in Fig. 3.1.

The corresponding CP-asymmetries will be discussed in the following subsections. We utilize the Majorana Feynman rules [117, 118, 119] for the RH neutrinos, and

---

[1]The coupling $\alpha_{ij} S \overline{N_i^c} P_L N_j + h.c$ is more commonly used to generate the right-handed neutrino masses M_i by having S develop a vev $\langle S \rangle$, spontaneously breaking a global lepton number symmetry. In such cases where an explicit mass term M_{ij} is forbidden, the matrix α_{ij} can be be made real and diagonal.
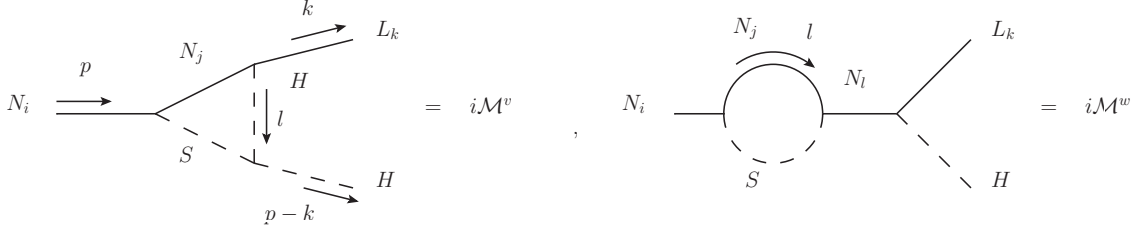
Figure 3.1: Two hidden sector decay channels for RHN that contribute to the CP asymmetry. The superscripts 'v', and 'w' stand for the vertex and wave function diagrams.

determine the imaginary parts of the loop functions using the standard Cutkosky rules [94].

Vertex Corrections: 2-body final states

The contribution of the diagram $i\mathcal{M}^v$ to the asymmetry is

$$\epsilon_i^v = 4 \sum_j \left(\frac{\mathrm{Im}\{(\lambda^\dagger\lambda)_{ji}\beta\alpha_{ij}\}}{(\lambda^\dagger\lambda)_{ii}M_i} \, \mathrm{Im}\{I_{jLL}\} + \frac{\mathrm{Im}\{(\lambda^\dagger\lambda)_{ji}\beta\alpha_{ij}^*\}}{(\lambda^\dagger\lambda)_{ii}M_i} \mathrm{Im}\{I_{jRL}\} \right), \qquad (3.6)$$

where I_{jLL} and I_{jRL} are loop function integrals. The vertex contribution splits into two halves, proportional to $\mathrm{Im}\{I_{jLL}\}$ and $\mathrm{Im}\{I_{jRL}\}$, corresponding to the mixing of the left- and right- chiralities of the Majorana fermions along the fermion lines, effectively leading to the two chirality chains

$$\begin{aligned} \nu_R(\mathrm{RH}) &\longrightarrow \nu_R^C(\mathrm{LH}) \longrightarrow L(\mathrm{LH}), \\ \nu_R^C(\mathrm{LH}) &\longrightarrow \nu_R^C(\mathrm{LH}) \longrightarrow L(\mathrm{LH}). \end{aligned} \qquad (3.7)$$

Because the final leptons (assumed massless) have a definite chirality, the Yukawa coupling forces the next-to-last neutrino to be of the same chirality as the final lepton, left-handed. The functions I_{jLL} and I_{jRL} correspond to the L-L-L and R-L-L chains respectively. The reason why the chirality chains do not combine, owes to the fact that α_{ij} is neither real nor diagonal. In the vertex contribution, there are three possible cuts which lead to an imaginary part: cuts along the S/N lines, the H/S lines and the H/N lines, each of which contains the two chirality chain contributions. Thus, each chirality chain function, $\mathrm{Im}\{I_{jLL}\}$ and $\mathrm{Im}\{I_{jRL}\}$ is the sum,

$$\mathrm{Im}\{I\} = \mathrm{Im}\{I\}^{S/N} + \mathrm{Im}\{I\}^{H/S} + \mathrm{Im}\{I\}^{H/N}. \qquad (3.8)$$
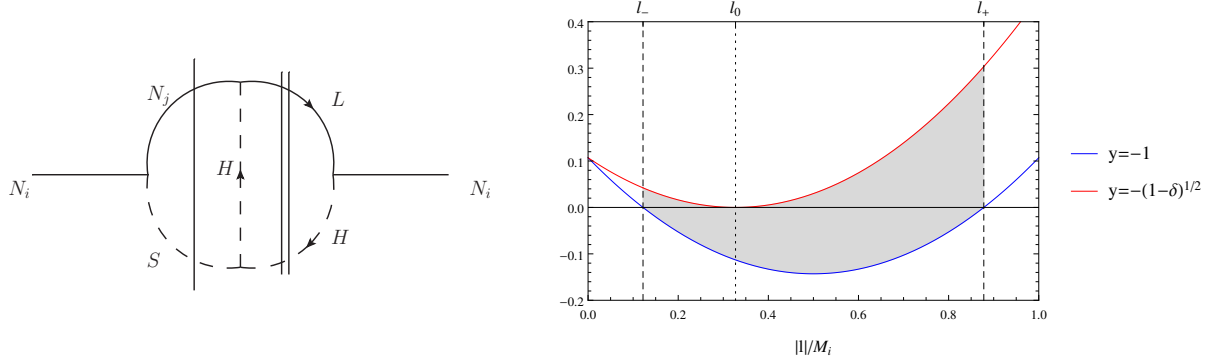
Figure 3.2: The left plot graphically represents the N/S cut. The right figure exhibits the quadratic constraint in Eq. (3.10). The vertical dashed lines represent the momentum $|\vec{l}|$ upper and lower bounds, $|\vec{l}|_\pm = M_i(1 \pm \sqrt{\delta})/2$, which become $|\vec{l}|_0 = M_i\sqrt{1-\delta}/2$ at $y = -\sqrt{1-\delta}$. The imaginary part of the vertex correction is non-zero contributions only from the gray area.

It will be convenient to graphically represent the interference terms in $|\mathcal{M}|^2$ which contribute to the imaginary part in the form of *bubble* diagrams. For now we focus on the N/S cut which is shown in Fig. 3.2 (the full set of cuts is presented later in Fig. 3.4a). The double line indicates external lines that are on-shell by definition in $|\mathcal{M}|^2$, in this case the final lepton and Higgs, while the single line shows the Cutkosky-cut. According to the Cutkosky rules, the N/S cut is given by

$$
\begin{aligned}
\text{Im}\{I_{LL}\}^{S/N} = 2\pi^2 \int \frac{d^4l}{(2\pi)^4} \frac{l \cdot k}{l^2} \delta((l+k)^2 - M_j^2)\delta((l+k-p)^2 - m_S^2) \\
\times \Theta(p^0 - l^0 - k^0)\Theta(k^0 + l^0).
\end{aligned}
\tag{3.9}
$$

The delta functions impose the on-shell condition for the N/S lines, and the Heaviside functions Θ require these on-shell lines to be physical (timelike) processes. In other words, imposing positivity of the energies $p^0 - l^0 - k^0$ and $k^0 + l^0$, requires that the cut diagram corresponds to the decay $N_i \to N_j S$ followed by the scattering $N_j S \to LH$. Combining the energy constraints also restricts the individual energies $l^0 = M_i(r_{ji} - \sigma_i)/2$, and $M_i/2 > l^0 > -M_i/2$. The on-shell conditions in turn, imply the quadratic constraint on the three momentum $\vec{l}$

$$
|\vec{l}|^2 + M_i|\vec{l}|y - \frac{M_i^2}{4}\Big(\delta(1, r_{ji}, \sigma_i) - 1\Big) = 0,
\tag{3.10}
$$

where we have introduced the shorthand notations

$$r_{ji} = \frac{M_j^2}{M_i^2}, \quad \sigma_i = \frac{m_S^2}{M_i^2}, \quad \delta(a,b,c) = (a-b-c)^2 - 4bc, \quad y = \cos\theta, \qquad (3.11)$$

For simplicity below, δ without specified variables will implicitly be understood to mean $\delta(1, r_{ji}, \sigma_i)$, unless stated otherwise. The angle θ lies between the 3-momenta $\vec{l}$ and $\vec{k}$. The combined constraints on l^0 given above imply the equivalent constraint, $1 > r_{ji} - \sigma_i > -1$. Since the kinematics must allow the decay $N_i \to N_j S$, the latter constraint requires that $1 > \sqrt{r_{ji}} + \sqrt{\sigma_i}$. Importantly, we observe that the diagram only has an imaginary part for decays of the next-to-lightest neutrinos. Similarly, the imaginary part is non-vanishing provided the quadratic equation for $|\vec{l}|$ in (3.10) has real solutions, thus imposing the condition $\delta > 0$, here again, satisfied if $1 > \sqrt{r_{ji}} + \sqrt{\sigma_i}$. The l^0 integration is trivial since its value is uniquely fixed. As usual, the remaining integration over $\vec{l}$ is split into the radial and angular part. In spherical coordinates with $\vec{k}$ along the z-axis, the azimuthal angle ϕ trivially integrates to 2π, and θ corresponds to the inclination angle of the spherical coordinate system. The leftover integrals over y and $|\vec{l}|$ are not independent because of the constraint (3.10). That constraint has been plotted in Fig. 3.2, where we see that the kinematics are constrained to the ranges $-1 \leqslant y \leqslant -\sqrt{1-\delta}$ and $M_i/2 \left(1 - \sqrt{\delta}\right) \leqslant |\vec{l}| \leqslant M_i/2 \left(1 + \sqrt{\delta}\right)$. The integration is nonvanishing within this range, leading to the result,

$$\mathrm{Im}\{I_{LL}\}^{N/S} = \frac{1}{32\pi} \left[-\sqrt{\delta} + r_{ji} \log\left(\frac{\sqrt{\delta + 4r_{ji}\sigma_i} - \sqrt{\delta}}{\sqrt{\delta + 4r_{ji}\sigma_i} + \sqrt{\delta}} \right) \right], \quad 1 \geqslant \sqrt{r_{ji}} + \sqrt{\sigma_i}.$$
$$(3.12)$$

Similar steps lead to the other chirality chain function, $\mathrm{Im}\{I_{jRL}\}^{N/S}$, for the N/S cut,

$$\mathrm{Im}\{I_{jRL}\}^{N/S} = \frac{\sqrt{r_{ji}}}{32\pi} \log\left(\frac{\sqrt{\delta + 4r_{ji}\sigma_i} - \sqrt{\delta}}{\sqrt{\delta + 4r_{ji}\sigma_i} + \sqrt{\delta}} \right), \quad 1 \geqslant \sqrt{r_{ji}} + \sqrt{\sigma_i}, \qquad (3.13)$$

Figure 3.3: Two 3-body decay diagrams contributing to the CP-asymmetry at the same order in couplings as the loop-corrected 2-body decays. As discussed in the text, their inclusion is important in ensuring that the full CP asymmetry is well-defined and free of infrared divergences.

as well as for the H/S cuts,

$$
\begin{aligned}
\mathrm{Im}\{I_{jRL}\}^{H/S} &= \frac{\sqrt{r_{ji}}}{32\pi} \log\left|\frac{1-r_{ji}}{r_{ji}}\right|\Bigg|_{\sigma_i=0}, \\
\mathrm{Im}\{I_{jLL}\}^{H/S} &= \frac{1}{32\pi}\left(1 + r_{ji}\log\left|\frac{1-r_{ji}}{r_{ji}}\right|\right)\Bigg|_{\sigma_i=0},
\end{aligned}
\tag{3.14}
$$

while the H/N cut gives a vanishing imaginary part $\mathrm{Im}\{I_{jLL}\}^{H/N} = \mathrm{Im}\{I_{jRL}\}^{H/N} = 0$. The notation $|_{\sigma_i=0}$ means that the imaginary part is only nonzero if $\sigma_i = 0$. Note that the N/S cut is divergent in the infrared limit $\sigma_i = 0$, where it is effectively equivalent to the decay $N_i \to N_j S$ followed by the scattering $N_j S \to LH$ mediated by the Higgs in the t-channel. The divergence, due to radiating massless scalars in the infrared collinear limit, is canceled by including the appropriate three-body decays as discussed below.

Vertex Corrections: 3-body final states

In Fig. 3.3, we show the two three-body final state amplitudes whose interference develops an imaginary part and contributes to the CP-asymmetry. The three-body final state CP-asymmetry $\epsilon_i^{(3)}$ measures the difference $(\Gamma(N_i \to LHS) - \Gamma(N_i \to \overline{LHS}))/(\Gamma(N_i \to LH, LHS) + \Gamma(N_i \to \overline{LH}, \overline{LHS}))$, with the total RHN decay rate in the denominator. The three-body final state decay rate being subdominant due to the reduced phase space, we can approximate $\epsilon_i^{(3)}$ as

$$
\epsilon_i^{(3)} \simeq \frac{\Gamma(N_i \to LHS) - \Gamma(N_i \to \overline{LHS})}{\Gamma_i}.
\tag{3.15}
$$

In general, the three-body CP-asymmetry arises from both $i\mathcal{M}_A(i\mathcal{M}_B)^* \sim \mathcal{O}(\lambda^2\beta\alpha)$ and $|i\mathcal{M}_B|^2 \sim \mathcal{O}(\lambda^2\alpha^2)$. Only the former term, which enters at the same order as the
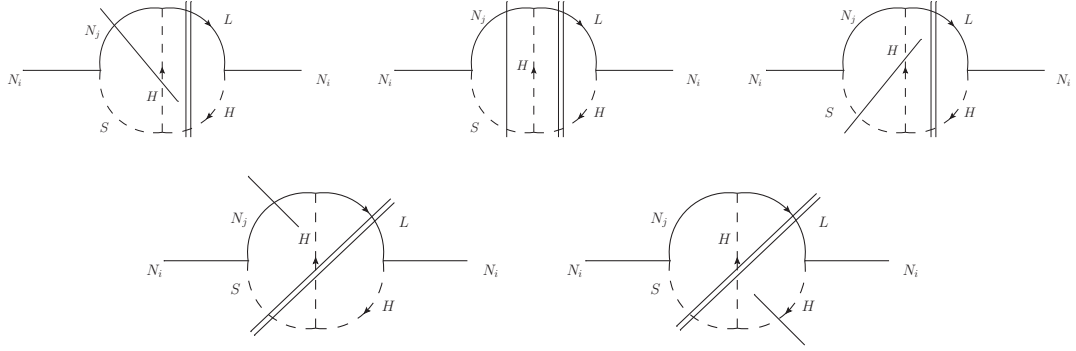
Figure 3.4: The bubble diagrams enumerating the cuts that contribute to the CP-asymmetry from both the vertex loop corrections (top) and 3-body final states (bottom). The external state lines that are on-shell by definition are cut with a double line, while the Cutkosky cuts are shown with a single line.

vertex contribution, is of interest here. The two contributing cuts through the H and the N_j propagators are represented in Fig. 3.4b as bubble diagrams. The result is

$$\epsilon_i^{(3)} = 4 \sum_j \left(\frac{\text{Im} \left\{ (\lambda^\dagger \lambda)_{ji} \beta \alpha_{ij} \right\}}{(\lambda^\dagger \lambda)_{ii} M_i} \text{Im}\{\mathcal{I}_{jLL}\}^{(3)} + \frac{\text{Im} \left\{ (\lambda^\dagger \lambda)_{ji} \beta \alpha_{ij}^* \right\}}{(\lambda^\dagger \lambda)_{ii} M_i} \text{Im}\{\mathcal{I}_{jRL}\}^{(3)} \right),$$

(3.16)

with

$$\text{Im}\{\mathcal{I}_{jLL}\}^{(3)} = \frac{r_{ji}}{32\pi} \log \left(\frac{\sqrt{\delta + 4r_{ji}\sigma_i + 2\sigma_i} + \sqrt{\delta}}{\sqrt{\delta + 4r_{ji}\sigma_i + 2\sigma_i} - \sqrt{\delta}} \right) - \frac{1}{32\pi} \left(1 + r_{ji} \log \left| \frac{1 - r_{ji}}{r_{ji}} \right| \right) \Bigg|_{\sigma_i=0},$$

$$\text{Im}\{\mathcal{I}_{jRL}\}^{(3)} = \frac{\sqrt{r_{ji}}}{32\pi} \left[-\sqrt{\delta} + \log \left(\frac{\sqrt{\delta + 4r_{ji}\sigma_i + 2\sigma_i} + \sqrt{\delta}}{\sqrt{\delta + 4r_{ji}\sigma_i + 2\sigma_i} - \sqrt{\delta}} \right) \right] - \frac{\sqrt{r_{ji}}}{32\pi} \log \left| \frac{1 - r_{ji}}{r_{ji}} \right| \Bigg|_{\sigma_i=0}.$$

(3.17)

The first terms in $\text{Im}\{\mathcal{I}_{jLL}\}^{(3)}$ and $\text{Im}\{\mathcal{I}_{jRL}\}^{(3)}$ come from cutting the N_j line, while the second terms come from cutting the S line, respectively combining with the N/S and H/S cuts of the tree-loop interference in (3.12, 3.13, 3.14), leading to the *corrected* vertex CP-asymmetry ϵ_i^v,

$$\epsilon_i^v = \sum_j \left(\frac{\text{Im} \left\{ (\lambda^\dagger \lambda)_{ji} \beta \alpha_{ij} \right\}}{8\pi (\lambda^\dagger \lambda)_{ii} M_i} \mathcal{F}_{jLL}^v(r_{ji}, \sigma_i) + \frac{\text{Im} \left\{ (\lambda^\dagger \lambda)_{ji} \beta \alpha_{ij}^* \right\}}{8\pi (\lambda^\dagger \lambda)_{ii} M_i} \mathcal{F}_{jRL}^v(r_{ji}, \sigma_i) \right), \quad (3.18)$$

where

$$\mathcal{F}^v_{jLL}(r_{ji}, \sigma_i) \equiv \left(-\sqrt{\delta} + r_{ji} \log G\right) \quad , \quad \mathcal{F}^v_{jRL}(r_{ji}, \sigma_i) \equiv \left(-\sqrt{r_{ji}}\sqrt{\delta} + \sqrt{r_{ji}} \log G\right),$$
(3.19)

and

$$G \equiv \frac{\sqrt{\delta + 4r_{ji}\sigma_i + 2\sigma_i} + \sqrt{\delta}}{\sqrt{\delta + 4r_{ji}\sigma_i + 2\sigma_i} - \sqrt{\delta}} \frac{\sqrt{\delta + 4r_{ji}\sigma_i} - \sqrt{\delta}}{\sqrt{\delta + 4r_{ji}\sigma_i} + \sqrt{\delta}}.$$
(3.20)

Note that the infrared divergence at $\sigma_i = 0$ has disappeared, resulting from a cancellation between (3.12), (3.13) and (3.17). A simple graphical understanding of this cancellation emerges by comparing the N/S cut diagram of Fig. 3.4a with the N_j-line cut diagram of Fig. 3.4b. In general they have different kinematics, but they coincide in the infrared limit where all the internal lines of the respective diagrams are allowed to be on-shell, permitting the emission of soft particles. The inclusion of the two-body and three-body final state contributions renders the CP-asymmetry well-defined.

Note also that the contributions that are non-vanishing only in the $\sigma_i = 0$ limit, i.e. those coming from the H/S cut in (3.14) and from the H-line cut in (3.17) also cancel out. This can again be understood by comparing the H/S-cut diagram of Fig. 3.4a and the H-cut of Fig. 3.4b, for which the kinematics are identical.

Wave-function Corrections

Once again, because of the Majorana nature of the Right-handed neutrinos, there can be chirality mixing, leading to the following 4 chirality chains in the right-hand diagram of Fig. 3.1:

$$\begin{aligned}
\nu_R(\text{RH}) &\to \nu_R(\text{RH}) \to \nu_R^C(\text{LH}) \to L(\text{LH}), \\
\nu_R(\text{RH}) &\to \nu_R^C(\text{LH}) \to \nu_R^C(\text{LH}) \to L(\text{LH}), \\
\nu_R^C(\text{LH}) &\to \nu_R(\text{RH}) \to \nu_R^C(\text{LH}) \to L(\text{LH}), \\
\nu_R^C(\text{LH}) &\to \nu_R^C(\text{LH}) \to \nu_R^C(\text{LH}) \to L(\text{LH}).
\end{aligned}$$
(3.21)

The two first chains contain only 1 chirality flip, the third contains 2 flips, and the last contains none. Each chain will be labeled by the chiralities of the two first lines in the loop, i.e. the RR, RL, LR, LL chains respectively. The asymmetry then takes

the following form,

$$\epsilon_i^w = \sum_{l,j} \left(\frac{\text{Im}\{(\lambda^\dagger\lambda)_{li}\alpha_{lj}\alpha_{ij}^*\}}{8\pi(\lambda^\dagger\lambda)_{ii}} \mathcal{F}_{jlLL}^w + \frac{\text{Im}\{(\lambda^\dagger\lambda)_{li}\alpha_{lj}^*\alpha_{ij}^*\}}{8\pi(\lambda^\dagger\lambda)_{ii}} \mathcal{F}_{jlLR}^w \right.$$
$$\left. + \frac{\text{Im}\{(\lambda^\dagger\lambda)_{li}\alpha_{lj}\alpha_{ij}\}}{8\pi(\lambda^\dagger\lambda)_{ii}} \mathcal{F}_{jlRL}^w + \frac{\text{Im}\{(\lambda^\dagger\lambda)_{li}\alpha_{lj}^*\alpha_{ij}\}}{8\pi(\lambda^\dagger\lambda)_{ii}} \mathcal{F}_{jlRR}^w \right). \tag{3.22}$$

Calculating the $\mathcal{F}^w$ loop functions is relatively simple as the imaginary part comes solely from the diagrams in which both lines in the loop are cut, which uniquely defines all the kinematics, trivializing the integrals. Thus we will simply state the final results,

$$\mathcal{F}_{jlLL}^w(r_{ji}, \sigma_i) \equiv \frac{\sqrt{\delta}}{2} \frac{\sqrt{\delta + 4r_{ji}}}{1 - r_{li}}, \quad \mathcal{F}_{jlLR}^w(r_{ji}, \sigma_i) \equiv \sqrt{\delta} \frac{\sqrt{r_{ji}}\sqrt{r_{li}}}{1 - r_{li}},$$
$$\mathcal{F}_{jlRL}^w(r_{ji}, \sigma_i) \equiv \sqrt{\delta} \frac{\sqrt{r_{ji}}}{1 - r_{li}}, \quad \mathcal{F}_{jlRR}^w(r_{ji}, \sigma_i) \equiv \frac{\sqrt{\delta}}{2} \frac{\sqrt{r_{li}}\sqrt{\delta + 4r_{ji}}}{1 - r_{li}}. \tag{3.23}$$

As noted earlier, we have used the shorthand notation r_{ji}, and $\delta = (1 - r_{ji} - \sigma_i)^2 - 4r_{ji}\sigma_i$. The kinematic constraint remains the same as for the vertex correction, $1 > \sqrt{r_{ji}} + \sqrt{\sigma_i}$.

Parametrization of the hidden sector CP-asymmetry

Here we are going to express find an expression for the CP-asymmetry that captures the characteristic scale. Starting with the hidden sector, and using the forms (3.18) and (3.22) for the vertex and wave function corrections, we make the bold approximation that the scale of the imaginary parts is similar to the magnitudes. We write

$$|\epsilon_i^v| \sim \sum_j \frac{|(\lambda^\dagger\lambda)_{ji}|}{(\lambda^\dagger\lambda)_{ii}} \frac{|\alpha_{ij}|}{8\pi} \frac{\beta}{M_i} \left(\mathcal{F}_{jLL}^v + \mathcal{F}_{jRL}^v \right),$$
$$|\epsilon_i^w| \sim \sum_{l,j} \frac{|(\lambda^\dagger\lambda)_{ji}|}{(\lambda^\dagger\lambda)_{ii}} \frac{|\alpha_{lj}\alpha_{il}|}{8\pi} \left(\mathcal{F}_{jlLL}^w + \mathcal{F}_{jlRL}^w + \mathcal{F}_{jlLR}^w + \mathcal{F}_{jlRR}^w \right). \tag{3.24}$$

Assuming the standard see-saw mechanism, we can replace the Yukawa couplings by the light active neutrino masses through the following relations [120],

$$m_\nu = v^2 \lambda^* M^{-1} \lambda^\dagger, \qquad \lambda = \frac{1}{v} U D_{\sqrt{m}} R^\dagger D_{\sqrt{M}}, \tag{3.25}$$

where the Higgs vacuum expectation value is $v = 174\,\text{GeV}$, and R is a (complex) orthogonal matrix, and the diagonal Majorana and active neutrino mass matrices are respectively $D_M = \text{diag}(M_1, M_2, M_3)$, and $D_m = \text{diag}(m_1, m_2, m_3)$. The matrix U is the so-called unitary PMNS matrix. Using this notation, we can write

$$(\lambda^\dagger \lambda)_{ji} = \frac{\sqrt{M_i M_j}}{v^2} \sum_b m_b R_{jb} R_{ib}^*, \qquad (\lambda^\dagger \lambda)_{ii} = \frac{M_i}{v^2} \sum_b m_b |R_{ib}|^2. \tag{3.26}$$

The Schwartz inequality $|\sum_b m_b R_{jb} R_{ib}^*|^2 \le \sum_\alpha m_\alpha |R_{j\alpha}|^2 \sum_\beta m_\beta |R_{i\beta}|^2$, then allows the couplings to be bounded from above

$$\frac{|(\lambda^\dagger \lambda)_{ji}|}{(\lambda^\dagger \lambda)_{ii}} \lesssim \sqrt{\frac{M_j \sum_b m_b |R_{jb}|^2}{M_i \sum_b m_b |R_{ib}|^2}} \sim \sqrt{\frac{M_j}{M_i}}. \tag{3.27}$$

The final approximation assumes all the entries of the orthogonal matrix R are similar in magnitude. When R is real, the orthogonality condition $R^T R = \mathbf{1}$ ensures that its elements satisfy $R_{ij} \le 1$. When R is complex, we have fewer constraints but bounding $|R_{ij}|$ by unity is a sufficient condition for orthogonality, and to obtain a characteristic estimate below we will simply assume $|R_{ij}| \sim 1$.

Because of kinematic constraints, we have $\epsilon_1 = 0$. For $i = 2$, the neutrino sum runs over $j = 1, 3$. However, the asymmetry vanishes when $j = 3$, since $M_3 > M_2$ is kinematically forbidden for the cut loop. The sum thus reduces to $j = 1$ only. For the wave-function corrections, we have two sums over $j, l = 1, 3$. The index j denotes the neutrino inside the loop, and is therefore constrained to $j = 1$ by the cut kinematics, but $l = 3$ is not forbidden. However by assumption $r_{32} \gg 1$, and in that limit the resulting CP-asymmetry is negligible. The sums therefore collapse to $j = l = 1$. Hence, we arrive at the parametric estimate,

$$
\begin{aligned}
\epsilon_2^v &\sim \frac{|\alpha_{21}|}{8\pi} \frac{\beta}{M_2} \sqrt{\frac{M_1}{M_2}} \left(\mathcal{F}_{jLL}^v + \mathcal{F}_{jRL}^v \right), \\
\epsilon_2^w &\sim \frac{|\alpha_{11}\alpha_{21}|}{8\pi} \sqrt{\frac{M_1}{M_2}} \left(\mathcal{F}_{jlLL}^w + \mathcal{F}_{jlRL}^w + \mathcal{F}_{jlLR}^w + \mathcal{F}_{jlRR}^w \right),
\end{aligned}
\tag{3.28}
$$
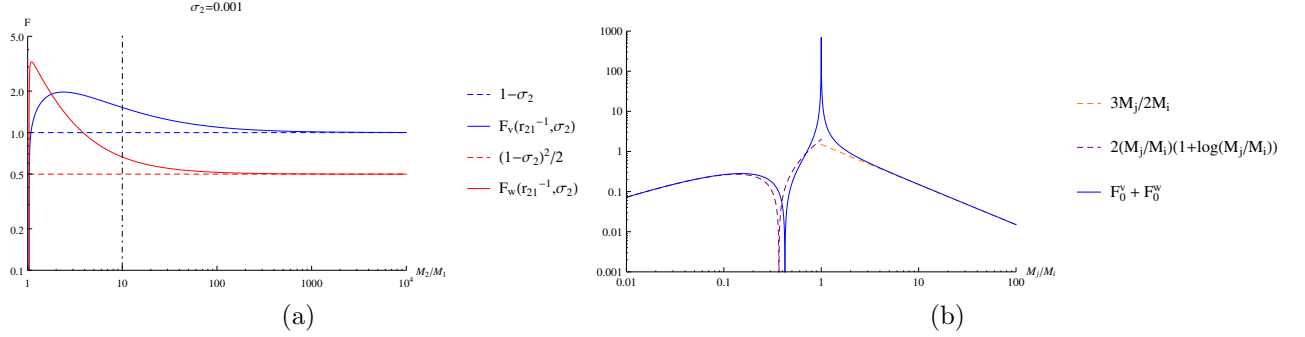
Figure 3.5: Plots of the full loop functions $\mathcal{F}$ (solid), and the approximations (dashed) discussed in this section, as a function of the RHN mass hierarchy.

The functions $\mathcal{F}$ depend upon the variable $1/r_{21}$, which tends to zero in the hierarchical regime, $r_{21} \gg 1$. In that limit, we find the asymptotic behaviour

$$
\begin{aligned}
\epsilon_2^v &\sim \frac{|\alpha_{21}|}{8\pi} \frac{\beta}{M_2} \sqrt{\frac{M_1}{M_2}} (1 - \sigma_2), \\
\epsilon_2^w &\sim \frac{|\alpha_{11}\alpha_{21}|}{16\pi} \sqrt{\frac{M_1}{M_2}} (1 - \sigma_2)^2.
\end{aligned}
\tag{3.29}
$$

In Fig. 3.5a, we compare the above approximate functions with the exact functions calculated in the main text, cf. Eqs. (3.18), (3.22). The approximations are excellent for large M_2/M_1, but only deviate from the exact answer by a factor of 2 for $M_2/M_1 \gtrsim 10$.

Standard Yukawa CP asymmetry   We also recall the conventional contribution to the CP-asymmetry, ϵ_0 [113, 114, 115, 116]. In general, the loop-induced vertex and wave-function contributions from N_i decays are,

$$
\epsilon_{0i}^v = \sum_{j \neq i} \frac{\mathrm{Im}\{(\lambda^\dagger \lambda)_{ji}^2\}}{8\pi (\lambda^\dagger \lambda)_{ii}} \mathcal{F}_0^v(r_{ji}), \qquad \epsilon_{0i}^w = \sum_{j \neq i} \frac{\mathrm{Im}\{(\lambda^\dagger \lambda)_{ji}^2\}}{8\pi (\lambda^\dagger \lambda)_{ii}} \mathcal{F}_0^w(r_{ji}),
\tag{3.30}
$$

with

$$
\mathcal{F}_0^v(r_{ji}) = \sqrt{r_{ji}} \left[1 - (1 + r_{ji}) \log\left(\frac{1 + r_{ji}}{r_{ji}}\right) \right], \qquad \mathcal{F}_0^w(r_{ji}) = \frac{\sqrt{r_{ji}}}{(1 - r_{ji})}.
\tag{3.31}
$$

Using Eq. (3.26) and the Schwartz inequality, we can again relate the Yukawa coupling to the light neutrino masses, and bound from above the magnitude of the

$$\beta=100 \text{ GeV} , \alpha=10^{-5}$$
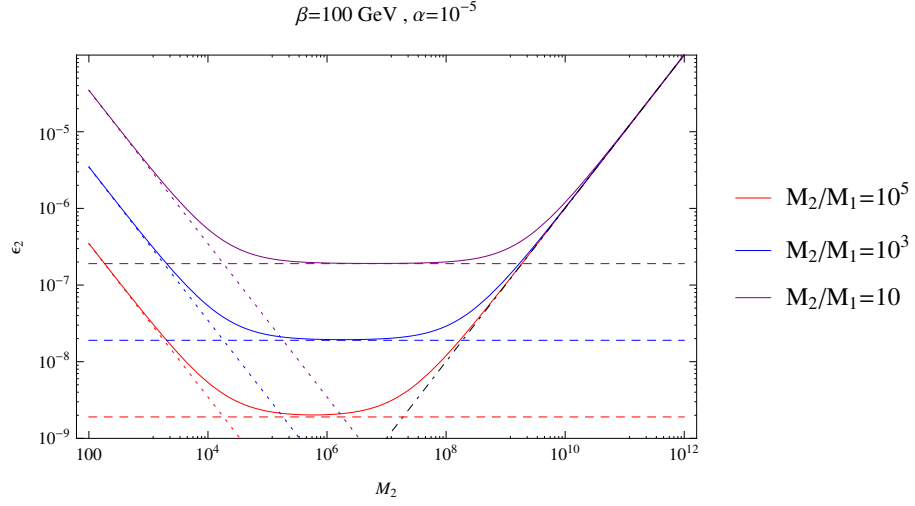
Figure 3.6: The differing contributions to the total CP-asymmetry ϵ_2 for various mass ratios M_2/M_1. The high mass ratio is dominated by the Yukawa-sourced CP-asymmetry, $\epsilon_0 \propto \sum_\alpha m_\alpha M_2/v^2$ (black, dot-dashed line). The low mass CP-asymmetry is proportional to the β coupling via the vertex correction, $\epsilon_{(\beta)} \sim \sqrt{M_1/M_2}|\alpha\beta|/M_2$ (dotted lines). In the intermediate mass range, the CP-asymmetry is dominantly generated by the wave function correction $\epsilon_{(\alpha)} \sim |\alpha|^2\sqrt{M_1/M_2}$ (dashed lines).

CP-asymmetry. Taking $|R_{ij}| \sim 1$, we find

$$|\epsilon_{0i}| \sim \frac{\sum_\alpha m_\alpha}{8\pi v^2} \sum_{j\neq i} M_j \left| \mathcal{F}_0^v(r_{ji}) + \mathcal{F}_0^w(r_{ji}) \right|. \tag{3.32}$$

The sum over the active neutrino masses is constrained by cosmological data, with bounds in the range $\sum_\alpha m_\alpha < 0.2 - 1\text{eV}$ [121, 122, 123, 124]. The additional assumption of a normal hierarchy leads to a stronger constraint $\sum_\alpha m_\alpha \gtrsim m_3 \simeq \sqrt{\Delta m_{31}^2} \simeq 0.04 - 0.05\text{eV}$ at the 3σ level [11, 12, 13, 14]. Throughout this chapter, we assume a normal hierarchy for the light neutrinos, taking $\sum_\alpha m_\alpha \sim m_3 \sim 0.05\text{eV}$. When the internal RHN is much heavier than the external neutrino, so that $r_{ji} \gg 1$, the loop function has the limit $|\mathcal{F}_0^v + \mathcal{F}_0^w| \sim 3/(2\sqrt{r_{ji}})$. At the other end of the spectrum, when the internal RHN is much lighter, $r_{ji} \ll 1$, we find $|\mathcal{F}_0^v + \mathcal{F}_0^w| \sim \sqrt{r_{ji}}|2 + \log(r_{ji})|$, as shown in Fig. 3.5b. The CP-asymmetry from N_1 decays receives contributions from internal $j = 2, 3$ heavy neutrinos, which imply $\sum_{j=2,3} M_j |\mathcal{F}_0^v(r_{j1}) + \mathcal{F}_0^w(r_{j1})| \sim 3M_1$. The CP-asymmetry from N_2 decays receives a contribution from $j = 3$ giving $3M_2/2$, and a contribution from $j = 1$ giving $M_2(M_1^2/M_2^2)|\log(M_2^2/M_1^2)| \ll M_2$, which is ne-

glected. In total, we obtain the standard parametric scaling of the CP-asymmetry,

$$|\epsilon_{01}| \sim \frac{3M_1 \sum_\alpha m_\alpha}{8\pi v^2}, \qquad |\epsilon_{02}| \sim \frac{3M_2 \sum_\alpha m_\alpha}{16\pi v^2}. \tag{3.33}$$

This is analogous to the Davidson-Ibarra bound [125], though somewhat less strict as it depends on $\sum_\alpha m_\alpha$ rather than $m_3 - m_1$, which is a consequence of taking $|R_{ij}| \sim 1$. In the standard case one can go further as the CP-asymmetry is sensitive to the $(\lambda^\dagger \lambda)_{ij}^2$ elements which depend on R_{ij}^2, as can be seen from the representation in (3.26). Thus, the orthogonality condition $\sum_k R_{ki}^2 = 1$ can be used directly, leading to the conventional Davidson-Ibarra bound. The hidden sector CP-asymmetry on the other hand, only depends on $(\lambda^\dagger \lambda)_{ij}$, in which case the orthogonality condition is less constraining, and we have taken $|R_{ij}| \sim 1$ to obtain a characteristic magnitude. For consistency, we have also taken that constraint to obtain the above magnitudes on the standard CP-asymmetries. In practice, the scaling is very similar for the normal hierarchy, where $m_3 - m_1 \sim m_3 \sim \sum_\alpha m_\alpha$.

Combining both the standard and hidden sector contributions gives the *total* $\epsilon_{1,2}$ CP-asymmetries,

$$\begin{aligned}
|\epsilon_1| &\sim \frac{3M_1 \sum_\alpha m_\alpha}{8\pi v^2}, \\
|\epsilon_2| &\sim \frac{3M_2 \sum_\alpha m_\alpha}{16\pi v^2} + \left(\frac{\beta}{M_2} + \frac{|\alpha_{11}|}{2}(1 - \sigma_2) \right) \frac{|\alpha_{21}|}{8\pi} \sqrt{\frac{M_1}{M_2}} (1 - \sigma_2).
\end{aligned} \tag{3.34}$$

The ϵ_2 function is exhibited for a given set of parameters $\{\beta, \alpha\}$ and various mass ratios in Fig. 3.6.

Summary

Most significantly, the kinematic constraint $1 > \sqrt{r_{ji}} + \sqrt{\sigma_i}$, prevents the lighter Neutrino flavor, N_1, from having any CP-odd decays through the Higgs portal, since by definition, $r_{21} > 1$. Only the heavier flavors, $N_{2,3}$ can contribute to the CP-asymmetry through the hidden sector decays. For the remainder of this chapter, we will generally focus on the minimal case with two heavy neutrinos N_1 and N_2, so that the hidden sector will play an important role through the decays of N_2. This presents us with the interesting possibility of taking N_1 parametrically light, where it could have other phenomenological consequences. At the same time, there is also the danger of significant washout of the asymmetry by scattering processes mediated

by N_1. We will discuss the latter issue in some detail in subsequent sections.

The full CP asymmetry is obtained by combining the above results for ϵ_i^v (3.18) and ϵ_i^w (3.22). For the hierarchical $N_1 - N_2$ regime, with $M_2/M_1 \geq 10$ that will be of interest later, the CP-asymmetry can be approximated by the following simple expressions,

$$
\begin{aligned}
\epsilon_1 &\sim \frac{3M_1 \sum_\alpha m_\alpha}{8\pi v^2}, \\
\epsilon_2 &\sim \frac{3M_2 \sum_\alpha m_\alpha}{16\pi v^2} + \left(\frac{\beta}{M_2} + \frac{|\alpha_{11}|}{2}(1 - \sigma_2) \right) \frac{|\alpha_{21}|}{8\pi} \sqrt{\frac{M_1}{M_2}}(1 - \sigma_2).
\end{aligned}
\tag{3.35}
$$

The index $\alpha = 1, 2, 3$, and m_α is the mass of the α-th active neutrino. Assuming a normal hierarchy among the light neutrino masses, we set $\sum_\alpha m_\alpha \simeq m_3 \simeq \sqrt{\Delta m_{31}^2} \sim 0.05\text{eV}$.

3.2   Two-stage Boltzmann evolution

In minimal leptogenesis, the RHN sector $\lambda_{ij} N_j L_i H + M_i N_i N_i$ provides the ingredients for two of Sakharov's conditions to be satisfied; L is violated due to the presence of both M_i and λ_{ij}, while there are physical CP-odd phases in λ_{ij}. The third and final condition is satisfied dynamically as the expansion of the universe provides a mechanism for L-violating processes to go out of equilibrium. For this to happen, the rate Γ_N of L-violating RHN decays must fall below the Hubble expansion rate H. This transition is controlled by the Gamow *equilibrium parameter*, $K = \Gamma_N/H(T = M)$ [60],[2] where the Hubble rate $H(T = M)$ sets the time scale, t_H, at which the equilibrium density becomes Boltzmann suppressed. Setting $K < 1$ ensures the particle lifetime is longer than the Hubble time, $\tau_N > t_H$, and an excess abundance develops. In that case, the rate of decays will be large compared to that of inverse decays in order for the neutrino abundance to be able to reach equilibrium, effectively putting the system out of equilibrium.

In Higgs Portal Leptogenesis (HPL), we require at least two Majorana neutrinos and there are two major implications. On one hand, the CP-asymmetry from N_2 decays (3.35) is enhanced for low masses, and can in fact become the dominant

---

[2]We will follow the literature and denote the Hubble-normalized N decay rate as K, while the modified Bessel function that generically appears in the thermal rates will consistently be written as $K_i(z)$, distinguished by the extra argument $z = M/T$.

contribution. This suggests the possibility of establishing a 'lower energy' theory of leptogenesis, mainly controlled by N_2 physics. On the other hand, the two RHN flavors leads to a novel evolution in the total lepton asymmetry. In minimal leptogenesis, the lepton asymmetry is primarily generated in a temperature range near the lightest RHN mass, $T \sim M_1$, since the decays and scattering are out-of-equilibrium for lower temperatures. The difference here is that, even though most of the lepton asymmetry can be generated through N_2 decays and inverse decays at temperatures around $T \sim M_2$, the lighter neutrino flavor N_1 potentially remains in equilibrium and can mediate rapid washout of the N_2-generated asymmetry. These interactions will be studied carefully below, to identify regimes in which N_1 is sufficiently weakly coupled that these new washout processes are suppressed.

3.2.1 Decay rates and scattering cross sections

Before going into the derivation of the Boltzmann equations, in Sec. 3.2.2, this subsection compiles the relevant decay rates and scattering cross sections used in the HPL Boltzmann equations. We summarize the relevant scattering processes in Fig. 3.7.

Decays and inverse decays

At tree level, one has the RHN decay rates to leptons,

$$\Gamma(N_i \to LH) = \Gamma(N_i \to \overline{LH}) = \sum_{k,\alpha,\beta} \Gamma(N_i \to L_k^\alpha H^\beta) = \frac{(\lambda^\dagger \lambda)_{ii}}{16\pi} M_i,$$

$$\Gamma_i = \Gamma(N_i \to LH) + \Gamma(N_i \to \overline{LH}) = \frac{(\lambda^\dagger \lambda)_{ii}}{8\pi} M_i. \tag{3.36}$$

The indices $\alpha, \beta = 1, 2$ refer to the SU(2) doublets, and enumerate the electron-type and the neutrino-type leptons. The index $k = 1, 2, 3$ runs through the three families, electron, muon, and tau. One of the hidden sector decays we encounter is $N_2 \to N_1 S$,

$$\Gamma(N_2 \to N_1 S) = \frac{|\alpha_{12}|^2 M_2}{16\pi} \left[\left(1 + \frac{M_1}{M_2}\right)^2 - \frac{m_S^2}{M_2^2} \right] \sqrt{\left(1 - \frac{M_1^2}{M_2^2} - \frac{m_S^2}{M_2^2}\right)^2 - 4\frac{M_1^2}{M_2^2}\frac{m_S^2}{M_2^2}}, \tag{3.37}$$

where we used the approximation that $\alpha_{ij} = \text{Re}\{\alpha_{ij}\}$, which is not generally true because of the complex phases contained in α, but the CP-odd contributions are not relevant here as the decay is L-conserving.

Visible sector scattering

These processes involve the SM quarks and leptons in external states.

- *s-channel*: the $N_i L \leftrightarrow Qt$ cross section and reduced cross section read

$$\sigma(N_i L \to Q\bar{t}) = \sum_{\alpha,k} \sigma(N_i L_k^\alpha \to Q\bar{t}) = \frac{(\lambda^\dagger \lambda)_{ii}}{8\pi} \frac{m_t^2}{v^2} \frac{1}{s},$$

$$\hat{\sigma}(N_i L \to Q\bar{t}) = \frac{(\lambda^\dagger \lambda)_{ii}}{8\pi} \frac{m_t^2}{v^2} \frac{(s - M_i^2)^2}{s^2}.$$

(3.38)

- *t-channel*: We consider $N_i Q \leftrightarrow Lt$ and $N_i t \leftrightarrow LQ$. Because the leptons and quarks are assumed massless, these two channels are in fact equal. We have the cross section and reduced cross sections

$$\sigma(N_i Q \to Lt) = \frac{(\lambda^\dagger \lambda)_{ii}}{8\pi} \frac{m_t^2}{v^2} \frac{1}{s} \left[\frac{s - 2M_i^2 + 2m_h^2}{s - M_i^2 + m_h^2} + 2\frac{M_i^2 - m_h^2}{s - M_i^2} \ln\left(\frac{s - M_i^2 + m_h^2}{m_h^2} \right) \right],$$

$$\hat{\sigma}(N_i Q \to Lt) = \frac{(\lambda^\dagger \lambda)_{ii}}{8\pi} \frac{m_t^2}{v^2} \frac{s - M_i^2}{s} \left[\frac{s - 2M_i^2 + 2m_h^2}{s - M_i^2 + m_h^2} + 2\frac{M_i^2 - m_h^2}{s - M_i^2} \ln\left(\frac{s - M_i^2 + m_h^2}{m_h^2} \right) \right].$$

(3.39)

Throughout this chapter, we take the approximation that the zero-temperature Higgs mass $m_h = 0$, but in this limit, these cross sections are infrared divergent. The regulator to use, however, is the thermal mass which can potentially be quite large at leptogenesis temperatures. In practice, the cross section is only logarithmically sensitive to the regulator, and we therefore make the conventional choice $m_h/M_i = 10^{-5}$.

Hidden sector scattering

- *s-channel*: $N_i L \leftrightarrow HS$ through the βHHS vertex. The cross section and reduced cross section are

$$\sigma(N_i L \to HS) = \sum_{\alpha,k} \sigma(N_i L_k^\alpha \to HS) = \frac{(\lambda^\dagger \lambda)_{ii}\beta^2}{8\pi} \frac{s - m_S^2}{s^3},$$

$$\hat{\sigma}(N_i L \to HS) = \frac{(\lambda^\dagger \lambda)_{ii}\beta^2}{8\pi} \frac{(s - m_S^2)(s - M_i^2)^2}{s^4}.$$

(3.40)

- *s-channel*: $N_i S \leftrightarrow LH$, through the hidden sector vertex $\alpha_{ij} N_i N_j S$. This process is mediated by N_j, and the amplitude should thus be summed over

all flavors. However, we shall simplify the discussion by considering only one internal flavor. In the the limit of massless S, the cross section takes the form

$$\sigma(N_i S \to LH) = \sum_j \sum_{\alpha,k} \sigma(N_i S \to L_k^\alpha H)$$

$$= \sum_j \frac{(\lambda^\dagger \lambda)_{jj} |\alpha_{ij}|^2}{16\pi} \frac{(s + M_i^2)(s + M_j^2) - 4sM_iM_j}{\sqrt{\delta(s, M_i^2, m_s^2)}((s - M_j^2)^2 + \mathcal{E}_j^2)},$$

$$\hat\sigma(N_i S \to LH) = \sum_j \frac{(\lambda^\dagger \lambda)_{jj} |\alpha_{ij}|^2}{16\pi} \frac{(s - M_i^2)}{s} \frac{(s + M_i^2)(s + M_j^2) - 4sM_iM_j}{(s - M_j^2)^2 + \mathcal{E}_j^2}, \qquad \mathcal{E}_j = M_j \Gamma_j.$$

$$(3.41)$$

- *s-channel*: $N_i N_j \leftrightarrow HH$ mediated by S. Taking the notation, $\delta(s, M_i, M_j) = (s - M_i^2 - M_j^2)^2 - 4M_i^2 M_j^2$, the cross section and reduced cross section are given by

$$\sigma(N_i N_j \to HH) = \frac{|\alpha_{ij}|^2 \beta^2}{32\pi} \frac{s - (M_i + M_j)^2}{\sqrt{\delta(s, M_i, M_j)}(s - m_S^2)^2},$$

$$\hat\sigma(N_i N_j \to HH) = \frac{|\alpha_{ij}|^2 \beta^2}{32\pi} \sqrt{\delta(s, M_i, M_j)} \frac{s - (M_i + M_j)^2}{s(s - m_S^2)^2}.$$

$$(3.42)$$

- *t-channel*: $N_i H \leftrightarrow LS$ and $N_i S \leftrightarrow LH$, both mediated by a Higgs. Care is needed in computing these cross sections, because the Higgs mediator can be produced on-shell. This is true even if the Higgs has a small but finite mass. Thus, these processes will almost always be divergent, as they include the kinematic regime where the RH neutrino decays on-shell to LH. It is therefore important to note that the cross section is regulated by the external neutrino decay width. This subtlety has been noted previously in a different context [126, 127]. Starting with $N_i H \to LS$, the amplitude squared takes the form

$$\sum_{\alpha,\beta,k} \sum_{spins} |i\mathcal{M}(N_i H^\beta \to L_k^\alpha S)|^2 = 2\beta^2 \left[\frac{(\lambda^\dagger \lambda)_{ii} M_i^2}{t^2 + \mathcal{E}_i^2} - (\lambda^\dagger \lambda)_{ii} \frac{t}{t^2 + \mathcal{E}_i^2} \right]. \quad (3.43)$$

Upon integration over the transfer momentum, the second term leads to a logarithmic divergence. The first term is naively more problematic because it leads to a linear divergence, $1/\mathcal{E}_i$. However, in the narrow width limit, upon integration this term gives the delta function $\delta(t)$. This is the signature of an

$$\lambda_1 \sim 6.\cdot 10^{-7},\ \alpha \sim 3.\cdot 10^{-5},\ \beta = 10^3\,\mathrm{GeV},\ M_2 = 10^4\,\mathrm{GeV},\ M_1 = 10^2\,\mathrm{GeV}$$
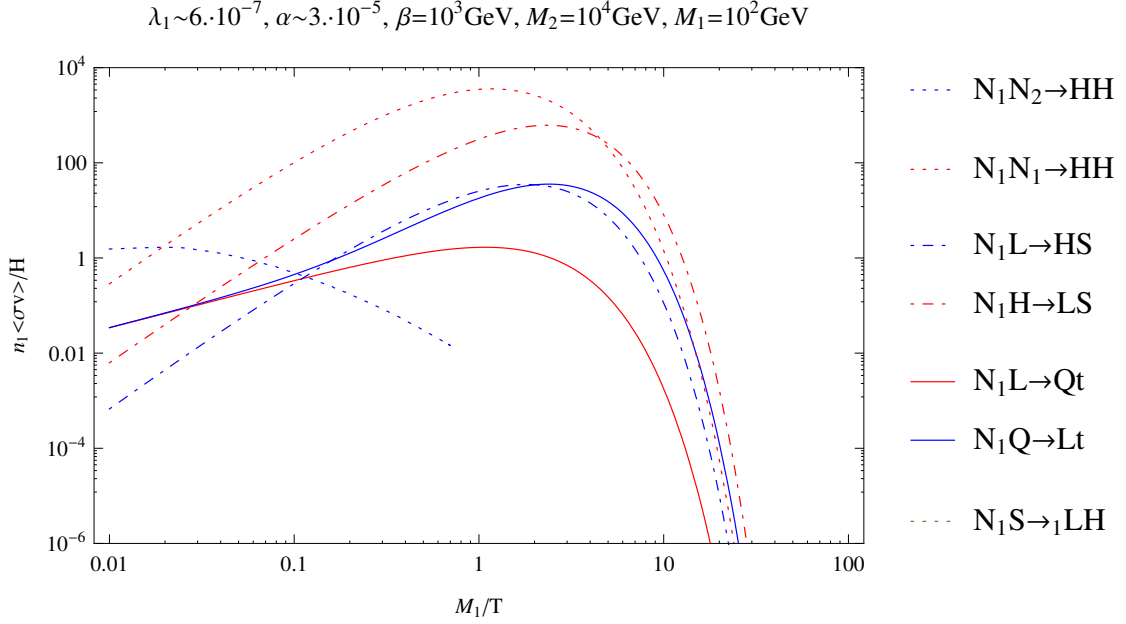
Figure 3.7: This plot is a summary of the important scattering processes to account for, in order to properly manage the effect of N_1 on the lepton asymmetry. The corresponding Feynman diagrams are shown in the main text, in Fig. 3.10.

on-shell mediator, which splits the scattering into the two on-shell subprocesses $N \to LH$ followed by $HH \to S$. The first part is already accounted for in the Boltzmann equations, and should be subtracted in order to avoid double-counting [128]. In effect, this is a t-channel RIS. The subtracted scattering cross section we use is then

$$
\begin{aligned}
\sigma(N_i H \to LS) &= \frac{(\lambda^\dagger \lambda)_{ii}\beta^2}{16\pi(s - M_i^2)^2} \log\left(\frac{s^2(s - M_i^2 - m_S^2)^2 + s^2 \mathcal{E}_i^2}{M_i^4 m_S^4 + s^2 \mathcal{E}_i^2}\right), \\
\hat{\sigma}(N_i H \to LS) &= \frac{(\lambda^\dagger \lambda)_{ii}\beta^2}{16\pi s} \log\left(\frac{s^2(s - M_i^2 - m_S^2)^2 + s^2 \mathcal{E}_i^2}{m_S^4 + s^2 \mathcal{E}_i^2}\right), \quad \mathcal{E}_i = M_i \Gamma_i.
\end{aligned}
\tag{3.44}
$$

The decay rate to account for in $\mathcal{E}_i$ is the *total* rate, that is $\mathcal{E}_1 = M_i \Gamma_1$ for N_1 but $\mathcal{E}_2 = M_2\left(\Gamma_2 + \Gamma_{21}\right)$ for N_2. This is model dependent, though we can safely assume that $\lambda^2, \alpha^2 \leqslant 10^{-5}$, which inspires our choice $\mathcal{E}_i/M_i^2 = 10^{-5}$. The cross section is only weakly dependent on the prescription, as the residual divergence is logarithmic.

3.2.2 Boltzmann equations

In the minimal leptogenesis scenario, typically once the neutrino decays go out-of-equilibrium, all the scattering processes also go out-of-equilibrium. The new feature in HPL is the possibility of having scattering processes in equilibrium during the period that a CP-asymmetry would be generated through out of equilibrium decays. The most significant are those L-violating scattering processes with an external N_1, whose abundance is not Boltzmann suppressed. The scattering processes that have an external N_2 are of course suppressed by the N_2 abundance which rapidly falls off exponentially. Among the scattering processes that violate the lepton number by $\Delta L = 1$ units, we include the scattering $N_i L \leftrightarrow Q\bar{t}$ in the s-channel, and $N_i Q \leftrightarrow Lt$, $Nt \leftrightarrow LQ$ in the t-channel. From the hidden sector, one includes the s-channel processes $N_i L \leftrightarrow HS$ mediated by a Higgs, and $N_i S \leftrightarrow LH$ mediated by a neutrino. In the t-channel one has $N_i S \leftrightarrow LH$ and $N_i H \leftrightarrow LS$ both mediated by a Higgs. A full treatment of neutrino-mediated scattering is complicated because of the λ_{ij} and α_{ij} flavor structures. For simplicity, we will ignore the flavor-mixing in these processes with intermediate neutrinos, e.g. $\sigma_{N_i S \leftrightarrow LH} = \sum_j \sigma_{N_i S \underset{j}{\leftrightarrow} LH}$, and assume the processes are dominated by one flavor. This is sufficient for order of magnitude estimates. Note that because of the α_{ij} coupling, we need to include interactions such as $N_i N_j \leftrightarrow HH$ mediated by S in the s-channel, which can efficiently deplete the neutrino abundance, and in turn affect the lepton asymmetry washout [129].[3]

As for the $\Delta L = 2$ interactions, one has $LH \leftrightarrow \overline{LH}$ mediated by a neutrino in the s-channel, and $LL \leftrightarrow HH$, $\overline{LL} \leftrightarrow HH$ mediated by a neutrino in the t-channel. We start by describing the Boltzmann equations for the lepton asymmetry, which are the most complex, and then review the neutrino abundance and the general features. Note that this work is concerned with the main dynamical features of the model presented above, focussing on the impact of the Higgs portal couplings. Thus, in deriving the Boltzmann equations, we study only the *total* lepton asymmetry, ignoring the often significant effects on individual lepton flavors [96, 97, 98, 99, 100, 101]. For our purposes, it will also be sufficient to utilize the CP-asymmetries calculated within zero-temperature field theory, although real-time thermal field theory provides a more complete formalism, see e.g. [131, 132, 133, 134, 135, 136, 137].

---

[3]In the context of standard leptogenesis, $\Delta N = 2$ interactions, e.g. $N_1 N_1 \to HH$ mediated by a lepton in the t-channel, are negligible since they scale as λ^4 which is suppressed for $M_1 \lesssim 10^{15}$GeV. Interactions in the $\Delta N = 2$ class have for instance been taken into account in the context of GUT theories in [130].

Lepton asymmetry

We are following the procedure elaborated in 2.2. Starting with the lepton asymmetry equation, we have

$$
\begin{aligned}
n_\gamma^{eq} z_1 H \frac{\partial Y_{L-\bar{L}}}{\partial z_1} = \sum_i & \left[\frac{Y_i}{Y_i^{eq}} \left(\gamma^{eq}_{N_i \to LH} - \gamma^{eq}_{N_i \to \overline{LH}} \right) - \frac{Y_L}{Y_L^{eq}} \gamma^{eq}_{LH \to N_i} + \frac{Y_{\bar{L}}}{Y_L^{eq}} \gamma^{eq}_{\overline{LH} \to N_i} \right. \\
& \left. - \frac{Y_{L-\bar{L}}}{Y_L^{eq}} \left(\frac{Y_i}{Y_i^{eq}} \gamma^{eq}_{N_i L \to Qt} + \frac{Y_i}{Y_i^{eq}} \gamma^{eq}_{N_i L \to HS} + 2\gamma^{eq}_{N_i Q \to Lt} + 2\gamma^{eq}_{N_i H \to LS} \right) \right] \\
& - \frac{Y_{L-\bar{L}}}{Y_L^{eq}} \left(\gamma^{eq}_{N_1 S \underset{1}{\to} LH} + \gamma^{eq}_{N_2 S \underset{1}{\to} LH} + \gamma^{eq}_{N_2 S \underset{2}{\to} LH} \right) \\
& + \frac{Y_1}{Y_1^{eq}} \left(\gamma^{eq,sub}_{N_1 S \underset{2}{\to} LH} - \gamma^{eq,sub}_{N_1 S \underset{2}{\to} \overline{LH}} \right) - \frac{Y_L}{Y_L^{eq}} \gamma^{eq,sub}_{LH \underset{2}{\to} N_1 S} + \frac{Y_{\bar{L}}}{Y_L^{eq}} \gamma^{eq,sub}_{\overline{LH} \underset{2}{\to} N_1 S} \\
& - 2\frac{Y_L}{Y_L^{eq}} \sum_j \gamma^{eq,sub}_{LH \to \overline{LH}_j} + 2\frac{Y_{\bar{L}}}{Y_{\bar{L}}^{eq}} \sum_j \gamma^{eq,sub}_{\overline{LH} \to LH_j} \\
& - 2\frac{Y_{L-\bar{L}}}{Y_L^{eq}} \sum_j \gamma^{eq}_{LL \to HH_j}.
\end{aligned}
$$

$$(3.45)$$

In this expression, we use the following notation,

$$
z_i = \frac{M_i}{T}, \qquad Y_i = \frac{n_i}{n_\gamma^{eq}}, \qquad Y_i^{eq} = \frac{3}{8} z_i^2 K_2(z_i), \tag{3.46}
$$

where $K_i(z)$ is a modified Bessel function of the second kind, along with the thermal cross sections,

$$
\gamma^{eq}_{i \to mn}(T) = n_i^{eq} \Gamma_{i \to mn} \left\langle \frac{M_i}{E} \right\rangle = n_i^{eq} \frac{K_1(z_i)}{K_2(z_i)} \Gamma_{i \to mn},
$$

$$
\gamma^{eq}_{ij \to mn}(T) = n_i^{eq} n_j^{eq} \langle v\sigma_{ij \to mn\cdots} \rangle = g_i g_j \frac{T^4}{32\pi^4} \int_{w_{min}}^{\infty} dw \sqrt{w} K_1\left(\sqrt{w}\right) \hat{\sigma}_{ij \to mn}\left(w \frac{m_i^2}{z_i^2}\right),
$$

$$(3.47)$$

where $w = s/T^2$, and the reduced cross section $\hat{\sigma}$ is given by

$$
\hat{\sigma}_{ij \to mn}(s) = \frac{1}{s} \delta\left(s, m_i^2, m_j^2\right) \sigma_{ij \to mn}(s), \qquad \delta(a, b, c) = (a - b - c)^2 - 4bc. \tag{3.48}
$$

In writing the above equation, we have assumed CP-invariance, $\gamma^{eq}_{\overline{ij}\to\overline{mn}} = \gamma^{eq}_{ij\to mn}$ in the scattering processes, along with CPT-symmetry, $\gamma^{eq}_{\overline{ij}\to\overline{mn}} = \gamma^{eq}_{mn\to ij}$. CP-violating corrections appear in the scattering amplitudes at fourth order in the coupling constants, which is of higher order than we will consider here. That being said, it is necessary to make an exception when dealing with the subtracted rates as discussed below.

The superscript 'sub' signifies that the process contains a real-intermediate-state (RIS) mediator that should be subtracted. Most famously, the process $LH \to \overline{LH}$ is mediated by a neutrino N_j in the s-channel which can be on-shell for a sufficiently high center of mass energy. The real intermediate state represents the physical process $LH \to N_j \to \overline{LH}$. However, these processes are already accounted for by decays and inverse decays, and therefore need to be removed. Similarly, $N_1 S \xrightarrow{2} LH$ has the real intermediate state $N_1 S \to N_2 \to LH$, which is also accounted for by decays and inverse decays. As it turns out, the t-channel process $N_i H \to LS$ also contains a real intermediate state, that needs to be removed. This point is explained in Appendix 3.2.1, where explicit formulas for the cross sections are displayed. For simplicity, all quarks and leptons, as well as the Higgs and scalar S are considered massless. This can be justified because leptogenesis necessarily occurs at temperatures above sphaleron decoupling, $T > T_{sphaleron} \sim 160\,\text{GeV} > m_H$ [138], though typically we shall take $M_2 > 1$ TeV. The singlet S mass is not yet stringently constrained, provided the Higgs portal coupling is not too large [139], but we will typically take it to be of the same order as the Higgs mass. With these simplifications, the t-channel processes $N_i Q \leftrightarrow Lt$ and $N_i t \to LQ$ have equal rates, and similarly for $N_i H \to LS$ and $N_i S \to LH$, which explains the factor of '2' sitting in front of these processes in Eq. (3.45) above.

Subtracted Rates and Real Intermediate States

In this subsection, we summarize the procedure used to account for real intermediate states. The source terms in the Boltzmann equations are systematically expanded in each of the couplings and one needs to avoid double counting the RIS contributions that appear in (naively) higher order scattering processes. Doing this consistently in standard leptogenesis requires the inclusion of all processes up to and including two-to-three scattering and the associated CP-asymmetries [140, 141]. For HPL, we will
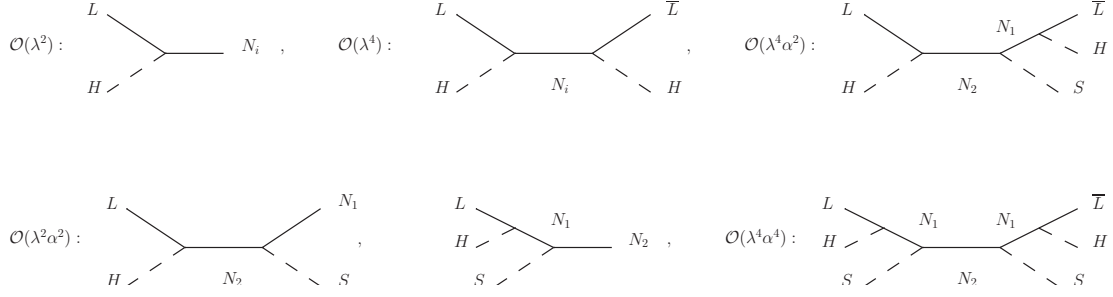
Figure 3.8: Classes of decay and scattering diagrams and sub-diagrams. We subtract the N_i real intermediate states coupling through α and λ order by order to avoid double counting, as discussed in the text.

do the same, extending the analysis to account for real intermediate states coupling via both the Yukawa λ_{ij} and the singlet α_{ij} interactions. The relevant tree-level diagrams are displayed in Fig. 3.8, although it's important to account also for loop corrections that contribute to the CP-asymmetries in scattering. As already mentioned, we will focus on the impact of the additional singlet decay channel and ignore the issue of neutrino flavor mixing in scattering amplitudes, e.g. $\gamma^{eq}_{LH \to \overline{LH}} = \sum_i \gamma^{eq}_{LH \to \overline{LH}_i}$, which has been discussed in detail elsewhere. The RIS calculation of the s-channel cross sections is generally a nontrivial task once the flavor structure is taken into account. However, given this simplifying assumption, we can use the result $\gamma^{sub} = \gamma - \gamma^{on-shell}$ [59, 95].

To proceed to discuss the subtracted rates, we first make the following definitions associated with N_2 decays,

$$
\begin{aligned}
\Gamma_{2T} &= \Gamma_2 + \Gamma_{N_2 \to N_1 S}, \\
\Gamma_2 &= \Gamma_{N_2 \to LH} + \Gamma_{N_2 \to \overline{LH}}, \\
\epsilon_2 \Gamma_2 &= \Gamma_{N_2 \to LH} - \Gamma_{N_2 \to \overline{LH}},
\end{aligned}
\implies
\begin{aligned}
\mathrm{Br}(N_2 \to LH) &= \frac{1 + \epsilon_2}{2} \frac{\Gamma_2}{\Gamma_{2T}}, \\
\mathrm{Br}(N_2 \to \overline{LH}) &= \frac{1 - \epsilon_2}{2} \frac{\Gamma_2}{\Gamma_{2T}}, \\
\mathrm{Br}(N_2 \to N_1 S) &= \frac{\Gamma_{21}}{\Gamma_{2T}} = 1 - \frac{\Gamma_2}{\Gamma_{2T}},
\end{aligned}
\tag{3.49}
$$

where Γ_{21} is shorthand notation for $\Gamma_{N_2 \to N_1 S}$, while N_1 only decays to leptons, so that

$$
\begin{aligned}
\Gamma_{1T} &= \Gamma_1, \\
\Gamma_1 &= \Gamma_{N_1 \to LH} + \Gamma_{N_1 \to \overline{LH}}, \\
\epsilon_1 \Gamma_1 &= \Gamma_{N_1 \to LH} - \Gamma_{N_1 \to \overline{LH}},
\end{aligned}
\implies
\begin{aligned}
\mathrm{Br}(N_1 \to LH) &= \frac{1 + \epsilon_1}{2}, \\
\mathrm{Br}(N_1 \to \overline{LH}) &= \frac{1 - \epsilon_1}{2}.
\end{aligned}
\tag{3.50}
$$

Building up the equations order by order, we have the following contributions:
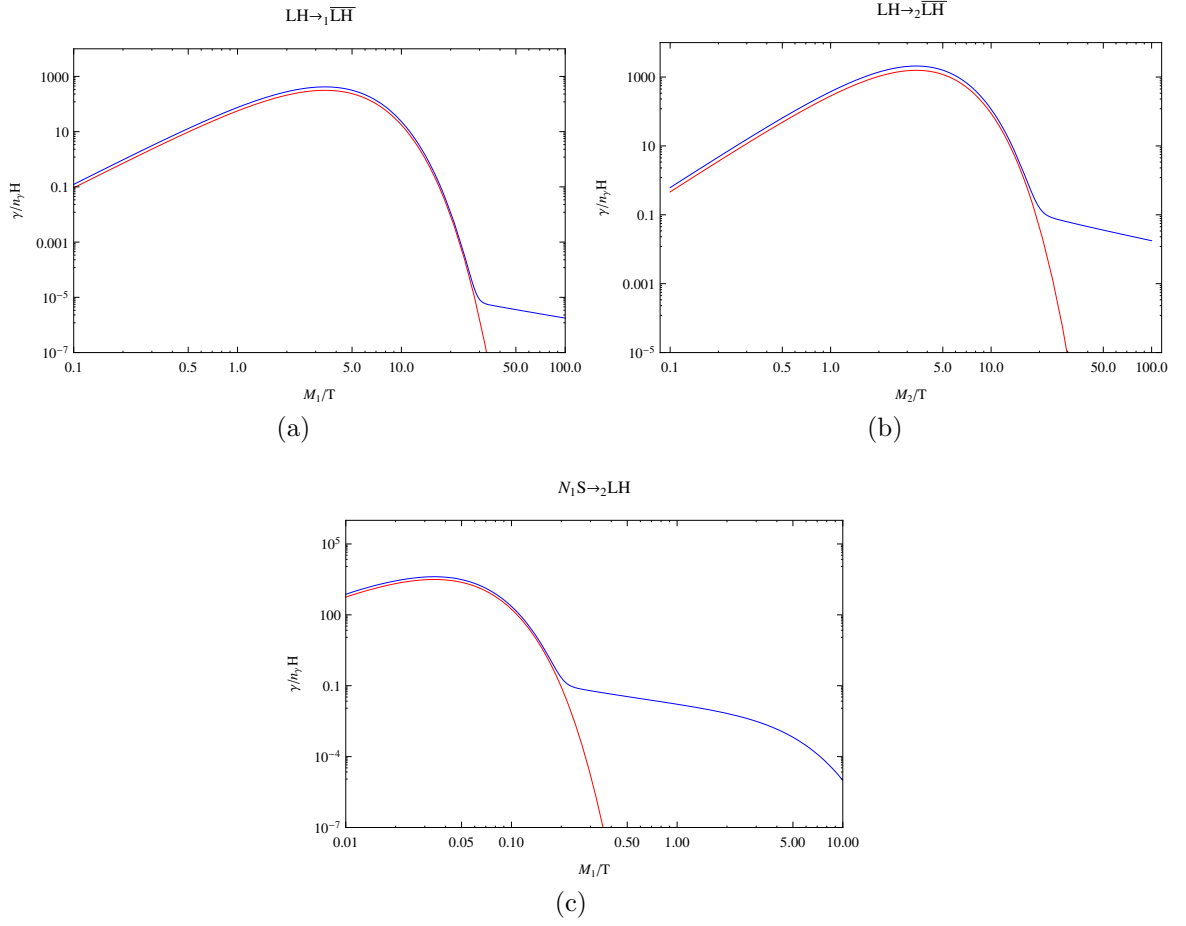
Figure 3.9: Plots of the un-subtracted thermal rates (blue), along with their on-shell parts (red). The plots in (a), (b) and (c) are for $LH \underset{1}{\rightarrow} \overline{LH}$, $LH \underset{2}{\rightarrow} \overline{LH}$, and $N_1 S \underset{2}{\rightarrow} LH$ respectively, generated using $\lambda_1 \sim 0.002$, $\lambda_2 \sim 0.07$, $\alpha_{12} \sim 0.07$, $M_2 = 10^{10}$GeV, $M_1 = 10^8$GeV.

- $\mathcal{O}(\lambda^2)$: 1-to-2 decays,

$$n_\gamma^{eq} z_1 H \frac{\partial Y_{L-\overline{L}}}{\partial z_1}\bigg|_{\lambda^2} = \sum_{i=1,2} \left[\frac{Y_i}{Y_i^{eq}} \left(\gamma_{N_i \rightarrow LH}^{eq} - \gamma_{N_i \rightarrow \overline{LH}}^{eq} \right) - \frac{Y_L}{Y_L^{eq}} \gamma_{LH \rightarrow N_i}^{eq} + \frac{Y_{\overline{L}}}{Y_L^{eq}} \gamma_{\overline{LH} \rightarrow N_i}^{eq} \right]$$

$$= \left(\frac{Y_1}{Y_1^{eq}} + 1 \right) \epsilon_1 \gamma_{D_1}^{eq} + \left(\frac{Y_2}{Y_2^{eq}} + 1 \right) \epsilon_2 \gamma_{D_2}^{eq} - \frac{Y_{L-\overline{L}}}{2Y_L^{eq}} \left(\gamma_{D_1}^{eq} + \gamma_{D_2}^{eq} \right).$$

$$(3.51)$$

This Boltzmann equation suffers from the well-known flaw that it does not respect Sakharov conditions. Indeed, even in equilibrium $Y_i = Y_i^{eq}$, a lepton asymmetry may be generated because of the non-vanishing source term. This is related to the fact that at $\mathcal{O}(\lambda^2)$, the set of interactions is incomplete because

$\Delta L = 2$ rates at (naive) $\mathcal{O}(\lambda^4)$ contain real intermediate state contributions that are in fact of order $\mathcal{O}(\lambda^2)$ and need to be included; see below.

- $\mathcal{O}(\lambda^4)$: $\Delta L = 2$ scattering (2-to-2),

$$
n_\gamma^{eq} z_1 H \frac{\partial Y_{L-\overline{L}}}{\partial z_1}\bigg|_{\lambda^4} = \sum_{j=1,2} \left[-2\frac{Y_L}{Y_L^{eq}} \gamma_{LH \xrightarrow{}_j \overline{LH}}^{eq,sub} + 2\frac{Y_{\overline{L}}}{Y_{\overline{L}}^{eq}} \gamma_{\overline{LH} \xrightarrow{}_j LH}^{eq,sub} \right]
$$
$$
= -2\epsilon_1 \gamma_{D_1}^{eq} - 2\epsilon_2 \frac{\Gamma_2}{\Gamma_{2T}} \gamma_{D_2}^{eq} - \frac{Y_{L-\overline{L}}}{Y_L^{eq}} \left(2\gamma_{\Delta L=2}^{eq,sub,2} + 2\gamma_{\Delta L=2}^{eq,sub,1} \right),
$$

$$(3.52)$$

where we used the definitions for the subtracted $\Delta L = 2$ rates,

$$
\gamma_{LH \xrightarrow{}_2 \overline{LH}}^{eq,on-shell} = \gamma_{LH \to N_2}^{eq} \mathrm{Br}(N_2 \to \overline{LH}) = \left(\frac{1-\epsilon_2}{2} \right)^2 \frac{\Gamma_2}{\Gamma_{2T}} \gamma_{D_2}^{eq} \approx \frac{1-2\epsilon_2}{4} \frac{\Gamma_2}{\Gamma_{2T}} \gamma_{D_2}^{eq},
$$
$$
\gamma_{LH \xrightarrow{}_2 \overline{LH}}^{eq,sub} = \gamma_{\Delta L=2}^{eq,sub,(2)} - \frac{\epsilon_2}{2} \frac{\Gamma_2}{\Gamma_{2T}} \gamma_{D_2}^{eq},
$$
$$
\gamma_{\Delta L=2}^{eq,sub,(2)} \equiv \gamma_{LH \xrightarrow{}_2 \overline{LH}}^{eq} - \frac{1}{4} \frac{\Gamma_2}{\Gamma_{2T}} \gamma_{D_2}^{eq},
$$
$$
\Delta\gamma_{\Delta L=2}^{eq,sub,(2)} \equiv \gamma_{LH \xrightarrow{}_2 \overline{LH}}^{eq,sub} - \gamma_{\overline{LH} \xrightarrow{}_2 LH}^{eq,sub} = -\epsilon_2 \frac{\Gamma_2}{\Gamma_{2T}} \gamma_{D_2}^{eq},
$$

$$(3.53)$$

and

$$
\gamma_{LH \xrightarrow{}_1 \overline{LH}}^{eq,on-shell} = \gamma_{LH \to N_1}^{eq} \mathrm{Br}(N_1 \to \overline{LH}) = \left(\frac{1-\epsilon_1}{2} \right)^2 \gamma_{D_1}^{eq} \approx \frac{1-2\epsilon_1}{4} \gamma_{D_2}^{eq},
$$
$$
\gamma_{LH \xrightarrow{}_1 \overline{LH}}^{eq,sub} = \gamma_{\Delta L=2}^{eq,sub,(1)} - \frac{\epsilon_1}{2} \gamma_{D_1}^{eq},
$$
$$
\gamma_{\Delta L=2}^{eq,sub,(1)} \equiv \gamma_{LH \xrightarrow{}_1 \overline{LH}}^{eq} - \frac{1}{4} \gamma_{D_1}^{eq},
$$
$$
\Delta\gamma_{\Delta L=2}^{eq,sub,(1)} \equiv \gamma_{LH \xrightarrow{}_1 \overline{LH}}^{eq,sub} - \gamma_{\overline{LH} \xrightarrow{}_1 LH}^{eq,sub} = -\epsilon_1 \gamma_{D_1}^{eq}.
$$

$$(3.54)$$

The unsubtracted $\Delta L = 2$ rates are CP-symmetric at $\mathcal{O}(\lambda^2)$, which implies that the subtracted rates are in fact CP-asymmetric. The functions $\gamma_{\Delta L=2}^{eq,sub,(i)}$ are the CP-conserving parts of the subtracted $\Delta L = 2$ rates, and have been plotted in Fig. 3.9a and 3.9b, showing that the CP-conserving subtracted rates are negligible.

Note that the RIS CP-asymmetry that comes from the N_1-mediated $\Delta L = 2$

rate corrects the flaw above in the Boltzmann equation (3.51). The $\Delta L = 2$ rates mediated by N_2 however do not fully correct the above Boltzmann equation. This is in contrast to the standard case, the reason being that $\mathrm{Br}(N_2 \to N_1 S) > 0$, so there is a second decay channel. Unlike in the standard case, for HPL, obtaining a consistent set of Boltzmann equations requires including the RIS contributions from higher order $\Delta L = 2$ scattering processes; see Eq. (3.55) below.

- $\mathcal{O}(\lambda^4 \alpha^2)$: $\Delta L = 2$ scattering (2-to-3),

$$
\begin{aligned}
n_\gamma^{eq} z_1 H \frac{\partial Y_{L-\bar{L}}}{\partial z_1}\bigg|_{\lambda^4 \alpha^2} = &- 4 \frac{Y_L}{Y_L^{eq}} \gamma_{LH \underset{2}{\to} \overline{LH}S}^{eq,sub} + 4 \frac{Y_{\bar{L}}}{Y_L^{eq}} \gamma_{\overline{LH} \underset{2}{\to} LHS}^{eq,sub} \\
= &- 2\epsilon_2 \frac{\Gamma_{21}}{\Gamma_{2T}} \gamma_{D_2}^{eq} - 4 \frac{Y_{L-\bar{L}}}{Y_L^{eq}} \gamma_{\Delta L=2}^{eq,(2-3)} \\
&- 2\Delta \gamma_{\Delta L=1}^{eq,sub} - 2\epsilon_1 \frac{\Gamma_{21}}{\Gamma_{2T}} \gamma_{D_2}^{eq},
\end{aligned}
\tag{3.55}
$$

where we have defined

$$
\begin{aligned}
\gamma_{LH \underset{2}{\to} \overline{LH}S}^{eq,on-shell} &= \gamma_{LH \underset{2}{\to} N_1 S}^{eq,sub} \frac{1 - \epsilon_1}{2} + \frac{(1 - \epsilon_1)(1 - \epsilon_2)}{4} \frac{\Gamma_{21}}{\Gamma_{2T}} \gamma_{D_2}^{eq}, \\
\gamma_{LH \underset{2}{\to} \overline{LH}S}^{eq,sub} &= \gamma_{LH \underset{2}{\to} \overline{LH}S}^{eq} - \gamma_{\Delta L=2}^{eq,(2-3)} + \frac{1}{4} \Delta \gamma_{\Delta L=1}^{eq,sub} + \frac{\epsilon_1 + \epsilon_2}{4} \frac{\Gamma_{21}}{\Gamma_{2T}} \gamma_{D_2}^{eq}, \\
\gamma_{\Delta L=2}^{eq,(2-3)} &= \gamma_{LH \underset{2}{\to} \overline{LH}S}^{eq} - \frac{1}{4} \gamma_{\Delta L=1}^{eq},
\end{aligned}
\tag{3.56}
$$

ignoring terms of order $\mathcal{O}(\lambda^6 \alpha^2)$ and above. The functions $\gamma_{\Delta L=1}^{eq}$ and $\Delta \gamma_{\Delta L=1}^{eq,sub}$ are the CP-conserving and CP-violating parts of the $N_1 S \underset{2}{\to} LH$ scattering terms, as is defined in equations (3.58) below.

In Eq. (3.55), the factors of 4 arise on accounting for both $LH \underset{2}{\to} \overline{LH}S$ and $LHS \underset{2}{\to} \overline{LH}$, which are CPT conjugates of each other. The first term on the first line is exactly what is needed to combine with the RIS term from Eq. (3.52) and correct the flaw in (3.51). The second line of Eq. (3.55) in fact contains terms that correspond to RIS contributions at $\mathcal{O}(\lambda^2 \alpha^2)$.

- $\mathcal{O}(\lambda^2 \alpha^2)$: $\Delta L = 1$ scattering (2-to-2) and 1-to-3 decays,

As noted above, at $\mathcal{O}(\lambda^4 \alpha^2)$ there are additional uncompensated terms. This is because the scattering processes at that order contain real intermediate states

of $\mathcal{O}(\lambda^2\alpha^2)$, the same order as the $N_1S \underset{2}{\to} LH$ scattering process and the $N_2 \underset{1}{\to} LHS$ three-body final state decay rate. In order to include the scattering properly, it is necessary to use the subtracted rate since the on-shell piece is equivalent to $N_1S \to N_2 \to LH$ which has already been accounted for. We have

$$
\begin{aligned}
n_\gamma^{eq} z_1 H \frac{\partial Y_{L-\overline{L}}}{\partial z_1}\bigg|_{\lambda^2\alpha^2} &= \frac{Y_1}{Y_1^{eq}}\left(\gamma^{eq,sub}_{N_1S\underset{2}{\to}LH} - \gamma^{eq,sub}_{N_1S\underset{2}{\to}\overline{LH}}\right) - \frac{Y_L}{Y_L^{eq}}\gamma^{eq,sub}_{LH\underset{2}{\to}N_1S} + \frac{Y_{\overline{L}}}{Y_L^{eq}}\gamma^{eq,sub}_{\overline{LH}\underset{2}{\to}N_1S} \\
&\quad + \frac{Y_2}{Y_2^{eq}}\left(\gamma^{eq}_{N_2\to LHS} - \gamma^{eq}_{N_2\to\overline{LHS}}\right) - \frac{Y_L}{Y_L^{eq}}\gamma^{eq}_{N_2\to\overline{LHS}} + \frac{Y_{\overline{L}}}{Y_L^{eq}}\gamma^{eq}_{N_2\to LHS} \\
&= \left(\frac{Y_1}{Y_1^{eq}}+1\right)\Delta\gamma^{eq,sub}_{\Delta L=1} - \frac{Y_{L-\overline{L}}}{2Y_L^{eq}}\gamma^{eq,sub}_{\Delta L=1} \\
&\quad + \left(\frac{Y_2}{Y_2^{eq}}+1\right)\epsilon_1\gamma_{N_2\to N_1 S} - \frac{Y_{L-\overline{L}}}{2Y_L^{eq}}\left(\gamma^{eq}_{N_2\to LHS}+\gamma^{eq}_{N_2\to\overline{LHS}}\right),
\end{aligned}
$$
$$(3.57)$$

where

$$
\begin{aligned}
\gamma^{eq,on-shell}_{N_1S\underset{2}{\to}LH} &= \gamma^{eq}_{N_1S\to N_2}\mathrm{Br}(N_2\to LH) = \frac{1+\epsilon_2}{2}\frac{\Gamma_{21}}{\Gamma_{2T}}\gamma^{eq}_{D_2}, \\
\gamma^{eq,sub}_{N_1S\underset{2}{\to}LH} &= \gamma^{eq}_{N_1S\underset{2}{\to}LH} - \frac{1}{2}\frac{\Gamma_{21}}{\Gamma_{2T}}\gamma^{eq}_{D_2} - \frac{\epsilon_2}{2}\frac{\Gamma_{21}}{\Gamma_{2T}}\gamma^{eq}_{D_2}, \\
\gamma^{eq,sub}_{\Delta L=1} &\equiv \gamma^{eq,sub}_{N_1S\underset{2}{\to}LH} + \gamma^{eq,sub}_{N_1S\underset{2}{\to}\overline{LH}} = \gamma^{eq}_{\Delta L=1} - \frac{\Gamma_{21}}{\Gamma_{2T}}\gamma^{eq}_{D_2}, \\
\Delta\gamma^{eq,sub}_{\Delta L=1} &\equiv \gamma^{eq,sub}_{N_1S\underset{2}{\to}LH} - \gamma^{eq,sub}_{N_1S\underset{2}{\to}\overline{LH}} = \Delta\gamma^{eq}_{\Delta L=1} - \epsilon_2\frac{\Gamma_{21}}{\Gamma_{2T}}\gamma^{eq}_{D_2}.
\end{aligned}
$$
$$(3.58)$$

The function $\gamma^{eq}_{\Delta L=1}/2$ determines the CP-conserving part of the scattering rate, and has been plotted in Fig. 3.9c, along with the RIS rate $\gamma^{eq}_{D_2}\Gamma_{21}/(2\Gamma_{2T})$. This shows that $\gamma^{eq,sub}_{\Delta L=1}$ is negligible. The CP-asymmetry in the scattering, $\Delta\gamma^{eq}_{\Delta L=1}$, is largely inherited from the on-shell part in such way that $\Delta\gamma^{eq,sub}_{\Delta L=1}$ is again negligible. We can convince ourselves of this by taking the ratio $\Delta\gamma^{eq,sub}_{\Delta L=1}/\gamma^{eq}_{\Delta L=1} \approx \Delta\gamma^{eq}_{\Delta L=1}/\gamma^{eq}_{\Delta L=1} - \epsilon_2 \approx 0$, as the CP-asymmetry in $\Delta L=1$ scatterings is equal to that of the neutrino leptonic decays. The CP-asymmetry in three-body final state decay rates can only come from the kinematic point where the intermediate line is on-shell, which means

$$
\begin{aligned}
\gamma^{eq,on-shell}_{N_2\to LHS} &= \gamma^{eq}_{N_2\to N_1 S}\frac{1+\epsilon_1}{2}, \\
\Delta\gamma^{eq}_{N_2\to LHS} &= \gamma^{eq,on-shell}_{N_2\to LHS} - \gamma^{eq,on-shell}_{N_2\to\overline{LHS}} = \epsilon_1\gamma_{N_2\to N_1 S}.
\end{aligned}
$$
$$(3.59)$$

Eq. (3.57) displays the same flaw as Eq. (3.51) in failing to follow Sakharov's criteria. Following the same logic as at $\mathcal{O}(\lambda^2)$, it is necessary to include (naively) higher order contributions, namely $\Delta L = 2$ scattering processes that contain RIS at $\mathcal{O}(\lambda^2 \alpha^2)$. Indeed, the second to last line of equation (3.55) fully corrects this problem at the scattering level. The last line of the same equation *partially* corrects the corresponding flaw at the level of three-body final state decays. In order to correct this rate completely, we need to consider yet higher order interactions, $\mathcal{O}(\lambda^4 \alpha^4)$; see below.

- $\mathcal{O}(\lambda^4 \alpha^4)$: $\Delta L = 2$ scattering (3-to-3),

  The 3-to-3 scattering process $LHS \underset{2}{\to} \overline{LH}S$ contains a real intermediate state,

$$
\gamma^{eq,son-shell}_{LHS \underset{2}{\to} \overline{LH}S} \supset \mathrm{Br}(LH \to N_1) \gamma^{eq}_{N_1 S \to N_2} \mathrm{Br}(N_2 \to N_1 S) \mathrm{Br}(N_1 \to \overline{LH}) \supset \frac{\epsilon_1}{2} \frac{\Gamma_{21}}{\Gamma_{2T}} \gamma^{eq}_{N_2 \to N_1 S},
$$
$$(3.60)$$

so that

$$
n^{eq}_\gamma z_1 H \frac{\partial Y_{L-\overline{L}}}{\partial z_1} = -2 \frac{Y_L}{Y^{eq}_L} \gamma^{eq,sub}_{LHS \underset{2}{\to} \overline{LH}S} + 2 \frac{Y_{\overline{L}}}{Y^{eq}_L} \gamma^{eq,sub}_{\overline{LH}S \underset{2}{\to} LHS}
$$
$$
\supset -2\epsilon_1 \frac{\Gamma_{21}}{\Gamma_{2T}} \gamma^{eq}_{N_2 \to N_1 S},
$$
$$(3.61)$$

which combines with the $-2\epsilon_1 \gamma^{eq}_{D_2} \Gamma_{21}/\Gamma_{2T}$ term of equation (3.55), leading to the combination $-2\epsilon_1 \gamma^{eq}_{N_2 \to N_1 S}$ that ultimately corrects the above flaw at the three-body final state decay level.

In conclusion, one obtains the correct Boltzmann equations at order $\mathcal{O}(\lambda^2)$, by combining the equations (3.51), (3.52) and (3.55) at order $\mathcal{O}(\lambda^2)$, $\mathcal{O}(\lambda^4)$, and $\mathcal{O}(\lambda^4 \alpha^2)$ respectively. If one wishes to include the $\Delta L = 1$ scattering and decays at order $\mathcal{O}(\lambda^2 \alpha^2)$, it is necessary to combine the contributions of $\mathcal{O}(\lambda^2 \alpha^2)$, $\mathcal{O}(\lambda^4 \alpha^2)$ and $\mathcal{O}(\lambda^4 \alpha^4)$ in equations (3.57), (3.55) and (3.61).

The need to include all these varied contributions to obtain the correct Boltzmann equations should not come as a surprise. Since there are two N_2 decay channels, whenever the decay $N_2 \to LH$ is part of a scattering process, we can write down an additional scattering diagram which has the $N_2 \to N_1 S \to LH$ decay chain as a sub-diagram. Because both $N_2 \to LH$ and $N_2 \to N_1 S \to LH$ can happen on-shell, they both contribute at the same order and therefore combine to provide a complete set of scattering contributions; complete in the sense that $\mathrm{Br}(N_2 \to LH) + \mathrm{Br}(N_2 \to$

$N_1 S) = 1$. This explains the necessity to include all terms of both $\mathcal{O}(\lambda^4)$ and $\mathcal{O}(\lambda^4 \alpha^2)$ to obtain the correct Boltzmann equations at $\mathcal{O}(\lambda^2)$.

We can also understand this conclusion at the level of unitarity and CPT invariance, which requires that $\sum_j |\mathcal{M}(i \to j)|^2 = \sum_j |\mathcal{M}(j \to i)|^2 = \sum_j |\mathcal{M}(\bar{i} \to \bar{j})|^2$. At $\mathcal{O}(\lambda_1^4)$ one has,

$$
\begin{aligned}
|\mathcal{M}(HL \underset{1}{\to} X)|^2\Big|_{\mathcal{O}(\lambda_1^4)} =& |\mathcal{M}(HL \to N_1)|^2 + |\mathcal{M}(HL \underset{1}{\to} LH)^{sub}|^2 + |\mathcal{M}(HL \underset{1}{\to} \overline{HL})^{sub}|^2 \\
=& |\mathcal{M}(HL \to N_1)|^2 + |\mathcal{M}(HL \underset{1}{\to} LH)|^2 + |\mathcal{M}(HL \underset{1}{\to} \overline{HL})|^2 \\
& - |\mathcal{M}(HL \to N_1)|^2 \mathrm{Br}(N_1 \to LH) - |\mathcal{M}(HL \to N_1)|^2 \mathrm{Br}(N_1 \to \overline{LH}) \\
=& |\mathcal{M}(HL \underset{1}{\to} LH)|^2 + |\mathcal{M}(HL \underset{1}{\to} \overline{HL})|^2 .
\end{aligned}
\tag{3.62}
$$

At this order both $|\mathcal{M}(HL \underset{1}{\to} LH)|^2$ and $|\mathcal{M}(HL \underset{1}{\to} \overline{HL})|^2$ are CP-symmetric in which case unitarity and CPT invariance are straightforwardly satisfied. Now, at $\mathcal{O}(\lambda_2^4 \alpha_{21}^2)$, it is necessary to include higher order scattering processes in order to obtain the same conclusion,

$$
\begin{aligned}
|\mathcal{M}(HL \underset{2}{\to} X)|^2\Big|_{\mathcal{O}(\lambda_2^4 \alpha_{21}^2)} =& |\mathcal{M}(HL \to N_2)|^2 + |\mathcal{M}(HL \underset{2}{\to} N_1 S)^{sub}|^2 \\
& + |\mathcal{M}(HL \underset{2}{\to} LH)^{sub}|^2 + |\mathcal{M}(HL \underset{2}{\to} \overline{HL})^{sub}|^2 \\
& + |\mathcal{M}(HL \underset{2}{\to} LHS)^{sub}|^2 + |\mathcal{M}(HL \underset{2}{\to} \overline{HL}S)^{sub}|^2 \\
=& |\mathcal{M}(HL \to N_2)|^2 + |\mathcal{M}(HL \underset{2}{\to} N_1 S)^{sub}|^2 + |\mathcal{M}(HL \underset{2}{\to} LH)|^2 \\
& + |\mathcal{M}(HL \underset{2}{\to} \overline{HL})|^2 + |\mathcal{M}(HL \underset{2}{\to} LHS)|^2 + |\mathcal{M}(HL \underset{2}{\to} \overline{HL}S)|^2 \\
& - |\mathcal{M}(HL \to N_2)|^2 \big(\mathrm{Br}(N_2 \to LH) + \mathrm{Br}(N_2 \to \overline{LH}) \big) \\
& - \big(|\mathcal{M}(HL \underset{2}{\to} N_1 S)^{sub}|^2 + |\mathcal{M}(HL \to N_2)|^2 \mathrm{Br}(N_2 \to N_1 S) \big) \\
=& |\mathcal{M}(HL \underset{2}{\to} LH)|^2 + |\mathcal{M}(HL \underset{2}{\to} \overline{HL})|^2 + |\mathcal{M}(HL \underset{2}{\to} LHS)|^2 \\
& + |\mathcal{M}(HL \underset{2}{\to} \overline{HL}S)|^2 ,
\end{aligned}
\tag{3.63}
$$

where we have used the relation

$$
|\mathcal{M}(HL \underset{2}{\to} LHS)^{sub}|^2 = |\mathcal{M}(HL \underset{2}{\to} N_1 S)|^2 \mathrm{Br}(N_1 \to LH),
\tag{3.64}
$$

and further split the rate $|\mathcal{M}(HL \rightarrow N_1 S)|^2$ into the subtracted and RIS parts. Recall that $\mathrm{Br}(N_1 \rightarrow LH) + \mathrm{Br}(N_1 \rightarrow \overline{LH}) = 1$. Thus the unitarity$+CPT$ constraint is again consistently satisfied at this order.

We are now in position to summarize the final Boltzmann equations. In practice, we can ignore the 1-to-3 decay rates, which are numerically subdominant compared to the 1-to-2 decays, and similarly we can ignore the 2-to-3 scatterings, which are subdominant compared to the 2-to-2 rates. The subtracted rates $\gamma^{eq,sub}_{N_1 S \rightarrow LH}$ and $\gamma^{eq,sub}_{\overline{LH}_i \rightarrow LH}$ can also be ignored as suggested by the plots in Fig. 3.9.

To simplify the above discussion, we have considered the subset of interactions that contain the α and λ coupling constants. In this chapter, we also consider the set of interactions involving the coupling β. However, among the set of scatterings one considers, there is no additional real intermediate state from this source, and we can directly re-write the Boltzmann equation for the final lepton asymmetry as,

$$
\begin{aligned}
z_1 \frac{\partial Y_{L-\bar{L}}}{\partial z_1} =& \epsilon_1 D_1 \left(\frac{Y_1}{Y_1^{eq}} - 1 \right) + \epsilon_2 D_2 \left(\frac{Y_2}{Y_2^{eq}} - 1 \right) \\
& - Y_{L-\bar{L}} \left(W_{ID_1} + W_{S_1} + W_{ID_2} + W_{S_2} \right),
\end{aligned}
\tag{3.65}
$$

where we have used the notation of the decay, scattering and washout functions D, W and S,

$$
D_i = \frac{\gamma^{eq}_{D_i}}{n^{eq}_\gamma H} = K_i z_i^2 Y_i^{eq} \frac{K_1(z_i)}{K_2(z_i)}, \qquad W_{ID_i} = \frac{1}{2 Y_L^{eq}} D_i, \qquad Y_i^{eq} = \frac{3}{8} z_i^2 K_2(z_i). \tag{3.66}
$$

The equilibrium parameter for leptonic decays K_i is defined as,

$$
K_i = \frac{\Gamma_i}{H(T = M_i)} = \frac{\tilde{m}_i}{m_*}, \tag{3.67}
$$

where the effective light neutrino mass scales $\tilde{m}_i$ and m_* are

$$
\tilde{m}_i = \frac{(\lambda^\dagger \lambda)_{ii} v^2}{M_i}, \qquad m_* = 8\pi v^2 \sqrt{\frac{8\pi^3 g_*}{90 M_p^2}} \sim 1.05 \cdot 10^{-3} \mathrm{eV}, \tag{3.68}
$$

emerging from the see-saw mechanism, with $g_* \sim 100$ the total number of degrees of freedom. We assume here the normal hierarchy among light neutrino masses. The washout functions are written in terms of the scattering function, $S_{ia \rightarrow mn} =$

$$\gamma^{eq}_{ia\to mn}/(n^{eq}_\gamma H),$$

$$W_{S_1} = \frac{1}{Y^{eq}_L}\left(2S_{N_1 t\to LQ} + S_{N_1 H\to LS} + S_{N_1 S\underset{1}{\to}LH}\right) + \frac{Y_1}{Y^{eq}_L Y^{eq}_1}\left(S_{N_1 L\to Qt} + S_{N_1 L\to HS}\right),$$

$$W_{S_2} = \frac{1}{Y^{eq}_L}\left(2S_{N_2 t\to LQ} + S_{N_2 H\to LS} + S_{N_2 S\underset{1}{\to}LH} + S_{N_2 S\underset{2}{\to}LH}\right) + \frac{Y_2}{Y^{eq}_L Y^{eq}_2}\left(S_{N_2 L\to Qt} + S_{N_2 L\to HS}\right).$$

$$(3.69)$$

Neutrino abundance

The Boltzmann equations for the RHN abundances can be determined in a similar manner to the lepton asymmetry discussed above,

$$
\begin{aligned}
z_1\frac{\partial Y_1}{\partial z_1} &= -\left(\frac{Y_1}{Y^{eq}_1} - 1\right)(D_1 + D_{21} + S_1) + \left(\frac{Y_2}{Y^{eq}_2} - 1\right)D_{21} \\
&\quad - \left(\frac{Y_1 Y_2}{Y^{eq}_1 Y^{eq}_2} - 1\right)S_{N_1 N_2\to HH} - \left(\frac{Y^2_1}{Y^{eq2}_1} - 1\right)S_{N_1 N_1\to HH}, \\
z_1\frac{\partial Y_2}{\partial z_1} &= -\left(\frac{Y_2}{Y^{eq}_2} - 1\right)(D_2 + D_{21} + S_2) + \left(\frac{Y_1}{Y^{eq}_1} - 1\right)D_{21} \\
&\quad - \left(\frac{Y_1 Y_2}{Y^{eq}_1 Y^{eq}_2} - 1\right)S_{N_1 N_2\to HH} - \left(\frac{Y^2_2}{Y^{eq2}_2} - 1\right)S_{N_2 N_2\to HH},
\end{aligned}
$$

$$(3.70)$$

with

$$S_1 = 2S_{N_1 L\to Qt} + 4S_{N_1 Q\to Lt} + 2S_{N_1 L\to HS} + 4S_{N_1 H\to LS} + 2S_{N_1 S\underset{1}{\to}LH},$$

$$S_2 = 2S_{N_2 L\to Qt} + 4S_{N_2 Q\to Lt} + 2S_{N_2 L\to HS} + 4S_{N_2 H\to LS} + 2S_{N_2 S\underset{1}{\to}LH} + 2S_{N_2 S\underset{2}{\to}LH}.$$

$$(3.71)$$

The subtracted rate for $N_1 S \to LH$ is very small, and has been ignored. The decay function for $N_2 \to N_1 S$ is defined as

$$D_{21} = K_{21}z^2_2\frac{K_1(z_2)}{K_2(z_2)}Y^{eq}_2, \qquad z_2 = \frac{M_2}{T} = \frac{M_2}{M_1}z_1, \qquad (3.72)$$

with K_{21} defined by analogy to K_1,

$$K_{21} = \frac{\Gamma_{21}}{H(T = M_2)} = |\alpha_{21}|^2\frac{v^2}{2m_* M_2} \sim |\alpha_{21}|^2\left(1.44\cdot\frac{10^{16}\mathrm{GeV}}{M_2}\right). \qquad (3.73)$$
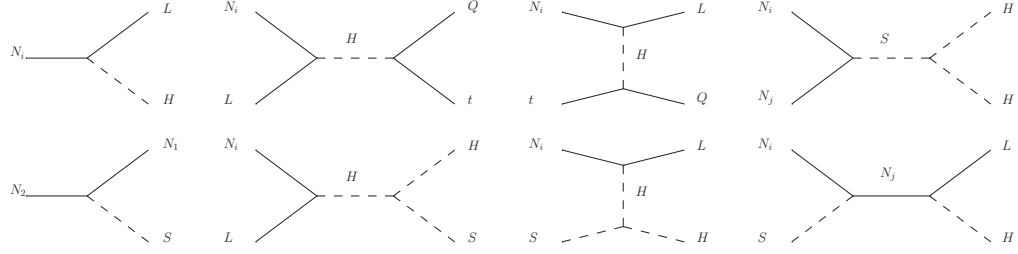
Figure 3.10: A list of the decay and scattering processes included in our Boltzmann equations. This list is not exhaustive, though it includes the dominant contributions. In the limit where the quarks, Higgs and singlet S are massless, the t-channel diagrams are counted twice since it is possible to swap $Q - t$ and $H - S$.

We have implicitly assumed the hierarchy $\{M_1, m_S\} \ll M_2$ in writing down K_{21} above; the exact decay rate is calculated in Appendix 3.2.1. Once again, the thermal equilibrium parameter for this process is $\mathcal{K}_{N_2 \to N_1 S} = D_{21}/Y_2^{eq}$, while for inverse decays $N_1 S \to N_2$ one has $\mathcal{K}_{N_1 S \to N_2} = D_{21}/Y_1^{eq}$.

As a summary, Fig. 3.10 lists the scattering processes that are relevant for the equations.

Physical Regimes

The underlying dynamics of this system is in the end quite similar to the simpler system which only accounts for decays and inverse decays (plus RIS contributions), which will be discussed in Section 3.2.3. At first sight it is surprising that the 2-to-2 scattering processes involving N_1, which can remain in equilibrium after N_2 decays, do not have a more significant role in washing out the asymmetry. Indeed, this intuition is realized if the couplings are sufficiently large as will be seen in the next section. However, there are natural parameter regimes in which the rates involving N_1 which change lepton number can be out of equilibrium while the rates that change the number density remain active. This feature is crucial for realizing viable HPL and will be discussed in more detail subsequently. For now, we briefly summarize the generation of a lepton asymmetry by breaking the evolution into three distinct phases:

1. **The N_2 phase**:

   This phase takes place at temperatures $T \sim M_2$, and is marked by N_2 interactions going out of equilibrium, efficiently generating a primary lepton asymmetry. If there is a large mass hierarchy between N_1 and N_2, the rates involving

N_1 may be sufficiently small (e.g. the decays which are proportional to the mass) that they are out of equilibrium, i.e. $D_1 \ll D_2, D_{21}$. In this case, the physics of this phase is almost that of a one-flavor system: the lepton asymmetry is generated through N_2 decays to leptons until the N_2 abundance becomes negligible. A second subdominant process can still be important, namely the mixing $N_2 - N_1$ that allows decays and inverse decays $N_2 \leftrightarrow N_1 S$ if α_{12} is sufficiently large. Because of this channel, the branching ratio of N_2 into leptons is reduced as compared to the one-flavor system, making the production of the lepton asymmetry less efficient. At the same time, this very channel populates N_1, which is then kicked out-of-equilibrium momentarily. Its ability to return to equilibrium depends on the rate of the inverse decay $N_1 S \to N_2$, as the decays $N_1 \to LH$ are generally out-of-equilibrium in this phase. The overpopulation of N_1 is not very important during this phase, but will have an effect on the lepton asymmetry at the later stage when N_1 decays come into equilibrium. The resulting primary lepton asymmetry can be parametrized by an efficiency factor κ_2,

$$Y_{L-\overline{L}}^{(2)} = \epsilon_2 \kappa_2 Y_2^{eq}(0). \tag{3.74}$$

This phase typically ends when $T \sim M_2/10$, i.e. $z_1 \sim 10 M_1/M_2$.

2. **The intermediate phase**:

Given a sizeable mass hierarchy between N_1 and N_2, the second phase is marked by a large temperature gap once N_2 has effectively disappeared, and before N_1 interactions come into equilibrium. Neither N_2- nor N_1-interactions are able to affect the lepton asymmetry, or the N_1 abundance, and the system effectively free streams leading to a plateau in $Y_{L-\overline{L}}$. This phase lasts for as long as the N_1 interactions remain out-of-equilibrium, and characteristically for a temperature range similar to the mass ratio. For example, if the decays and inverse decays dominate, the approximations discussed in Appendix 2.2 indicate that the phase ends when $z_1 \sim \sqrt{2/K_1}$. If scattering effects are also significant, then the transition to the N_1 phase can occur somewhat earlier.

3. **The N_1 phase**:

This phase is marked by N_1 interactions being in-equilibrium which efficiently deplete the neutrino abundance and lepton asymmetry. Assuming again a sizeable mass hierarchy, since the N_2 abundance is negligible and N_2 interactions

are effectively turned off, $D_2, D_{21} \ll D_1$, the dynamics again approximates a purely one-flavor system. The distinction is that the initial lepton asymmetry is not zero, having been generated in the N_2 phase, and there is a possible N_1 overabundance $Y_1 > Y_1^{eq}$ due to $N_2 \to N_1 S$ decays during the first phase. The final lepton asymmetry results from the competition between N_1 mediated processes that wash out the pre-existing lepton asymmetry from the N_2 phase, and those at the end of the N_1 phase that contribute to the asymmetry. The result can again be parametrized via an efficiency factor κ_1,

$$Y_{L-\bar{L}} = Y_{L-\bar{L}}^{(2)} e^{-\int_{\mathcal{Z}}^{\infty} dz'(W_1/z')} + \epsilon_1 \kappa_1 Y_1^{eq}(0). \tag{3.75}$$

where the washout function $W_1 = W_{ID_1} + W_{S_1}$ is discussed above. The variable $\mathcal{Z}$ marks the transition point after the N_2 phase, once the washout processes become active.

Summarizing the full 2-level process, the final asymmetry resulting from the three phases can be parametrized by the two efficiency factors κ_1 and κ_2,

$$Y_{L-\bar{L}}^f = \epsilon_2 \left(\kappa_2 e^{-\int_{\mathcal{Z}}^{\infty} dz'(W_1/z')} + \frac{\epsilon_1}{\epsilon_2} \kappa_1 \right) Y_2^{eq}(0). \tag{3.76}$$

We proceed in the next section to consider explicit examples which exhibit these features in detail. However, before considering the general case, we will first study a simplified toy model that allows some analytic understanding of the physics.

3.2.3 Toy model of the 2-stage evolution

In this subsection, in order to isolate some of the dominant physical effects, we study a toy model of the 2-level Boltzmann equations, accounting only for decays and inverse decays and ignoring the impact of 2-to-2 scattering. For simplicity, we also take the CP-asymmetry to be constant, using $\epsilon_1 = \epsilon_2 = 10^{-8}$, although this constraint will be relaxed towards the end of the section. The Boltzmann equations are as written in
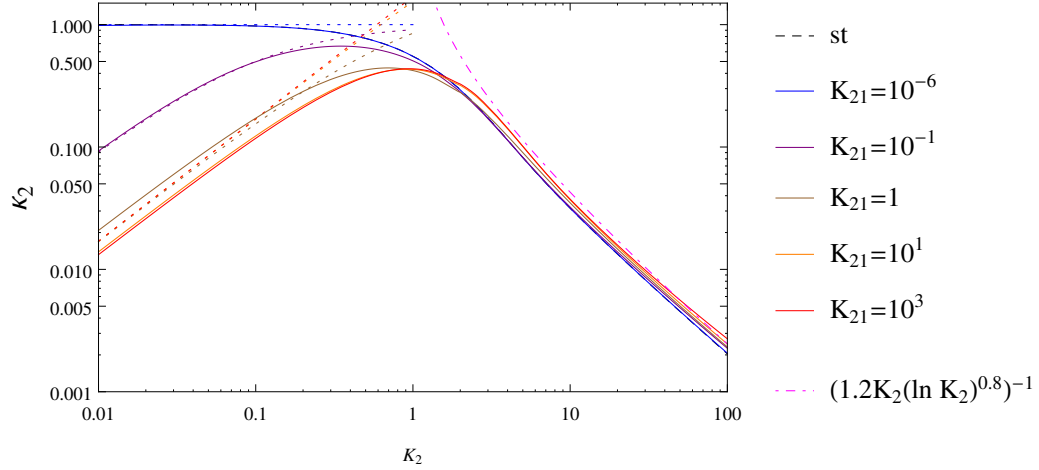
Figure 3.11: Plots of the efficiency factor κ_2, as a function of K_2, for various values of K_{21}. In the limit $K_{21} \ll K_2$, the efficiency factor approaches its value in one-flavor standard leptogenesis (shown here in black, dashed, buried under the blue line). Increasing K_{21} has a significant effect on the efficiency factor at low K_2. The asymptotic behavior is also shown (dotted lines) for low K_2, from (3.81) and (3.83).

Eq. (3.65) and (3.70), of section 3.2.2, but without scattering,

$$
\begin{aligned}
z_1 \frac{\partial Y_1}{\partial z_1} &= -\left(\frac{Y_1}{Y_1^{eq}} - 1\right)(D_1 + D_{21}) + \left(\frac{Y_2}{Y_2^{eq}} - 1\right)D_{21}, \\
z_1 \frac{\partial Y_2}{\partial z_1} &= -\left(\frac{Y_2}{Y_2^{eq}} - 1\right)(D_2 + D_{21}) + \left(\frac{Y_1}{Y_1^{eq}} - 1\right)D_{21}, \\
z_1 \frac{\partial Y_{L-\overline{L}}}{\partial z_1} &= \epsilon_1 D_1 \left(\frac{Y_1}{Y_1^{eq}} - 1\right) + \epsilon_2 D_2 \left(\frac{Y_2}{Y_2^{eq}} - 1\right) - Y_{L-\overline{L}} \frac{D_1 + D_2}{2 Y_L^{eq}}.
\end{aligned}
\tag{3.77}
$$

The decay functions are as defined above, and we take the initial conditions as a vanishing lepton asymmetry $Y_{L-\overline{L}} = 0$, and equilibrium initial abundances $Y_{1,2} = Y_{1,2}^{eq}$. The N_2-phase ends at around $\mathcal{Z} \sim 10 M_1/M_2 < 1$, and we can numerically integrate $\int_{\mathcal{Z}}^\infty dz' W_{ID_1}/z' \sim 1.2 K_1$. Applying the general result of (3.76) leads to an approximate final asymmetry,

$$
Y_{L-\overline{L}}^f \simeq \frac{3}{4}\left(\epsilon_2 \kappa_2 e^{-1.2 K_1} + \epsilon_1 \kappa_1\right).
\tag{3.78}
$$

N_2 efficiency factor: κ_2

In the N_2 phase, the scenario of interest here is characterized by having N_1 out-of-equilibrium with $D_1 \ll D_2, D_{21}$. Integrating the $Y_{L-\overline{L}}$ equation in (3.77) then leads

to the efficiency factor κ_2,

$$
\begin{aligned}
\kappa_2 Y_2^{eq}(0) &= \int_0^{\mathcal{Z}} dz' \frac{D_2}{z'} \left(\frac{Y_2}{Y_2^{eq}} - 1 \right) e^{-\int_{z'}^{\mathcal{Z}} dz''(W_{ID_2}/z'')}, \\
&= -\frac{K_2}{K_2 + K_{21}} \int_0^{\mathcal{Z}} dz' \left(\frac{\partial Y_2}{\partial z'} - \frac{D_{21}}{z'} \left(\frac{Y_1}{Y_1^{eq}} - 1 \right) \right) e^{-\int_{z'}^{\mathcal{Z}} dz''(W_{ID_2}/z'')}.
\end{aligned}
\tag{3.79}
$$

For concision, we have used the variable z, although strictly this is z_1. Evaluating κ_2 numerically, we obtain the contours shown in Fig. 3.11, as a function of K_2 for various values of K_{21}. To obtain an analytic approximation we focus on the regime $K_2 \ll 1$, where K_{21} has the largest effect. In this limit, the washout from inverse decays is quite limited, $\exp(-\int_{z'}^z dz'' W_{ID_2}/z'') \sim 1$, so that the first part of the efficiency factor is trivial to integrate $\int_0^z dz' \partial Y_2/\partial z' = Y_2(z) - Y_2(0) \to -Y_2(0)$, since by definition we integrate to the point where the N_2 abundance drops to zero. Thus

$$
\kappa_2 Y_2^{eq}(0) \simeq \frac{K_2}{K_2 + K_{21}} Y_2^{eq}(0) + \frac{K_2}{K_2 + K_{21}} \int_0^{\mathcal{Z}} dz' \frac{D_{21}}{z'} \left(\frac{Y_1}{Y_1^{eq}} - 1 \right),
\tag{3.80}
$$

owing to the initial condition $Y_2(0) = Y^{eq}(0)$. Taking the limit $K_{21} \ll K_2$, the equations decouple in such a way that $Y_1 \sim Y_1^{eq}$, and the second term above is subdominant leading to the efficiency factor,

$$
\kappa_2 \sim \frac{K_2}{K_2 + K_{21}} \quad \text{when} \quad K_{21} \ll K_2 \ll 1.
\tag{3.81}
$$

In the decoupled limit, the efficiency factor logically tends to the one-flavor value. If instead we take the limit $K_{21} \gg K_2$, the second term becomes significant, if not dominant, and we have to integrate the equations explicitly. In this limit, the branching ratio of N_2 into leptons is small, so that $D_{21} \gg D_2$. At the same time, $D_{21} \gg D_1$ in the N_2 phase. As a result, the $Y_{1,2}$ equations simplify to $\partial Y_2/\partial z_1 = -\partial Y_1/\partial z_1$, so that the total number density $Y_1 + Y_2$ is constant. This makes sense, since N_2's decay dominantly into N_1's. We thus find,

$$
Y_2(\mathcal{Z}) + Y_1(\mathcal{Z}) = Y_2(0) + Y_1(0) = 2Y_1^{eq}(0).
\tag{3.82}
$$

The first phase ends when $Y_2(\mathcal{Z}) = 0$, so that $Y_1(\mathcal{Z}) = 2Y_1^{eq}(0)$, and the term $Y_1(\mathcal{Z})/Y_1^{eq}(\mathcal{Z}) - 1 \sim 1$. The calculation of $\int_0^z dz' D_{21}/z'$ is most easily performed numerically, and for $z \geq 10$ the integral converges to 1.7. We conservatively take this
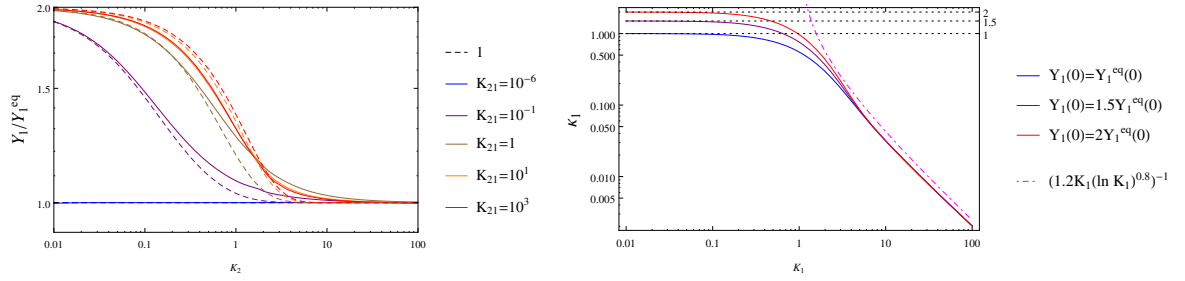
(a) Neutrino overabundance at the end of the N_2 phase

(b) Efficiency factor during the N_1 phase

Figure 3.12: The plot on the left (a) shows the N_1 abundance $Y_1(\mathcal{Z})$ offset compared to equilibrium at the end of the first phase due to the $N_2 \to N_1 S$ decay, referring to equation (3.87) along with the approximations (3.88). These values are also the initial conditions for the abundance at the start of the very last phase. The plot on the right (b) represents the efficiency factor κ_1 for various initial values of $Y_1(\mathcal{Z})$ at the start of the N_1 phase, as given in the left plot.

result to obtain

$$\kappa_2 \sim 1.7 \frac{K_2 K_{21}}{K_2 + K_{21}} \quad \text{when} \quad K_{21} \gg K_2 \ll 1. \tag{3.83}$$

Fig. 3.11 exhibits both the numerical results for κ_2 along with the approximations (3.81) and (3.83); the agreement is good in the region $K_2 \geq K_{21}$, but less so for $K_{21} \geq K_2$. The $K_2 \gg 1$ regime is similar to a one-flavor case, and the coupling $N_2 - N_1$ does not have a large effect. Thus we can refer to the established literature [66] for an approximate expression for κ_2 in this region,

$$\kappa_2 \simeq \frac{1}{1.2 K_2 (\log K_2)^{0.8}} \quad \text{when} \quad K_2 \gg 1. \tag{3.84}$$

N_1 efficiency factor: κ_1

The N_1 phase is characterized by negligible N_2 abundance, and with N_2 interactions being out-of-equilibrium $D_2, D_{21} \ll D_1$. Thus the physics is once again equivalent to the one-flavor case. The efficiency factor κ_1 is obtained by integrating the Boltzmann equation for the lepton asymmetry,

$$\begin{aligned}
\kappa_1 Y_1^{eq}(0) &= \int_{\mathcal{Z}}^{\infty} dz' \frac{D_1}{z'} \left(\frac{Y_1}{Y_1^{eq}} - 1 \right) e^{- \int_{z'}^{\infty} dz'' (W_{ID_1}/z'')}, \\
&= - \int_{\mathcal{Z}}^{\infty} dz' \frac{\partial Y_1}{\partial z'} e^{- \int_{z'}^{\infty} dz'' (W_{ID_1}/z'')}.
\end{aligned} \tag{3.85}$$
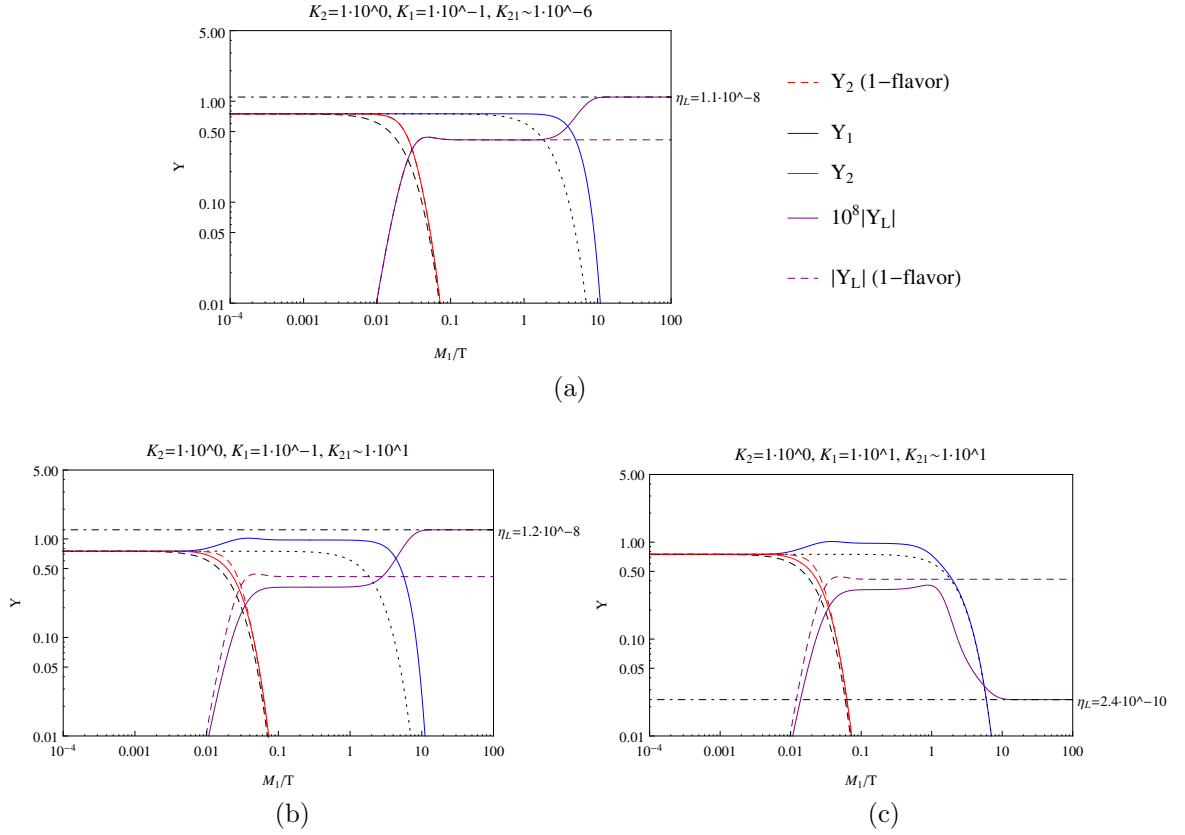
Figure 3.13: Plot (a) shows the N_2 and N_1 abundances (red and blue)) and $Y_{L-\bar{L}}$ (purple) in the toy 2-flavor model, compared to the N_2 abundance (in dashed red) and the lepton asymmetry (in dashed purple) in the one-flavor case. Plots (b,c) show further examples of the 2-level toy model. The coupling $N_2 \to N_1 S$ allows N_2 to cope better with expansion, which causes a reduction of the generated lepton asymmetry. In turn, this results in the N_1 abundandance being further out-of-equilibrium. The color coding is the same in all these and subsequent plots.

In the limit $K_1 \ll 1$, the washout is minimal, leaving

$$\kappa_1 Y_1^{eq}(0) = Y_1(\mathcal{Z}). \tag{3.86}$$

The efficiency factor depends on the value of the abundance once the third phase starts. Since Y_1 is constant in the intermediate phase, this is the same as the final abundance at the end of the first phase. In Fig. 3.12a, we show numerical results for $Y_1(\mathcal{Z})$ as a function of K_2 for various values of K_{21}. In calculating κ_2, we estimated that $Y_1(\mathcal{Z}) = 2$ at the end of the first phase, which is true in the limit $K_2 \sim 0$, and $\partial(Y_1 + Y_2)/\partial z_1 = 0$. When $K_2 \ll 1$ but not zero, $Y_1 + Y_2$ is no longer constant, and

instead we have

$$Y_1(\mathcal{Z}) = 2Y_1^{eq}(0) - \int_0^{\mathcal{Z}} dz' \frac{D_2}{z'} \left(\frac{Y_2}{Y_2^{eq}} - 1 \right).$$ (3.87)

This function is plotted in Fig. 3.12a, along with the analytical approximations. Thus, to a good approximation, we have

$$\kappa_1 = \frac{Y_1(\mathcal{Z})}{Y_1^{eq}(0)} = 1 + \frac{K_{21}}{K_2 + K_{21}} e^{-K_2} \quad \text{when} \quad K_1 \ll 1.$$ (3.88)

For large $K_2 \gg 1$, the behavior approaches the decoupled limit. Numerical results for the efficiency factor κ_1 are displayed in Fig. 3.12b as a function of K_1 for varying initial conditions. At the other end of the spectrum, as in standard leptogenesis, the efficiency factor is [66],

$$\kappa_1 \sim \frac{1}{1.2K_1(\ln K_1)^{0.8}} \quad \text{when} \quad K_1 \gg 1.$$ (3.89)

Final lepton asymmetry in the toy model

In Fig. 3.13a, we show an example of a decoupled system, with the parameters $\{K_2, K_1, K_{21}\} = \{1, 0.1, 10^{-6}\}$. From Fig. 3.11, we find the efficiency factor $\kappa_2 \sim 0.5$, while Fig. 3.12a tells us that the over-abundance at the exit of the first phase will be zero (decoupling limit), and Fig. 3.12b then implies that $\kappa_1 \sim 1$. Inserting these values into Eq. (3.78) leads to $Y_{L-\overline{L}}^f \sim 1.1 \cdot 10^{-8}$, which is in excellent agreement with the numerically determined result. Two examples of coupled system are shown in Fig. 3.13b and 3.13c with the parameters $\{K_2, K_1, K_{21}\} = \{1, 0.1, 10\}$ and $\{K_2, K_1, K_{21}\} = \{1, 10, 10\}$ respectively. Using Figs. 3.11, and 3.12, we find the efficiency factors $\{\kappa_2, \kappa_1\} = \{0.4, 1.3\}$ and $\{\kappa_2, \kappa_1\} = \{0.4, 0.03\}$ and obtain $Y_{L-\overline{L}}^f \sim 1.3 \cdot 10^{-8}$ and $Y_{L-\overline{L}}^f = 2.25 \cdot 10^{-10}$ respectively.

With this understanding of the toy model, we turn in the next section to an analysis of the full system including scattering. It should already be apparent that viable models will be those in which N_1 is sufficiently weakly coupled that the most dangerous effect, rapid washout via N_1-mediated inverse decays and 2-to-2 scattering, is suppressed. With this constraint, the residual effects of scattering are generally quite small.

3.3 Results in the Hierarchical regime

The focus in this section will be on studying the solutions to the Boltzmann equations in the hierarchical regime, $M_2/M_1 \gg 1$. As shown in Fig. 3.5a in Appendix A, the exact and large M_2/M_1 expressions for the CP asymmetry are within a factor of two for $M_2/M_1 > 10$, which will serve as a practical definition of this regime. Qualitatively, the physical behaviour should be similar for all mass ratios outside the resonant regime [106, 107], $M_2 - M_1 \sim \Gamma_{1,2}/2$, which we will not consider here.

The two flavor HPL model is distinct from standard leptogenesis in at least two ways. The first difference concerns the mass dependence of the CP-asymmetry. As discussed in Sec. 3.1, the CP-asymmetry presents distinct high and the low mass regimes. The high mass regime, $M_2 \gtrsim 10^8 \text{GeV}$, is determined by the Standard Yukawa contribution to the CP-asymmetry. The low mass regime is instead determined by the hidden sector contribution to the CP-asymmetry, proportional to the trilinear coupling β/M_i. This liberates the model from the Davidson-Ibarra bound on the CP-asymmetry, and allows for viable low scale scenarios.

The other significant difference with standard leptogenesis concerns the dynamics. In the minimal model, the main contribution to the CP-asymmetry comes from the decays and inverse decays into leptons, and the scattering processes are largely subdominant. This is in part because as the temperature falls below $T \sim M_1$, all the L-violating scattering rates are suppressed due to Boltzmann suppression of the neutrino abundance. For HPL, the situation is different due to the emphasis on the CP-asymmetry generated by N_2 decays, and the importance of the evolution between $T \sim M_2$ and $T \sim M_1$. As a consequence, scattering processes involving N_1 have the potential to affect the lepton asymmetry quite significantly, and need to be considered carefully.

3.3.1 Viable Scenarios

We will impose two requirements on realistic scenarios, namely the ability to reproduce the observed baryon asymmetry, and similarly that they admit a consistent light neutrino mass spectrum. The first requirement translates within leptogenesis to a specific lepton asymmetry at the temperature where $B + L$-violating sphaleron processes fall out of equilibrium. For the Standard Model field content, the equilibrated lepton and baryon asymmetries are related by $\eta_L = -(51/28)\eta_B$ [91]. The additional singlet in the Higgs portal model only affects this by changing the critical

temperature of the electroweak crossover [111]. Since we assume $\langle S \rangle = 0$, then at least for relatively weak $H - S$ mixing the impact should be small [142]. We therefore require $|\eta_L| \simeq 1 \cdot 10^{-9}$, given the Planck result for $\Omega_b h^2$ [121], which translates to the baryon-to-photon ratio $\eta_B \simeq (6.04 \pm 0.09) \cdot 10^{-10}$ [143].

For the second requirement, since the see-saw mechanism is a motivating factor for leptogenesis, we also require consistency with current data on the mass squared differences, e.g. $\Delta m_{21}^2 = m_2^2 - m_1^2 \simeq (7.5 \pm 0.5) \cdot 10^{-5} \mathrm{eV}^2$ [11, 12, 13, 14]. The see-saw mechanism determines an *effective* light neutrino mass $\tilde{m}_i \sim \lambda_i^2 v^2 / M_i$, which we can trade for the thermal equilibrium parameters $K_i = \tilde{m}_i / m_*$ from (3.67), and write down an *effective* mass squared difference, $K_2^2 - K_1^2 \simeq \mathcal{O}(\Delta m_{21}^2 / m_*^2)$. However, this relation relies on the equality $\tilde{m}_i \simeq m_i$ between the effective and the physical light neutrino masses, which only holds when the neutrino flavor structure is nearly diagonal [130]. More generally, the precise relation can be relaxed, so we will consider models to be viable if the interactions are in the range $K_2 \sim \mathcal{O}(1 - 10)$.

In the rest of this subsection, we present example scenarios that satisfy the above constraints on the neutrino masses and the lepton asymmetry. For each case we present three figures: (i) the Boltzmann evolution of the neutrino abundances and the lepton asymmetry, (ii) the relevant thermal rates of decays, inverse decays and scattering, and finally (iii) the CP-asymmetry 'landscape' in which the theory is situated. In the following subsection, we provide further details showing the impact of varying the parameters of the theory, while relaxing the constraints imposed here on viable models. In particular, we show that the dynamics of the high mass regime is most sensitive to $\{K_1, K_2\}$, whereas the low mass dynamics responds to $\{K_2, K_1, \alpha, \beta\}$.

It is useful to distinguish 'high' and 'low' mass regimes, based primarily on the mass dependence of the N_2 CP-asymmetry. We focus below on the relative impact of two-to-two scattering processes, compared to the toy model discussed above.

- **High-scale models**

  An example of a high scale scenario is shown in Fig. 3.14a. The high mass regime is marked by the dominance of the Yukawa sector in contributing to the CP-asymmetry, so that $\epsilon_2 \sim (3/16\pi v^2) \sum_\alpha m_\alpha M_2 \sim \epsilon_1 (M_2/2M_1)$, as displayed in Fig. 3.14c. The general result in Eq. (3.76) reduces to

$$Y_{L-\bar{L}}^f \sim \frac{9 \sum_\alpha m_\alpha}{64\pi v^2} M_2 \left(\kappa_2 e^{-\int_{\bar{z}}^{\infty} dz'(W_1/z')} + 2\frac{M_1}{M_2}\kappa_1 \right). \tag{3.90}$$

(a) $\{M_2, M_1, K_2, K_1, K_{21}, \beta\} = \{10^9 \text{GeV}, 10^5 \text{GeV}, 8, 0.2, 40, 50 \text{GeV}\}$

(b)

(c)
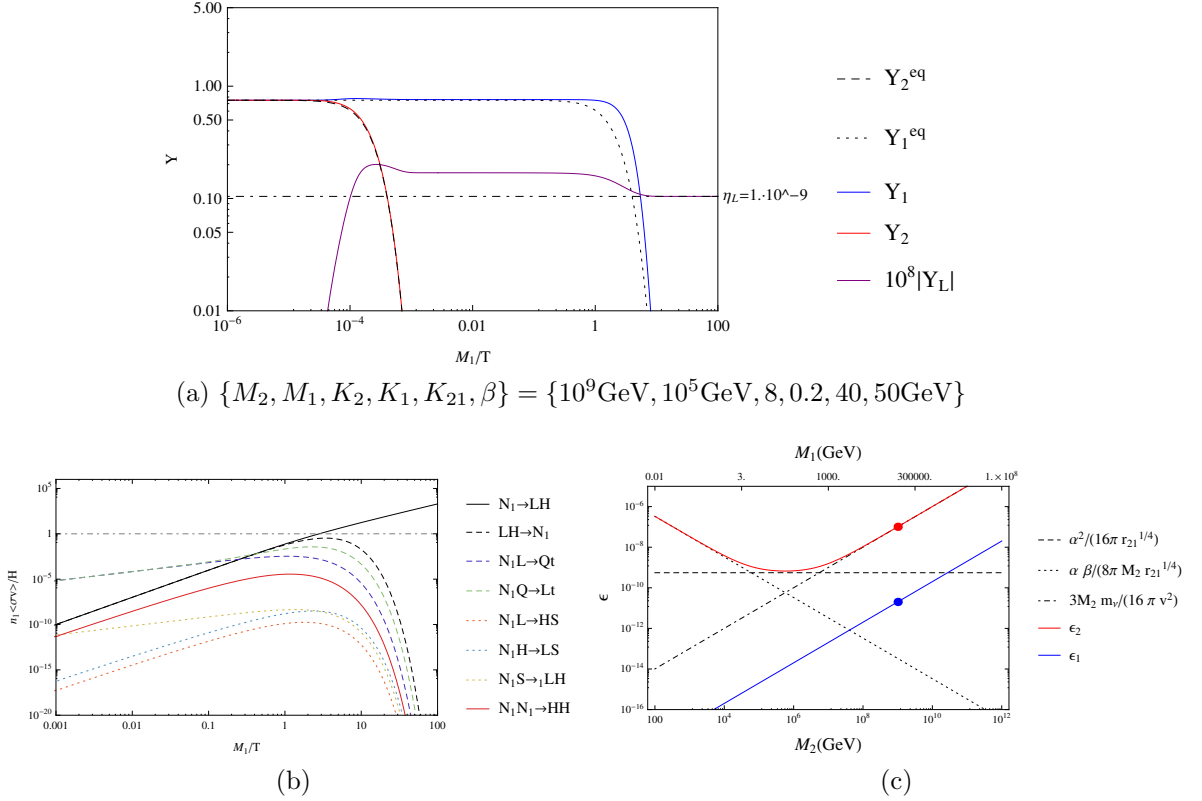
Figure 3.14: These plots show a viable example of the high scale scenario. We show the evolution of the abundances and (rescaled) asymmetry (a), and the relative rates (b) as a function of temperature. In this regime, the CP-asymmetry is dominated by the standard Yukawa contribution, $\epsilon_i \propto m_\nu M_i / v^2$, and the final plot (c) displays the CP-asymmetries $\epsilon_{1,2}$ as functions of M_2, for a constant mass ratio, $M_2/M_1 = 10^4$. With a large mass hierarchy, there would be plenty of time for N_1-mediated processes to wash out all of the lepton asymmetry unless the N_1 interactions are sufficiently suppressed, hence the very small Yukawa λ_1.

The lepton-number changing processes mediated by the hidden sector scale as $\sim |\lambda|^2 \beta^2 / M^2$, and are suppressed compared to Yukawa-mediated scattering which scales as $\sim |\lambda|^2 m_t^2 / v^2$. This is shown in Fig. 3.14b. Additional scattering processes such as $N_i S \underset{j}{\rightarrow} LH$ scale as $|\alpha|^2 |\lambda|^2$ and are therefore suppressed if $|\alpha|^2 \ll 1$, which holds for all the viable scenarios we consider here. The lepton-number conserving scattering process $N_i N_i \rightarrow HH$, mediated by S in the s-channel, scales as $|\alpha|^2 \beta^2 / M^2$ and is again suppressed. Finally, the lepton-mediated t-channel $N_i N_i \rightarrow HH$ scattering is suppressed by a factor $|\lambda|^2 \ll 1$, and has no visible effect on the neutrino abundance.

It follows that the efficiency factors $\kappa_{1,2}$ determined above can be used as a reasonably good approximation here, as the scattering corrections are small.

(a) $\{M_2, M_1, K_2, K_1, K_{21}, \beta\} = \{20\text{TeV}, 2\text{TeV}, 7, 0.001, 3 \cdot 10^5, 50\text{GeV}\}$

(b)

(c)
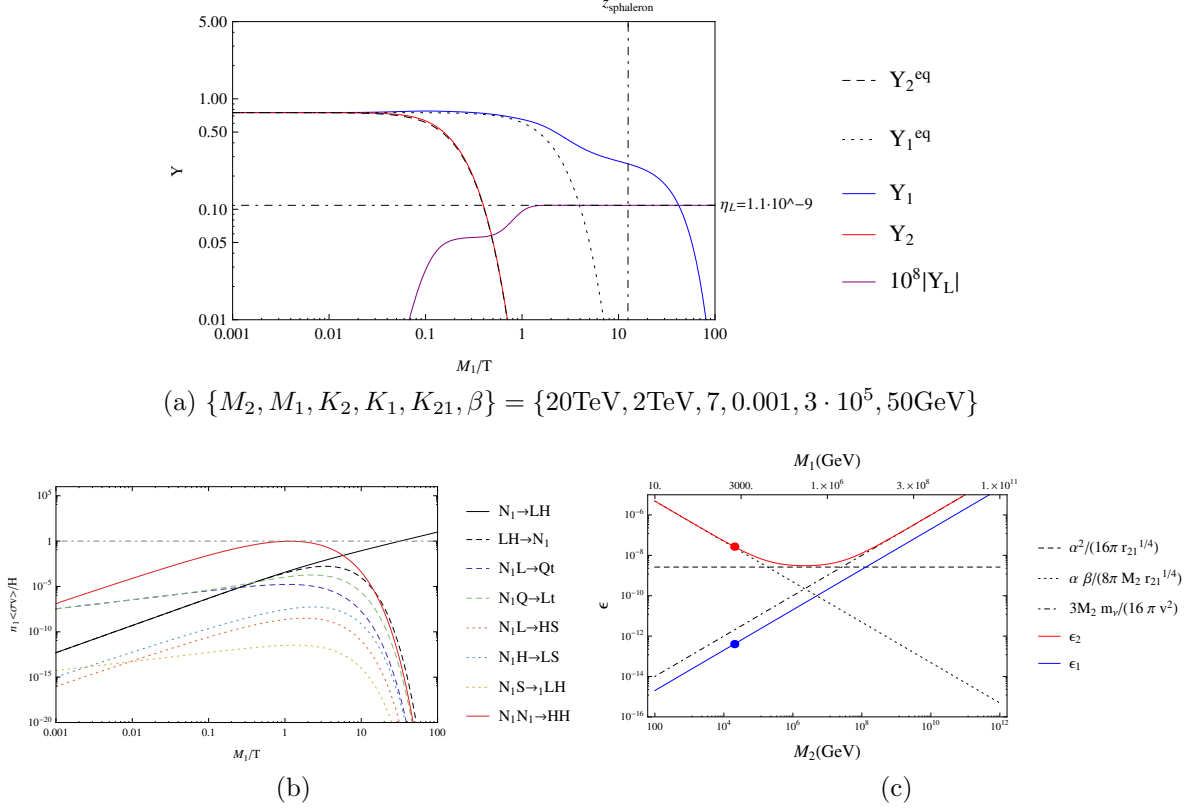
Figure 3.15: These plots, in the same format as Fig. 3.14, show a viable example in the low mass regime. The hidden sector-sourced CP-asymmetry from N_2 decays is the dominant contribution. The dominant scattering processes are also mediated by the hidden sector. This is also an explicit example of a scenario leading to a lepton asymmetry enhancement, thanks to the evolution traversing the sphaleron freezeout temperature.

Indeed, the dominant N_i scattering processes are controlled by the same equilibrium parameter K_i, and the Boltzmann-suppressed number density for $T < M_i$ and the fast expansion rate at $T > M_i$ limits their range of activity.

The possibility of having $\Delta L = 1, 2$ scattering processes mediated by N_1 that remain in equilibrium long after the lepton asymmetry $Y_{L-\bar{L}}^{(2)}$ has been generated, is an important feature of HPL. In practice, these processes need to be suppressed, and remain out of equilibrium in viable models to avoid too much washout. For masses chosen so that $\beta/M_1 \ll m_t/v$, the washout function is dominated by the Yukawa processes $\int_{\mathcal{Z}}^{\infty} dz'(W_1/z') \simeq cK_1$, where $c \sim 1.2 + 1.4(m_t/v)^2 \sim 2.5$. With $K_2 \sim 1 - 10$, satisfying the neutrino mass constraint, one has $\kappa_2 \sim 1/(cK_2)$, and taking a mass ratio large enough that the

κ_1 term can be neglected, we find the constraint

$$Y^f_{L-\bar{L}} \sim \frac{9\sum_\alpha m_\alpha}{64\pi v^2} M_2 \frac{e^{-cK_1}}{cK_2} > \eta_L \simeq 10^{-9}. \tag{3.91}$$

With the neutrino mass constraint $\sum_\alpha m_\alpha \sim m_3$ as input, this implies the lower bound $M_2 > (10^7 \mathrm{GeV}) \cdot cK_2 e^{cK_1}$. In standard one-flavor leptogenesis, we instead obtain the simpler bound, $M_1 \gtrsim 10^7 \mathrm{GeV}$. This is because the equilibrium parameter is constrained to satisfy $K_1 < 1$, so that $\kappa_1 \sim 1$, and because scattering processes are not in equilibrium long enough to provide any significant washout.

- **Low-scale models**

A viable low scale example is shown in Fig. 3.15a. The CP-asymmetry ϵ_2 for low values of M_2 is controlled by the hidden sector couplings $\{\alpha, \beta\}$, i.e. $\epsilon_2 \propto (\beta/M_2 + |\alpha_{21}|/2)\,|\alpha_{21}|/r_{21}^{1/4}$. At the same time, because the CP-asymmetry ϵ_1 is sourced purely from the Yukawa sector, it becomes negligible at low mass, $\epsilon_1 \propto \sum_\alpha m_\alpha M_1/v^2 \ll \epsilon_2$, as exemplified by Fig. 3.15c. In this case, Eq. (3.76) reads,

$$Y^f_{L-\bar{L}} \simeq \frac{3}{32\pi}\kappa_2 \left(\frac{\beta}{M_2} + \frac{|\alpha_{21}|}{2}\right) \frac{|\alpha_{21}|}{r_{21}^{1/4}} e^{-\int_{\mathcal{Z}}^\infty dz(W_1/z')}. \tag{3.92}$$

This relation relies on a hierarchical separation between the N_2 and N_1 phases, which is only marginally satisfied in Fig. 3.15a where $M_2/M_1 = 10$. Nevertheless, the above relation encodes the two competing effects, namely the enhancement of the low-mass CP-asymmetry, and also the increased washout. Generating a larger CP-asymmetry requires an increase in the ratio β/M, which at the same time increases the scattering rates and the washout (see the next subsection for details of the relative effects). Independent of the precise dynamics, for the relevant couplings, $K_2 \sim 1 - 10$, the efficiency factor will generally lie in the range $\kappa_2 \sim 0.01 - 0.5$ (see Fig. 3.11). The washout function depends on the scattering processes, and we can approximate $\int_{\mathcal{Z}}^\infty dz' W_1/z' \sim (3+2\beta/M_1)K_1$, so that $\exp(-\int_{\mathcal{Z}}^\infty dz' W_1/z') \sim 0.5-1$ for $K_1 \sim 0.01-0.1$ and $\beta/M_1 \sim 1$. As an example, taking $\kappa_2 \exp(-\int_{\mathcal{Z}}^\infty dz' W_1/z') \sim 0.1$ implies the following characteristic

(a) $\{M_2, M_1, K_2, K_1, K_{21}, \beta\}$ = (b) $\{M_2, M_1, K_2, K_1, K_{21}, \beta\}$ =
$\{1500\text{GeV}, 155\text{GeV}, 1, 0.5, 10^5, 20\text{GeV}\}$ $\{10^9\text{GeV}, 130\text{GeV}, 8, 0.5, 4 \cdot 10^3, 1\text{GeV}\}$
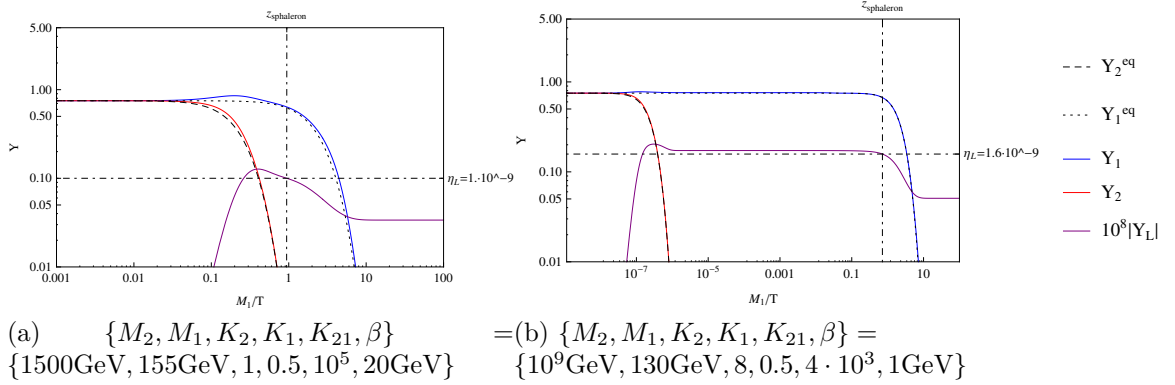
Figure 3.16: Scenarios representing low (a) and high (b) scale models which take advantage of the sphaleron cutoff temperature in order to liberate the parameters from stringent constraints.

constraint on the lepton asymmetry,

$$Y^f_{L-\bar{L}} \sim \frac{3}{32\pi} \left(\frac{\beta}{M_2} + \frac{|\alpha_{21}|}{2} \right) \frac{|\alpha_{21}|}{r_{21}^{1/4}} 10^{-1} > \eta_L \simeq 10^{-9}, \qquad |\alpha_{21}| \frac{\beta}{M_2} \sqrt{\frac{M_1}{M_2}} > 3 \cdot 10^{-7}, \tag{3.93}$$

where small couplings $|\alpha_{21}| \ll \beta/M_2$ have been assumed, and typically we will use $|\alpha_{21}| \sim 10^{-5}$. Given the above approximations, the light neutrino mass scale is a subleading parameter and does not appear in this bound.

An feature worth noting is the sensitivity to low temperature boundary conditions, namely the temperature at which $B+L$-violating sphaleron transitions go out of equilibrium, $T_{sphaleron} = 159\pm1\text{GeV}$ [138]. The lepton asymmetry at this point effectively determines the final baryon asymmetry, while further evolution is observationally relatively unconstrained. This is phenomenologically interesting as it is usually quite difficult to find viable models with a large washout from N_1. However, if we choose M_2 above and M_1 well below the temperature at which sphaleron processes freeze out, the baryon asymmetry is generated right after N_2 falls out-of-equilibrium, and will not be washed out at lower scales even if the lepton asymmetry is highly suppressed through N_1 processes. The N_1 sector effectively decouples in this case. A low mass example is shown in Fig. 3.16a. Note that $T_{sphaleron} > M_1 > m_H$ in this case, since $M_1 < m_H$ would require the inclusion of interactions such as $N_1 L \leftrightarrow H$, that have not been considered thus far.[4] In the low mass regime, many interactions are relevant which cause significant washout of the lepton asymmetry. As a consequence,

---

[4]Note that such processes may also arise on including thermal corrections to the scalar masses.

(a) $\{M_2, M_1, K_2, K_1, K_{21}, \beta\} =$
$\{10^8 \text{GeV}, 10^4 \text{GeV}, 0.8, 0.4, 4 \cdot 10^2, 50 \text{GeV}\}$

(b) $\{M_2, M_1, K_2, K_1, K_{21}, \beta\} =$
$\{2 \cdot 10^3 \text{GeV}, 200 \text{GeV}, 0.8, 0.04, 400, 500 \text{GeV}\}$
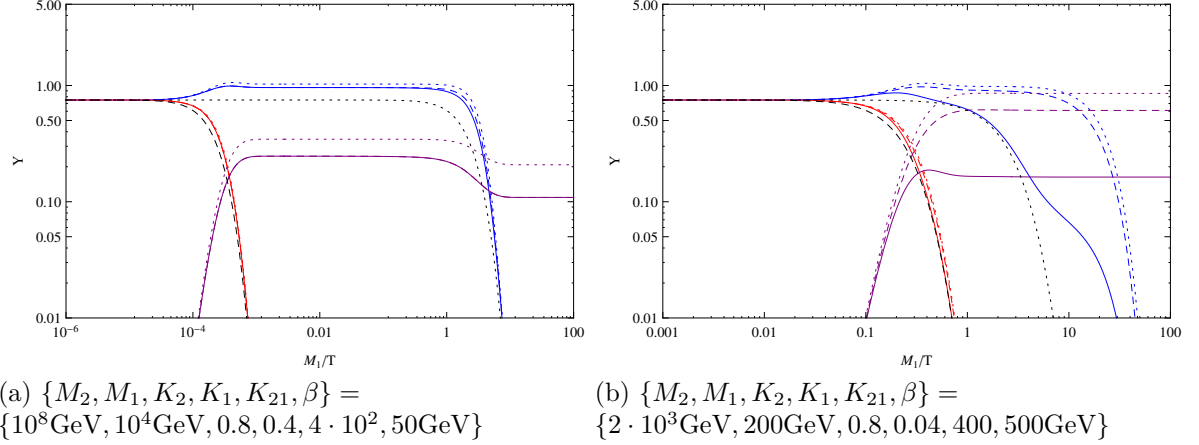
Figure 3.17: Plots showing the impact of $\Delta L = 1$ and $\Delta N = 2$ processes on the dynamics for high scales $\{M_2, M_1\} = \{10^8, 10^4\}$GeV (on the left) and low scales $\{M_2, M_1\} = \{2, 0.2\}$TeV (on the right). The color coding, blue, red, purple and black, is the same as in Fig. 3.14a 3.15a, 3.16a. The dotted pattern is for decays only, dashed for decays plus $\Delta L = 1$ scattering, and plain for decays plus $\Delta L = 1$ and $\Delta N = 2$ scattering.

the range of parameters available for low mass scenarios is quite limited. On the other hand, an example of a high mass scenario which also takes advantage of the sphaleron cutoff temperature is shown in figure Fig. 3.16b. In that situation, all of the lepton asymmetry is generated out of the first phase, from N_2 leptonic decays. In this case, with $M_1 < T_{sphaleron}$, the physics of N_1, including the hidden sector interactions, are only weakly constrained. An interesting aspect of this scenario is the possibility of exploring models where the lightest RH neutrino is so light and weakly coupled to leptons, that its lifetime could be long enough to play an independent cosmological role, potentially in the form of sterile neutrino dark matter [144, 145]. In such cases, the N_1 abundance will have to be sufficiently depleted for consistency with constraints on the dark matter abundance. This can be achieved through adjusting the $N_1 N_1 \rightarrow HH$ rate.

3.3.2 Aspects of the dynamics

In this subsection, we relax some of the constraints required for physical scenarios and focus on the various dynamical components that come into play: the decays and scattering processes on one hand, and the various parameters on the other.

Decays and inverse decays versus scattering

The impact of the decays, inverse decays and scattering is summarized in Fig. 3.17. We overlay three solutions: (i) just decays and inverse decays (dotted lines), (ii) decays, inverse decays and $\Delta L = 1$ scattering (dashed lines), and finally (iii) decays, inverse decays and $\Delta L = 1$ and $\Delta N = 2$ scattering (plain lines).

Starting with the high mass regime, the hidden sector scattering processes, e.g. $N_i H \rightarrow LS$, $N_i N_i \rightarrow HH$, are subdominant compared to the Yukawa-mediated processes since $\beta/M_i \ll m_t/v$. This can be seen from Fig. 3.17a, where $\Delta L = 1$ scattering has a significant effect relative to decays, whereas the $\Delta N = 2$ scatterings have no visible effect. In practice, the decays and inverse decays remain the dominant effect, and the results from section 3.2.3 can be reasonably well applied.

The low mass regime is marked instead by the significant, if not dominant, effect of hidden sector scattering processes, given $\beta/M_i \sim m_t/v$. Looking at the plot in Fig. 3.17b, the effect of adding $\Delta L = 1$ scattering is similar to that in the high mass regime, however the impact of $\Delta N = 2$ processes is greatly enhanced. Although these processes do not violate lepton number, $\Delta L = 0$, they act to maintain the neutrino abundance closer to equilibrium. As a consequence, both the $\Delta L = 1$ processes (e.g. decays) and the inverse processes (e.g. inverse decays) remain in equilibrium for longer, leading to an enhanced lepton washout in that regime.

Parameter Dependence

The dependence of the dynamics on the parameters is displayed in Fig. 3.18. The subsection above considered examples of viable models that satisfy the basic constraints, and focused on constraining the relevant parameters accordingly. We now ignore those constraints, and instead vary the parameters $\{K_2, K_1, K_{21}, \beta\}$ to study their impact in both high and low mass regimes.

- $\{K_2, K_1\}$:- Figs. 3.18a and 3.18b exhibit the effects of K_2 and K_1 in the large mass regime. When the N_1 and N_2 phases can be hierarchically separated, they both act as independent one flavor systems according to the respective efficiency factors $\kappa_{1,2}$. Consequently, we expect little deviation from the toy model that was studied previously.

  Figs. 3.18c and 3.18d exhibit the effects of K_2 and K_1 in the low mass regime. This regime requires a smaller mass ratio to achieve sufficient CP-asymmetry,

therefore the overlap of the N_2 and N_1 phases induces more intricate dynamics, though we observe that the impact of K_2 and K_1 can still be separated.

- $\{K_{21}, \beta\}$:- Figs. 3.18e and 3.18f exhibit the effects of varying K_{21} and β in the low mass scale regime. The primary effect is on the magnitude of the lepton asymmetry, via the impact on the CP-asymmetry of N_2. However, there are also effects due to scattering. Indeed, in both cases the maximal lepton asymmetry is achieved for mid-range values, $K_{21} = 500$ and $\beta = 500\text{GeV}$ respectively. This illustrates the fact that beyond a given threshold, increasing these parameters increases the scattering washout more significantly which more than compensates for the increase in the CP-asymmetry.

3.4 Summary

This chapter has considered a minimal extension of leptogenesis that arises by opening up the Higgs portal with a new singlet scalar. This scalar can also couple at the renormalizable level to the RH neutrinos which introduces a new (hidden sector) source of CP violation into the theory. The new RHN decay channels that are opened allow Higgs portal leptogenesis to avoid the stringent constraints of the Davidson-Ibarra bound, with viable low scale scenarios that we have considered in detail. The new decay channels are only available for the next-to-lightest RH neutrinos, which has a number of interesting implications for phenomenology. We conclude in this section by mentioning a number of these as directions for future work.

- *First-order leptogenesis*: The new decay channels, e.g. $N_2 \rightarrow N_1 + S$ do not violate lepton number. Thus, this model falls into a general category in which the next-to-lightest RH neutrinos have both L-violating and L-conserving decays. As has recently been emphasized [109], such models allow the original Weinberg-Nanopoulos theorem [108] to be evaded in that the loop-level amplitude can be of first-order in the L-violating vertex. This is clear from the analysis in Section 2, and thus the HPL model is a simple example illustrating this general feature.

- *Light (CP violating) sterile neutrinos*: Since the new sources of the CP-asymmetry arise from decays of the next-to-lightest RH neutrino states, it is possible to effectively decouple N_1 from leptogenesis. Indeed, since the normal heirarchy still

allows one parametrically light (or massless) active neutrino, we can consider taking N_1 to be, for example, in the keV mass range for sterile neutrino dark matter. It would be interesting to explore whether the washout constraints on the interactions allow for viable thermal production modes in the early universe. It is notable that, since α_{ij} contains multiple CP-odd phases, this model would generically imply some new low energy contributions (albeit suppressed) to CP-violating observables.

- *Dynamical seesaw scale*: We assumed throughout that the scalar S was in a stable vacuum throughout the range of cosmological evolution relevant for leptogenesis. This needn't be the case, and the full scalar potential $V(H, S)$ could allow for some evolution in $\langle S \rangle$, which would in turn affect the RH neutrino mass scale. Some of these issues were recently considered in [129], and it would be interesting to explore the implications of having an early epoch where, for example, the RH neutrino mass scale were to pass through zero due to a phase transition in the scalar potential.[5]

---

[5]We thank Maxim Pospelov for suggesting this possibility, and related discussions.

(a) $K_2 = \{0.1, 5, 10\}$ (plain, dashed, dotted)

(b) $K_1 = \{0.1, 5, 10\}$ (plain, dashed, dotted)

(c) $K_2 = \{0.1, 5, 10\}$ (plain, dashed, dotted)

(d) $K_1 = \{0.1, 5, 10\}$ (plain, dashed, dotted)

(e) $K_{21} = \{10, 500, 1000\}$ (plain, dashed, dotted) (f) $\beta = \{10, 500, 1000\}$GeV (plain, dashed, dotted)
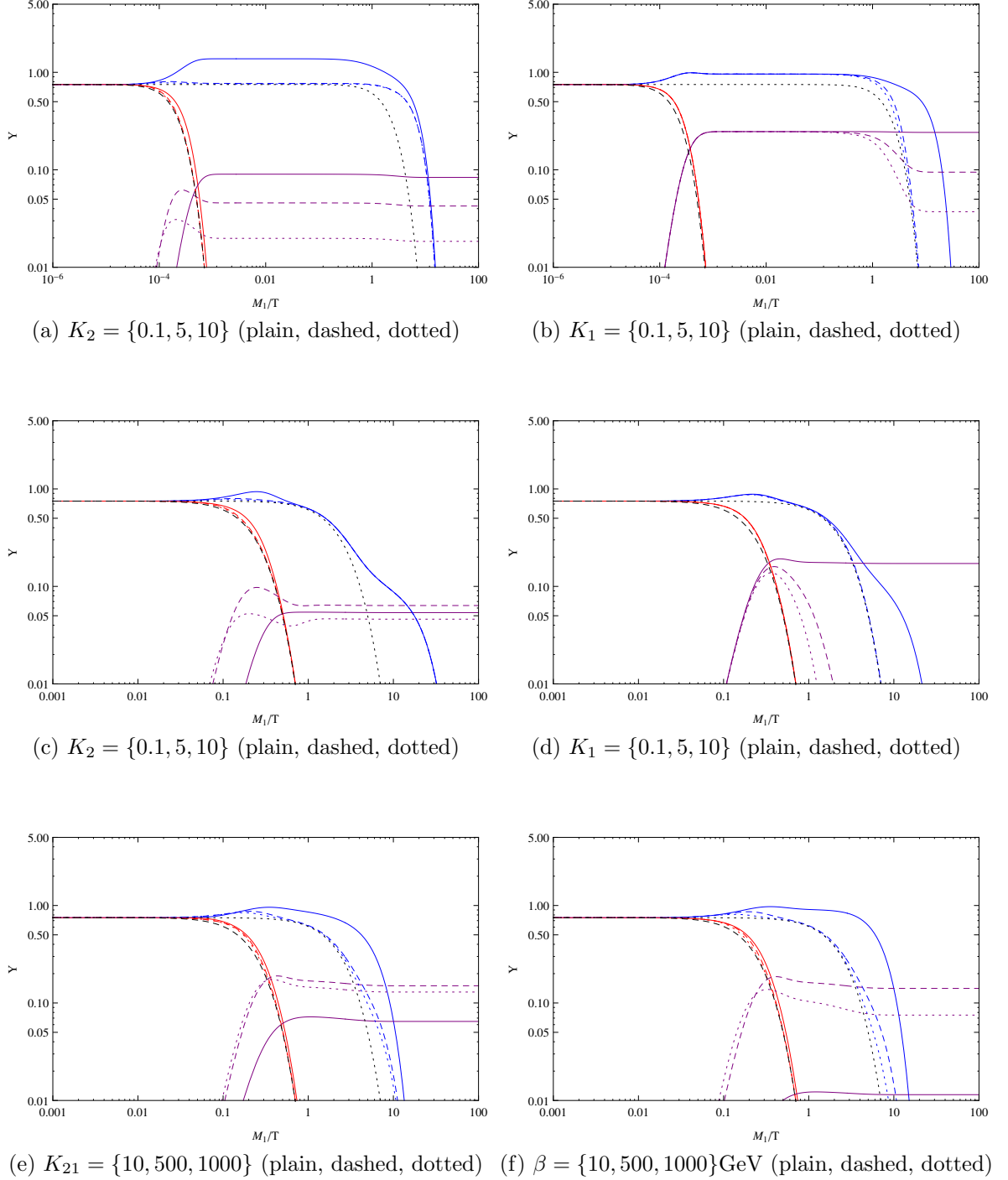
Figure 3.18: The effect of $\{K_2, K_1, K_{21}, \beta\}$ on the dynamics for high $\{M_2, M_1\} = \{10^8, 10^4\}$GeV (top two plots), and low $\{M_2, M_1\} = \{2, 0.2\}$TeV (bottom four plots) mass regimes. The color coding, blue, red, purple and black, is the same as Fig. 3.14a 3.15a, 3.16a, while the dotted, dashed and plain lines represent the variation of each parameter.

Chapter 4

Light singlet neutrinos and precision phenomenology

In the previous section, we analyzed an extension to N_1-leptogenesis by including the neutrino and Higgs portals. The main conclusion was that it is possible to create a model of leptogenesis whose mass scale is closer to the electroweak mass scale.

In this section, we ask the question about experimental constraints imposed on low energy new physics models. More specifically, the previous chapter used a neutrino model that includes singlet neutrinos to the service of leptogenesis, but did not provide strong constraints on the model itself. The goal here is to impose independent constraints on models that involve light singlet neutrinos. One of the results of the previous chapter was the possibility of having one singlet neutrino below the electroweak scale. Here, we focus on models that exclusively involve light new particles with masses below the electroweak scale.

Accelerator-based particle physics has the goal of probing the shortest distance scales directly, by colliding particles and their constituents at high energies. Thus far, all high energy data is well described by the Standard Model (SM) of particles and fields, with the last missing element, the Higgs boson, identified recently [1, 2]. Considerable attention is therefore focused on the search for 'new physics' (NP) that may complement the SM by addressing some of its shortcomings. However, the most prominent empirical evidence for new physics, associated for example with neutrino mass and dark matter, does not necessarily point to an origin at shorter distance scales.

Fortunately, experiments at the energy frontier are not the only tools available to

probe NP; they are supplemented by searches at the precision (and intensity) frontier (see *e.g.* [146]). Precision observables, particularly those that probe violations of exact or approximate symmetries of the Standard Model such as CP and flavor, play an important role in the search for new physics [30, 147, 148, 149]. Their reach in energy scale, through loop-induced corrections from new UV physics, can often extend well beyond the direct reach of high energy colliders. However, measurements at low energies may be sensitive not only to NP corrections coming from the short distances, but also to NP at longer distances (lower mass) with extremely weak coupling to the SM. It is therefore prudent to ask for which precision observables can measured deviations from SM predictions *unambiguously* be identified with short-distance NP at the electroweak (EW) scale or above? Alternatively, one can ask when such deviations might also admit an interpretation in terms of new low-scale hidden sector degrees of freedom. This is the question we will address in this chapter.

The sensitivity of any constraint on new physics is determined on one hand by the precision of the measurement in question, and on the other by the accuracy and precision of any SM calculations required to disentangle background contributions. If the effective Lagrangian is schematically written in the form $\mathcal{L} = \mathcal{L}_{\mathrm{SM}} + \mathcal{L}_{\mathrm{NP}}$, the possibility of discovery relies on being able to reliably bound the NP contribution to the observable away from zero. The natural tendency to interpret results in terms of operators in $\mathcal{L}_{\mathrm{NP}}$ induced by ultraviolet NP can be problematic, as $\mathcal{L}_{\mathrm{NP}}$ can in general also receive contributions from light weakly-coupled degrees of freedom. This dilemma is nicely illustrated by the theoretical interpretation of a NP discovery that has already occurred, namely the observation of neutrino flavor oscillations. The experimental results are most straightforwardly interpreted in terms of the masses and mixing of the light active neutrino species [31, 152]. However, as is well known, there are a number of possible explanations for their origin. These include a short-distance explanation in terms of the dimension-five Weinberg operator [153], $\mathcal{L}_{\mathrm{NP}} \propto (HL)(HL)/\Lambda_{\mathrm{UV}}$ with $\Lambda_{\mathrm{UV}} \gg \langle H \rangle$, which generates neutrino masses scaling as $\langle H \rangle^2/\Lambda_{\mathrm{UV}}$. There are also a variety of different UV completions for this operator, with and without heavy right-handed neutrino states, present throughout the theory literature. While this interpretation is certainly valid, there is also the possibility of interpreting neutrino mass as a consequence of very light states N, with $m_N \ll m_W$ and the quantum numbers of right-handed neutrinos [151, 154, 150, 145, 155, 144]. Such states would typically be very weakly coupled to the SM, thus escaping direct detection. The most prominent model in this class is the simple three-generation extension of the SM with
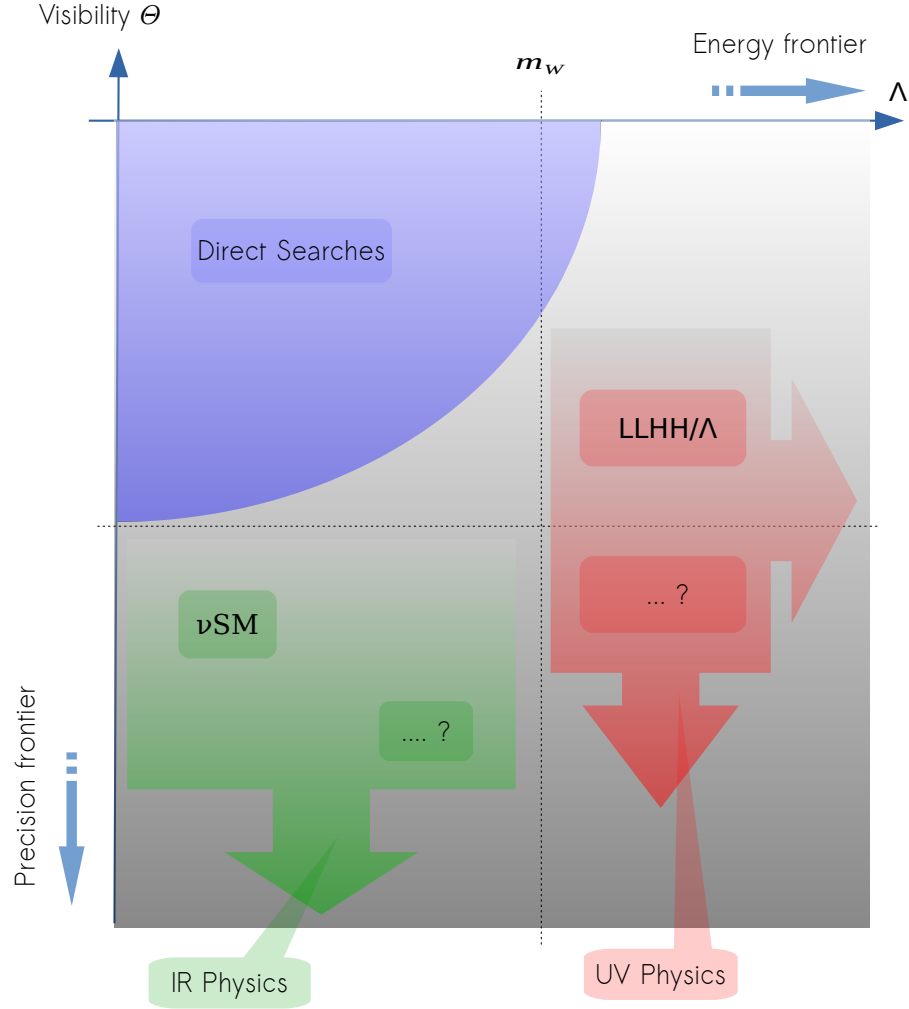
Figure 4.1: Landscape for theories of particle physics, include the SM and beyond, in the space of Energy frontier and Precision frontier, which are proxies for the characteristic energy scales and characteristic coupling scales of BSM physics. Current collider experiments currently probe the top left quadrant, while the Weinberg dimension-5 operator has been used as an example of operator populating the UV new physics region, and the model νSM of massive pseudo-Dirac neutrinos [150, 151] as an example of new physics populating the IR new physics region. The arrows indicate the pressure imposed on models through increasing experimental sensitivity. The blue visible area is accessible through direct searches.

N states that allow Dirac masses for the active neutrinos, referred to as the νSM model. Thus we see that neutrino oscillations can be interpreted as the result of UV or IR new physics (or both).

A schematic summary of the question asked in this section is shown in Fig. 4.1, which represents the landscape of all theories beyond the SM and including the SM.

We can categorize theories along two axes; one axis represents the energy frontier, which is a proxy for the characteristic energy scale of particle theories, and the precision scale axis, which is a proxy for the coupling strength of the hidden sector with the SM. The SM lies in the top left quadrant in this space, as all its particle content are within the reach of current collider experiments. Further down the Energy Frontier dimension, new physics particles have characteristic mass scales that are beyond the energy reach of current experiments (direct or indirect), and are hidden as a consequence. Further down the Precision Frontier dimension, new physics theories are increasingly weakly coupled to the SM, and require a high sensitivity to be detected which is beyond the feasibility of current experiments.

As a summary, we attempt at filling this space with observables that uniquely involve either UV or IR physics, whose observation would thus uniquely point to new physics lying in either the UV or IR regions. The two mechanisms for generating the light neutrino masses introduced earlier, namely the νSM model and the Weinberg dimension-5 operators, have been shown as examples of two models that uniquely involve light new physics or heavy new physics, respectively.

4.1 Effective theories and low energy model building

A simple characterization of UV/IR new physics scenarios follows by making the division at the electroweak scale, so that the chiral electroweak $SU(2)_L \times U(1)_Y$ structure is maintained,

$$\mathcal{L}_{\mathrm{NP}} = \mathcal{L}_{\mathrm{UV}} + \mathcal{L}_{\mathrm{IR}}. \tag{4.1}$$

New UV physics can then universally be described at the EW scale by a series of higher dimensional operators constructed from SM degrees of freedom,

$$\mathcal{L}_{\mathrm{UV}} = \sum_{d \geq 5} \frac{1}{\Lambda_{\mathrm{UV}}^{d-4}} \mathcal{O}_d. \tag{4.2}$$

Maintaining SM gauge invariance explicitly, we demand that $\mathcal{O}_d$ can be written in an $SU(2)_L \times U(1)_Y$ invariant form. The lowest dimension $d = 5$ includes only $LHLH$-type operators, which contribute to neutrino mass. The number of operators grows rapidly at $d = 6$ and above [156, 157, 158, 159, 160, 161, 162, 163, 164, 165, 166, 167, 168]. We impose no restrictions on these operators, other than that $\Lambda_{\mathrm{UV}} \gg m_Z$,

so that they can consistently be written in $SU(2)_L \times U(1)_Y$ invariant form. Unless these new operators violate some of the well-tested exact or approximate discrete symmetries of the SM, Λ_{UV} can be taken fairly close to the EW scale. It is important to notice that the new states appearing at Λ_{UV} could be charged under any of the SM gauge groups, and some of the most stringent constraints in cases where no specific symmetries are violated now come from the LHC.

In comparison, new IR physics is rather more constrained. A convenient categorization of light NP scenarios can be constructed as follows:

A. Portals: As we saw in the Introduction, Sec. 1, portal interactions are operators of dimension $d \leq 4$ that couple the SM fields to a neutral hidden sectors through a restricted set of renormalizable interaction channels, the vector, Higgs and neutrino portals (see e.g. [57]). Such models of light new physics are fully UV complete without any additional charged states.

B. Anomaly free (neutral): Light hidden sectors can also be charged under anomaly-free combinations of SM symmetries. For those combinations, such as $B - L$ or $L_\mu - L_\tau$, that do not involve individual quark flavors, additional (light and neutral) Higgs fields may be necessary to retain a viable mass spectrum, but these extra states can be SM-neutral. Therefore, these scenarios also fall into the category of UV-complete and gauge-neutral hidden sectors.

C. Anomaly free (charged): Light hidden sectors charged under anomaly-free, but quark-flavor non-universal, symmetries such as $Q_{f_1} - Q_{f_2}$ require new charged Higgs states to restore the mass spectrum. Thus, these new physics scenarios generally require charged states at or above the EW scale.

D. Anomalous: Light hidden sectors charged under anomalous SM symmetries, such as B or L, necessarily require additional (heavy) charged states at or above the EW scale, and so again do not fall into the category of IR new physics scenarios considered here. Indeed, as emphasized for example by Preskill [169], from the low energy perspective, anomalous theories are phenomenologically analogous to UV new physics scenarios with a specific UV cutoff.

Based on this categorization, we will limit our attention to cases A and B, namely those which do not require new charged states at or above the EW scale for consistency. Thus we construct our model examples according to the following rules:

- The dimensionality of operators in the IR sector is restricted to $d \leq 4$, as a necessary condition for UV completeness.

- The IR sector cannot contain new SM-charged states. (Otherwise, such states will have to be close to or above the EW scale modulo some exceptional cases where masses as low as ~ 60 GeV may still be viable [170]). New charged states fall into the category of NP at the EW scale, and form part of $\mathcal{L}_{\mathrm{UV}}$.

- The gauge extensions of the SM are restricted to anomaly-free combinations, which is also a generic requirement of UV completeness [169].

- We shall not question naturalness of possible mass hierarchies, $m_{\mathrm{IR}} \ll m_W$, and will take them as given.

We impose no further constraints on the content of the models to be considered below. The categories A and B consist of new physics fields neutral under the Standard Model group, and which couple to it via relevant and marginal $d \leqslant 4$ operators. As we discussed in the Introduction, those are portal interactions, and they require new scalars S_i, neutral fermions N_i and/or new $U(1)$ gauge boson(s) V_μ [171, 172, 173, 174, 175]. The most economical renormalizable portal interactions for these states can be written in the form

$$\mathcal{L}_{\mathrm{IR}} = \kappa B^{\mu\nu} V_{\mu\nu} - H^\dagger H (\beta S + \gamma S^2) - \lambda L H N + \mathcal{L}_{\mathrm{hid}}, \qquad (4.3)$$

and can trivially be generalized to multiple new fields and to a charged version of S, $S^2 \to |S|^2$. The β and λ couplings were used in Chapter. 3 to model Higgs Portal Leptogenesis. Once coupled to the SM through these channels, the IR hidden sector can be almost arbitrarily complicated. S and N can couple to a complex hidden sector involving dark abelian or non-abelian gauge groups, possibly with additional scalar or fermion states charged under those hidden gauge groups. The full hidden sector Lagrangian simply needs to comply with the conditions above. The portal interactions in (4.3) are complete under the assumption that the SM is strictly neutral under the extra $U(1)$. However, this is unnecessarily restrictive. Light NP models (in case B) may also include non-anomalous gauged versions of global symmetries such as $B - L$ and $L_i - L_j$ etc, where SM fields receive charges under the new $U(1)$.

It is also important to discuss some examples of theories that *do not* satisfy the above criteria. For example, a light pseudoscalar a coupled via the axion portal to

a SM fermion ψ, $\frac{1}{f_a}\partial_\mu a\,\bar{\psi}\gamma^\mu\gamma_5\psi$, clearly requires UV completion at some high energy scale $\sim f_a$. Interestingly, a light scalar directly coupled to the scalar fermion density, $S\bar{\psi}\psi$, is allowed, provided that this coupling descends from the Higgs portal $ASH^\dagger H$, once the heavy SM Higgs particle is integrated out. This means, of course, that the ratio of the effective Yukawa couplings of S to ψ will obey the same relations as in the SM, and any deviations from this pattern would imply the existence of new Higgs doublets charged under the SM, and hence some new physics at or above the EW scale.

We turn in the next section to discuss a range of precision observables, and seek to determine which of them can receive significant contributions from IR new physics. Table 1 summarizes the results from the next section, and refines the schematic classification of Fig. 4.1 according to the categorization A–D of new physics models introduced above.

4.2 Leptonic Precision observables

We turn to leptonic flavor-violating observables. In analyzing IR new physics scenarios, it will be convenient to have in mind a specific hidden sector coupled through the neutrino portal. In particular, to the three left-handed active neutrinos ν_l, $l = e, \mu, \tau$, we add corresponding right-handed neutrinos N_R, plus a number of extra singlet fermion states N_S. In our search for light NP models able to induce appreciable deviations of precision measurements in the lepton sector, it will prove advantageous to look in detail at a model that uses an inverse seesaw scheme for neutrino masses [176, 177, 178, 179],

$$-\mathcal{L}_\nu \supset \begin{pmatrix} \nu_L & N_R & N_S \end{pmatrix} \begin{pmatrix} 0 & m_D & 0 \\ m_D & 0 & M_D \\ 0 & M_D & \epsilon \end{pmatrix} \begin{pmatrix} \nu_L \\ N_R \\ N_S \end{pmatrix}, \qquad (4.4)$$

in the regime $\epsilon \ll m_D, M_D$. The Dirac mass terms m_D, M_D arise from Yukawa terms $\lambda \overline{N}_R H \nu_L$ and $\lambda' \overline{N}_S H \nu_L$ upon the Higgs doublet acquiring a vacuum expectation value $m_D = \lambda \langle H \rangle$, $M_D = \lambda' \langle H \rangle$. The Dirac masses are matrices, but in the simplest example of only one active flavor, one right-handed neutrino and one additional singlet, this model predicts one light and two heavy mass eigenstates, $m_\nu, M_\pm$ respec-
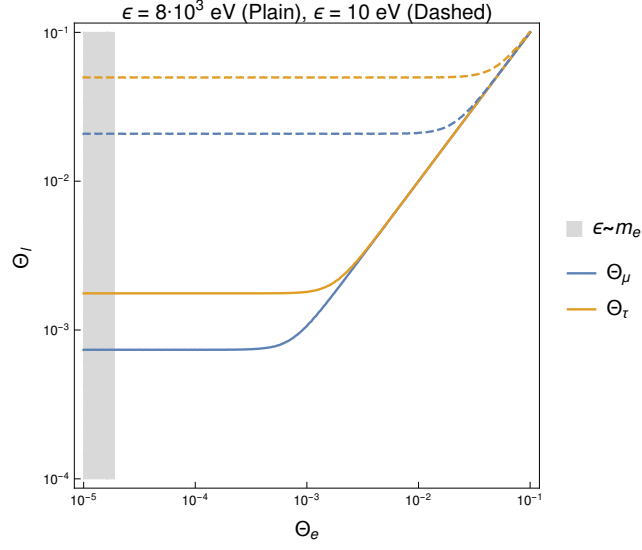
Figure 4.2: A plot of the angles $\Theta_{\mu,\tau}$ given by equations (4.8), with $M_D = 3$ GeV. The gray band is inconsistent with the assumption that $\epsilon \ll m_D$.

tively, given by

$$m_\nu \sim \frac{m_D^2}{R^2}\epsilon + \mathcal{O}(\epsilon^2), \quad M_\pm \sim R \pm \frac{M_D^2}{2R^2}\epsilon + \mathcal{O}(\epsilon^2), \tag{4.5}$$

with $R^2 = m_D^2 + M_D^2$. In order to accommodate the light neutrino mass spectrum, we choose $m_D \lesssim M_D$, and $\epsilon \gtrsim m_\nu$. To lowest order, the unitary matrix U that transforms the mass eigenstates into the flavor eigenstates takes the form,

$$\begin{pmatrix} \nu_L \\ N_R \\ N_S \end{pmatrix} = U \begin{pmatrix} \nu_i \\ N_+ \\ N_- \end{pmatrix}, \quad U \approx \begin{pmatrix} \frac{M_D}{R} & \frac{m_D}{\sqrt{2}R} & i\frac{m_D}{\sqrt{2}R} \\ \frac{m_D M_D \epsilon}{R^3} & \frac{1}{\sqrt{2}} & -i\frac{1}{\sqrt{2}} \\ -\frac{m_D}{R} & \frac{M_D}{\sqrt{2}R} & i\frac{M_D}{\sqrt{2}R} \end{pmatrix}. \tag{4.6}$$

In the $m_D \ll M_D$ limit, the active neutrino states almost coincide with the flavor states $\nu_i \simeq \nu_l$, and the two singlets combine into heavy physical states $N_\pm \simeq (N_S \pm N_R)/\sqrt{2}$. The mixing between active-hidden and hidden-hidden neutrino states can also be measured by a set of three characteristic angles,

$$\theta_{\nu S} \approx \theta_{\nu N} \approx \frac{m_D}{\sqrt{2}M_D}, \quad \theta_{NS} \approx -\frac{\pi}{4} + \frac{m_D^2}{4M_D^2}. \tag{4.7}$$

Because the $\nu-S$ and $\nu-N$ mixing angles are so similar, we define the angle $\Theta_i \equiv \theta_{\nu_i N}$ to characterize the visible-hidden mixing.

We will generally make the assumption that the matrices M_D, ϵ are diagonal and universal, so that they are characterized by one scale also denoted M_D, ϵ respectively (this may involve some tuning, since in general it is not possible to simultaneously diagonalize both matrices). The visible Dirac masses m_D are nearly diagonal, but not universal, so that m_D can be characterized by three parameters $m_{De,\mu,\tau}$, thus $m_{\nu_l} \approx \epsilon m_{Dl}^2/M_D^2$. The first two constraints on the model are those from the neutrino mass squared differences, $\Delta m_{21}^2 = m_{\nu_2}^2 - m_{\nu_1}^2$ and $\Delta m_{32}^2 = m_{\nu_3}^2 - m_{\nu_2}^2$,

$$\Theta_\mu^4 \simeq \frac{\Delta m_{21}^2}{4\epsilon^2} + \Theta_e^4, \quad \Theta_\tau^4 \simeq \frac{\Delta m_{32}^2 + \Delta m_{21}^2}{4\epsilon^2} + \Theta_e^4. \tag{4.8}$$

These functions have been plotted for clarity in Fig. 4.2. As we will see in the rest of this section, constraints can be imposed on Θ_e, cutting off some of the available parameter space.

4.2.1 Lepton flavor violation

As we will see, lepton flavor violation in the Standard Model comes from the fact that it is not possible to simultaneously diagonalize the charged current sector and the lepton mass sector.

The kinetic term for the lepton doublets and lepton singlets is $1/2\overline{L}_i\gamma^\mu D_\mu L_i$, where $i = e, \mu, \tau$ is the lepton flavor and where the covariant derivative includes the non-abelian gauge couplings, $D_\mu = \partial_\mu - igA_\mu^a T^a - ig'YB_\mu$. The index $a = 1, 2, 3$ counts the three SU(2) generators T^a, and $Y = Q - T^3$ is the U(1)$_Y$ generator with Q the electric charge. The A_μ^a and B_μ fields are not the mass eigenstates, instead, the physical $W^\pm, Z$ and A_μ weak and hypercharge gauge bosons are given,

$$\text{Charged weak bosons:} \quad W_\mu^\pm = \frac{1}{\sqrt{2}}\left(A_\mu^1 \mp iA_\mu^2\right), \quad m_W = \frac{gv}{2}$$

$$\text{Neutral weak bosons:} \quad Z_\mu = \frac{1}{\sqrt{g^2 + g'^2}}\left(gA_\mu^3 - g'B_\mu\right), \quad m_W = \frac{\sqrt{g^2 + g'^2}v}{2} \tag{4.9}$$

$$\text{Hypercharge boson:} \quad A_\mu = \frac{1}{\sqrt{g^2 + g'^2}}\left(g'A_\mu^3 + gB_\mu\right), \quad m_A = 0$$

the weak angle (or Weinberg angle) is such that $\cos\theta_w = g/\sqrt{g^2 + g'^2}$, $\sin\theta_w = g'/\sqrt{g^2 + g'^2}$. In this basis, the charged current, neutral current, and electromagnetic

current interactions, mediated by $W^\pm$, Z and A respectively read,

$$\mathcal{L}_{\text{CC}} = \frac{g}{\sqrt{2}} \left[W_\mu^+ \bar{\nu}_{Li} \gamma^\mu e_{Li} + W_\mu^- \bar{e}_{Li} \gamma^\mu \nu_{Li} \right]$$

$$\mathcal{L}_{\text{NC}} = \frac{g}{\cos\theta_w} Z_\mu \left[\bar{\nu}_{Li} \gamma^\mu \nu_{Li} + \bar{e}_{Li} \gamma^\mu \left(-\frac{1}{2} + \sin^2\theta_w \right) e_{Li} + \bar{e}_{Ri} \gamma^\mu \left(\sin^2\theta_w \right) e_{Ri} \right] \quad (4.10)$$

$$\mathcal{L}_{\text{EM}} = \left(-\bar{e}_L \gamma^\mu e_L - \bar{e}_R \gamma^\mu e_R \right) A_\mu$$

where e_{Li}, ν_{Li} are the charged and neutral component of the lepton doublet, $L_i = (e_{Li}\ \nu_{Li})^T$. Note that we only included the leptonic currents, and we will introduce the hadronic currents in the next section. The leptons in those currents are written in the flavor basis. The leptons acquire a mass upon the Higgs doublet developing a vacuum expectation value,

$$f_{ij} \bar{e}_{Ri} H P_L L_j \to f_{ij} v \bar{e}_{Ri} e_{L_j}. \quad (4.11)$$

We can use one unitary transformation U^e to rotate each of the lepton fields such that $U^{e\dagger} f v U^e$ is diagonal. In the minimal Standard Model where neutrinos are massless, we have the freedom to rotate the neutrino fields by the same matrix as the charged lepton. In such way the charged, neutral, and electromagnetic interactions remain unchanged and diagonal since

$$\bar{\nu}_{Li} \gamma^\mu e_{Li} \ \to \ \bar{\nu}_{Li} \gamma^\mu U^{e\dagger} U^e e_{Li} = \bar{\nu}_{Li} \gamma^\mu e_{Li}, \quad (4.12)$$

due to the unitary condition $U^\dagger U = 1$.

In reality, though, neutrinos are massive, and the above rotation are more complicated. Indeed, when neutrinos have masses they have both chiralities, $\nu_{R,L}$ and Dirac mass terms $m_{\nu ij} \bar{\nu}_{Li} \nu_{Rj}$. Applying different field rotations for the neutrino and charged leptons will keep the neutral and electromagnetic currents unchanged, however, the charged current will change to,

$$\mathcal{L}_{\text{CC}} = \frac{g}{\sqrt{2}} \left[W_\mu^+ \bar{\nu}_{Li}^m \left(U^{\nu\dagger} U^e \right) \gamma^\mu e_{Li}^m + W_\mu^- \bar{e}_{Li}^m \left(U^{e\dagger} U^\mu \right) \gamma^\mu \nu_{Li}^m \right] \quad (4.13)$$

The extra matrix is the PMNS unitary matrix $V_{PMNS} = \left(U^{\nu\dagger} U^e \right)$. Because it is not diagonal in the flavor, it allows for flavor changing charged currents. The fact that neutrino masses break lepton flavor conservation results in the effect of neutrino oscillations $\nu_{Li} \to \nu_{Lj}$, which is experimentally well documented.
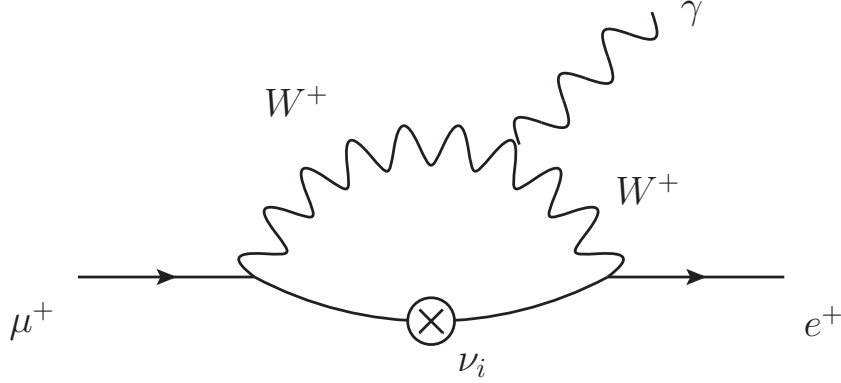
Figure 4.3: Dominant loop level diagram mediating $\mu \to e\gamma$.

It is important to distinguish neutral flavor violation from charged lepton flavor violation. So far, we have introduced neutral flavor violation, i.e. flavor violation in the neutrino sector, apparent from neutrino flavor oscillations.

Charged lepton flavor violation on the other hand, involves the flavor violation in the charged lepton sector, e, μ, τ. In principle, the fact that charged leptons do come in three flavors, means that mass eigenstates and flavor eigenstates are related through a unitary transformation, which should allow for flavor oscillations. However, because the only source of lepton violation is mediated in the SM model through neutrino and W exchange according to the charged lepton currents $\mathcal{L}_{CC}$ in Eq. 4.13, charged lepton flavor violation is mediated at least at the one-loop order involving two orders of the PMNS matrix. Inevitably, the scale of the PMNS matrix elements, and the light neutrino masses which are very small compared to the W mass causes the loop corrections to be highly suppressed. To this day, charged lepton flavor violation has never been observed.

Nevertheless, experiments are trying to detect it through various decay and interaction channels, with very high precision. For that reason, charged lepton flavor violation observables constitute good precision observables of the SM. Below, we will enumerate the best constraints in that sector.

$\mu \to e\gamma$

The best limit on $\mu \to e\gamma$ is [180, 181],

$$\mathrm{Br}(\mu^- \to e^-\gamma) < 5.7 \cdot 10^{-13}. \tag{4.14}$$

The MEG-II upgrade is expected to have an order of magnitude better sensitivity [182]. The small magnitude of this branching ratio makes it an important observable to test new physics. Within the context of the SM, this process proceeds through a $W - \nu$ loop, an example of which is shown in Fig. 4.3. Including corrections from the massive neutrinos, the result is $\text{Br}(\mu \to e\gamma) = (3\alpha/32\pi)\delta_\nu^2$ [183, 184, 185, 120, 186], with

$$\delta_\nu = 2 \sum_{i=\nu,\pm} U_{ei}^* U_{\mu i} g\left(\frac{m_i^2}{m_W^2}\right), \tag{4.15}$$

where

$$g(x) = \int_0^1 d\alpha \frac{1-\alpha}{1-\alpha+\alpha x} \left[2(1-\alpha)(2-\alpha) + \alpha(1+\alpha)x\right]. \tag{4.16}$$

In the small x limit, $g(x \ll 1) \approx 5/3 - x/2$, and using unitarity we find $\delta_\nu \approx -\sum_{i=\nu,\pm} U_{ei}^* U_{\mu i} m_i^2/m_W^2$. Furthermore, unitarity also implies $U_{e\nu}^* U_{\mu\nu} = -\sum_{i=\pm} U_{ei}^* U_{\mu i}$, leading to a dependence of δ_ν on the neutrino mass square differences $m_\pm^2 - m_\nu^2$ [187]. The small neutrino mass squared differences enforce a very small branching ratio scale. This suppression mechanism is the same the GIM mechanism, which suppresses the quark flavor violation.

Within our model of the neutrino masses introduced earlier, charged lepton flavor violation is mediated at loop level through the same loop as the Standard Model contribution, Fig. 4.3, except its magnitude is dominated by the masses of the sterile neutrinos $M_\pm$ via the contributions $\delta_\nu \approx -\Theta_e \Theta_\mu (M_+^2 + M_-^2)/m_W^2$. Thus we have

$$\text{Br}(\mu \to e\gamma) \approx \frac{3\alpha}{8\pi} \frac{M_D^4}{m_W^4} \Theta_e^2 \Theta_\mu^2 < 5.7 \cdot 10^{-13}. \tag{4.17}$$

Inspection of this formula shows that there is ample room to saturate this inequality with light NP: taking $\Theta_e^2 \Theta_\mu^2 \sim 10^{-8}$ and $M_D < m_W$ allows for $\text{Br}(\mu \to e\gamma)$ at a level close to its upper bound.

$\mu - e$ **conversion**

For this particular light NP model, stronger sensitivity actually comes from $\mu - e$ conversion in nuclei [188, 189, 190]. Within the Standard Model, there are two transition channels for this process. First, the *photonic* transition, which proceeds via the same diagram as the $\mu \to e\gamma$ on-shell transition, except the photon is now connected to the nucleus, shown in Fig. 4.4a. The second, the *non-photonic* transition, occurs either through Z-boson exchange or a box diagram mediated by W-bosons.
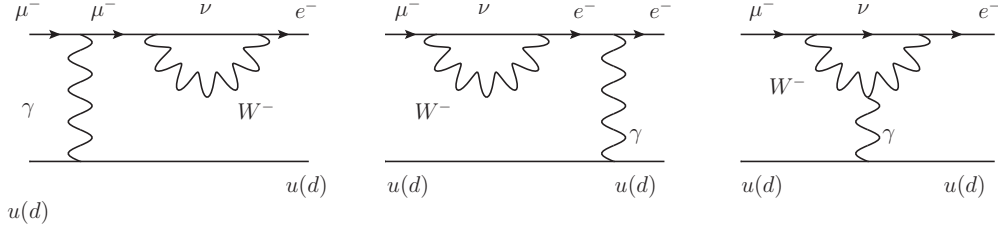
(a) Photon diagrams that cause the $\mu - e$ conversion in nuclei environments. We did not include the diagrams mediated by the Z boson.
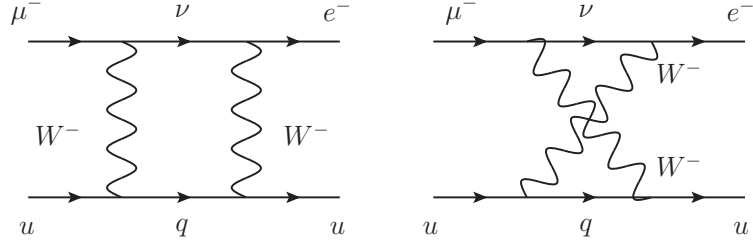
(b) Photon diagrams that cause the $\mu - e$ conversion in nuclei environments

Figure 4.4: Set of photonic, and non-photonic diagrams that contribute to the $\mu - e$ conversion rate in nuclei environments.

Within the model considered here, the non-photonic transition is dominated by the box diagram. Since we focus on the light neutrino regime, we utilize the result that the box diagram receives a large enhancement (in this case) compared to the photonic transition, $\Gamma_{\not\gamma}/\Gamma_{\gamma} \sim 10^3$ [188], and the box diagram dominates the $\mu - e$ conversion rate. The conversion rate compared to muon capture in the nucleus, $R_{\mu-e} = \Gamma(\mu - e)/\Gamma_{capture}$, is given by

$$R_{\mu-e} \approx \left(\frac{3 G_F m_W^2}{4\sqrt{2}\pi^2} \right)^2 \frac{E_e p_e}{m_\mu^2} |F_{ch}|^2 \rho \times \delta_\nu^2, \tag{4.18}$$

where

$$\rho \approx Z \frac{|3/2\beta_0(1 + N/Z) + \beta_1/2(1 - N/Z)|^2}{6|1.62 Z/A - 0.62|}, \tag{4.19}$$

is an enhancement factor accounting for the coherent nature of the transition. The charge form factor can be experimentally determined for various elements, the largest of which is about $|F_{ch}| \approx 0.5$ [191, 190]. The parameters $\beta_0 \sim 30$, $\beta_1 \sim 25$, and the factor $E_e p_e/m_\mu^2 \approx 1$. The best current limit is $R_{\mu-e} \leqslant 7.0 \cdot 10^{-13}$ from experiments using gold ^{197}Au [192], for which $Z = 79$, and the coherent enhancement factor is

$\rho \approx 1.6 \cdot 10^6$. Therefore, using the above expression for δ_ν, we have

$$R_{\mu-e} \approx 6.5\delta_\nu^2 \approx 26\frac{M_D^4}{m_W^4}\Theta_e^2\Theta_\mu^2 \leqslant 7.0 \cdot 10^{-13}, \tag{4.20}$$

which is a stronger constraint on mass and mixing by two orders of magnitude than the $\mu \to e\gamma$ branching ratio. Various experiments, either running or in the planning stages, aim to increase sensitivity by several orders of magnitude [193, 194]. This inequality can again be saturated with $M_D \ll m_W$.

4.2.2 Lepton Universality

Lepton universality tests that the coupling of the three flavors to the gauge bosons are equal. More precisely, the neutrino sector of the charged current interactions take the form,

$$\mathcal{L}_{CC} = \frac{g}{\sqrt{2}}W_\mu^+\overline{\nu}_l\gamma^\mu e_{Li} + h.c \tag{4.21}$$

where the SU(2) gauge coupling g. The coupling is diagonal in the flavor basis. As discussed in the previous section, when neutrinos are massless, both the charged lepton field and the neutrino can be rotated to their respective mass eigenstates using the same unitary matrix U^e, maintaining the diagonal structure. However, this is not possible anymore when neutrinos have masses, because both field must be rotated using two different matrices $U^\nu \neq U^e$, bringing the PMNS matrix $V_{PMNS} = U^{\nu\dagger}U^e$, which is unitary but not diagonal in the flavor basis.

A way to test universality, is to relax this form of the charged current coupling by allowing each flavor to couple according to the three coupling $g_{e,\mu,\tau}$. There exist various standard decay channels to test lepton universality (see *e.g.* [195, 196, 186]). In particular, we will focus on $\mu-e$ universality in τ decays, through the R_τ observable defined as

$$R_\tau = \frac{\Gamma(\tau^- \to e^-\nu\nu)}{\Gamma(\tau^- \to \mu^-\nu\nu)}. \tag{4.22}$$

In the SM, because the neutrinos are massless, the flavor eigenstates ν_l and mass eigenstates ν_i coincide so that $\Gamma(\tau^- \to e^-\nu\nu) = \Gamma(\tau^- \to e^-\nu_\tau\nu_l)$. For massive neutrinos, and multiple neutrino states, the masses are linear combinations of flavor eigenstates, and $\Gamma(\tau^- \to e^-\nu\nu) = \sum_{i,j}\Gamma(\tau^- \to l^-\nu_i\nu_j)$. The R_τ ratio has recently been measured by BaBar, $R_\tau = 0.9796 \pm 0.0016 \pm 0.0036$ [197], which we will approximate as $R_\tau \approx 1 \pm \Delta R_\tau$, with $\Delta R_\tau = 0.0052$. In general, the decay rate takes the
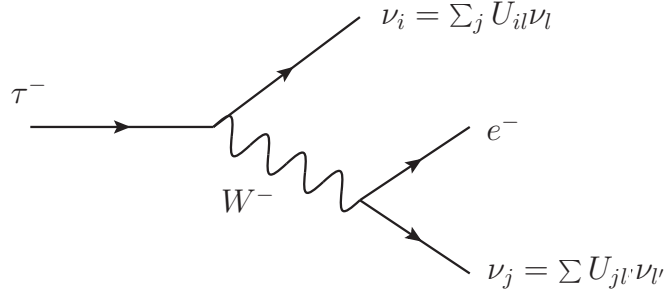
Figure 4.5: Diagram representing the $\tau \to e\nu\nu$ decay process. A similar diagram represents $\tau \to e\nu\nu$. The ratio of the two is a test of the universality of the charged lepton coupling.

form [198, 199],

$$\Gamma(\tau^- \to l^- \nu\nu) = \frac{G_F^2 m_\tau^5}{192\pi^2} \sum_{ij} |U_{\tau i}|^2 |U_{lj}|^2 I\left(\frac{m_l^2}{m_\tau^2}, \frac{m_{\nu_{i,j}}^2}{m_\tau^2}\right). \tag{4.23}$$

To a good approximation, we can take the active neutrino masses to vanish, and the splitting between the two sterile neutrino states to be negligible, $M_+ - M_- \sim \epsilon \ll m_\tau$. Thus, the kinematic function I splits into three categories, where either zero, one or two of the sterile states are produced, respectively denoted $I_{0,1,2}$, with each depending only on the mass scales, but not the flavors. These are plotted in Fig. 4.6, and are very insensitive to the outgoing lepton masses m_μ and m_e. As a result,

$$\begin{aligned}\Gamma(\tau^- \to l^- \nu\nu) \propto\ & I_0^l \sum_{i,j} |U_{\tau\nu_i}|^2 |U_{l\nu_j}|^2 + I_2^l \sum_{i,j} |U_{\tau N_i}|^2 |U_{lN_j}|^2 \\ & + I_1^l \sum_{i,j} \left(|U_{\tau N_i}|^2 |U_{l\nu_j}|^2 + |U_{\tau\nu_i}|^2 |U_{lN_j}|^2\right),\end{aligned} \tag{4.24}$$

where I_0 represents the phase space factor for τ decays into the visible neutrinos, is independent of the sterile neutrino masses. I_2 is the phase space factor for the τ decay into two sterile neutrinos N, and drops to zero fast as $m_N > m_\tau$. I_1 is the phase space factor for the τ decay into one sterile and one visible neutrino. Those three functions are represented in Fig. 4.6.

Using unitarity, we express the visible-visible mixing as $\sum_j |U_{l\nu_j}|^2 = 1 - \sum_i |U_{lN_i}|^2 \approx 1 - N_h \Theta_l^2$, using the assumption $U_{lN_i} = \Theta_l$, with N_h the number of hidden flavors. This approximation is valid as long as $1 - N_h \Theta_l^2 > 0$. The constraint comes from requiring
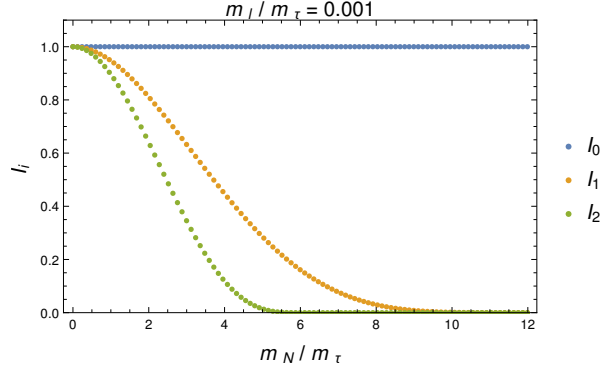
Figure 4.6: Phase space factors I_2, I_1, I_0 for the $\tau \to l\nu\nu$ decay into two sterile neutrinos, N, one sterile neutrino, or zero sterile neutrino, respectively. These functions appear in Eq. (4.24)

that $\Delta R_\tau = 1 - \Gamma(\tau \to \mu\nu\nu)/\Gamma(\tau \to e\nu\nu) < 0.0052$ be within the experimental errors.

The actual significance of this constraint depends on the concrete realization of the mass and mixing pattern. For example, in the situation where the heavy neutrino eigenstates cannot be kinematically produced, the final constraint can be presented as $N_h|\Theta_\mu^2 - \Theta_e^2| < 10^{-2}$. A somewhat stronger universality constraint can be derived by comparing charged pion decay modes. These constraints can be saturated with $\Theta_l^2 \sim O(10^{-2})$ and, as we saw above, such a mixing pattern can easily arise from new singlet neutrino states with a mass below the electroweak scale.

In summary, using the neutrino mass differences to express $\Theta_{\mu,\tau}$ as functions of ϵ, Θ_e, we can present the LFV and universality constraints above in the parameter plots shown in Fig. 4.7. It is clear that this simple light NP model, with sub-EW scale singlet fermionic states, can induce deviations in $\mu \to e$ conversion or lepton universality at the level of the current experimental sensitivity. Therefore, if future experiments detect a non-zero result, further work will be required to unambiguously differentiate between light and heavy NP models.

4.2.3 Lepton number violation

In the Standard Model extended with massive neutrinos, lepton number violation is intricately linked to the mechanism generating the neutrino masses. The simplest and general paradigm for neutrino masses comes from the Weinberg operator [148, 153],

$$\mathcal{L}_{\text{Weinberg}} \sim \frac{C_5}{\Lambda} LLHH \;\to\; \mathcal{L}_{\nu \text{ mass}} \sim \frac{C_5 v^2}{\Lambda} \overline{\nu}^C \nu. \tag{4.25}$$
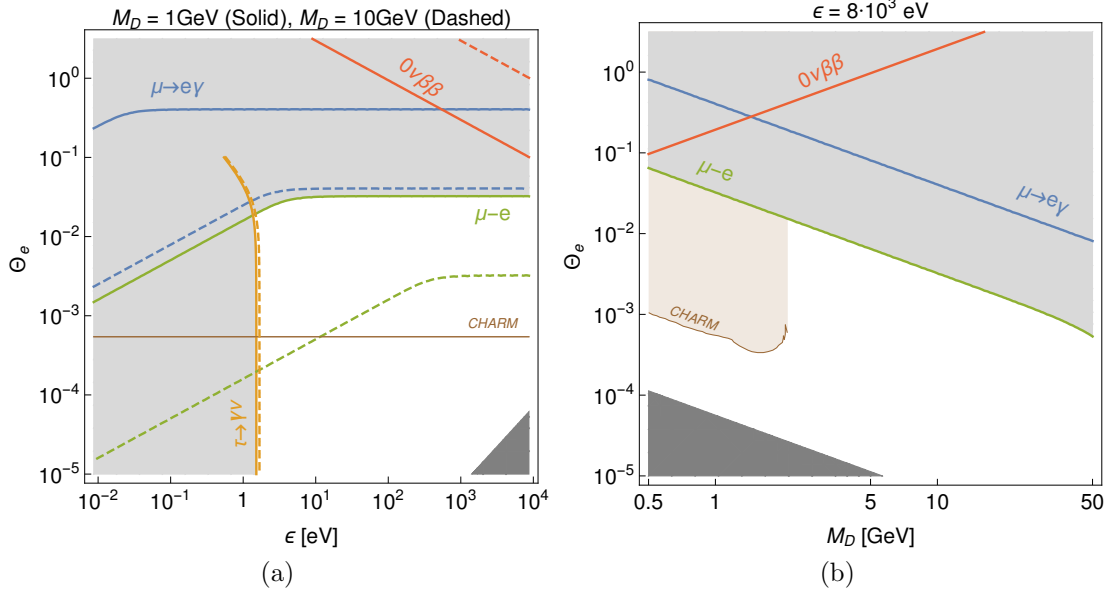
Figure 4.7: Plots showing the allowed regions in (a) $\{\epsilon, \Theta_e\}$ and (b) $\{M_D, \Theta_e\}$ respectively, with $N_h = 2$. The lines correspond to saturation of the respective bounds. M_D is bounded above by the requirement $M_D < m_W$, and from below by the $0\nu\beta\beta$ constraint $M_D \gg 0.1$ GeV. We note that at large ϵ, the $\mu - e$ conversion constraint is by far the strongest, though universality becomes stronger at low ϵ. The darker gray area represents the regime where $\epsilon/m_e > 10^{-1}$, with ϵ no longer 'small'. For completeness, we also show a constraint from on-shell production of sterile states at the CHARM fixed target experiment [200], which applies for $M_D < 2\,\text{GeV}$.

This dimension-5 operator is the lowest-dimensional non-renormalizable operator involving Standard Model fields that can lead to non-zero masses. This operator is also the source of $\Delta L = 2$ lepton number violation. Thus, at this level, it is seen that neutrino masses and lepton number violation are intricately related.

The most stringent experimental test for lepton number violation comes from neutrinoless double β-decay ($0\nu\beta\beta$), which are two simultaneous instances of β-decays. If neutrinos are Majorana, i.e. their own antiparticle, then the two outgoing neutrinos can annihilate each other. The Feynman diagram of this process is shown in Fig. 4.8. The calculation of this diagram gives the decay half-life to the order of,

$$T^{0\nu} = G^{0\nu}|M^{0\nu}|^2 m_\nu^{\text{eff}}, \tag{4.26}$$

where $G^{0\nu}$ is the phase space factor and $M^{0\nu}$ is the nuclear matrix element (scalar product of initial and final nuclei), and with $m_\nu^{\text{eff}} = -\sum_i U_{ei}^2 m_i$ the effective neutrino
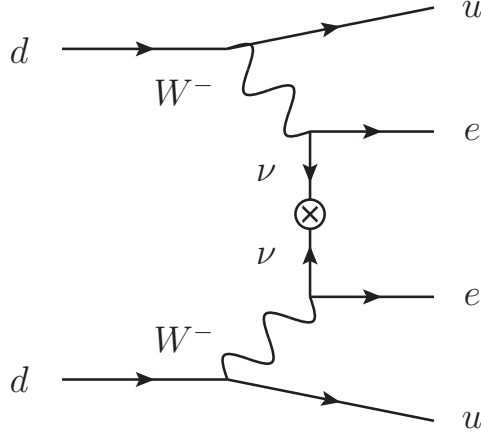
Figure 4.8: Neutrinoless double beta decay diagram. The two neutrinos can annihilate each other, contributing a factor of the neutrino mass, represented by the circled cross.

mass. It is important to note that this expression of the half-life assumes that the lepton number violating vertex only consists of the Majorana singlet neutrino, interacting according to the type-I see-saw mechanism. However, the source of the lepton number violation may come from above the electroweak breaking scale, e.g. type-II and III of the neutrino mass models, which involve triplet scalar and fermion respectively. Therefore, the sole measurement of the decay halftime is not sufficient to determine the source of the lepton number violation, but complementary measurements ought to be made. [148] Neutrinoless double beta decay $\beta\beta_{0\nu}$ is the primary observable for lepton number (L) violation, and the current limits [19, 20, 21, 22, 23, 24] are normally interpreted directly in terms of the light neutrino mass spectrum [201, 202].

The observation of this process has deep implications for the nature of the neutrinos [203]. On the one hand, assuming that neutrinos are Majorana, then it is clear that the process displayed in Fig. 4.8 can take place via the Majorana mass insertion. On the other hand, it may also be that this vertex is not mediated by the Majorana mass term, but some other unknown lepton number violating operator. Nevertheless, the positive observation of neutrino-less double beta decay would still imply neutrinos are Majorana, since the diagram of Fig. 4.8 can contribute to the correction of a neutrino propagator through weak boson processes. In other words, observing neutrinoless double beta decay would be proof that neutrino are Majorana, whether or not the diagram of Fig.4.8 is mediated by a Majorana mass insertion.

Given the existing mass limits on the light eigenstates, the decay rate depends on the effective Majorana mass $m_\nu^{\text{eff}} = \sum_i U_{ei}^2 m_i$. Even without performing a dedicated

analysis, it is clear that any future evidence for a non-zero $m_\nu^{\rm eff}$ will not be able to differentiate between light and heavy NP models. Indeed, in the simplest Type I see-saw model, $m_\nu^{\rm eff} \sim \mathcal{O}({\rm eV})$ can arise from models with $e.g.$ $M_R \sim 1$ GeV or $M_R \sim 10^{10}$ GeV, and therefore both interpretations would be possible.

Recall that the heavy mass eigenstates N_i mix with ν_e, so that the mass eigenstates can be written as $N_i = U_{ei}\nu_e + \cdots$. It will be sufficient to work with the following analytic approximation for the decay rate [204],

$$\Gamma(\beta\beta_{0\nu}) \sim \frac{G_F^4 Q^5 \cos^4\theta_C}{60\pi^3}|\mathcal{M}|^2, \tag{4.27}$$

where $Q + M(Z,A) - M(Z+1,A)$ is the endpoint energy, and the amplitude takes the approximate form,

$$\mathcal{M} = \sum_i U_{ei}^2 m_i \int \frac{d^4p}{(2\pi)^4}\left(\frac{w(p_0,|\vec{p}|)}{p^2 - m_i^2 + i\epsilon}\right)$$

$$\longrightarrow \frac{iE_F p_F w_0}{4\pi^3}\begin{cases} m_\nu^{\rm eff} + \cdots & \text{for } p_F \gg m_i, \\ \frac{p_F^2}{3}\sum_i \frac{U_{ei}^2}{m_i} + \cdots & \text{for } p_F \ll m_i. \end{cases} \tag{4.28}$$

The nuclear form factor $w(p_0,|\vec{p}|)$ has been approximated by a step function $w \sim w_0\Theta(p_0 - E_F)\Theta(|\vec{p}| - p_F)$, with $w_0 \sim 4$ MeV^{-1} [204] in terms of the nucleon Fermi momentum $p_F \sim 100$ MeV. (A more precise interpolating formula is given in [205].)

When the dominant contribution is from the light active neutrinos, the experimental bounds translate to $m_\nu^{\rm eff} \lesssim 0.12 - 0.38$eV [21, 22]. It is also instructive to separately estimate the sensitivity to the exchange of heavier neutrino eigenstates. Note that when the singlet mass $m_N \gg p_F$, the experimental constraints lead to a bound on $(p_F^2/3)\sum_i U_{ei}^2/m_i$ instead. Within the neutrino mass model described in the previous section, we find

$$\sum_i \frac{U_{ei}^2}{m_i} \simeq \frac{U_{e+}^2}{M_+} + \frac{U_{e-}^2}{M_-} \simeq \Theta_e^2\left(\frac{M_- - M_+}{M_+M_-}\right), \tag{4.29}$$

where $M_- - M_+ \simeq -\epsilon$, and $M_-M_+ \simeq M_D^2$. Thus, in the regime $M_D \simeq 1$ GeV, we use the bound $0.3(p_F/M_D)^2\Theta_e^2\epsilon \lesssim 0.3$eV.

The above bound is displayed in Fig. 4.7 for comparison with the LFV constraints. LNV provides a subleading constraint within this particular inverse seesaw model, since the lepton number violating parameter is ϵ which is taken to be small compared

to the other mass scales. However, as already emphasized above, more significant sensitivity to the mixing angle arises in the standard seesaw model, where we enlarge the Majorana terms in the mass matrix.

4.2.4 Lepton anomalous magnetic moments

The interaction between the spin and an external magnetic moment is the magnetic dipole interaction. Classically, it takes the simple Hamiltonian density form,

$$\mathcal{H} = -\vec{B} \cdot \vec{M}, \quad \vec{M} = g\frac{e}{2m}\vec{S}, \tag{4.30}$$

where $\vec{M}$ is the magnetic dipole moment, and the classical g-factor $g = 2$ can be obtained via the Dirac equation with electromagnetic potentials and in the non-relativistic limit. The classical magnetic dipole moment for a rotating charged particle is $|e|/2m$. Loop level corrections cause deviations from the $g = 2$ classical result, and it is standard to parametrize the g-factor via the *anomalous moment*,

$$a = \frac{g - 2}{2}. \tag{4.31}$$

The Standard Model one-loop contributions are shown in Fig. 4.9. For the electron the theoretical prediction takes the value [206]

$$a_e^{th} = 115965218178 \pm 77 \cdot 10^{-14}, \tag{4.32}$$

whereas the experimental value is [207, 208]

$$a_e^{th} = 11596521807 \pm 27 \cdot 10^{-14}. \tag{4.33}$$

The electron anomalous magnetic moment is the most precise test of QED, to the point that it is used to fix the fine structure constant.

On the other hand, there is a discrepancy between the theoretical and experimental results for muon anomalous magnetic moments. The theoretical predictions is at the level of

$$a_\mu^{th} = 116591803 \pm 1 \pm 42 \pm 26 \cdot 10^{-11}, \tag{4.34}$$
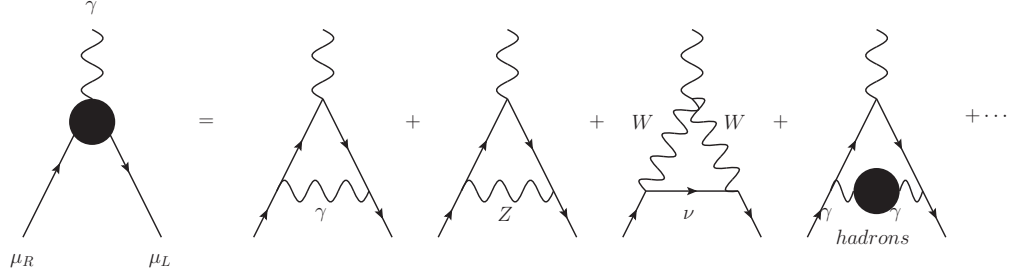
Figure 4.9: Standard Model contributions to the muon magnetic moment

whereas the experimental result is

$$a_\mu^{exp} = 116592091 \pm 54 \pm 33 \cdot 10^{-11}. \tag{4.35}$$

The discrepancy between the two is

$$\Delta a_\mu = a_\mu^{exp} - a_\mu^{th} = 255 \pm 63 \pm 49 \cdot 10^{-11}. \tag{4.36}$$

exhibiting a roughly 3.5σ discrepancy [209] between the measurement and the SM prediction. This discrepancy is well-known and is interpreted in terms of new physics, with the idea that so-far-unobserved new particles can contribute to the loop corrections. A recent analysis on models of dark photon was performed by the BESIII experiment [210], putting constraints on the anomalous magnetic moment, as summarized in Fig. 4.10.

While many UV interpretations exist (see *e.g.* [211]), Δa_μ(NP) can just as easily result from one-loop contributions of light particles. At the effective Lagrangian level, both $g'V_\nu\bar\mu\gamma^\nu\mu$ and $\lambda'S\bar\mu\mu$ can supply the requisite correction,

$$g', \lambda' \sim 10^{-3} \text{ with } m_{V(S)}\lambda m_\mu \implies \Delta a_\mu \sim 10^{-9}. \tag{4.37}$$

This fact is well-appreciated in the literature [212, 213, 214].

The vector model has UV completions involving a kinetically mixed vector, or alternatively a symmetry based on gauged muon number, such as $L_\mu - L_\tau$. Dedicated searches for 'dark photons' [57] have now placed a number of restrictions on the parameter space of this model. At this point, the kinetically mixed vector option to explain $\Delta a_\mu \simeq 3 \times 10^{-9}$ is essentially ruled out through direct production experiments *assuming V* decays back primarily to SM states [215, 216]. Moreover, the alternative
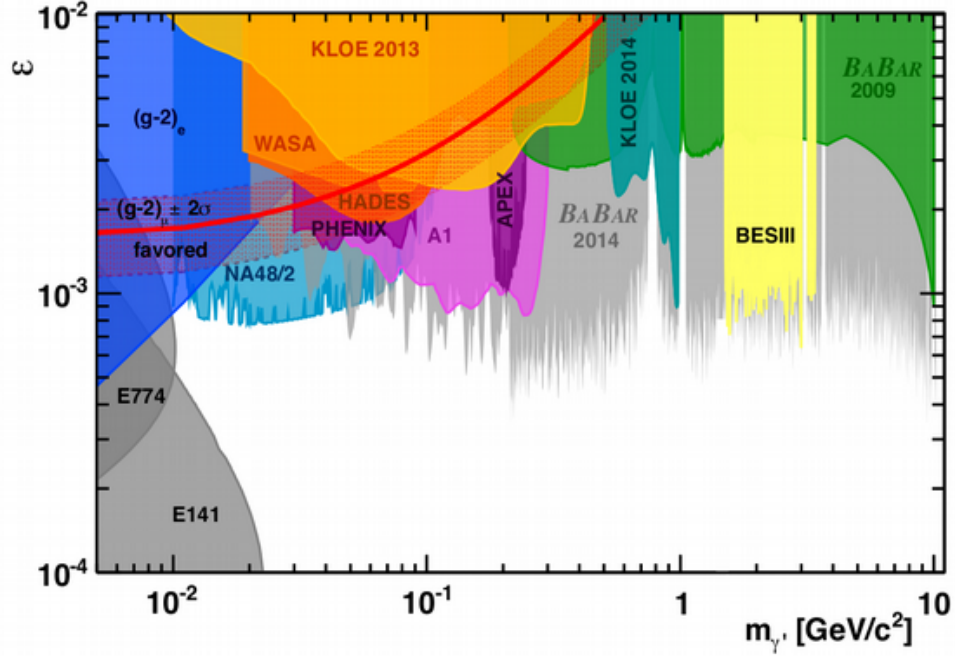
Figure 4.10: Parameter space of the hidden photon mass compared to kinetic coupling, taken from [210].

option of vectors decaying to light dark matter is also significantly constrained [217, 218, 219]. On the other hand, a model with mutliple (cascading) decays of V into the hidden sector can be ruled out only via missing energy signatures, and up to now, significant parameter space is still open for $\Delta a_\mu \sim O(10^{-9})$. The $L_\mu - L_\tau$ explanation is even less constrained, with only trident neutrino production providing an adequate level of sensitivity [220, 221]. We conclude that there are multiple IR models of NP that can lead to the observable shifts in $g-2$, while at the same time escaping direct detection constraints.

In contrast, models based on scalar particles do not provide large shifts to Δa_μ. For example, UV completion via Higgs mixing would imply

$$\lambda' \simeq \frac{A m_\mu}{m_h^2} \ll 10^{-3}, \tag{4.38}$$

as other constraints on the model force A to be much smaller than the weak scale, $A \ll m_h$. Thus, larger values of λ' would require additional NP to appear at the weak scale.

4.2.5 Leptonic Electric dipole moments

At the classical level, the electric dipole moment interaction is the interaction between the spin and the external electric field,

$$\mathcal{H}_{\text{EDM}} = d_e \vec{E} \cdot \frac{\vec{S}}{|\vec{S}|}. \tag{4.39}$$

Electric dipole moments interactions violate the time reversal T, and parity P symmetries. This can easily be seen on account that electric field is invariant under time-reversal, $\vec{E} \to \vec{E}$ while spin is not, $\vec{S} \to -\vec{S}$. Thus, under time-reversal, $\vec{S} \cdot \vec{E} \to -\vec{S} \cdot \vec{E}$. On the other hand, under parity transformation, spin is a pseudo vector, $\vec{S} \to \vec{S}$, but the electric field is a vector, $\vec{E} \to -\vec{E}$. Hence, under parity, the electric dipole moment interaction $\vec{S} \cdot \vec{E} \to -\vec{S} \cdot \vec{E}$.

The relativistic generalization of the classical electric dipole moment interaction is,

$$\mathcal{L} = -d\frac{i}{2}\overline{\psi}\left[\gamma_\mu, \gamma_\nu\right]\gamma_5\psi F^{\mu\nu} \tag{4.40}$$

Given that the combined discrete symmetry CPT is conserved by relativistic quantum field theories, the violation of T implies violation of CP. Hence, at the relativistic level, electric dipole moments are among the most sensitive probes of CP-violation. Hadronic CP-violation has been observed in meson oscillation experiments, e.g. *Kaons*. Therefore, it is known that CP is broken by the weak interactions. As a consequence, no symmetry forbids the existence of the interaction above.

Electric dipole moments (EDMs) constitute an important class of precision CP-odd observables. There are several channels by which CP violation can be communicated from the light NP degrees of freedom to the SM within a UV-complete model. CP-odd mediation can occur via the neutrino portal, and the phases in the Yukawa matrix Y_N, provided there are at least two singlet neutrinos N_i. The second channel is the Higgs portal. While obviously CP-even by itself, the scalar mediator can couple to a light NP sector in a manner that explicitly breaks CP, and this may be communicated to the SM via higher-order loop effects. In this section we consider leptonic EDMs induced through the neutrino portal before turning to more generic light NP mechanisms. Hadronic EDMs, which are distinct in that they can be generated at or close to the current level of sensitivity through the QCD θ-term, will be considered later in Sec. 4.3.

Paramagnetic atoms are those that align with an external magnetic field, and
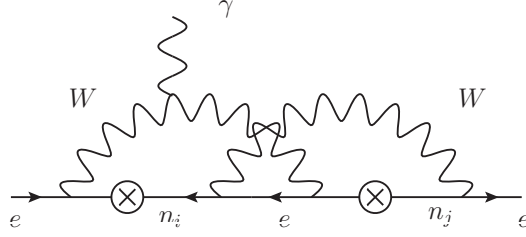
Figure 4.11: An example of a W-loop diagram contributing to the lepton EDM. The crosses indicate neutrino mass insertions.

have unpaired electrons. The EDM of the paramagnetic atom is inherited from the unpaired electron EDM. Schiff theorem certifies that neutral atoms shield external electric fields, and would imply that no atomic electric dipole moment can be induced, making the electron EDM unobservable. However, Schiff theorem can be broken under certain circumstances. In the case of paramagnetic atoms, relativistic effects pertaining to spin-orbit coupling in the atom violates the theorem. This is the main mechanism that allows the electron EDM to not be screen and induce an atomic EDM [222]. Measurements using the Thorium Monoxide (ThO) molecule give the most sensitive measurements of the electron's EDM. [223]

We first consider the same neutrino mass matrix studied in the previous subsection. In order for an EDM to exist, there must be a non-zero CP-violating phase. This is the case if the number of neutrino states is larger than three. Indeed, as we discussed earlier in the context of the charged lepton flavor violation, the diagonalization of the lepton masses involves a unitary transformation for the neutrino and for the charged lepton fields. The transformation manifests itself in the charged currents as $V = U_\nu^\dagger U_e$. If the number of neutrino states if three or larger, then the complex phases of V cannot be removed by field redefinitions. In the Standard Model, the V matrix contains one physical CP-phase if the neutrinos are Dirac, and three if the neutrinos are Majorana. Our model has at least five neutrino states, namely the three left-handed neutrinos plus the two sterile neutrinos $N_{R,S}$. Therefore, our model does contain non-zero CP-violating phases.

In the SM extended with massive neutrinos, it is possible to generate an EDM at the two-loop level [224, 225, 226], an example of which is shown in Fig. 4.11. These

diagrams can be shown to scale as

$$d_e \sim e m_e \left(\frac{G_F}{16\pi^2}\right)^2$$

$$\times \sum_{i<j} \Gamma_{ij} m_i m_j \frac{(m_j^2 - m_i^2)}{m_W^2} F\left(\frac{m_i}{m_W}, \frac{m_j}{m_W}, \frac{m_e}{m_W}\right), \tag{4.41}$$

where $\Gamma_{ij} = \text{Im}\left\{(U_{ei}^*)^2 U_{ej}^2\right\}$, and $i, j = \nu, \pm$ are the neutrino mass eigenstates, and F is a loop function. Up to now, we have ignored the possible CP-odd phases in this model. However, in general not all the mass parameters are real. We choose to leave the physical CP-odd phase in $m_D = |m_D| e^{i\eta}$, and to ease the notation, replace $|m_D|$ simply with m_D. Given that the mixing angles are $m_D/M_D \lesssim 0.1$, we see that the contribution from the diagram with two internal light neutrinos will be tiny, $\mathcal{O}(m_{\nu_1} m_{\nu_2} \Delta m_{21}^2)$. Thus, we need only look at the cases where either one or two internal neutrinos are heavy, respectively called the $h-l$ or $h-h$ contributions. Looking at the $h-h$ contribution, the mixing that enters is Γ_{+-}, but both U_{e+}^2 and U_{e-}^2 have the same phase since they are controlled by m_D/M_D. The CP-odd phase thus cancels from the $h-h$ contribution. Next, the $h-l$ contribution is proportional to $\Gamma_{\nu e \pm} \sim \pm m_D^2/(2M_D^2)\sin(2\eta)$, whereas $m_{\nu_e} M_\pm (M_\pm^2 - m_{\nu_e}^2) \sim m_D^2 M_D \epsilon \pm 3/2 m_D^2 \epsilon^2$. As a result, the $h-l$ contribution to the EDM vanishes at $\mathcal{O}(\epsilon)$. So at the lowest non-vanishing order, we have

$$d_e = d_e^{h-l} \sim \Theta_e^4 \frac{M_D^2}{m_W^2} \frac{\epsilon^2}{\Delta m_{21}^2} \cdot 10^{-53} \sin(2\eta) e \, \text{cm}, \tag{4.42}$$

assuming the function $F\left(\frac{m_{\nu_e}}{m_W}, \frac{M_\pm}{m_W}, \frac{m_e}{m_W}\right)$ is of order unity. Within the allowed parameter space of Fig. 4.7, the above EDM is maximal for $\epsilon^2/\Delta m_{21}^2 \lesssim 10^{12}$, $M_D/m_W \sim 10^{-2}$ and $\Theta_e \lesssim 10^{-2}$, leading to an upper bound $d_e < 10^{-53} e \cdot \text{cm}$. The suppression of the upper bound arises from the size of the Majorana mass term ϵ, which is set by the constraint on the active neutrino mass squared differences. Therefore, within this model it is not possible to generate a sizeable EDM. However, a far larger EDM is possible in a variant of this model with an extra visible-hidden Dirac mass coupling

m_2. Namely, we switch gear and consider the following extended mass matrix,

$$- \mathcal{L}_\nu \supset \begin{pmatrix} \nu_L & N_R & N_S \end{pmatrix} \begin{pmatrix} 0 & m_{D_1} & m_{D_2} \\ m_{D_1} & M_R & \epsilon \\ m_{D_2} & \epsilon & M_S \end{pmatrix} \begin{pmatrix} \nu_L \\ N_R \\ N_S \end{pmatrix}, \tag{4.43}$$

in the regime $M_{R,S} \gg m_{D_i}, \epsilon$. The limiting case $\epsilon = M_R = 0$ leads to two light neutrinos, and only one heavy neutrino, and will not lead to enhanced EDMs. Therefore we are forced to consider the full spectrum, and treating ϵ as a perturbation leads to

$$m_\nu \approx m_\nu^0 + 2\frac{m_{D_1} m_{D_2}}{M_R M_S}\epsilon,$$
$$M_\pm \approx M_\pm^0 \pm \frac{\epsilon}{\Delta M}\left(\epsilon + 2\frac{m_{D_1} m_{D_2}}{M_\pm}\right), \tag{4.44}$$

where $m_\nu^0 \simeq (m_{D_1}^2 - m_{D_2}^2)/M$, $M_+^0 \simeq M_S$, $M_-^0 \simeq M_R$, $\Delta M = M_S - M_R$ is the Majorana mass splitting, and $M = (M_R + M_S)/2$ is the Majorana mass scale. Even though we are in a see-saw-like scenario with large Majorana masses, M_D easily evades the light neutrino mass constraints since they are now controlled by the fine tuning of $m_{D_2}^2 - m_{D_1}^2$. For simplicity we have ignored the phase in the mass eigenstates. As a consequence, to lowest order in $\epsilon(\sim 0)$ [225],

$$d_e \sim e m_e \left(\frac{G_F}{16\pi^2}\right)^2 \frac{\Delta M}{M}\frac{m_{D_1}^2 m_{D_2}^2}{M^4}M^2$$
$$\times \left(\frac{32}{3}\ln\left(\frac{M}{M_W}\right) - \frac{260}{9} + \frac{112}{27}\pi^2\right)\sin(2\eta), \tag{4.45}$$
$$\sim \left(3 \cdot 10^{-35}\ e\,\text{cm}\right)\frac{m_{D_1}^2 m_{D_2}^2}{M^4}\frac{M_S^2 - M_R^2}{\text{GeV}^2}\sin(2\eta).$$

The ratios $m_{D_i}/M \lesssim 10^{-1}$ are the visible-hidden mixing angles. Thus, on choosing a mass scale $M_S^2 - M_R^2 \sim M_S^2 \simeq 10^2\ \text{GeV}^2$, one finds $d_e \lesssim 10^{-37}e \cdot \text{cm}$. Allowing for significant fine tuning, it is possible to enhance this upper bound to $\sim 10^{-33}\text{e} \cdot \text{cm}$, which is still considerably lower than the current experimental upper limit $d_e < 8.7 \times 10^{-29}e \cdot \text{cm}$ [223]. Therefore, we conclude that the sterile neutrino CP violating portal falls short of inducing d_e close to the current experimental bound.

Taking a more general approach, we now consider a more complex light hidden sector. We introduce a Dirac fermion ψ charged under $U(1)_V$ with CP-violating
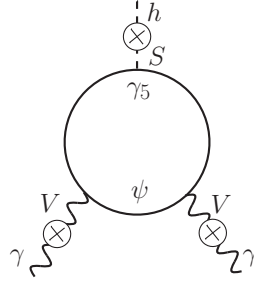
Figure 4.12: The CP-odd $hF\tilde{F}$ vertex.

couplings to the scalar singlet S [227, 228, 229, 230, 231, 232],

$$\mathcal{L}_{\text{hid}}^{\text{CP}} = \bar{\psi}i\gamma^\mu D_\mu^V \psi + \bar{\psi}(m_\psi + S(Y_S + i\tilde{Y}_S\gamma_5))\psi. \tag{4.46}$$

where $D_\mu^V = \partial_\mu - e'q_\psi V_\mu$. This hidden sector CP-violation can then be mediated to the SM via the CP-even vector and Higgs portals.

Loops of ψ can induce the CP-odd $SV\tilde{V}$ vertex shown in Fig. 4.12, which will contribute to EDMs at higher loop order, via e.g. Barr-Zee-type diagrams. For example, integrating out the scalar and one of the vector legs, one obtains a 'dark V-EDM' operator of the electron, which will in turn translate to the effective 'EDM radius' operator (analogous to the charge radius). Schematically, this process of integrating out short distance scales can be presented as

$$SV_{\mu\nu}\tilde{V}^{\mu\nu} \rightarrow \frac{i}{2}\bar{\psi}_e\sigma^{\mu\nu}\gamma_5\psi_e V_{\mu\nu} \rightarrow \frac{i}{2}\bar{\psi}_e\sigma^{\mu\nu}\gamma_5\psi_e\frac{\Box F_{\mu\nu}}{m_V^2}. \tag{4.47}$$

Denoting the coefficient in front of $\frac{i}{2}\bar{\psi}_e\sigma^{\mu\nu}\gamma_5\psi_e\Box F_{\mu\nu}$ as $r_{d_f}^2$, we can utilize existing EDM calculations. For simplicity, we assume that V is parametrically lighter than S and ψ, so the EDM radius takes the form (see e.g. [233])

$$r_{d_f}^2 = \frac{|e|\alpha'\tilde{Y}_S m_f}{16\pi^3 v m_\psi m_V^2}\kappa^2 \sin(2\theta)\left[g(m_\psi^2/m_h^2) - g(m_\psi^2/m_S^2)\right], \tag{4.48}$$

where the loop function is given by

$$g(z) = \frac{z}{2}\int_0^1 dx \frac{1}{x(1-x)-z}\ln\left(\frac{x(1-x)}{z}\right), \tag{4.49}$$

and satisfies $g(1) \sim 1.17$, $g(z \ll 1) \sim z(\ln z)^2/2$ and $g(z \gg 1) \sim \frac{1}{2}\ln z$. Within the

fully hierarchical regime,

$$m_V \ll m_S \ll m_\psi, \tag{4.50}$$

and taking $\theta \sim -Av/(m_h^2) \ll 1$, we have

$$r_{d_f}^2 = -\frac{|e|\alpha'\tilde{Y}_S m_f}{16\pi^3 v m_\psi m_V^2} \times \kappa^2 \theta \ln(m_\psi^2/m_S^2). \tag{4.51}$$

This operator leads to the usual $s - p$ mixing of atomic orbitals, and the atomic EDM linked to the electron spin direction. While a full atomic calculation is required to deduce the size of the matrix element, we will resort to estimating its size by saturating $\square$ with the square of the inverse radius of a K-shell. Then, the effective EDM radius translates to an electron EDM of size $d_e^{\text{eq}} \sim (Z\alpha m_e)^2 r_{d_e}^2$, as long as $m_V > Z\alpha m_e$. Taking $m_V \sim (m_e\alpha Z)$, $q_\psi = 1$, $\alpha' = \alpha$, $\tilde{Y}_S = 1$ and taking the log to be $\mathcal{O}(1)$, we arrive at the estimate

$$d_e^{\text{eq}} \sim 4 \times 10^{-33} \, e \cdot \text{cm} \times \left(\frac{1\,\text{GeV}}{m_\psi}\right) \left(\frac{\kappa}{10^{-4}}\right)^2 \left(\frac{\theta}{10^{-3}}\right), \tag{4.52}$$

which is still well below the current sensitivity to the electron EDM [223]. The main difficulty is in taking m_V in the sub-MeV range, where $g-2$ of the electron imposes a strong limit on kinetic mixing, $\kappa < 10^{-4}$. We note in passing that extracting a proper limit on the 'dark V-EDM', or $r_{d_e}^2$, is a well-motivated problem for atomic physics, in line with the recent investigation of CP-odd operators induced by a mediator of mass comparable to the inverse atomic scale [234].

Another contribution to the experimentally accessible paramagnetic EDMs of atoms and molecules is the semi-leptonic interaction $C_S \bar{N} N \bar{e} i\gamma_5 e$. This operator can also be generated through the $hV\tilde{V}$ vertex, and allows access to a regime with larger m_V for which the constraints on κ are somewhat weaker. However, this contribution is still not at a level that can approach the current experimental sensitivity. Thus, at least within this restricted class of hidden sectors, we conclude that paramagnetic EDMs (and specifically lepton EDMs) are in practice a probe of UV new physics.
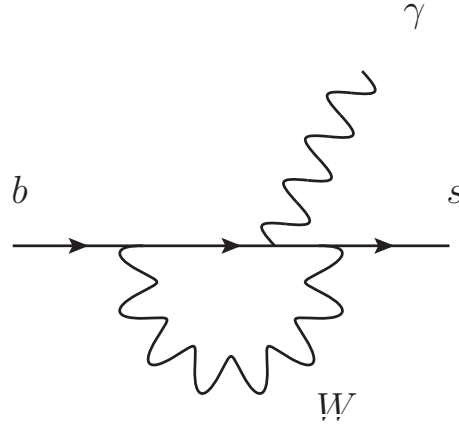
Figure 4.13: $b \to s\gamma$ process in the Standard Model.

4.3 Hadronic Precision observables

4.3.1 Hadronic flavor violation

The formalism for hadronic flavor violation is very similar to that of lepton flavor violation, as it comes from the charged and neutral current interactions between the quarks and the charged or neutral gauge bosons,

$$
\begin{aligned}
\mathcal{L}_{\mathrm{CC}} =& \frac{g}{\sqrt{2}} \left[W_\mu^+ \overline{u}_{Li} \gamma^\mu d_{Li} + W_\mu^- \overline{d}_{Li} \gamma^\mu u_{Li} \right], \\
\mathcal{L}_{\mathrm{NC}} =& \frac{g}{\cos\theta_w} Z_\mu \left[\overline{u}_{Li} \gamma^\mu \left(\frac{1}{2} - \frac{2}{3} \sin^2\theta_w \right) u_{Li} + \overline{u}_{Ri} \gamma^\mu \left(-\frac{2}{3} \sin^2\theta_w \right) u_{Ri} \right. \\
& \left. + \overline{d}_{Li} \gamma^\mu \left(-\frac{1}{2} + \frac{1}{3} \sin^2\theta_w \right) d_{Li} + \overline{d}_{Ri} \gamma^\mu \left(\frac{1}{3} \sin^2\theta_w \right) d_{Ri} \right], \\
\mathcal{L}_{\mathrm{EM}} =& -\overline{q}_L \gamma^\mu q_L - \overline{q}_R \gamma^\mu q_R,
\end{aligned}
\tag{4.53}
$$

where d_{Li}, u_{Li} are the bottom and top components of the SU(2) doublet $Q_{Li} = (u_{Li}\ d_{Li})^T$. This is written in the flavor basis. Rotations to the mass basis involves independent unitary matrices for the left- and right-handed fields, U^f. Because of the Higgs Yukawa interaction that give the quarks their mass, the left- and right-handed unitary matrices are different, so the rotation of the quark terms makes the CKM matrix appear, $V_{CKM} = (U^u)^\dagger U^d$. This procedure, however, keeps the neutral currents unchanged inducing no flavor changing neutral currents. This however is true only at tree level, since there exist loop level processes, such as $b \to s\gamma$, in Fig. 4.13.

There are a couple of features which clearly distinguish these observables, particularly concerning the role of light new physics. Firstly, since the RH states are charged, there is no analogue of the neutrino portal, and thus no renormalizable flavor-violating interactions that do not involve new charged states. Given the existing limits on new light degrees of freedom which are charged, this pushes hadronic flavor violating observables into a category that is primarily sensitive to UV new physics. Having said this, the second distinguishing feature is that the SM itself provides non-negligible contributions to hadronic flavor violation through the CKM matrix. This allows for new flavor violating transitions to occur on introducing purely flavor-diagonal light NP. An example is the kinetic mixing between V and γ (or Z) in (4.3) that can induce flavor-violating transitions of the form $b \to sV$ and thus $b \to s\gamma^*(Z^*)$. However, given the constraints on kinetic mixing, this mechanism is too weak to produce sizeable effects without additional $V - Z$ mass mixing that in turn requires new UV physics [235]. Moreover, utilizing a W-boson loop at leading order for example, the SM contributes to $\mathrm{Br}(\bar{B} \to X_s\gamma) = (3.60 \pm 0.30) \cdot 10^{-4}$ [236], while the BaBar sensitivity is $\mathrm{Br}(\bar{B} \to X_s\gamma) \simeq (3.15 \pm 0.23) \cdot 10^{-4}$ [237]. Thus, the sensitivity to new physics is also limited by the precision of SM calculations.

Since these observables are not primarily sensitive to light new physics in the categories that we have delineated, we will not consider them in detail. However, it is worth outlining how a model with low energy flavor violation can be realized, albeit one that still relies on additional heavy charged states for consistency. We consider a model in which we gauge an anomaly-free $U(1)'$ combination of quark flavors, $Q_{f1} - Q_{f2}$ [238, 239], with a diagonal (and vectorial) gauge coupling of the form [240, 241, 242, 243],

$$\mathcal{L}_{Z'} = g_z Z'_\mu \sum_{q=Q_f,u_f,d_f} z_f \bar{q}\gamma^\mu q, \tag{4.54}$$

with e.g. $z_{Q_3} = z_b = -z_{Q_2} = -z_s = 1$. On transforming to the mass eigenstate basis, this non-universal coupling will generate a flavor-violating $b - s - Z'$ vertex, and mediate sizable flavor violating transitions. In practice, this imposes significant constraints on the combinations of $g_z z_{Q,b,s}$, and is usually used to motivate flavor-universal $U(1)'$ charge assignments. Here, we are interested in having a light Z' that can indeed mediate these transitions at the level to which current experiments are sensitive. If we assign integer charges, then a small gauge coupling $g_z \sim 10^{-5}$ will be sufficient for this purpose. As has recently been emphasized [239], $K^0 - \bar{K}^0$

mixing requires $g_z|z_{Q_2} - z_{Q_1}| < 10^{-5}M_{Z'}/(1\,\text{GeV})$, while $B^0 - \bar{B}^0$ mixing imposes similar constraints on $g_z|z_{Q_3} - z_{Q_1}|$. An explicit Z' model based on 'horizontal' flavor symmetries, related to possible anomalies in B^0 decays, can be found in [244].

The gauging of flavor non-universal symmetries leads to further model building requirements for the quark mass spectrum, as the Yukawa matrices are now subject to additional constraints. Additional charged Higgs fields are required, which necessarily lie above the EW scale given the current LHC constraints. Thus, while quark flavor-violation could be mediated via a light Z', the model would necessarily involve charged states above the EW scale, and thus UV new physics.

4.3.2   Hadronic Electric Dipole Moments

The dominant contribution to hadronic EDMs (e.g. the neutron EDM) comes from the QCD sector, and in particular from the QCD θ term, $\sim \theta G^a_{\mu\nu}\tilde{G}^{\mu\nu\,a}$. Diamagnetic atoms can also be used to probe CP-violation in the QCD sector, as they violate the naive Schiff screening of the nuclear EDM via finite size effects, namely the mismatch between the charge and dipole distributions of the nucleus.

Hadronic EDMs can also be induced using the mechanism outlined above, via the hidden sector Barr-Zee diagram, although again necessarily below the current level of sensitivity. However, hadronic EDMs can also be generated by the QCD θ-term, which is a marginal operator [245, 246, 247, 248]. The strongest current limits in this sector are from the EDM of the neutron [249]

$$|d_n| < 2.9 \times 10^{-26}e\,\text{cm}, \tag{4.55}$$

and the EDM of the Hg atom [250],

$$|d_{Hg}| < 3.1 \times 10^{-29}e\,\text{cm}, \tag{4.56}$$

where the apparent strength of the Hg EDM bound is tempered by Schiff screening of the nuclear EDM [1]. The contribution of $\bar{\theta}$ to the neutron EDM takes the form (see e.g. [252]),

$$d_n(\bar{\theta}) \sim 3 \times 10^{-26}\left(\frac{\bar{\theta}}{10^{-10}}\right)e\text{cm}. \tag{4.57}$$

---

[1]Few months after our publication, an updated measurement on the Mercury EDM was published, giving an order of magnitude improvement on the upper bound $d_{\text{Hg}} < 7.4 \cdot 10^{-30}\text{e} \cdot \text{cm}$ [251].

This leads to the current constraint of $\bar{\theta} < 10^{-10}$. The contribution of $\bar{\theta}$ to d_{Hg} is more complex, and for some time it appeared that it would be isospin-suppressed, with the Schiff moment for Hg primarily sensitive to the CP-odd isovector pion-nucleon coupling $\bar{g}^1(\bar{\theta}) \sim 0.001\bar{\theta}$ rather than the isoscalar coupling $\bar{g}^0(\bar{\theta}) \sim 0.05\bar{\theta}$. However, more recent analyses of the Hg Schiff moment have indicated that $\bar{g}^0$ may provide a comparable contribution to $\bar{g}^1$ [253]. Taking the current 'best values' [147] indicates that

$$d_{Hg}(\bar{\theta}) \sim 5 \times 10^{-30} \left(\frac{\bar{g}^0(\bar{\theta})}{0.05 \times 10^{-10}} + \mathcal{O}(\bar{g}^1(\bar{\theta})) \right) \; e\text{cm}. \tag{4.58}$$

This is a factor of 6 below the current bound, but given that the precision of the calculation is generally understood to be at the order of magnitude level [252, 147], it is clear that a nonzero detection of d_{Hg} could not unambiguously be distinguished from the effect of nonzero $\bar{\theta}$.

We conclude that, at current levels of sensitivity, nonzero detections of the dominant hadronic EDM observables could be explained without additional UV new physics, simply through CP-odd QCD physics in the form of $\bar{\theta}$. Further improvements in the sensitivity to d_n could of course change this picture.

4.3.3 Baryon number violation

New non-SM sources of baryon number violation, for which the primary precision experiments are searches for proton decay, necessarily require new UV physics. The minimal baryonic vertex that converts two quarks into an anti-quark and a lepton corresponds to a higher-dimensional operator that *requires* new charged states in any UV completion of which we are aware. Therefore any detection of proton decay or $n - \bar{n}$ oscillation will most likely point to the weak scale or above, as a possible source of baryon number violation. An alternative means of introducing a low energy mediation mechanism is to gauge B (see e.g. [254]) within a more extended gauge group, and rely on a new non-perturbative sector to break this new gauge symmetry. This, however, may not necessarily lead to any proton decay, or any other baryon number-violating observable without the participation of new charged fields in the UV.

4.4 Summary

Empirical evidence for new physics, e.g. neutrino oscillations or dark matter, does not always provide us with much guidance as to a natural mass or energy scale. As noted in the Introduction, there are UV and IR scenarios for neutrino oscillations, both of which are currently viable. Sometimes it is argued that the evidence for dark matter points to NP at a UV scale at or above the electroweak scale (i.e. via the 'WIMP miracle'). While this may be true for examples such as the MSSM neutralino or the QCD axion, which require UV completion with states above the EW scale, there are many viable examples of dark matter based on UV complete models that do not introduce additional heavy degrees of freedom: these include keV-scale sterile neutrinos, and light scalar and vector fields that are populated via the freeze-in mechanism and/or vacuum misalignment (see *e.g.* [255],[256],[257] for some early ideas). Therefore, the existence of dark matter cannot unambiguously be used as a pointer to new UV physics, any more than the existence of neutrino mass can be used in the same way. This may change if, for example, very energetic products of dark matter annihilation or decay are discovered that would be hard to accommodate within the light NP paradigm. Nonetheless, the observation that various scenarios currently remain open and experimentally testable has motivated the analysis in this paper, namely surveying the possible implications of light NP for precision measurements.

We have explored the sensitivity of several classes of precision observables to UV-complete models of light NP. While it is common to automatically interpret precision measurements in terms of generic UV new physics scenarios, we have emphasized that many of these observables are often most simply considered within models of weakly-coupled hidden sectors. Our findings are summarized in the table, where we see that,

Observable	(A,B) Portals	(C,D) UV-incomplete
LFV	✓	✓
LU	✓	✓
$(g-2)_l$	✓	✓
LNV	✓	✓
LEDMs		✓
HFV		✓
BNV		✓

except for the Leptonic EDMs, leptonic observables can generally be accounted for by UV or IR physics models equally. In that sense, the positive observation of one
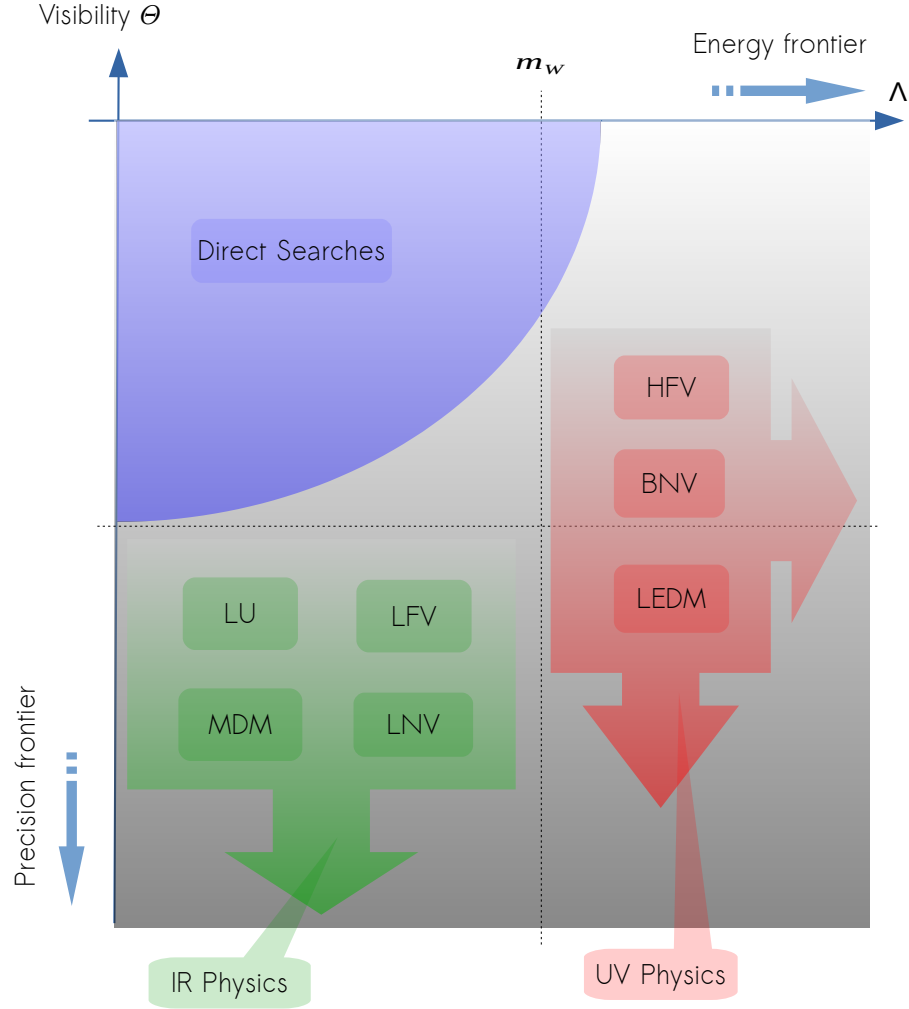
Figure 4.14: While new high energy physics can contribute to all precision observables, as discussed in this paper there are interesting classes of observables that are also sensitive to low-mass new physics. These are shown in green, and test lepton universality (LU), lepton flavor violation (LFV), lepton $g-2$ (MDM), and lepton number violation (LNV). However, observables in the hadronic sector in red, e.g. hadronic flavor violation (HFV) and baryon number violation (BNV), and also lepton electric dipole moments (LEDMs) generally require some new high scale physics. The arrows indicate the pressure imposed on models through increasing experimental sensitivity.

precision leptonic observables cannot be used to unambiguously point to a specific energy regime. On the other hand, the hadronic sector is unlike the leptonic sector in the sense that all fields, including right-handed ones, are charged under the SM group (either electromagnetic, weak or strong force). As a result, there is no hadronic equivalent to leptonic portals, such as the neutrino portal for instance. Hence, new physics either couples through new charged states, or through non-renormalizable op-

erators, none of those qualify as light new physics under our conventions. A graphical summary is provided by the parameter space introduced in Section 4, but with the blanks filled in, is shown in Fig. 4.14.

Operationally, the measurement of any deviation from a SM prediction will necessarily lead to a lengthy process to uncover its origin. Even conclusive evidence for a new phenomenon (neutrino oscillation, dark matter) still entails further work to discriminate between viable interpretations involving light NP and physics at the EW scale and above. Currently, this process is underway for the measurement of $g - 2$ for muons, where both light NP and EW scale phenomena may in principle be causing the discrepancy with SM predictions. Another existing hint of a deviation, in hadronic flavor physics (semileptonic B decays at LHCb), points instead to models of NP which necessarily involve new degrees of freedom at the EW scale or above. The exercise performed in this paper generalizes these examples to a broader set of precision observables and broader classes of models for light NP. In particular, we have found that the neutrino portal allows for a description of many observables in the leptonic sector, while observation of a nonzero electron EDM or related leptonic CP-violating observables would point to NP at or above the electroweak scale. In addition, we observed that several classes of observables that intrinsically involve hadronic flavor violation, baryon number violation, or changes to the charged currents (and thus electroweak symmetry breaking), seemingly allow an unambiguous interpretation in term of new short-distance physics.

Chapter 5

Conclusions

The Standard Model of particle physics is a marvel of precision physics. Based on the concept of symmetries, it provides a unified picture for the fundamental particles so far observed experimentally, and their interactions. In spite of the multiple experimental confirmations, though, there is mounting evidence that the model is not complete and that there is physics beyond the Standard Model. Among others, here are three shortcomings that have been relevant throughout this thesis.

Firstly, the Standard Model was designed with massless neutrinos, which was consistent with the experimental precision of the time. However, neutrino oscillation experiments of the past decade have demonstrated beyond doubt that neutrinos do have mass, which begs for a neutrino mass generating mechanism. Several candidate mechanisms exist, though all of them require field that do not belong to the Standard Model. Secondly, our existence is evidence that the universe is asymmetric in the density of baryon and antibaryon. Theories that attempt to explain this asymmetry require sources of CP-violation. The Standard Model does violate CP-violation, however, the quark sector CP-violation has been shown to be insufficient to explain the asymmetry alone. It is still unclear whether the lepton sector contains CP-violation, but even if it does its source requires beyond-the-standard-model fields. New physics with extra CP-violating sources is required at the high temperatures of the early universe. Finally, signs of dark matter coming from astronomical observations of the rotation of galaxies, astrophysical simulations of the big scale structure of the universe, and measurements of the cosmic microwave background anisotropies cannot be explained within the Standard Model. New, stable, states that are weakly coupled to the Standard Model are necessary in order to build a tentative theory containing dark matter candidates.

The dark matter sector could be just as complex as the visible sector, with fermions, scalar and gauge bosons. In the special case where the dark sector is neutral under the Standard Model, it is referred to as the hidden sector. A powerful way to introduce a hidden sector is through the use of portal interactions, which are relevant and marginal operators that couple Standard Model fields to fields that are neutral under the Standard Model group. The power of this method is that the number of such interactions is very limited. In fact, in four dimensions, there are only four portals: the gauge portal couples the photon to a dark photon, the two Higgs portals couple the Higgs doublet to a scalar singlet, and the neutrino portal couples a singlet fermion to the Higgs doublet and left-handed neutrino.

In the first part of the thesis, we introduced the standard paradigm to explain the origin of the matter-antimatter in the universe, called vanilla leptogenesis. It relies on the Standard Model Lagrangian augmented by the neutrino portal as well as the so-called Majorana mass term for the singlet fermion. Although very successful, the typical energy scale of the theory is far beyond the reach of present and future collider experiments.

In the second part of the thesis, we attempted to lower the scale of leptogenesis to an energy regime which can potentially be probed by current experiments. We attempted to do so by enlarging the model of vanilla leptogenesis with a hidden sector, in particular making use of the trilinear portal operator between two Higgs doublets and the singlet scalar field. This coupling opens up an extra CP-violating decay channel available to the second-lightest right-handed neutrino, N_2, and inaccessible to the lightest. We found that, being of dimension one, the trilinear coupling β leads to a parametric dependence of the CP-asymmetry as β/M_2. Not only this provides an enhancement at low RHM mass M_2, but is also breaks free from the suppression due to the small neutrino masses, which is the case of the standard CP-asymmetry. Thus, from the CP-asymmetry standpoint, the model favors a N_2-generated leptogenesis, at low N_2 mass. Moreover, by solving a system of Boltzmann equations, we proved that the N_2 dynamics of the model does allow the right-handed neutrino to produce the correct lepton (hence baryon) asymmetry in the universe. Especially, we found that it is possible to engineer models where the N_2 mass is of the order of TeV, and N_1 can potentially be lower than the electroweak symmetry breaking scale.

Even though the portal interactions help lowering the scale of leptogenesis, due to the fact that the exact mechanism of leptogenesis is not known, no strong constraints can be put on portal interactions. Instead, strong bounds on interactions can be put

when compared to observables that are precisely measured, namely the electroweak precision observables. In the third part of the thesis, we put constraints on the portal interactions in the energy regime below the electroweak scale. More precisely, we asked whether it is possible to identify a set of observables which, granted a deviation from the Standard Model predictions, would unequivocally be the sign of new physics above the electroweak scale. In order for that, we looked at two kinds of observables. On the one hand, those that test symmetries of the Standard Model, such as CP, lepton flavor, lepton number and baryon number, which allow to put upper bounds on the portal coupling strengths. On the other hand, anomalous observables, i.e. observables whose experimental measurements deviates from the Standard Model prediction, e.g. muon magnetic dipole moment. We analyzed both leptonic and hadronic observables. For the leptonic sector, we used a simple model of hidden neutrinos, and were able to draw its parameter space, with a region of the parameter space that is not ruled out and can fit all observables. From this observation, we concluded that leptonic observables generally make poor pointers, because they can equally well accommodate low energy or high energy new physics, whereas hadronic observables are good pointers to high energy new physics because they can hardly accommodate low energy physics without inconsistencies.

Part II

Condensed Matter

Chapter 6

Introduction

The phenomenon of superconductivity was discovered [258] during experiments on the behavior of the low temperature resistivity of materials, [259] showing that the resistivity of metals drops to zero below a critical temperature, T_c. Further hallmark effects of superconductivity are the Meissner effect [258], whereby the magnetic fields are expelled from the bulk of the superconductor, and the quantization of the magnetic flux inside a ring. The first major formalism attempting to understand superconductivity was developed by the London brothers, who wrote the now famous London equations [260, 261, 262]. These are a set of phenomenological equations added to the four Maxwell's equations, designed to account for the zero resistance and the Meissner effects. They allow calculations of current densities inside the superconductor, as well as magnetic field penetration lengths.

Further progress came in the form of the Ginzburg-Landau theory of phase transitions, based on the existence of an observable, ψ, called the order parameter [263]. When $|\psi|^2 > 0$ we have a superconducting state. It was hypothesized that supercurrents were carried by *superconducting electrons* whose nature was unknown, but whose density was given by $|\psi|^2$. The beauty of Ginzburg-Landau theory is that it allows all superconducting phenomena such as the the Meissner effect, zero resistance, flux quantization, etc to be derived solely from the standpoint of spontaneous gauge symmetry breaking (i.e. with ψ condensing into a value of arbitrary complex phase) [264].

The microscopic theory of superconductivity was developed by Bardeen, Cooper and Schrieffer (BCS) [265, 266, 267]. It gives a very good description of the low temperature superconductors (with $T_c < 40$ K). According to the BCS theory, the microscopic origin of superconductivity is that the symmetry is broken due to the

condensation of the conduction electrons into pairs called Cooper pairs. The condensation takes place due to an attractive force between electrons mediated by lattice vibrations (phonons). Only a handful of materials have electron-phonon interaction strong enough to overcome the repulsive electron-electron (Coulomb) interaction. This special class of materials will become superconducting at some (low) critical temperature. BCS theory shows that the order parameter ψ is directly proportional to the wave function of two electrons in a bound Cooper pair. The superconducting ground state is formed by the superposition of a large number of Cooper-pair bosons with wave functions coherent with respect to each other, just like a Laser is a collection of quantum coherent photons. In that sense superconductivity is an example of a macroscopic quantum state, i.e., a state of many electrons showing pure quantum behavior (the superfluid flow of a charged quantum fluid).

An exciting application of the macroscopic quantum coherence property is that it enables the design of quantum bits (qubits) using large superconducting devices on a single chip [268]. As a result, superconductor-based architectures of quantum computing are winning the race for the development of scalable quantum computers. For example, the group of John Martinis at Google has succeeded in demonstrating a fully coherent quantum adiabatic algorithm using 9 qubits and over 1000 quantum gates [269]. The company D-Wave systems, Inc. is already commercializing analogic quantum computers with over 1024 qubits, used for quantum adiabatic minimization of any function. Some of these adiabatic algorithms show clear signs of quantum coherence [270]. The big enemy of quantum coherence is noise. Electrical and/or magnetic noise leads to transitions between quantum states and loss of quantum coherence.

This takes us to the motivation of the condensed matter part of this thesis. Superconductors, like all materials, are never pure: They contain a number of different impurities at their surface and in the bulk. Most of these impurities possess a local magnetic moment, in the sense that they have an overall spin due to their valence shells being partly filled. As we show here, these impurities lead to energy levels within the superconducting energy gap, the so called Yu-Shiba-Rusinov (YSR) subgap states [271, 272, 273]. When electrons transition between these subgap states they give rise to fluctuation of charge or electric dipole moment (electric noise) or to fluctuation of their magnetic moment (magnetic flux noise). The former is one of the dominant sources of decoherence in the Xmon qubits being developed by Google [269], and the latter is the dominant source of noise in the Superconducting QUantum

Interference Device (SQUID) qubits being developed by D-Wave systems [274]. The goal of this thesis is to develop a quantum theory of multi-electron impurity states in supercondutors that is able to describe the subgap energy levels, eigenstates, and magnetic or electric transitions between them.

Further motivation for developing such a theory are recent experimental advancements in two very different fields of physics. Recently, scanning tunnelling microscopy experiments were able to detect for the first time the orbital splitting of YSR states in a superconductor [275, 276]. The experiment by Ruby et al. [276] revealed the spatial structure of manganese impurities in superconducting lead, making evident the signature of admixture between Mn d-orbitals and Pb's s and p bands. This result cannot be explained by the usual assumption of an impurity as a classical spin, with no orbital degeneracy [271, 272, 273]. It instead requires a model that accounts for the quantum behaviour of the impurity's spin and orbital degrees of freedom. In this thesis, we establish a model of a quantum impurity based on the Anderson model in a BCS superconductor, generalized to include orbital degeneracy.

The other advancement that we wish to note here is the development of superconducting atom chips as a platform to perform spectroscopy and manipulation of clouds of neutral ions [277]. These experiments used lasers to excite atomic states that are trapped in potential wells generated by superconducting circuits shaped in the form of a coplanar waveguide. This enabled quantum read-out and manipulation of neutral ions [278, 279], including Rydberg states with large radial quantum number n [280, 281]. Because these ions are in proximity to a superconductor, their atomic states will also get dressed in the form of YSR subgap states. The model for this effect is identical to an impurity model, except that the coupling to the superconductor is expected to be much weaker. Therefore, it is interesting to consider optical transitions between YSR states as opening novel channels for read-out and manipulation of atomic states using superconducting devices.

Part II of the thesis is organized as follows. Chapter 7 describes the BCS theory of superconductivity, along with a description of the two methods used extensively throughout the research part of the thesis: the Bogoliubov canonical transformation and the equation of motion methods. Chapter 8 describes the basic theory of impurity states in superconductors. We start by proving and discussing Anderson's theorem, that relates the appearence subgap states to breaking a special kind of time reversal symmetry. Next we introduce two quantum impurity models that break this time invariance: the Kondo model and the Anderson model, and describe the canonical

Schrieffer-Wolff transformation that relates the two. Although the Kondo model is in general not exactly solvable, it becomes exactly solvable in the special limit where the impurity spin is treated as a classical vector. Yu, Shiba and Rusinov embedded this model in a superconductor, thus providing the first model to lead to subgap states. They showed that, as a result of the spin-dependent interaction of the conduction electrons with the impurity spin, two bound states appear within the energy gap: one lies above the Fermi level (electron-like), while the other lies below the Fermi level (hole-like). These are the Yu-Shiba-Rusinov (YSR) states.

Chapter 9 describes our original research. There we generalize the s-wave quantum impurity approach by establishing a model for a general l-wave quantum impurity. We solve the system exactly in two extreme limits: (I) in the case of no Coulomb repulsion, $U = 0$, at finite energy gap Δ, and (II) in the limit of large energy gap, at arbitrary Coulomb energy $U \geq 0$. In case (I), the exact quasiparticle energy spectrum is qualitatively similar to the subgap energy spectrum derived from the classical spin model. This is an important result, for it shows that in the absence of Coulomb repulsion the quantum and classical models are equivalent (not in the sense of a Schrieffer-Wolff transformation, but rather in the sense of a non-linear mapping between the parameters of the Anderson+BCS model and the exchange energy J for the classical spin model. Such a mapping makes the value of the subgap energies identical in the $U = 0$ quantum and classical models.

The approximation developed in case (II) becomes an exact solution in the limit of infinite energy gap $(\Delta \to \infty)$. It leads to an effective Hamiltonian for YSR states that fully captures the results of the superconducting proximity effect, i.e. the tendency of impurity orbital states to form Cooper-pairs. The induced on-site Cooper pairing, combined with orbital degeneracy, allows Cooper pairs to be populated by as many as $2(2l + 1)$ electrons. The remarkable conclusion is that symmetries allow Cooper pairs to have total angular momentum higher than $\boldsymbol{J} = 0$, i.e. we find Cooper pairs in $\boldsymbol{S}$, $\boldsymbol{P}$, $\boldsymbol{D}, \cdots$ total orbital angular momenta. This is unlike the s-impurity cases, where only $\boldsymbol{S}$ impurities are allowed. Even though the quasiparticle picture breaks down when $U > 0$, we are still able to numerically find the eigenspectrum, revealing a rich spectrum.

In addition to considering impurity electrons that are in single l orbital, we also consider the case where impurities have access to more than one orbital, e.g. $l = 0, 1$. In this case, Cooper pairs arise from a mixture of s- and p-electrons. The availability of mixed orbital Cooper pairs opens the door to considering optical transitions. Indeed,

because photons carry angular momentum $l = 1$, absorption and emission events are subject to the selection rules $\Delta l = 1$. Since one-photon transitions permit only one-electron to undergo a transition, we are able to enumerate the selection rules that apply to the YSR states, $\boldsymbol{S} \leftrightarrow \boldsymbol{P}$, etc. We end chapter 9 with final remarks on the presence of one-photon optical transitions between YSR states, and enumerate the selection rules.

Chapter 7

Bardeen-Cooper-Schrieffer (BCS) theory of superconductivity

The theory of Bardeen-Cooper-Schrieffer (BCS) [265, 266, 267], proposes that a metal becomes superconductor because the conduction electrons pair in bound states. Of course, the repulsive Coulomb interaction between electrons normally prevents them from forming bound states, so the attractive potential is actually phonon-mediated.

The physical intuition is understood as follows [282]: at high temperatures the conduction electrons behave as a Fermi gas, and the lattice vibrations are quite important. As the temperature decreases so do the phonon thermal energies. Below a certain critical temperature T_c, the thermal fluctuations are so low that conduction electrons traveling through the lattice locally deform the lattice structure by attracting the positively charged ions of the lattice, thus creating an increase in the density of positive charges around the electron which, in turn, attracts nearby electrons. Effectively, the lattice-mediated interaction results in an attractive electron-electron potential.

In the ground state, the electrons in a metal form a Fermi gas of independent electrons. As was shown by Cooper, an attractive potential between electrons results in a state where it is energetically more favorable for electron to bind in pairs; this is referred to as the instability of the Fermi sea against electron pairing.

In Section 7.1, we discuss the instability of the Fermi sea against a small attractive electron-electron potential, and discuss its origin from the electron-phonon interactions. We are going to introduce the BCS Hamiltonian, and solve it through a Bogoliubov transformation. In Section 7.2, we introduce the method of the equa-

tion of motion to solve the energy spectrum and quasiparticle operators of the BCS Hamiltonian.

7.1 Introduction to the BCS theory

7.1.1 Instability of the Fermi sea

Let's first, think about the wavefunction for a Cooper pair between two electrons of momentum and spin states $(\boldsymbol{k}_1, \sigma_1)$ and $(\boldsymbol{k}_2, \sigma_2)$, where $\sigma_{1,2} = \left|\uparrow\right\rangle, \left|\downarrow\right\rangle$. In the lowest energy configuration, the kinetic energy of the pair vanishes, so that the internal dynamics is such that the two electrons have opposite momenta $\boldsymbol{k}_1 = -\boldsymbol{k}_2 \equiv \boldsymbol{k}$. The wave function is generally written as a product of the space wave function and spin wave functions as, [282]

$$
\begin{aligned}
\psi_0(\boldsymbol{r}_1, \boldsymbol{r}_2) &= \sum_{\boldsymbol{k}} g_{\boldsymbol{k}} e^{i\boldsymbol{k}\cdot\boldsymbol{r}_1} e^{-i\boldsymbol{k}\cdot\boldsymbol{r}_2} f(s_1, s_2) \\
&= \sum_{\boldsymbol{k}} g_{\boldsymbol{k}} \Big[\cos(\boldsymbol{k}\cdot(\boldsymbol{r}_1 - \boldsymbol{r}_2))(\left|\uparrow\downarrow\right\rangle - \left|\downarrow\uparrow\right\rangle) \\
&\qquad\qquad + i\sin(\boldsymbol{k}\cdot(\boldsymbol{r}_1 - \boldsymbol{r}_2))\{\left|\uparrow\downarrow\right\rangle + \left|\downarrow\uparrow\right\rangle, \left|\uparrow\uparrow\right\rangle, \left|\downarrow\downarrow\right\rangle\} \Big]
\end{aligned}
\tag{7.1}
$$

Based on the parity of the cosine, we expect it to lead to a lower energy wave function. Thus the ground states should be dominated by the cosine term,

$$
\psi_0(\boldsymbol{r}_1 - \boldsymbol{r}_2) = \sum_{\boldsymbol{k}} g_{\boldsymbol{k}} \cos(\boldsymbol{k}\cdot(\boldsymbol{r}_1 - \boldsymbol{r}_2))(\left|\uparrow\downarrow\right\rangle - \left|\downarrow\uparrow\right\rangle).
\tag{7.2}
$$

The Shrodinger equation for that system looks like

$$
\left(-\frac{\hbar^2}{2m}\boldsymbol{\nabla}_{\boldsymbol{r}_1}^2 - \frac{\hbar^2}{2m}\boldsymbol{\nabla}_{\boldsymbol{r}_2}^2 + V(\boldsymbol{r}_1, \boldsymbol{r}_2) \right) \psi_0 = E\psi_0
\tag{7.3}
$$

Plugging in the wave function Eq. (7.2), we get

$$
(E - 2\epsilon_{\boldsymbol{k}})g_{\boldsymbol{k}} = \sum_{\boldsymbol{k}'} g_{\boldsymbol{k}'} V_{\boldsymbol{k}\boldsymbol{k}'}
\tag{7.4}
$$

We introduce an ansatz for the attractive potential,

$$V_{\boldsymbol{k},\boldsymbol{k}'} = \begin{cases} -V & \text{if} \quad E_F < \epsilon_{k,k'} < \hbar\omega_c + E_F, \\ 0 & \text{otherwise,} \end{cases} \tag{7.5}$$

with $V > 0$. This ansatz is *ad hoc*, but will be justified later in Sec. 7.1.2, where we will discuss the origin of the attractive potential. For those momenta that fall within $k_F \pm \omega_c/v_F$, we have $g_{\boldsymbol{k}} = -V\sum_{\boldsymbol{k}'} g_{\boldsymbol{k}'}/(E - 2\epsilon_{\boldsymbol{k}})$, and by further summing of the momentum k, we obtain the condition,

$$\sum_{\boldsymbol{k}} g_{\boldsymbol{k}} = -V \sum_{\boldsymbol{k}} \frac{\sum_{\boldsymbol{k}'} g_{\boldsymbol{k}'}}{E - 2\epsilon_{\boldsymbol{k}}} \iff 1 = -V \sum_{\boldsymbol{k}} \frac{1}{E - 2\epsilon_{\boldsymbol{k}}} \tag{7.6}$$

By converting the sum into an integral over energies, we find that

$$\begin{aligned} \frac{1}{V} &= \frac{N_0}{2} \int_{E_F}^{E_F + \hbar\omega_c} \frac{d\epsilon_{\boldsymbol{k}}}{\epsilon_{\boldsymbol{k}} - E/2} \\ &= \frac{N_0}{2} \ln\left(\frac{2E_F + 2\hbar\omega_c - E}{2E_F - E}\right) \end{aligned} \tag{7.7}$$

where ρ_F is the density of states at the Fermi level. This above relation is solved for

$$E = 2E_F + \hbar\omega_c \left(1 - e^{2/\rho_F V}\right)^{-1} \tag{7.8}$$

Most conventional superconductors have $\rho_F V \lesssim 0.3$. In the small $\rho_F V$ limit, the exponential term dominates over 1, and leads to

$$E = 2E_F - 2\hbar\omega_c e^{-2/\rho_F V} < 2E_F \tag{7.9}$$

That relation indicates that the energy of the two paired electrons is lower than the energy of two unpaired electrons at E_F. Therefore, under the assumption of the potential made above, the Fermi sea is unstable and no longer the ground state [266]. The new ground state is a collection of paired electron states. It is interesting to note that the binding energy Eq. (7.9) is not analytic at $V = 0$, i.e. the formation of the Cooper pair can not be described using perturbation theory on the attractive interaction V.

7.1.2 Origin of attractive electron-electron interaction

In this section, we are going to look at the microscopic origin of the electron-electron potential used in Eq. (7.5). It includes two components: the screened Coulomb interaction and the electron-phonon interaction.

Coulomb interaction and Thomas-Fermi screening

The Coulomb interaction comes from the electron-photon interaction, which at the second order in perturbation theory, leads to the potential,

$$V(\boldsymbol{q}) = \frac{4\pi e^2}{q^2}. \tag{7.10}$$

This potential corresponds to the first diagram in Fig. 7.1. The divergence at $q = 0$ can be cured by considering corrections to the photon propagator. The corrections consist in the summation of an infinite series of electron loops, represented by the second and third Feynman diagrams of Fig. 7.1. One loop correction takes the form, $V(\boldsymbol{q})\Pi_{\boldsymbol{q}}V(\boldsymbol{q})$ and the infinite series,

$$\begin{aligned}
V_s(\boldsymbol{q}) =& V(\boldsymbol{q}) + V(\boldsymbol{q})\Pi_{\boldsymbol{q}}V(\boldsymbol{q}) + V(\boldsymbol{q})\Pi_{\boldsymbol{q}}V(\boldsymbol{q})\Pi_{\boldsymbol{q}}V(\boldsymbol{q}) \\
=& \frac{V(\boldsymbol{q})}{1 - \Pi_{\boldsymbol{q}}V(\boldsymbol{q})} \\
=& \frac{4\pi e^2}{q^2 + k_s^2},
\end{aligned} \tag{7.11}$$

where the momentum k_s defined as, $k_s^2 \equiv -q^2\Pi_{\boldsymbol{q}}V(\boldsymbol{q})$, defines a screening length for the Coulomb interaction. In the long-wavelength limit $|\boldsymbol{q}| \ll |\boldsymbol{l}|$, the screening parameter takes the form [283, 284]

$$k_s^2 = \frac{3e^2 N}{2V\kappa E_F}, \tag{7.12}$$

where κ is the dielectric constant of the material. This is known as the Thomas-Fermi screening. The screened potential remains positive for all values of the momentum, and cannot convey an attractive electron-electron force.
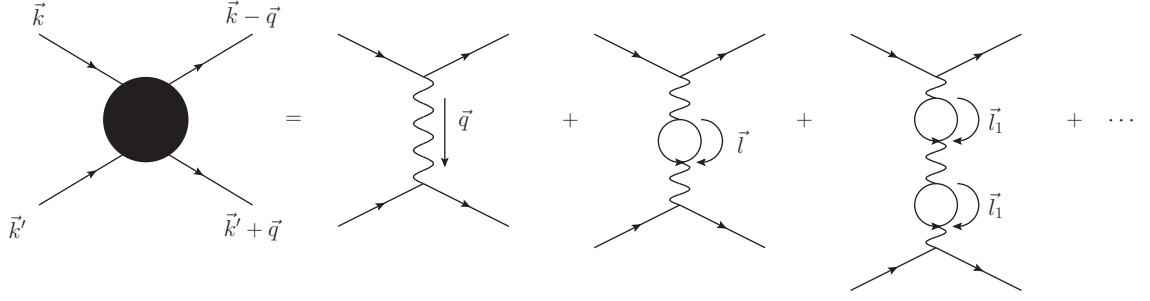
Figure 7.1: Series representing the corrections the electron-electron Coulomb interaction, leading to the Thomas-Fermi screening. The first diagram on the right hand side is the bare Coulomb repulsion, and the subsequent terms in the series are the corrections to the photon propagator.

Electron-phonon interaction

The study of the critical temperature of different superconducting materials lead to the relation between the critical temperature T_c and the isotopic mass M,

$$\sqrt{M}T_c = \text{constant.} \tag{7.13}$$

This is known as the isotopic effect. Frohlich used this results to infer the lattice host plays a role in superconductivity through the lattice phonons [285]. The electron-phonon interactions are captured in the Hamiltonian,

$$H_{e-ph} = i \sum_{k,q} D_q c_{k+q}^\dagger c_k \left(a_q - a_{-q}^\dagger \right), \tag{7.14}$$

where D_q is the strength of the electron-phonon coupling.

The effect of the electron-phonon interaction on the electron-electron interaction is represented by the Feynman diagram in Fig. 7.2 whose contribution is,

$$V_{e-e}^{e-ph} = \sum_q |D_q|^2 \frac{2\hbar\omega_q}{(\epsilon_{\boldsymbol{k}} - \epsilon_{\boldsymbol{k-q}})^2 - (\hbar\omega_q)^2}, \tag{7.15}$$

where $\epsilon_{\boldsymbol{k}}$ and $\epsilon_{\boldsymbol{k-q}}$ are the external electron energies, and $\hbar\omega_q$ is the phonon mediator energy. Evidently, the phonon potential is negative for energies $|\epsilon_k - \epsilon_{\boldsymbol{k-q}}| < \hbar\omega_q$. The maximum phonon energy is set by the Debye frequency, $\omega_q < \omega_D$, which therefore is also the cutoff for the negative potential, hence when $|\epsilon_k - \epsilon_{\boldsymbol{k-q}}|$ is larger than that cutoff Debye energy there will be no Cooper-pair binding. The screened Coulomb
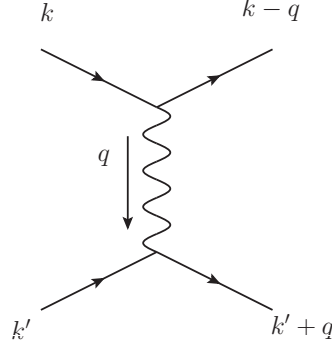
Figure 7.2: Feynman diagram representing the electron-electron *attraction* mediated by the electron-phonon interaction. When this attraction is stronger than the screened Coulomb repulsion the electrons are able to bind forming Cooper pairs.

interaction remains positive, but for strong enough electron-phonon coupling D_q, the negative interaction becomes dominant.

This motivates the approximation of the BCS pairing energy as follows,

$$V_{e-e} = \begin{cases} -V & \text{if} \quad |\epsilon_k - E_F|, |\epsilon_{k-q} - E_F| < \hbar\omega_c, \\ 0 & \text{otherwise}, \end{cases} \tag{7.16}$$

where $V > 0$.

7.1.3 Quasiparticle operators: the Bogoliubov transformation

In the second quantization and grand-canonical formalism, this attractive potential leads to the Hamiltonian

$$\mathcal{H} = \sum_{ks} \xi_k n_{ks} + \sum_{kl} V_{kl} c_{l\uparrow}^\dagger c_{-l\downarrow}^\dagger c_{-k\downarrow} c_{k\uparrow}, \tag{7.17}$$

where $\xi_k = \epsilon_k - E_F$. The first terms gives the kinetic energy of the individual pairs, while the second gives the potential energy between pairs. Indeed, you can see that the second term destroys $-k \downarrow, k \uparrow$ and creates $-l \downarrow, l \uparrow$.

Being quartic in the electron operators means this Hamiltonian cannot be solved exactly analytically. Instead, we resort to the mean-field approximation. We first

define a fluctuation operators $d_{\boldsymbol{k}}$ that measures the deviations, [286]

$$d_{\boldsymbol{k}} = c_{\boldsymbol{k}\downarrow} c_{-\boldsymbol{k}\uparrow} - \langle c_{\boldsymbol{k}\downarrow} c_{-\boldsymbol{k}\uparrow} \rangle. \tag{7.18}$$

The expectation value $\langle c_{\boldsymbol{k}\downarrow} c_{-\boldsymbol{k}\uparrow} \rangle$ vanishes in the normal state, because the normal state conserves the number of particles. In terms of this operator, $\mathcal{H}$ takes the form,

$$\mathcal{H} = \sum_{\boldsymbol{k}\sigma} \xi_k c_{\boldsymbol{k}\sigma}^\dagger c_{\boldsymbol{k}\sigma} + \sum_{\boldsymbol{k}\boldsymbol{l}} V_{\boldsymbol{k}\boldsymbol{l}} \left[d_{\boldsymbol{l}}^\dagger d_{\boldsymbol{k}} + d_{\boldsymbol{k}} \left\langle c_{\boldsymbol{l}\uparrow}^\dagger c_{-\boldsymbol{l}\downarrow}^\dagger \right\rangle + d_{\boldsymbol{l}}^\dagger \langle c_{-\boldsymbol{k}\downarrow} c_{\boldsymbol{k}\uparrow} \rangle + \left\langle c_{\boldsymbol{l}\uparrow}^\dagger c_{-\boldsymbol{l}\downarrow}^\dagger \right\rangle \langle c_{-\boldsymbol{k}\downarrow} c_{\boldsymbol{k}\uparrow} \rangle \right]. \tag{7.19}$$

The mean-field approximation consists of ignoring terms at the second order in the fluctuation operator, i.e. $d_{\boldsymbol{l}}^\dagger d_{\boldsymbol{k}}$. By defining the energy parameter,

$$\Delta_{\boldsymbol{k}} = - \sum_{\boldsymbol{l}} V_{\boldsymbol{k}\boldsymbol{l}} \langle c_{-\boldsymbol{k}\downarrow} c_{\boldsymbol{k}\uparrow} \rangle, \tag{7.20}$$

we find the mean-field approximation of the Hamiltonian,

$$\mathcal{H}_{\text{BCS}} = \sum_{\boldsymbol{k}\sigma} \xi_k c_{\boldsymbol{k}\sigma}^\dagger c_{\boldsymbol{k}\sigma} - \sum_{\boldsymbol{k}} \left[\Delta_{\boldsymbol{k}}^* c_{\boldsymbol{k}\uparrow}^\dagger c_{-\boldsymbol{k}\downarrow}^\dagger + \Delta_{\boldsymbol{k}} c_{-\boldsymbol{k}\downarrow} c_{\boldsymbol{k}\uparrow} \right] + \sum_{\boldsymbol{k}} b_{\boldsymbol{k}} \Delta_{\boldsymbol{k}} \tag{7.21}$$

This is the Bardeen-Cooper-Schrieffer (BCS) Hamiltonian. The last term, $\sum_{\boldsymbol{k}} b_{\boldsymbol{k}} \Delta_{\boldsymbol{k}}$, is a constant, it is possible to remove it by offsetting the Hamiltonian by an overall constant. H_{BCS} can be diagonalized by the use of two quasi-particle operators $\gamma_{\boldsymbol{k}0}$ and $\gamma_{\boldsymbol{k}1}$, which are related to the c operators through the unitary transformation,

$$\begin{pmatrix} c_{\boldsymbol{k}\uparrow} \\ c_{-\boldsymbol{k}\downarrow}^\dagger \end{pmatrix} = \begin{pmatrix} u_{\boldsymbol{k}}^* & v_{\boldsymbol{k}} \\ -v_{\boldsymbol{k}}^* & u_{\boldsymbol{k}} \end{pmatrix} \begin{pmatrix} \gamma_{\boldsymbol{k}0} \\ \gamma_{\boldsymbol{k}1}^\dagger \end{pmatrix}, \tag{7.22}$$

with the condition $|u_{\boldsymbol{k}}|^2 + |v_{\boldsymbol{k}}|^2 = 1$. This transformation is called the Bogoliubov transformation, and the γ operators are the Bogoliubov operators. Inversely,

$$\begin{pmatrix} \gamma_{\boldsymbol{k}0} \\ \gamma_{\boldsymbol{k}1}^\dagger \end{pmatrix} = \begin{pmatrix} u_{\boldsymbol{k}} & -v_{\boldsymbol{k}} \\ v_{\boldsymbol{k}}^* & u_{\boldsymbol{k}}^* \end{pmatrix} \begin{pmatrix} c_{\boldsymbol{k}\uparrow} \\ c_{-\boldsymbol{k}\downarrow}^\dagger \end{pmatrix}, \tag{7.23}$$

The operator $\gamma_{\boldsymbol{k}0}^\dagger$ either creates a spin down with probability $|u_{\boldsymbol{k}}|^2$, or annihilates a spin up with probability $|v_{\boldsymbol{k}}|^2$. Both have the same net effect of decreasing the spin by $1/2$, and vice versa for $\gamma_{\boldsymbol{k}1}$.
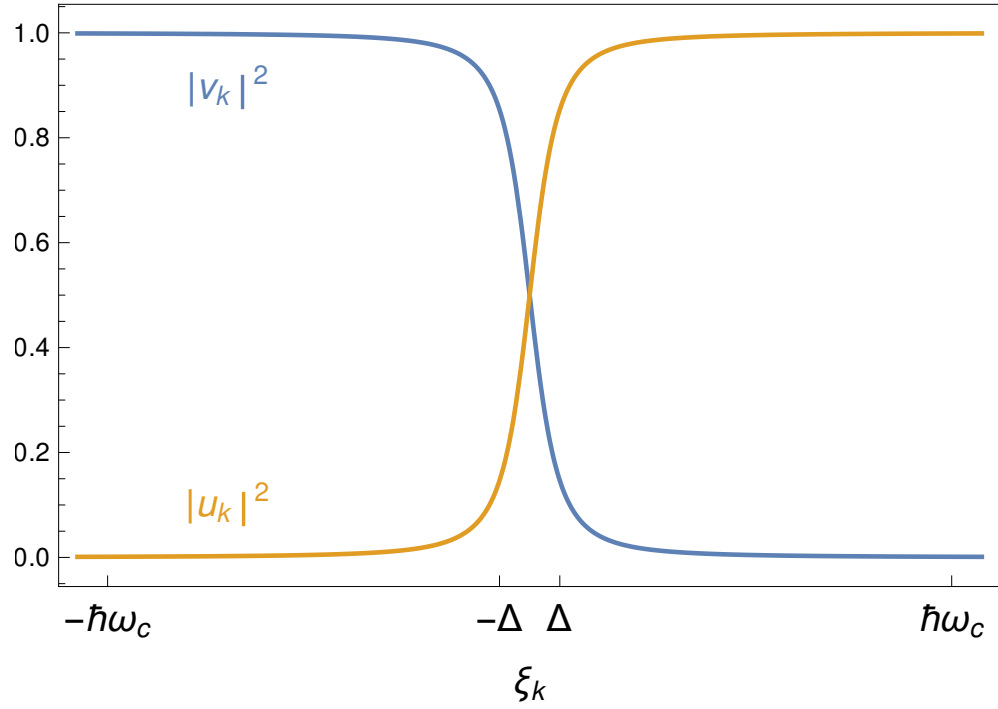
Figure 7.3: Coefficients of the Bogoliubov transformation, $|u_k|^2$ and $|v_k|^2$, where we used $\hbar\omega_c \sim 20|\Delta|$.

Inserting this basis change into $\mathcal{H}_{\mathrm{BCS}}$ results in the diagonal form of the BCS Hamiltonian,

$$\mathcal{H}_{\mathrm{BCS}} = \sum_{\boldsymbol{k}} E_{\boldsymbol{k}} \left(\gamma_{\boldsymbol{k}0}^\dagger \gamma_{\boldsymbol{k}0} + \gamma_{\boldsymbol{k}1}^\dagger \gamma_{\boldsymbol{k}1} \right) + \sum_{\boldsymbol{k}} \left(\xi_{\boldsymbol{k}} - E_{\boldsymbol{k}} \right), \tag{7.24}$$

with the quasi-particle energies $E_k^2 = \xi_{\boldsymbol{k}}^2 + \Delta_{\boldsymbol{k}}^2$. Imposing that non-diagonal terms such as $\gamma_0 \gamma_1$ vanish leads to the constraints,

$$2\xi_{\boldsymbol{k}} + \Delta_{\boldsymbol{k}}^* v_{\boldsymbol{k}}^2 - \Delta_{\boldsymbol{k}} u_{\boldsymbol{k}}^2 = 0, \quad |v_{\boldsymbol{k}}|^2 = \frac{|u_{\boldsymbol{k}}|^2}{|\Delta_{\boldsymbol{k}}|^2} \left(E_{\boldsymbol{k}} - \xi_{\boldsymbol{k}} \right)^2, \tag{7.25}$$

which are satisfied by the solutions,

$$|v_{\boldsymbol{k}}|^2 = \frac{1}{2} \left(1 - \frac{\xi_{\boldsymbol{k}}}{E_{\boldsymbol{k}}} \right), \quad |u_{\boldsymbol{k}}|^2 = \frac{1}{2} \left(1 + \frac{\xi_{\boldsymbol{k}}}{E_{\boldsymbol{k}}} \right). \tag{7.26}$$

The terms $\gamma_{\boldsymbol{k}0}^\dagger \gamma_{\boldsymbol{k}0} + \gamma_{\boldsymbol{k}1}^\dagger \gamma_{\boldsymbol{k}1}$ correspond to the energy of quasiparticle excitations. The ground state is defined as the state with no quasiparticle excited, i.e. $\gamma_{\boldsymbol{k}0}|\mathrm{GS}\rangle =$
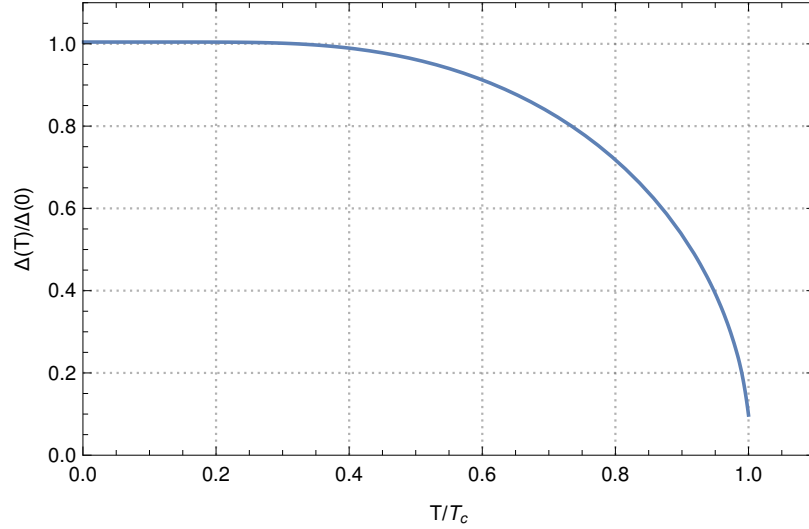
Figure 7.4: Temperature dependence of the BCS energy gap, as the numerical solution to the BCS energy gap self-consistent equation

$\gamma_{\boldsymbol{k}1}|\text{GS}\rangle = 0$ for all $\boldsymbol{k}$. The ground state energy is,

$$E_{\text{GS}} = \sum_{\boldsymbol{k}} \left(\xi_{\boldsymbol{k}} - E_{\boldsymbol{k}} \right), \tag{7.27}$$

and the solution for the ground state wave function, $\prod_{\boldsymbol{k}} \gamma_{\boldsymbol{k}0}\gamma_{\boldsymbol{k}1}|0\rangle = |\text{GS}\rangle$, which is,

$$|\text{GS}\rangle = \prod_{\boldsymbol{k}} \left(u_{\boldsymbol{k}} + v_{\boldsymbol{k}} c_{\boldsymbol{k}\uparrow}^{\dagger} c_{-\boldsymbol{k}\downarrow}^{\dagger} \right) |0\rangle. \tag{7.28}$$

7.1.4 Energy gap self-consistent equation

Using the result of the Bogoliubov transformation, we can solve the equation of the gap energy,

$$\Delta_{\boldsymbol{k}} = -\sum_{l} V_{\boldsymbol{k}l} \langle c_{-l\downarrow} c_{l\uparrow} \rangle = \sum_{l} V_{\boldsymbol{k}l} v_l u_l^* \left\langle 1 - \gamma_{l0}^{\dagger} \gamma_{l0} - \gamma_{l1}^{\dagger} \gamma_{l1} \right\rangle \tag{7.29}$$

Averages of cross terms like $\langle \gamma\gamma \rangle$ vanish. The quasi-particle operators $\gamma_{\boldsymbol{k}0}, \gamma_{\boldsymbol{k}1}$ are both associated with the same energy E_k, and are both equivalent to adding or removing one electron. Therefore, they obey the Fermi-Dirac statistics,

$$\left\langle \gamma_{\boldsymbol{k}0}^{\dagger} \gamma_{\boldsymbol{k}0} \right\rangle = \left\langle \gamma_{\boldsymbol{k}1}^{\dagger} \gamma_{\boldsymbol{k}1} \right\rangle = f(E_{\boldsymbol{k}}) = \left(1 + e^{\beta E_{\boldsymbol{k}}} \right)^{-1}, \tag{7.30}$$

where $\beta = 1/k_B T$. The gap energy self-consistent equation reads,

$$\Delta_{\boldsymbol{k}} = -\sum_l V_{\boldsymbol{kl}} v_l u_l^* \left(1 - 2\left\langle \gamma_l^\dagger \gamma_l \right\rangle\right)$$
$$= -\sum_l V_{\boldsymbol{kl}} \frac{\Delta_l}{2E_l} \tanh\left(\beta \frac{E_l}{2}\right) \tag{7.31}$$

using the BCS approximation, $V_{\boldsymbol{kl}} = -V$ and $\Delta_l = \Delta$, in such way that we find

$$\frac{1}{V} = \frac{1}{2}\sum_l \frac{\tanh\left(\frac{\beta}{2}E_l\right)}{E_l}, \tag{7.32}$$

Going to the continuum limit, and integrating, we find

$$\frac{1}{\rho_F V} = \int_0^{\hbar\omega_c} d\xi_{\boldsymbol{k}} \frac{\tanh\left(\frac{\beta}{2}\sqrt{\xi_{\boldsymbol{k}}^2 + \Delta^2}\right)}{\sqrt{\xi_{\boldsymbol{k}}^2 + \Delta^2}}, \tag{7.33}$$

We introduce the following variables,

$$x = \beta_c \xi, \quad \delta = \frac{\Delta(T)}{\Delta(0)}, \quad y = \frac{\beta}{\beta_c}, \quad \beta_c = \frac{1}{kT_c} \tag{7.34}$$

We note that the factor $\beta_c \Delta_0$ can be determined experimentally, and for weakly coupled superconductors typically takes the value $\beta_c \Delta_0 \approx 1.764$. The calculation of the critical temperature can be done by solving the above equation at $T = T_c$ where $\Delta(T_c) = 0$, and gives $\beta_c \hbar\omega_c = e^{1/N_0 V}/1.13$. A numerical solution is plotted in Fig. 7.4, where we have used typical values $\rho_F V \approx 0.3$. Numerically, we have the relationship $\hbar\omega_c \simeq 14\Delta(0)$.

7.2 Introduction to the equation of motion approach

The equation of motion method is well known to calculate dynamical quantities, such as Green's functions and other correlation functions. It is based on the Heisenberg equation of motion for operators. The Heisenberg equation of motion gives the time derivative $\dot{A}(t)$ of an operator $A(t)$ as the commutator with the Hamiltonian, $\dot{A}(t) = -i\left[A(t), H\right]/\hbar$.

In the following, we are going to use this equation to derive the Green's functions for electrons in a superconductors. Then, we will apply this method to finding the solution of the electron operators themselves. The technique will prove to be equivalent to the Bogoliubov transformation.

7.2.1 Normal and anomalous BCS Green's functions

First, we rewrite the pairing Hamiltonian as a sum over the momenta and spin degrees of freedom,

$$H_{\text{BCS}} = \sum_{\boldsymbol{k}} \sum_{\sigma} \left[\xi_{\boldsymbol{k}} c_{\boldsymbol{k}\sigma}^{\dagger} c_{\boldsymbol{k}\sigma} - \Delta\sigma \left(c_{\boldsymbol{k}s}^{\dagger} c_{-\boldsymbol{k}-\sigma}^{\dagger} + c_{-\boldsymbol{k}-\sigma} c_{\boldsymbol{k}\sigma} \right) \right] \tag{7.35}$$

where the spin degree of freedom is $\sigma = \pm 1/2$. The Heisenberg equation of motion for the conduction electrons lead to the equation,

$$\begin{aligned}
\dot{c}_{\boldsymbol{k}\sigma}(t) &= -\frac{i\epsilon_k}{\hbar} c_{\boldsymbol{k}\sigma}(t) - 2\sigma \frac{i\Delta}{\hbar} c_{-\boldsymbol{k}-\sigma}^{\dagger}(t), \\
\dot{c}_{-\boldsymbol{k}-\sigma}^{\dagger}(t) &= \frac{i\epsilon_k}{\hbar} c_{-\boldsymbol{k}-\sigma}^{\dagger}(t) - 2\sigma \frac{i\Delta^*}{\hbar} c_{\boldsymbol{k}\sigma}(t).
\end{aligned} \tag{7.36}$$

The second equation is obtained from the first equation by flipping the momentum and spin variables, and taking the complex conjugation. In fact, the second equation is the particle-hole transformed of the first.

The *normal* retarded Green's function for electrons, $G_{\boldsymbol{k}\sigma}^{R}(t)$, is defined according to the usual definition,

$$G_{\boldsymbol{k}\sigma}^{R}(t) = -i\theta(t) \left\langle \left\{ c_{\boldsymbol{k}\sigma}(t), c_{\boldsymbol{k}\sigma}^{\dagger}(0) \right\} \right\rangle. \tag{7.37}$$

We can calculate this function by taking its time derivative, and making use of the system of equation of motion, Eq. (7.36), we find,

$$\dot{G}_{\boldsymbol{k}\sigma}^{R}(t) = -i\delta(t) \left\langle \left\{ c_{\boldsymbol{k}\sigma}(0), c_{\boldsymbol{k}\sigma}^{\dagger}(0) \right\} \right\rangle - \frac{i\xi_k}{\hbar} G_{\boldsymbol{k}\sigma}^{R}(t) - 2\sigma \frac{i\Delta}{\hbar} F_{\boldsymbol{k}\sigma}^{R}(t). \tag{7.38}$$

where the delta function comes from the time derivative of the Heaviside function, $\dot{\theta}(t) = \delta(t)$, and the canonical commutation relation among electron operators gives,

$\left\{ c_{\boldsymbol{k}\sigma}(0), c_{\boldsymbol{k}\sigma}^{\dagger}(0) \right\} = 1$. Here, we defined a novel Green's function,

$$F_{\boldsymbol{k}\sigma}^{R}(t) = -i\theta(t)\left\langle \left\{ c_{-\boldsymbol{k}-\sigma}^{\dagger}(t), c_{\boldsymbol{k}\sigma}^{\dagger}(0) \right\} \right\rangle. \tag{7.39}$$

This function correlates an electron in state $\{\boldsymbol{k}, \sigma\}$ at time $t = 0$ to a hole in state $\{-\boldsymbol{k}, -\sigma\}$ at time t. This correlation exists as a consequence of the electron-electron pairing mechanism, $\Delta c_{\boldsymbol{k}\sigma}^{\dagger} c_{-\boldsymbol{k}-\sigma}^{\dagger}$. The function $F_{\boldsymbol{k}\sigma}^{R}(t)$ is called the *anomalous* Green's function because it only arises in superconducting systems and vanishes otherwise, unlike the *normal* Green's function, $G_{\boldsymbol{k}\sigma}^{R}(t)$ [286].

In order to close the system of equations for the Green's function, we also write down the equation of motion for the anomalous Green's function, which makes use of the bottom equation in Eq. (7.36). We find,

$$\dot{F}_{\boldsymbol{k}\sigma}^{R}(t) = -i\delta(t)\left\langle \left\{ c_{-\boldsymbol{k}-\sigma}^{\dagger}(0), c_{\boldsymbol{k}\sigma}^{\dagger}(0) \right\} \right\rangle + \frac{i\xi_k}{\hbar}F_{\boldsymbol{k}\sigma}^{R}(t) - 2\sigma\frac{i\Delta^*}{\hbar}G_{\boldsymbol{k}\sigma}^{R}(t). \tag{7.40}$$

The canonical commutation relations impose $\left\{ c_{-\boldsymbol{k}-\sigma}^{\dagger}(0), c_{\boldsymbol{k}\sigma}^{\dagger}(0) \right\} = 0$. The system of equations $\{\dot{G}_{\boldsymbol{k}\sigma}^{R}(t), \dot{F}_{\boldsymbol{k}\sigma}^{R}(t)\}$ is solved by going to Fourier space, $t \to \omega$, where the system takes the form,

$$\begin{aligned}
(\hbar\omega - \xi_k)G_{\boldsymbol{k}\sigma}^{R}(\omega) &= \hbar + 2\sigma\Delta F_{\boldsymbol{k}\sigma}^{R}(\omega), \\
(\hbar\omega + \xi_k)F_{\boldsymbol{k}\sigma}^{R}(\omega) &= 2\sigma\Delta^* G_{\boldsymbol{k}\sigma}^{R}(\omega).
\end{aligned} \tag{7.41}$$

In order to avoid the poles in frequency space, $\hbar\omega = \pm\xi_k$, we analytically continue the frequencies in the complex plane $\omega \to \omega + i\eta$ with $\eta \to 0^+$. It is possible to perform this continuation because the Green's function are retarded and have a definite time ordering, $t > 0$. Had the function been advanced, the continuation would have been in the lower complex plane.

We can solve this system by multiplying the first equation by $(\hbar\omega + \xi_k)$ and using inserting the bottom equation. We find,

$$\left[(\hbar\omega + i\eta)^2 - \xi_k^2 \right] G_{\boldsymbol{k}\sigma}^{R}(\omega + i\eta) = \hbar(\hbar\omega + \xi_k + i\eta) + |\Delta|^2 G_{\boldsymbol{k}\sigma}^{R}(\omega + i\eta), \tag{7.42}$$

Giving the solution,

$$G_{\boldsymbol{k}\sigma}^{R}(\omega + i\eta) = \hbar\frac{\hbar\omega + \xi_k + i\eta}{(\hbar\omega + i\eta)^2 - E_k^2}, \tag{7.43}$$

with the quasiparticle energies, $E_k^2 = \xi_k^2 + |\Delta|^2$. The Green's function has two poles,
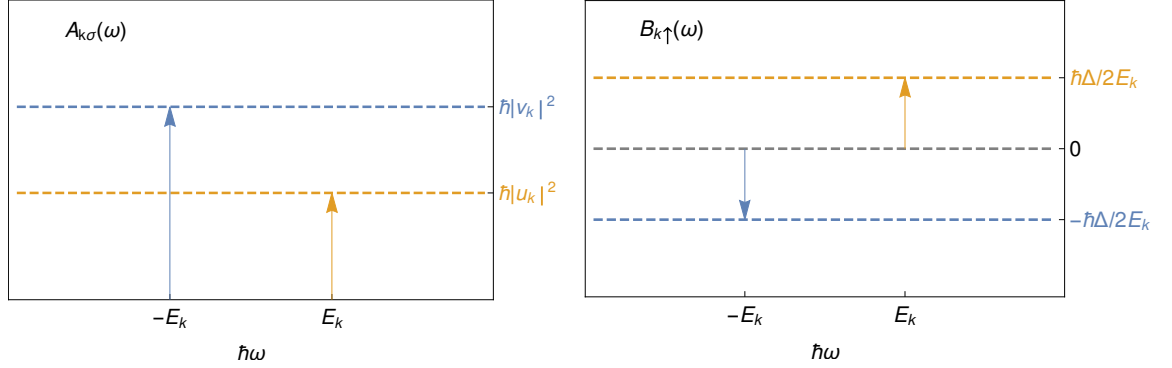
Figure 7.5: Normal (left) and anomalous (right) Green's function for BCS. The positive (negative) pole represents the particle(hole)-like excitation.

$\hbar\omega = \pm E_k$, corresponding to two quasiparticle energies. The spectral density of electrons at those poles is given by the imaginary part of the normal Green's function, $\mathcal{A}_{k\sigma}(\omega)$, as

$$
\begin{aligned}
\mathcal{A}_{k\sigma}(\omega) =& -\frac{1}{\pi}\mathrm{Im}\left\{G^R_{k\sigma}(\omega + i\eta)\right\} \\
=& \hbar\left[\frac{E_k + \xi_k}{2E_k}\delta(\hbar\omega - E_k) + \frac{E_k - \xi_k}{2E_k}\delta(\hbar\omega + E_k)\right].
\end{aligned}
\tag{7.44}
$$

Thus, we find that the two poles $\hbar\omega = \pm E_k$ has positive spectral weight $(E_k \pm \xi_k)/2E_k$ respectively, and are electron-like and hole-like respectively.

According to the top equation in Eq. (7.41), the anomalous Green's function is obtained as,

$$
\begin{aligned}
F^R_{k\sigma}(\omega + i\eta) =& 2\sigma\frac{i\hbar}{\Delta}\left[(\hbar\omega - \xi_k + i\eta)G^R_{k\sigma}(\omega) - \hbar\right] \\
=& \hbar\frac{2\sigma\Delta^*}{(\hbar\omega + i\eta)^2 - E_k^2}.
\end{aligned}
\tag{7.45}
$$

The anomalous spectral function is then expressed as,

$$
\begin{aligned}
\mathcal{B}_{k\sigma}(\omega) =& -\frac{1}{\pi}\mathrm{Im}\left\{F^R_{k\sigma}(\omega + i\eta)\right\} \\
=& 2\sigma\hbar\frac{\Delta^*}{2E_k}\left[\delta(\hbar\omega - E_k) - \delta(\hbar\omega + E_k)\right].
\end{aligned}
\tag{7.46}
$$

The anomalous and normal retarded Green's functions are plotted in Fig. 7.5.

7.2.2 Alternative to the Bogoliubov transformation

Unlike in the previous section, where the Bogoliubov transformations were introduced *ad hoc*, in this section, we are going to show a method which derives that transformation. The method relies on the Heisenberg equation of motion. This method is a convenient algorithm, easily applicable to more complicated problems, for that reason this method will be extensively used throughout the thesis.

The Heisenberg equation of motion for the conduction electrons, Eq. (7.36), is transformed into the Fourier space,

$$
\begin{aligned}
(\hbar\omega - \xi_k) \, c_{\boldsymbol{k}\sigma}(\omega) &= 2\sigma\Delta c^\dagger_{-\boldsymbol{k}-\sigma}(-\omega), \\
(\hbar\omega + \xi_k) \, c^\dagger_{-\boldsymbol{k}-\sigma}(-\omega) &= 2\sigma\Delta^* c_{\boldsymbol{k}\sigma}(\omega)
\end{aligned}
\tag{7.47}
$$

Multiplying the first equation by $\hbar\omega + \xi_k$, and using the second equation, one readily finds

$$
(\hbar\omega + \xi_{\boldsymbol{k}}) \, (\hbar\omega - \xi_{\boldsymbol{k}}) \, c_{\boldsymbol{k}\sigma}(\omega) = |\Delta|^2 c_{\boldsymbol{k}\sigma}(\omega) \quad \Longrightarrow \quad \left[(\hbar\omega)^2 - E_k^2\right] c_{\boldsymbol{k}\sigma}(\omega) = 0, \tag{7.48}
$$

Where the energy $E_k = \sqrt{|\Delta|^2 + \xi_k^2}$. It is not possible to analytically continue frequencies $\omega \to \omega + i0^+$ because the operators are not time-ordered. We make use of the property that the solution of an equation of the sort $xf(x) = 0$ is of the form $f(x) \propto \delta(x)$. Here, the argument of the delta function has two zeros at $\pm E_p$, leading to the solution of the conduction electron operator in the form,

$$
c_{\boldsymbol{k}\sigma}(\omega) = \sum_{\alpha} \kappa^\alpha_{\boldsymbol{k}\sigma} \delta\left(\hbar\omega - \alpha E_k\right), \tag{7.49}
$$

where $\alpha = \pm$ and the two operators $\kappa^\pm$ are so far undetermined. The time-reversed electron operator $c^\dagger_{-\boldsymbol{k}-\sigma}(-\omega)$ can be obtained in two ways. First, by time-reversing the above solution for $c_{\boldsymbol{k}\sigma}(\omega)$ leading,

$$
\begin{aligned}
c^\dagger_{-\boldsymbol{k}-\sigma}(-\omega) &= \sum_{\alpha} \left(\kappa^\alpha_{-\boldsymbol{k}-\sigma}\right)^\dagger \delta\left(\hbar\omega + \alpha E_k\right) \\
&= \sum_{\alpha} \left(\kappa^{-\alpha}_{-\boldsymbol{k}-\sigma}\right)^\dagger \delta\left(\hbar\omega - \alpha E_k\right),
\end{aligned}
\tag{7.50}
$$

where we flipped the sign $\alpha \to -\alpha$ to obtain the second line. Second, by virtue the

top equation in Eq. (7.36), i.e. $c^\dagger_{-\boldsymbol{k}-\sigma}(-\omega) = (\hbar\omega - \xi_k)\, c_{\boldsymbol{k}\sigma}(\omega)/(2\sigma\Delta)$, we get

$$c^\dagger_{-\boldsymbol{k}-\sigma}(-\omega) = \sum_\alpha 2\sigma \frac{\alpha E_k - \xi_k}{\Delta} \kappa^\alpha_{\boldsymbol{k}\sigma} \delta\left(\hbar\omega - \alpha E_k\right). \tag{7.51}$$

By equating the two solutions, Eq. (7.50) and Eq. (7.51), we find the relation among the κ operators as,

$$\left(\kappa^{-\alpha}_{-\boldsymbol{k}-\sigma}\right)^\dagger = 2\sigma \frac{\alpha E_k - \xi_k}{\Delta} \kappa^\alpha_{\boldsymbol{k}\sigma}. \tag{7.52}$$

This relation proves that the two $\kappa^\pm$ are redundant, and therefore not entirely physical. We decide to eliminate κ^- in preference for κ^+,

$$\kappa^-_{\boldsymbol{k}\sigma} = -2\sigma \frac{E_k - \xi_k}{\Delta^*} \left(\kappa^+_{-\boldsymbol{k}-\sigma}\right)^\dagger. \tag{7.53}$$

The conduction electron operator in real time is obtained by integrating the solution $c_{\boldsymbol{k}\sigma}(\omega)$. In particular, at $t = 0$, we find,

$$\begin{aligned}
c_{\boldsymbol{k}\sigma}(0) &= \int \frac{d\omega}{2\pi} c_{\boldsymbol{k}\sigma}(\omega) \\
&= \frac{1}{2\pi\hbar}\left[\kappa^+_{\boldsymbol{k}\sigma} + \kappa^-_{\boldsymbol{k}\sigma}\right] \\
&= \frac{1}{2\pi\hbar}\left[\kappa^+_{\boldsymbol{k}\sigma} - 2\sigma \frac{E_k - \xi_k}{\Delta^*}\left(\kappa^+_{-\boldsymbol{k}-\sigma}\right)^\dagger\right].
\end{aligned} \tag{7.54}$$

The operators $\kappa^+_{\boldsymbol{k}\sigma}$ are not yet the physical operators, because they do not satisfy canonical commutation relations. We define new operators $\gamma_{\boldsymbol{k}\sigma}$ as $\kappa^+_{\boldsymbol{k}\sigma} = 2\pi\hbar u_{\boldsymbol{k}}\, \gamma_{\boldsymbol{k}\sigma}$ such that the conduction electron operator can finally be expressed in terms of the physical $\gamma_{\boldsymbol{k}\sigma}$ operators,

$$c_{\boldsymbol{k}\sigma}(0) = u_{\boldsymbol{k}}\gamma_{\boldsymbol{k}\sigma} - 2\sigma \frac{\Delta}{|\Delta|} v_{\boldsymbol{k}}\gamma^\dagger_{-\boldsymbol{k}-\sigma}, \tag{7.55}$$

where,

$$v_{\boldsymbol{k}} = \frac{E_k - \xi_k}{|\Delta|} u_{\boldsymbol{k}} \tag{7.56}$$

The conduction electron operators satisfy the canonical anticommutation relations, $\left\{c_{\boldsymbol{k}\sigma}, c^\dagger_{\boldsymbol{k}'\sigma'}\right\} = \delta_{\boldsymbol{k}\boldsymbol{k}'}\delta_{\sigma\sigma'}$. By further imposing that the new operators also satisfy
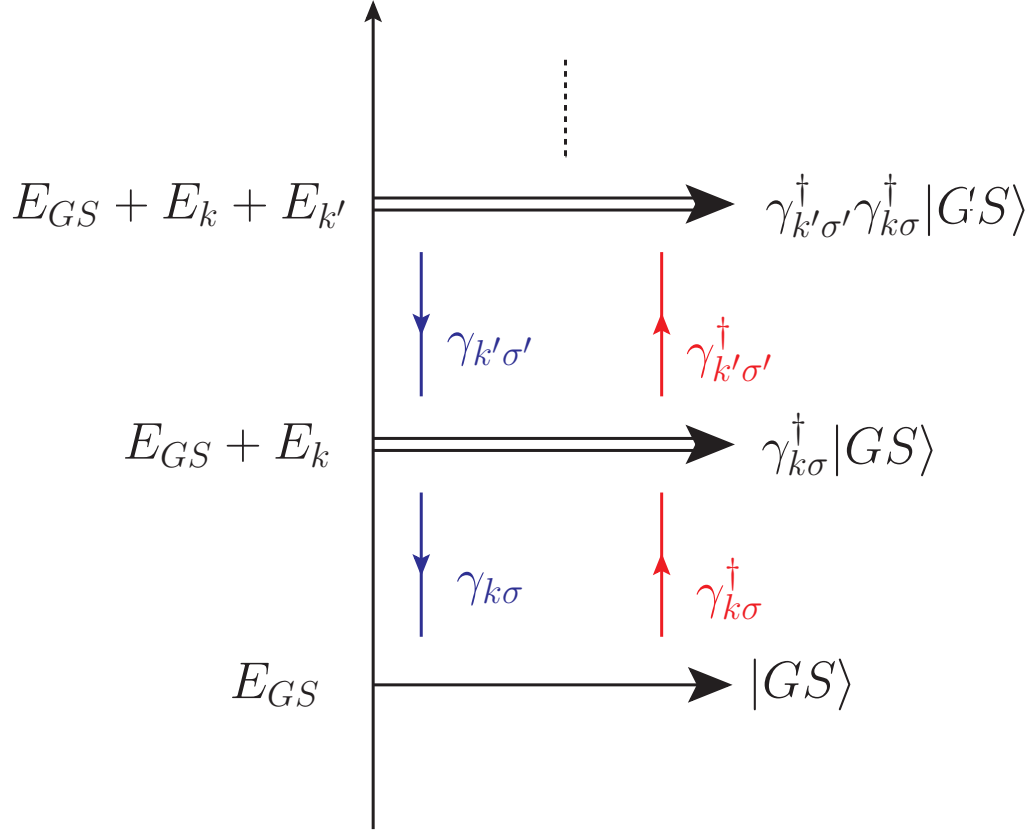
Figure 7.6: Energy spectrum of the BCS theory. The ground state contains no quasiparticle, and the operators $\gamma_{ks\sigma}^{\dagger}$ add into the vacuum state quasiparticles of energy E_k.

canonical commutation relations, $\left\{ \gamma_{\boldsymbol{k}\sigma}, \gamma_{\boldsymbol{k}'\sigma'}^{\dagger} \right\} = \delta_{\boldsymbol{k}\boldsymbol{k}'}\delta_{\sigma\sigma'}$, then we obtain,

$$|u_{\boldsymbol{k}}|^2 = \frac{1}{2}\left(1 + \frac{\xi_k}{E_k}\right), \quad |v_{\boldsymbol{k}}|^2 = \frac{1}{2}\left(1 - \frac{\xi_k}{E_k}\right). \tag{7.57}$$

These coefficients satisfy $|u_k|^2 + |v_k|^2 = 1$. Inverting the relation Eq. (7.55) to express the $\gamma_{\boldsymbol{k}\sigma}$ operators, we obtain,

$$\gamma_{\boldsymbol{k}\sigma} = u_k^* c_{\boldsymbol{k}\sigma} + 2\sigma \frac{\Delta}{|\Delta|} v_k c_{-\boldsymbol{k}-\sigma}^{\dagger}. \tag{7.58}$$

We recognize here the two Bogoliubov operators that were defined in the previous section, the two above operators $\gamma_{\boldsymbol{k}\uparrow}$, $\gamma_{\boldsymbol{k}\downarrow}$ are the two Bogoliubov operators that in the previous section were called as $\gamma_{0\boldsymbol{k}}$, $\gamma_{1\boldsymbol{k}}$ respectively. Without loss of generality,

we set the arbitrary phase of u_k to zero, i.e. $u_k = |u_k|$.

We may now plug in these solutions back into the hamiltonian. Doing so leads to the form of the BCS Hamiltonian,

$$H_{\text{BCS}} = \sum_{\boldsymbol{k},\sigma} E_k \gamma^\dagger_{\boldsymbol{k}\sigma} \gamma_{\boldsymbol{k}\sigma} + \frac{1}{2} \sum_{\boldsymbol{k},\sigma} (\xi_k - E_k). \tag{7.59}$$

The ground state is defined as the state that has no quasiparticle, $\gamma_{\boldsymbol{k}\sigma} |\text{GS}\rangle = 0$. The energy of the ground state is readily obtained,

$$E_{\text{GS}} = \langle \text{GS}| H_{\text{BCS}} |\text{GS}\rangle = \frac{1}{2} \sum_{\boldsymbol{k},\sigma} (\xi_k - E_k) = \sum_{\boldsymbol{k}} (\xi_k - E_k). \tag{7.60}$$

The picture that emerges is that the ground state is the state with no quasiparticles, and the $\gamma^\dagger_{\boldsymbol{k}\sigma}$ successively add quasiparticles onto the state. The BCS energy spectrum is sketched in Fig. 7.6.

7.3 BCS Hamiltonian in the spherical wave basis

In the following chapters, for reasons that will soon become clear, it will be important to change the electron basis from the plane wave to the spherical wave basis, and express the BCS Hamiltonian, Eq. (7.35), in the new basis. This section describes the basis change. The change of basis is performed through

$$c^\dagger_{\boldsymbol{k}\sigma} = \sum_{l,m} \langle klm\sigma | \boldsymbol{k}\sigma \rangle c^\dagger_{klm\sigma}, \tag{7.61}$$

where $k = |\boldsymbol{k}|$. It is convenient to integrate over a sphere of radius R and volume V. The plane wave functions are normalized as $\langle \boldsymbol{r} | \boldsymbol{k} \rangle = e^{i\boldsymbol{k}\cdot\boldsymbol{r}}/\sqrt{V}$, while the spherical harmonics wave functions,

$$\langle \boldsymbol{r} | klm \rangle = \sqrt{\frac{2}{R}} k \, j_l(kr) Y_l^m(\hat{\boldsymbol{r}}), \tag{7.62}$$

have been normalized in such way that $\langle klm|k'l'm'\rangle = \delta_{ll'}\delta_{mm'}\delta_{kk'}$. We now use the plane wave expansion in the spherical wave basis,

$$e^{i\boldsymbol{k}\cdot\boldsymbol{r}} = 4\pi \sum_{l=0}^{\infty} \sum_{m=-l}^{l} i^l j_l(kr) Y_l^m(\hat{\boldsymbol{r}})[Y_l^m(\hat{\boldsymbol{k}})]^*, \tag{7.63}$$

divide by $\sqrt{V}$ with $V = 4\pi R^3/3$ and write in terms of Eq. (7.62) to get

$$c_{\boldsymbol{k}\sigma}^\dagger = \frac{\sqrt{6\pi}}{kR} \sum_{l,m} i^l [Y_l^m(\hat{\boldsymbol{k}})]^* c_{klm\sigma}^\dagger. \tag{7.64}$$

The BCS Hamiltonian for a conventional (s-wave) superconductor in the plane wave basis is

$$H_{\text{BCS}} = \sum_{\boldsymbol{k}} \sum_{\sigma} \left[\xi_{\boldsymbol{k}} c_{\boldsymbol{k}\sigma}^\dagger c_{\boldsymbol{k}\sigma} - \Delta\sigma \left(c_{\boldsymbol{k}\sigma}^\dagger c_{-\boldsymbol{k}-\sigma}^\dagger + c_{-\boldsymbol{k}-\sigma} c_{\boldsymbol{k}\sigma} \right) \right]. \tag{7.65}$$

Using the orthogonality condition on spherical harmonics, we find the conduction energy part,

$$\sum_{\boldsymbol{k}} \xi_{\boldsymbol{k}} c_{\boldsymbol{k}\sigma}^\dagger c_{\boldsymbol{k}\sigma} = \sum_{k} \sum_{l,m} \xi_k c_{klm\sigma}^\dagger c_{klm\sigma}. \tag{7.66}$$

plugging Eq. (7.64) into the pairing Hamiltonian, and using

$$\sum_{\boldsymbol{k}} = \frac{V}{(2\pi)^3} \int dk\, k^2 \int d\Omega_k = \frac{R^2}{6\pi} \sum_{k} k^2 \int d\Omega_k, \tag{7.67}$$

along with the complex conjugation property of the spherical harmonics, $[Y_l^m(\hat{\boldsymbol{k}})]^* = (-1)^m Y_l^{-m}(\hat{\boldsymbol{k}})$, and the parity transformation, $Y_l^m(-\hat{\boldsymbol{k}}) = (-1)^l Y_l^m(\hat{\boldsymbol{k}})$, the Cooper pairing terms takes the form,

$$\sum_{\boldsymbol{k}} c_{\boldsymbol{k}\sigma}^\dagger c_{-\boldsymbol{k}-\sigma}^\dagger = \sum_{k} \sum_{l,m} (-1)^m c_{klm\sigma}^\dagger c_{kl-m-\sigma}^\dagger. \tag{7.68}$$

Putting those two pieces together, we obtain the BCS Hamiltonian in spherical wave basis,

$$H_{\text{BCS}} = \sum_{k} \sum_{lm\sigma} \left[\xi_k c_{klm\sigma}^\dagger c_{klm\sigma} - \Delta\sigma(-1)^m c_{klm\sigma}^\dagger c_{kl-m-\sigma}^\dagger + h.c. \right]. \tag{7.69}$$

7.4 Summary

In this chapter, we looked at the origin of the attractive effective potential between two electrons, mediated by the electron-phonon interactions. We found that as a result of the attractive potentials, the Fermi level in unstable against the formation of electron-electron pairs, called Cooper pairs. An energy gap Δ opens symmetrically at the Fermi level, representing the energy needed to excite an electron from the Fermi sea to the conduction band.

We derived the BCS Hamiltonian as the mean-field approximation of the electron Hamiltonian with four Fermion operators as the attractive interaction. We further introduced a set of Bogoliubov operators that diagonalize the BCS Hamiltonian. This approach shows that the energy eigenstates are quasiparticles that are linear superpositions of an electron in state $\boldsymbol{k}, \sigma$ and a hole in state $-\boldsymbol{k}, -\sigma$.

Finally, we introduced the Heisenberg equation of motion method to derive dynamical quantities. We first derive the normal and anomalous electron Green's functions. While the normal Green's function has the information of the spectral weight of the quasiparticles, the anomalous Green's function gives the amount of correlation between an electron and hole. We also used this method to independently derive the Bogoliubov transformation. Even though the method is completely equivalent to the Bogoliubov transformation, it has the advantage of easily being generalized to more complex systems. A combination of those two techniques will be the basis of the calculations in this thesis.

In the following section we introduce impurities to our model, and look at the effect of superconductivity on their state.

Chapter 8

Impurities in superconductors and Yu-Shiba-Rusinov (YSR) states

In nature, materials are never pure, they are always contaminated with impurities. Hence, it is important to understand their impact in order to describe materials realistically. impurities break the translation symmetry of the crystal, leading to scattering between conduction electrons and a reduction on their conductivity. Moreover, the fluctuation of impurity charge and spin degrees of freedom cause electric and magnetic noise, leading to limitations on the operation of sensitive quantum devices [269, 274].

Impurities are atoms with atomic species differing from the atoms of the host material. They can interact with the host material via a number of ways, e.g. via lattice phonons, electron scattering, electron-electron interactions.

Impurity atoms with filled electronic shells and no valence electrons will act either as a Coulomb scattering centre (if they are charged) or as a hard sphere scatterer (if they are neutral). In both cases these filled-shell impurities will just contribute a single-electron *potential scattering* term to the material's Hamiltonian. Impurities with *un*filled shells and a finite number of valence electrons, it will have an overall spin which will interact with the conduction electron spins. In this case the effect of the impurity on the material's electronic properties and vice versa becomes much richer and complicated. [287]

In superconductors, early studies of impurities showed that bulk properties, such as the critical temperature, were insensitive to the concentration of some kinds of impurities, and quite sensitive to other kinds [288]. This puzzle was solved by Anderson's theorem [289], that showed that only scattering centers that violate time-reversal of

the Cooper pairs are able to reduce or add states to the superconducting energy gap.

This theorem is important for us because it clarifies the conditions for the existence of subgap bound states. It shows that impurities whose potential break time-reversal weaken superconductivity, allowing the appearance of physical states populating the subgap region. Conversely, the observation of subgap states is the signature of a scattering potential that breaks time-reversal.

In particular, the presence of impurities with spin (due to unfilled shells) will interact with Cooper pairs via spin-dependent scattering, thus inducing the creation of states that populate the subgap region, called the Yu-Shiba-Rusinov (YSR) states [271, 272, 273]. In this chapter, we start by proving Anderson's theorem, and then move on to describing models of quantum impurities, *viz.* Anderson, Kondo and Shiba. The simplest model that violates the Anderson theorem and that leads to YSR states is the Shiba model, which is the limit of the Kondo model for a classical spin impurity. Finally, we are going to derive the energy spectrum of the Shiba model and discuss the emergence of YSR states.

8.1 Anderson theorem and the existence of subgap states

Cooper pairs are bound states between conduction electrons that are the time-reversal of each other, and as such the BCS pairing Hamiltonian is symmetric under time reversal. Anderson's theorem [289, 290] asserts that scattering centers do not break the time reversal symmetry of conduction electrons will not affect the superconducting energy gap, essentially because these do not lead to spin-dependent interactions that break Cooper-pairs.

Let's start with the wave function solutions of electrons $\psi_{\boldsymbol{k}}$ with energy $\xi_{\boldsymbol{k}}$ in a normal conductor, with no impurity,

$$H_0 \psi_{\boldsymbol{k}} = \epsilon_k \psi_{\boldsymbol{k}}. \tag{8.1}$$

where H_0 is the normal conductor Hamiltonian (free Fermi gas of electrons). In that basis, we showed in Sec. 7.1.2, that the superconducting pairing Hamiltonian takes the form,

$$H_\Delta = -\sum_{\boldsymbol{k},\boldsymbol{k}'} V_{\boldsymbol{k},\boldsymbol{k}'} c^\dagger_{\boldsymbol{k}\uparrow} c^\dagger_{\boldsymbol{k}'\downarrow} c_{-\boldsymbol{k}\downarrow} c_{-\boldsymbol{k}'\uparrow} \tag{8.2}$$

Let's pretend that we have the wave function solutions to the conducting electrons and scattering problem, that is we have the wave functions,

$$(H_0 + H') \psi_n = \epsilon_n \psi_n, \tag{8.3}$$

where H' is the scattering center. The two basis are related through the matrix elements,

$$\psi_n = \sum_{\boldsymbol{k}} \langle \boldsymbol{k} | n \rangle \, \psi_{\boldsymbol{k}}, \tag{8.4}$$

with the normalization condition $\sum_{\boldsymbol{k}} | \langle \boldsymbol{k} | n \rangle |^2 = 1$. If the scattering potential H' does not break time reversal, then the time-reversed wave functions of ψ_n, that is ψ_{-n}^* is also a wave function of the same Hamiltonian with the same energies,

$$(H_0 + H') \psi_{-n}^* = \epsilon_n \psi_{-n}^*. \tag{8.5}$$

Given the new basis of electron wave functions, we can calculate the electron-electron pairing potential via phonon exchange, as we discussed in Sec. 7.1.2. Given that the ψ_n basis is related to the $\psi_{\boldsymbol{k}}$ basis through amplitudes $\langle \boldsymbol{k} | n \rangle$, the phonon-electron interaction is modified by the insertion of those coefficients to,

$$
\begin{aligned}
H_{e-ph} = &i \sum_{\boldsymbol{k}, \boldsymbol{k}'} D_{\boldsymbol{k}'-\boldsymbol{k}} c_{\boldsymbol{k}'}^\dagger c_{\boldsymbol{k}} \left(a_{\boldsymbol{k}'-\boldsymbol{k}} - a_{\boldsymbol{k}-\boldsymbol{k}'}^\dagger \right) \\
\implies \quad &H'_{e-ph} = i \sum_{n,n'} \left[\sum_{\boldsymbol{k}, \boldsymbol{k}'} \langle \boldsymbol{k}' | n' \rangle^* \langle \boldsymbol{k} | n \rangle \, D_{\boldsymbol{k}'-\boldsymbol{k}} \left(a_{\boldsymbol{k}'-\boldsymbol{k}} - a_{\boldsymbol{k}-\boldsymbol{k}'}^\dagger \right) \right] c_{n'}^\dagger c_n.
\end{aligned}
\tag{8.6}
$$

The consequence is that the new electron pairing potential takes the form,

$$H_\Delta = \sum_{n,n'} V_{nn'} c_n^\dagger c_{-n}^\dagger c_{-n'} c_{n'}, \tag{8.7}$$

where

$$V_{nn'} = \sum_{\boldsymbol{k}, \boldsymbol{k}'} \frac{| \langle \boldsymbol{k} | n \rangle |^2 | \langle \boldsymbol{k}' | n' \rangle |^2 |D_{\boldsymbol{k}'-\boldsymbol{k}}|^2 2\hbar\omega_{\boldsymbol{k}'-\boldsymbol{k}}}{(\epsilon_n - \epsilon_{n'})^2 - (\hbar\omega_{\boldsymbol{k}'-\boldsymbol{k}})^2}. \tag{8.8}$$

The simplification that was used in the context of BCS for the electron-electron pairing was that of a constant potential for electron's energies below a threshold.

Using this approximation here, then the new pairing potential takes the form,

$$
V_{nn'} = \begin{cases} V \sum_{\boldsymbol{k},\boldsymbol{k}'} |\langle \boldsymbol{k}|n\rangle|^2 |\langle \boldsymbol{k}'|n'\rangle|^2 & |\epsilon_n - E_F|, \ |\epsilon_{n'} - E_F| < \hbar\omega_c, \\ 0 & \text{otherwise.} \end{cases} \tag{8.9}
$$

With the normalization condition $\sum_{\boldsymbol{k}} |\langle \boldsymbol{k}|n\rangle|^2 = 1$, we see that the new pairing strength is the same as the old pairing strength.

It is important to emphasize what is meant by "breaking time reversal symmetry" in the Anderson theorem. Here time reversal is applied only to the conduction electrons forming the SC condensate, with e.g. impurity spins left unchanged (Of course, the interaction of a conduction electron with a localized spin does not fundamentally break time-reversal symmetry, in that it is invariant under the application of time reversal to both the cond. electrons and the imp. spin). The point that we wish to emphasize here is that once we allow conduction electrons to interact with localized impurity electrons *with spin*, Eq. (8.5) and (8.7) are not valid anymore, in the sense that we must include creation/destruction operators associated to the localized impurity. As we show below an impurity with spin always leads to subgap states.

8.2 Impurity models

An impurity has a field $\psi(\boldsymbol{r})$ associated to it, which is written in second quantization form [291],

$$
\psi(\boldsymbol{r}) = \sum_{\boldsymbol{k},\sigma} \phi_{\boldsymbol{k}}(\boldsymbol{r}) c_{\boldsymbol{k}\sigma} + \sum_{\sigma} \phi_d(\boldsymbol{r}) d_\sigma, \tag{8.10}
$$

where the operator $c_{\boldsymbol{k}\sigma}$ annihilates a conduction electron in state $\{\boldsymbol{k}, \sigma\}$, with the associated spatial wave function $\phi_{\boldsymbol{k}}(\boldsymbol{r})$, when the electron is in the conduction band, whereas d_σ annihilates a electron state σ when the electron is on the impurity site, with the associated orbital wave function $\phi_d(\boldsymbol{r})$. The total Hamiltonian for the electrons,

$$
\begin{aligned}
H &= \int d^3\boldsymbol{r}\, \psi^\dagger(\boldsymbol{r}) \left(-\frac{\boldsymbol{\nabla}^2}{2m} + U(\boldsymbol{r}) \right) \psi(\boldsymbol{r}). \\
&+ \frac{1}{2} \int d^3\boldsymbol{r}_1 \int d^3\boldsymbol{r}_2 \psi^\dagger(\boldsymbol{r}_1)\psi(\boldsymbol{r}_1) \frac{e^2}{|\boldsymbol{r}_2 - \boldsymbol{r}_1|} \psi^\dagger(\boldsymbol{r}_2)\psi(\boldsymbol{r}_2).
\end{aligned} \tag{8.11}
$$

The first line includes the usual kinetic term, $-\boldsymbol{\nabla}^2/2m$, and a potential term, $U(\boldsymbol{r})$, that includes effects of the lattice as well as a potential term arising from the impurity. The second line includes an electron-electron Coulomb interaction, e^2/r_{ij}. Although the exact impurity dynamics involves all the terms that are generated by the general Hamiltonian, in Eq. (8.11), only a subset of those is sufficient if we are interested to capture a specific kind of phenomenon. In this thesis, we focus on the impurity magnetic properties.

The kinetic and potential parts lead to the following set of operators,

$$\int d^3\boldsymbol{r}\psi^\dagger(\boldsymbol{r}) \left(-\frac{\boldsymbol{\nabla}^2}{2m} + U(\boldsymbol{r})\right) \psi(\boldsymbol{r}) = \sum_{\boldsymbol{k}\sigma} \epsilon_{\boldsymbol{k}} c^\dagger_{\boldsymbol{k}\sigma} c_{\boldsymbol{k}\sigma} + \sum_\sigma \epsilon_d d^\dagger_\sigma d_\sigma + \sum_{\boldsymbol{k},\boldsymbol{k}'\sigma} B_{\boldsymbol{k}\boldsymbol{k}'} c^\dagger_{\boldsymbol{k}'\sigma} c_{\boldsymbol{k}\sigma}$$
$$+ \sum_{\boldsymbol{k}\sigma} V_{\boldsymbol{k}} \left(c^\dagger_{\boldsymbol{k}\sigma} d_\sigma + d^\dagger_\sigma c_{\boldsymbol{k}\sigma}\right),$$

(8.12)

where the conduction electron's energies $\epsilon_k = \hbar^2 \boldsymbol{k}^2/2m$, and the impurity energy level ϵ_d. The $B_{\boldsymbol{k}\boldsymbol{k}'}$ determines the scattering of conduction electrons off the impurity site potential. It affects the momentum of the conduction electrons, and will be ignored since it does not lead to interesting spin and magnetic effects. The last term, $V_{\boldsymbol{k}}$, is the so-called hybridization,

$$V_{\boldsymbol{k}} = \int d^3\boldsymbol{r}\phi^*_{\boldsymbol{k}\sigma}(\boldsymbol{r})U(\boldsymbol{r})\phi_{d\sigma}(\boldsymbol{r}),$$

(8.13)

accounts for the tunneling probability of electrons from the conduction band to the impurity site.

The Coulomb interaction, on the second line of Eq. (8.11), leads to many electron-electron interaction terms. We ignore most of them on account that they describe electron scattering off the impurity but do not lead to magnetic effects. Among the terms generated by the Coulomb interaction, we maintain two that lead to magnetic phenomena. First, we have the spin-dependent exchange interaction, called H_{sd},

$$H_{sd} = -\sum_{\boldsymbol{k},\boldsymbol{k}'} J_{\boldsymbol{k}\boldsymbol{k}'} \left(c^\dagger_{\boldsymbol{k}\sigma}\boldsymbol{\sigma}_{\sigma\sigma'}c_{\boldsymbol{k}'\sigma'}\right) \cdot \left(d^\dagger_\sigma\boldsymbol{\sigma}_{\sigma\sigma'}d_{\sigma'}\right)$$

(8.14)

with the exchange energy,

$$J_{\boldsymbol{k},\boldsymbol{k}'} = \int d^3\boldsymbol{r}_1 d^3\boldsymbol{r}_2 \phi_{\boldsymbol{k}}^*(\boldsymbol{r}_1)\phi_d(\boldsymbol{r}_1)\frac{e^2}{|\boldsymbol{r}_1 - \boldsymbol{r}_2|}\phi_{\boldsymbol{k}'}(\boldsymbol{r}_2)\phi_d^*(\boldsymbol{r}_2) \tag{8.15}$$

where $\boldsymbol{\sigma} = \{\sigma^x,\ \sigma^y,\ \sigma^z\}$ are the Pauli matrices. This interaction leads to spin flip processes, where a scattering event causes the conduction electron spin to flip while the impurity spin flips in the opposite direction.

The second term we are going to keep is the following quartic term,

$$H_{\text{Coulomb}} = U n_{d\uparrow} n_{d\downarrow}, \tag{8.16}$$

which represents the on-site Coulomb repulsion energy with

$$U = \int d^3\boldsymbol{r}_1 d^3\boldsymbol{r}_2 |\phi_d(\boldsymbol{r}_1)|^2 \frac{e^2}{|\boldsymbol{r}_1 - \boldsymbol{r}_2|}|\phi_d(\boldsymbol{r}_2)|^2, \tag{8.17}$$

and the number densities for the impurity electrons $n_{d\sigma} = d_\sigma^\dagger d_\sigma$. This interaction term affects on the occupancy of an impurity level; it has no effect if the level is singly occupied, but has important consequences if the level is doubly occupied.

Two models are widely used to describe the magnetic state of impurities, namely, the Kondo model and the Anderson model. The Kondo model accounts for the energy and conduction electron energies as well as the exchange interaction, $J_{\boldsymbol{k},\boldsymbol{k}'}$ while disregarding the Coulomb repulsion U and the hybridization $V_{\boldsymbol{k}}$. Conversely, the Anderson model accounts for the hybridization and Coulomb repulsion, though ignores the spin-flip interaction.

Below we introduce the two models, and will show that the two models are related via a unitary transformation.

8.2.1   The Anderson model

Among the Hamiltonian terms introduced at the start of this Section, the Anderson impurity model accounts for the conduction electron and impurity energy levels, in addition to the hybridization and the on-site Coulomb repulsions [292]. The Anderson

Hamiltonian reads,

$$H_{\text{Anderson}} = \sum_{\boldsymbol{k}\sigma} \xi_k c_{\boldsymbol{k}\sigma}^\dagger c_{\boldsymbol{k}\sigma} + \sum_\sigma \xi_d d_\sigma^\dagger d_\sigma$$
$$+ \sum_{\boldsymbol{k}\sigma} V_{\boldsymbol{k}} \left(c_{\boldsymbol{k}\sigma}^\dagger d_\sigma + d_\sigma^\dagger c_{\boldsymbol{k}\sigma} \right) + U n_{d\uparrow} n_{d\downarrow}, \tag{8.18}$$

where we introduced the energies $\xi_k = \epsilon_{\boldsymbol{k}} - \mu$ and $\xi_d = \epsilon_d - \mu$ which measure the conduction energy and impurity level with respect to the chemical potential.

The hybridization coupling, $V_{\boldsymbol{k}}$, implies that the conduction electrons or impurity electrons are not energy eigenstates. Because of hybridization, the impurity state may decay into the conduction band; it is no longer a bound state, but instead becomes a scattering resonance with a width Γ and a lifetime $\tau \sim \hbar/\Gamma$.

Below, we are going to solve the Anderson model exactly for the case with no Coulomb repulsion, $U = 0$, then we will introduce Coulomb repulsion, and use the mean-field approximation to solve the system. Our treatment uses the equation of motion approach, as introduced in Sec. 7.2. Finally, we are going to discuss the limitations of the Anderson model with regards to the Kondo effect.

Without on-site Coulomb repulsion U

The Heisenberg equation of motion for the conduction and impurity electrons, $\dot{c}_{k\sigma}(t) = -i/\hbar\,[H, c_{k\sigma}(t)]$ and $\dot{d}_\sigma(t) = -i/\hbar\,[H, d_\sigma(t)]$ read, [293]

$$\dot{d}_\sigma(t) = -\frac{i\xi_d}{\hbar} d_\sigma(t) - \frac{i}{\hbar} \sum_{\boldsymbol{k}} V_{\boldsymbol{k}}^* c_{\boldsymbol{k}\sigma}(t),$$
$$\dot{c}_{\boldsymbol{k}\sigma}(t) = -\frac{i\xi_k}{\hbar} c_{\boldsymbol{k}\sigma}(t) - \frac{i}{\hbar} V_{\boldsymbol{k}} d_\sigma(t). \tag{8.19}$$

Using the definition of the retarded Green's function for the impurity, $G_\sigma^R(t) = -i\theta \left\langle \left\{ d_\sigma(t), d_\sigma^\dagger(0) \right\} \right\rangle$, taking the time derivative, and using the equation of motion above, we find the closed system of equation,

$$\dot{G}_\sigma^R(t) = -i\delta(t) - \frac{i\xi_d}{\hbar} G_\sigma^R(t) - \frac{i}{\hbar} \sum_{\boldsymbol{k}} V_{\boldsymbol{k}}^* F_{\boldsymbol{k}\sigma}^R(t),$$
$$\dot{F}_{\boldsymbol{k}\sigma}^R(t) = -\frac{i\xi_k}{\hbar} F_{\boldsymbol{k}\sigma}^R(t) - \frac{i}{\hbar} V_{\boldsymbol{k}} G_\sigma^R(t), \tag{8.20}$$

with the function, $F_\sigma^R(t) = -i\theta \left\langle \left\{ c_{\boldsymbol{k}\sigma}(t), d_\sigma^\dagger(0) \right\} \right\rangle$. In Fourier space, this system takes the form,

$$(\hbar\omega - \xi_d) G_\sigma^R(\omega) = \hbar + \sum_{\boldsymbol{k}} V_{\boldsymbol{k}\sigma}^* F_{\boldsymbol{k}\sigma}^R(\omega)$$

$$(\hbar\omega - \xi_k) F_{\boldsymbol{k}\sigma}^R(\omega) = V_{\boldsymbol{k}\sigma} G_\sigma^R(\omega). \tag{8.21}$$

Since the Green's functions are retarded, we are able to analytically continue the frequency to $\omega \to \omega + i\eta$ and $\eta \to 0^+$. This allows us to divide the second equation by $1/(\hbar\omega - \xi_k + i\eta)$ while avoiding the pole at $\hbar\omega = \xi_k$. The second equation allows us to calculate,

$$F_{\boldsymbol{k}\sigma}^R(\omega + i\eta) = \frac{V_{\boldsymbol{k}\sigma}}{\hbar\omega - \xi_k + i\eta} G_\sigma^R(\omega + i\eta), \tag{8.22}$$

The equation of motion for the impurity operator now takes the form,

$$G_\sigma^R(\omega + i\eta) = \hbar \frac{1}{\hbar\omega - \xi_d - \Sigma(\omega + i\eta) + i\eta}. \tag{8.23}$$

where the self energy, $\Sigma(\omega + i\eta)$ is expressed as,

$$\Sigma(\omega + i\eta) = \sum_{\boldsymbol{k}} \frac{|V_{\boldsymbol{k}}|^2}{\hbar\omega - \xi_k + i\eta}. \tag{8.24}$$

The function $\Sigma(\omega + i\eta)$ is contains a real part and an imaginary part,

$$\sum_{\boldsymbol{k}} \frac{|V_{\boldsymbol{k}}|^2}{\hbar\omega - \xi_k + i\eta} = \Sigma(\omega) - i\Gamma(\omega). \tag{8.25}$$

The real part $\Sigma(\omega)$ represents the impurity level self-energy,

$$\Sigma(\omega) = \mathcal{P} \sum_{\boldsymbol{k}} \frac{|V_{\boldsymbol{k}}|^2}{\hbar\omega - \xi_k}, \tag{8.26}$$

and the imaginary part, $\Gamma(\omega)$, represents the impurity width,

$$\Gamma(\omega) = \pi \sum_{\boldsymbol{k}} |V_{\boldsymbol{k}}|^2 \delta(\hbar\omega - \xi_k) = \pi\rho(\omega) \left\langle |V_{\boldsymbol{k}}|^2 \right\rangle (\omega), \tag{8.27}$$

with the average of the squared matrix element over the solid angle, $\left\langle |V_{\boldsymbol{k}}|^2 \right\rangle (\omega) = \int d\Omega |V_{\boldsymbol{k}}|^2 / 4\pi$, at the energy $\xi_k = \hbar\omega$. Therefore, the retarded impurity Green's
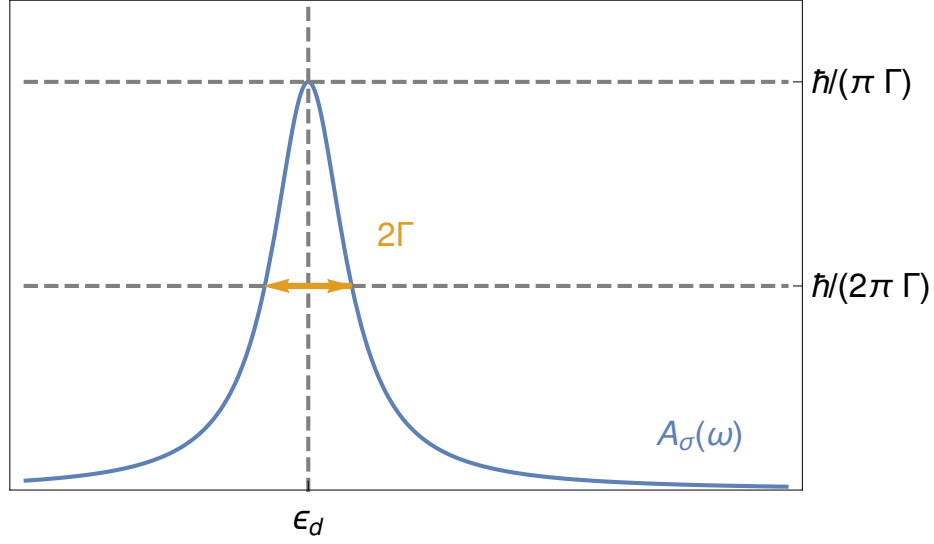
Figure 8.1: Spectral function $\mathcal{A}_\sigma(\omega)$ for an Anderson impurity hybridized with a conductor.

function takes the form,

$$G_\sigma^R(\omega + i\eta) = \hbar \frac{\hbar\omega - \xi_d - \Sigma(\omega) - i\Gamma(\omega)}{(\hbar\omega - \xi_d - \Sigma(\omega))^2 + \Gamma(\omega)^2}. \tag{8.28}$$

The spectral function is easily obtained as,

$$\mathcal{A}_\sigma(\omega) = -\frac{1}{\pi}\text{Im}\left\{G_\sigma^R(\omega + i\eta)\right\} = \frac{\hbar}{\pi} \frac{\Gamma(\omega)}{(\hbar\omega - \xi_d - \Sigma(\omega))^2 + \Gamma(\omega)^2}. \tag{8.29}$$

The energy of the physical state is located at $\hbar\omega = \tilde{\xi}_d$, defined by the location of the maximum of the spectral function,

$$\tilde{\xi}_d = \xi_d + \Sigma(\tilde{\xi}_d), \tag{8.30}$$

and the spectral weight at $\tilde{\xi}_d$ is,

$$\mathcal{A}_\sigma(\tilde{\xi}_d) = \frac{\hbar}{\pi} \frac{1}{\Gamma(\tilde{\xi}_d)}. \tag{8.31}$$

The spectral function $\mathcal{A}_\sigma(\omega)$ is a Lorentzian centered around $\tilde{\xi}_d$ of width $\Gamma(\omega)$. In this situation, the physical state is a scattering resonance. [Quantum theory of solids, Kittel] The spectral function $\mathcal{A}_\sigma(\omega)$ is represented in Fig. 8.1.

With Coulomb repulsion $U > 0$

The introduction of the on-site Coulomb repulsion introduces in the Hamiltonian the interaction,

$$H_{\text{Coulomb}} = U n_\uparrow n_\downarrow, \tag{8.32}$$

and leads to the modification of the equation of motion as follows,

$$\begin{aligned}
\dot{d}_\sigma(t) &= -\frac{i\xi_d}{\hbar} d_\sigma(t) - \frac{i}{\hbar} \sum_{\boldsymbol{k}} V_{\boldsymbol{k}}^* c_{\boldsymbol{k}\sigma}(t) - \frac{iU}{\hbar} H_\sigma^R(t), \\
\dot{c}_{\boldsymbol{k}\sigma}(t) &= -\frac{i\xi_k}{\hbar} c_{\boldsymbol{k}\sigma}(t) - \frac{i}{\hbar} V_{\boldsymbol{k}} d_\sigma(t).
\end{aligned} \tag{8.33}$$

with the definition of yet another retarded Green's function,

$$H_\sigma^R(t) = -i\theta(t) \left\langle \left\{ n_{-\sigma}(t) d_\sigma(t), d_\sigma^\dagger(0) \right\} \right\rangle. \tag{8.34}$$

In order to find a closed system of equations, we have to calculate the time derivative, $\dot{H}_\sigma^R(t)$, but because it involves trilinear terms, higher order functions will be introduced. In fact, because the Coulomb interaction $n_\uparrow n_\downarrow$ is quartic in the impurity operator, the system of equation is infinite. Instead, we will use the mean-field approach to relate higher order operators to lower order operators, by approximating the trilinear terms as,

$$n_{-\sigma}(t) d_\sigma(t) \approx \langle n_{-\sigma} \rangle \, d_\sigma(t) + d_{-\sigma}^\dagger(t) \langle d_{-\sigma} d_\sigma \rangle - \left\langle d_{-\sigma}^\dagger d_\sigma \right\rangle d_{-\sigma}(t). \tag{8.35}$$

Since superconductivity is absent in the system, the expectation value $\langle d_{-\sigma} d_\sigma \rangle = 0$ vanishes, and since the tunneling coupling $V_{\boldsymbol{k}}$ does not introduce spin flips, the expectation value $\left\langle d_{-\sigma}^\dagger d_\sigma \right\rangle = 0$ also vanishes. Hence, we are left with the simple approximation

$$H_\sigma^R(t) \approx \langle n_{-\sigma} \rangle \, G_\sigma^R(t), \tag{8.36}$$

which closes our system by simply causing a shift of the impurity level by $U \langle n_{-\sigma} \rangle$.

$$\begin{aligned}
\dot{d}_\sigma(t) &= -\frac{i}{\hbar} \left(\xi_d + U \langle n_{-\sigma} \rangle \right) d_\sigma(t) - \frac{i}{\hbar} \sum_{\boldsymbol{k}} V_{\boldsymbol{k}}^* c_{\boldsymbol{k}\sigma}(t), \\
\dot{c}_{\boldsymbol{k}\sigma}(t) &= -\frac{i\xi_k}{\hbar} c_{\boldsymbol{k}\sigma}(t) - \frac{i}{\hbar} V_{\boldsymbol{k}} d_\sigma(t).
\end{aligned} \tag{8.37}$$

From here, the calculation proceeds in the exact same way as in the case with $U = 0$, giving the Green's function,

$$G_\sigma^R(\omega + i\eta) = \frac{\hbar}{\hbar\omega - \xi_d - \Sigma(\omega) - U\langle n_{-\sigma}\rangle + i\Gamma(\omega)} \tag{8.38}$$

and the spectral function,

$$\mathcal{A}_\sigma(\omega) = \frac{\hbar}{\pi} \frac{\Gamma(\omega)}{[\hbar\omega - \xi_d - \Sigma(\omega) - U\langle n_{-\sigma}\rangle]^2 + \Gamma(\omega)^2} \tag{8.39}$$

It is typical to assume the self energy and the decay rate to be constant functions of frequency, $\Sigma(\omega) \equiv \Sigma$, and $\Gamma(\omega) \equiv \Gamma$. The self-energy renormalizes the impurity energy level, $\tilde{\xi}_d = \xi_d + \Sigma$.

The average number of spins is self-consistently determined at zero temperature via the spectral function, [292]

$$\langle n_\sigma\rangle = \int_{-\infty}^0 d\omega\,\mathcal{A}_\sigma(\omega), \tag{8.40}$$

where the upper bound of the energies is set to the Fermi level, which is the highest energy of filled state at zero temperature. The integral of the spectral function can be performed exactly, and we end up on the equations,

$$\langle n_\sigma\rangle = \frac{1}{\pi}\cot^{-1}\left(\frac{\tilde{\xi}_d + U\langle n_{-\sigma}\rangle}{\Gamma}\right). \tag{8.41}$$

Anderson used this model to study the conditions under which an impurity develops a magnetic moment. This self-consistent equation can be solved for the number densities of spin $\langle n_\sigma\rangle$ for various parameters U and Γ. It has two kinds of solutions, one where $\langle n_\sigma\rangle = \langle n_{-\sigma}\rangle$, which leads to a non-magnetic state of the impurity. The other solution is such that $\langle n_\sigma\rangle \neq \langle n_{-\sigma}\rangle$, which implies a magnetic state of the impurity.

The existence of a magnetic state would mean the spontaneous of spin symmetry breaking. His solution [292] turned out to be famously wrong. In reality, the impurity never breaks its local spin symmetry; instead, the impurity spin is screened out by a cloud of conduction electron spins oriented antiparallel to it (the Kondo cloud).

8.2.2 The Kondo model

The Kondo model for the impurity includes the energy levels for the conduction electron and for the impurity, as well as the exchange energy,

$$H_{\text{Kondo}} = \sum_{\boldsymbol{k}\sigma} \xi_{\boldsymbol{k}} c^\dagger_{\boldsymbol{k}\sigma} c_{\boldsymbol{k}\sigma} + \sum_\sigma \xi_d d^\dagger_\sigma d_\sigma - \sum_{\boldsymbol{k},\boldsymbol{k}'} J_{\boldsymbol{k}\boldsymbol{k}'} \left(c^\dagger_{\boldsymbol{k}\sigma} \boldsymbol{\sigma}_{\sigma\sigma'} c_{\boldsymbol{k}'\sigma'} \right) \cdot \left(d^\dagger_\sigma \boldsymbol{\sigma}_{\sigma\sigma'} d_{\sigma'} \right). \quad (8.42)$$

This model incorporates magnetic effects arising from the quantum state of the impurity and the conduction electrons.

Most famously, it played an essential role in the explanation of the Kondo effect [294]. The Kondo effect was discovered experimentally from measurements of resistance as a function of temperature. When certain kinds of impurities were added to the material, an unexpected resistance minimum appeared as a function of temperature. At the time, all known mechanisms of conduction electron scattering caused the resistance of materials to decrease as the temperature decreases. In contrast, after adding impurities, it was observed that resistance goes through a minimum, before increasing again with decreasing temperature. Kondo was able to explain this effect analytically by calculating resisitivity to third order in the exchange energy of his model, Eq. (8.42).

Because of the quartic nature of the Coulomb interaction, however, it is impossible to fully capture the Kondo effect analytically. A satisfactory description of the Kondo effect requires the renormalization group method developed by Wilson. This shows that the conduction electrons form a many-body singlet state with the impurity in such way to screen out its spin. This many-body bound state is called the Kondo cloud, with a binding energy equal to $k_B T_K$, where T_K is the Kondo temperature, [287]

$$T_K \sim \sqrt{JE_F} \exp\left(-\frac{1}{|J|\rho_F}\right). \quad (8.43)$$

The Kondo effect is non-perturbative as can be seen from the fact that the coupling J appears in the denominator of the argument of the exponential, and is thus not accessible from perturbation theory for small J. This non-perturbative aspect is quite similar to the dependence of the Cooper pair binding energy on the pairing potential, see Eq. (7.9).

It turns out that the Kondo and Cooper-pairing effects compete against each other. As a result, when $\Delta > 3k_B T_K$ the Kondo effect is not important [295], and a

mean-field-like Hamiltonian such as BCS is able to capture the physics of an impurity in a superconductor. This thesis will focus in the regime of large Δ or low T_K, with the Kondo cloud not qualitatively affecting the physics of the impurity.

8.2.3 Equivalence of the Anderson and Kondo models

In a normal metal

It can be shown that the two models, the Kondo model and the Anderson model are equivalent. The equivalence was first brought to light by Schrieffer and Wolff through the use of a canonical transformation, showing that the two models are equivalent in the limit of a weak hybridization. [296] This is achieved thanks to a canonical transformation from the original hamiltonian H to a new hamiltonian $\bar{H}$ related via,

$$
\begin{aligned}
\bar{H} &= e^S H e^{-S} \\
&= H + [S, H] + \frac{1}{2!}[S, H] + \cdots \\
&= H_0 + H_{\text{hyb}} + [S, H_0] + [S, H_{\text{hyb}}] + \cdots
\end{aligned}
\tag{8.44}
$$

We can set the matrix S in such way that $\bar{H}$ does not contain linear order in V by imposing the condition,

$$
[H_0, S] = H_{\text{hyb}},
\tag{8.45}
$$

which can be satisfied if the operator S is expressed as,

$$
S = \sum_{\boldsymbol{k}\sigma} \left[\frac{V_k}{\xi_k - \xi_d - U} n_{-\sigma} + \frac{V_k}{\xi_k - \xi_d} (1 - n_{-\sigma}) \right] c_{\boldsymbol{k}\sigma}^\dagger d_\sigma + h.c.
\tag{8.46}
$$

The resulting Hamiltonian,

$$
\bar{H} \approx H_0 + \frac{1}{2}[S, H_{\text{hyb}}] + \frac{1}{3}[[S, H_{\text{hyb}}], H_{\text{hyb}}] + \cdots ,
\tag{8.47}
$$

contains many terms. Among those, the following interaction

$$
-\frac{1}{4} \sum_{\boldsymbol{k},\boldsymbol{k}'} J_{\boldsymbol{k}\boldsymbol{k}'} \left(\psi_{\boldsymbol{k}'}^\dagger \boldsymbol{\sigma} \psi_{\boldsymbol{k}} \right) \cdot \left(\psi_d^\dagger \boldsymbol{\sigma} \psi_d \right),
\tag{8.48}
$$

where $\boldsymbol{\sigma}$ are the Pauli matrices, and the spinors $\psi_{\boldsymbol{k}}$ and ψ_d are,

$$\psi_{\boldsymbol{k}} = \begin{pmatrix} c_{\boldsymbol{k}\uparrow} \\ c_{\boldsymbol{k}\downarrow} \end{pmatrix}, \quad \psi_d = \begin{pmatrix} d_\uparrow \\ d_\downarrow \end{pmatrix}. \tag{8.49}$$

This term is responsible for spin-flips. This is the exchange interaction of the Kondo model which was introduced earlier, with

$$J_{\boldsymbol{k}\boldsymbol{k}'} = V_{\boldsymbol{k}'} V_{\boldsymbol{k}}^* \left[\frac{1}{\xi_k - \xi_d - U} + \frac{1}{\xi_{k'} - \xi_d - U} - \frac{1}{\xi_k - \xi_d} - \frac{1}{\xi_{k'} - \xi_d} \right]. \tag{8.50}$$

Specifically, at $k \simeq k' \simeq k_F$, then $\xi_k \simeq \xi_{k'} \simeq 0$ and

$$J_{k_F k_F} \simeq 2|V_{k_F d}|^2 \frac{U}{\xi_d(\xi_d + U)}. \tag{8.51}$$

The resulting model is the same as the Kondo model we introduced earlier. It is important to note, however, that several terms have been ignored to obtain the form of the transformed Hamiltonian $\overline{H}$.

Nevertheless, it can be concluded that the two models contain the same physics. In particular, the Kondo model has been used to explain the onset of the Kondo cloud. As mentioned earlier, this effect is a non-perturbative effect arising from the Coulomb repulsion energy, i.e. it is impossible to capture the Kondo effect at any finite order in perturbation theory. In view of the equivalence between the Kondo and Anderson models, it can be concluded that the Anderson model also requires a non-perturbative renormalization group approach to capture its full physics. In particular, the Anderson model also has a many-body singlet (the Kondo cloud) as its ground state.

In a superconductor

The same procedure of canonical transformation, can be applied to the case of an Anderson impurity in a superconductor. As a reminder, the quasiparticle of BCS is not a single electron excitation, but rather a electron-hole excitation whose creation and annihilation operators are the Bogoliubov operators,

$$c_{\boldsymbol{k}\sigma} = u_k \gamma_{\boldsymbol{k}\sigma} - 2\sigma v_k \gamma_{-\boldsymbol{k}-\sigma}^\dagger, \tag{8.52}$$

where,

$$|u_k|^2 = \frac{1}{2}\left(1 + \frac{\xi_k}{E_k}\right), \quad |v_k|^2 = \frac{1}{2}\left(1 - \frac{\xi_k}{E_k}\right).$$ (8.53)

The result is that the hybridization coupling can be expressed in terms of BCS quasi-particles,

$$
H_{\text{Anderson}}^{\text{SC}} = \sum_{k,\sigma} E_k \gamma_{k\sigma}^\dagger \gamma_{k\sigma} + \sum_\sigma \xi_d d_\sigma^\dagger d_\sigma + U n_\uparrow n_\downarrow
$$
$$
+ \sum_{k\sigma} V_k \left[\left(u_k^* \gamma_{k\sigma}^\dagger - 2\sigma v_k^* \gamma_{-k-\sigma} \right) d_\sigma + d_\sigma^\dagger \left(u_k \gamma_{k\sigma} - 2\sigma v_k \gamma_{-k-\sigma}^\dagger \right) \right],
$$ (8.54)

where the first line is the unperturbed H_0 Hamiltonian, and the second line includes the hybridization V_k. Performing a unitary transformation, $\overline{H}_{\text{Anderson}}^{\text{SC}} = e^S H_{\text{Anderson}}^{\text{SC}} e^{-S}$, and imposing that the terms linear in V_k vanish through the condition, $[H_0, S] = H_{\text{hyb}}$, gives the solution for S. In turn, the transformed Hamiltonian contains several operators, one of which being the spin flip, which reads, [297]

$$
\overline{H}_{\text{spin flip}} = -\frac{1}{4}\sum_{k,k'} J_{kk'} \left(\psi_{k'}^\dagger \boldsymbol{\sigma} \psi_k\right) \cdot \left(\psi_d^\dagger \boldsymbol{\sigma} \psi_d\right)
$$
$$
+ \sum_{k,k'\sigma} \sigma T_{kk'} c_{k'-\sigma}^\dagger c_{-k-\sigma}^\dagger d_\sigma^\dagger d_\sigma + h.c.,
$$ (8.55)

where the $J_{kk'}$

$$
J_{kk'} = V_{k'} V_k^* \left[\frac{u_{k'}^2}{E_{k'} - \xi_d - U} + \frac{u_k^2}{E_k - \xi_d - U} - \frac{u_{k'}^2}{E_{k'} - \xi_d} - \frac{u_k^2}{E_k - \xi_d} \right.
$$
$$
\left. - \frac{v_{k'}^2}{E_{k'} + \xi_d + U} - \frac{v_k^2}{E_k + \xi_d + U} + \frac{v_{k'}^2}{E_{k'} + \xi_d} + \frac{v_k^2}{E_k + \xi_d} \right]
$$ (8.56)

is the equivalent to the exchange coupling found in the normal metal case. Additionally, we find a contribution to the spin-flip term that does not exist in the normal case,

$$
T_{kk'} = V_{k'} V_k^* u_k v_k \left[\frac{1}{E_k - \xi_d - U} + \frac{1}{E_k + \xi_d + U} - \frac{1}{E_k - \xi_d} - \frac{1}{E_k + \xi_d} \right]
$$ (8.57)

8.3 Classical impurity: the Shiba model and YSR states

The Shiba model is the limit of the Kondo model when the impurity spin is considered classical, i.e. we replace the impurity spin quantum operator $d^\dagger \boldsymbol{\sigma} d$ with a classical vector $\boldsymbol{S}$,

$$H_{\text{Shiba}} = \sum_{\boldsymbol{k}\sigma} \xi_{\boldsymbol{k}} c_{\boldsymbol{k}\sigma}^\dagger c_{\boldsymbol{k}\sigma} - \sum_{\boldsymbol{k},\boldsymbol{k}'} J_{\boldsymbol{k}\boldsymbol{k}'} \left(c_{\boldsymbol{k}\sigma}^\dagger \boldsymbol{\sigma}_{\sigma\sigma'} c_{\boldsymbol{k}'\sigma'} \right) \cdot \boldsymbol{S}. \tag{8.58}$$

In this way, the exchange interaction $J_{\boldsymbol{k},\boldsymbol{k}'}$ is not longer quartic, but is quadratic in conduction electron operators, $c_{\boldsymbol{k}\sigma}$, which makes it exactly solvable. The Shiba model breaks time-reversal invariance, because the classical spin $\boldsymbol{S}$ remains unchanged when the conduction electron's spins flip, thus violating the Anderson theorem, leading to subgap bound states. Here we embed the Shiba model in a superconductor modeled by BCS theory written in spherical wave basis as was derived in Sec. 7.3,

$$\begin{aligned}
H_{\text{BCS}} &= \sum_k \sum_{m,\sigma} \left[\xi_k c_{km\sigma}^\dagger c_{km\sigma} - \sigma(-1)^m \Delta c_{km\sigma}^\dagger c_{k-m-\sigma}^\dagger + h.c. \right] \\
&= \sum_k \sum_m \chi_{km}^\dagger \left[\xi_k \sigma_z - (-1)^m \Delta \sigma_x \right] \chi_{km},
\end{aligned} \tag{8.59}$$

where the azimuthal quantum number $m = -l, \cdots, l$ and the spin quantum number $\sigma = \pm 1/2$, i.e. there are $2(2l+1)$ electron operators. The momentum sum runs over the magnitude of the momentum. The second line is written in the basis,

$$\chi_{km} = \begin{pmatrix} c_{km\uparrow} \\ c_{k-m\downarrow}^\dagger \end{pmatrix}, \tag{8.60}$$

in which space the Green's function,

$$G_{km}^0(t) = -i\theta(t) \left\langle \left\{ \chi_{km}(t), \chi_{km}^\dagger(0) \right\} \right\rangle, \tag{8.61}$$

has the Fourier transform,

$$G_{km}^0(\omega) = \frac{\hbar}{\hbar\omega - \xi_k \sigma_z - (-1)^m \Delta \sigma_x} = \hbar \frac{\hbar\omega + \xi_k \sigma_z + (-1)^m \Delta \sigma_x}{(\hbar\omega)^2 - (\xi_k^2 + \Delta^2)}. \tag{8.62}$$

In addition to the spin-flip interaction, we also include the spin-independent po-
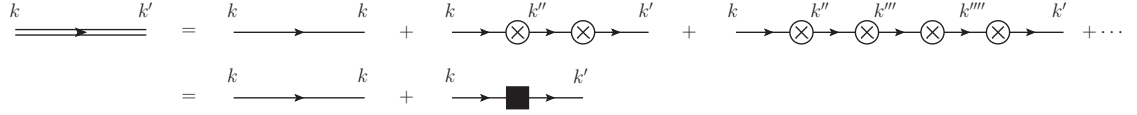
Figure 8.2: This is the Dyson equation. The double line represents the exact electrons Green's function, the single lines represents the unperturbed Green's function, and the circled cross represents the spin interactions $J\boldsymbol{\sigma}\cdot\boldsymbol{S}$. The black square on the second line represents the T-matrix.

tential interaction,

$$V\sum_{k,k'}\sum_{m,\sigma}c^{\dagger}_{k,m,\sigma}c_{k',m,\sigma}. \tag{8.63}$$

which conserves time-reversal symmetry to contrast with the spin-dependent exchange interaction, thus providing an explicit example of the Anderson theorem. We will see that if the only scattering potential was scalar, no bound state would be formed.

For simplicity, the classical spin is taken along the z-axis, $\boldsymbol{S} = S\boldsymbol{e}_z$, so that $S\sum_{\sigma}2\sigma c^{\dagger}_{k,m,\sigma}c_{k',m,\sigma}$. We can do that without loss of generality, because BCS theory is rotation symmetric, so the spin can always be rotated to point in any other direction. The scattering Hamiltonian takes the form,

$$H_{\text{scatt}} = \sum_{m}\sum_{k,k'}\chi^{\dagger}_{km}\left(JS + V\sigma_z\right)\chi_{k'm}. \tag{8.64}$$

The exact Green's function can be expressed through the Dyson equation in terms of the T-matrix as,

$$G_{k,k',m}(\omega) = G^{0}_{km}(\omega)\delta_{kk'} + G^{0}_{km}(\omega)T_m(\omega)G^{0}_{k'm}(\omega), \tag{8.65}$$

where $T_m(\omega)$ is the T-matrix of the m-channel. Note again that the exact Green's function is diagonal in m since no interaction generates affects it.

The Dyson equation is represented in terms of Feynman diagrams in Fig. 8.2. The T-matrix is extracted from the series as,

$$\begin{aligned}
T_m(\omega) =& \mathcal{J} + \mathcal{J}\sum_{k''}G^{0}_{k''}(\omega)\mathcal{J} + \mathcal{J}\sum_{k''}G^{0}_{k''}(\omega)\mathcal{J}\sum_{k''}G^{0}_{k''}(\omega)\mathcal{J} + \cdots \\
=& \mathcal{J}\left[1 - \sum_{k''}G^{0}_{k''}(\omega)\mathcal{J}\right]^{-1}
\end{aligned} \tag{8.66}$$
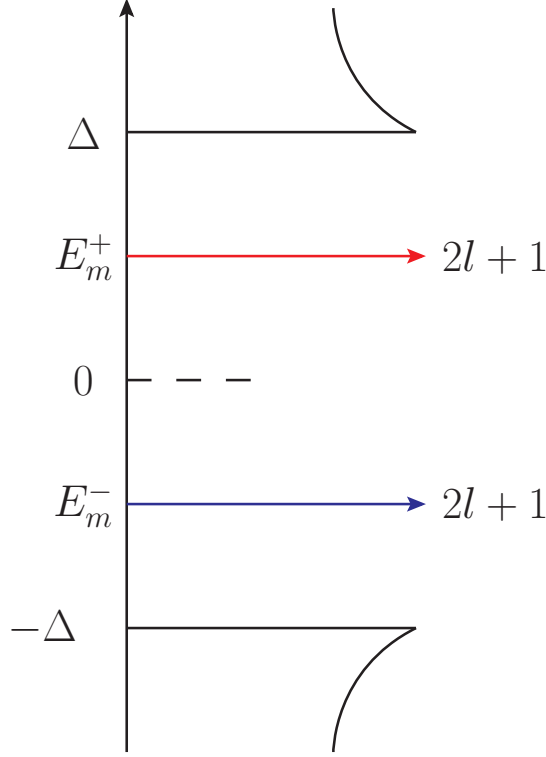
Figure 8.3: Hole-like (blue) and electron-like (red) YSR states arising from the classical impurity.

In this equation we defined the shorthand notation $\mathcal{J} = JS + V\sigma_z$. The infinite series $\sum_n x^n = (1-x)^{-1}$ has been used to obtain the second line. The sum of the Green function over the momenta is found to be,

$$\sum_k G^0_{km}(\omega) = -\pi\rho_F\hbar\frac{\hbar\omega + (-1)^m\Delta\sigma_2}{\sqrt{\Delta^2 - (\hbar\omega)^2}}. \tag{8.67}$$

The free Green's function G^0 do not contain poles within the energy gap. Therefore, the only poles within the gap come from the T matrix, which then corresponds to the only physical subgap excitations. The calculation of the T-matrix results in, [276]

$$T_m(\omega) = \frac{1}{\pi\rho_F}\frac{(\alpha^2 - \beta^2)\hbar\omega + (\alpha + \beta\sigma_z)\sqrt{\Delta^2 - (\hbar\omega)^2} + (-1)^m(\alpha^2 - \beta^2)\Delta\sigma_x}{(1 - \alpha^2 + \beta^2)\sqrt{\Delta^2 - (\hbar\omega)^2} + 2\alpha\hbar\omega}, \tag{8.68}$$

from which we deduce the poles location at,

$$E_m^\pm = \pm\Delta\frac{1-\alpha^2+\beta^2}{\sqrt{(1-\alpha^2+\beta^2)^2+4\alpha^2}}.\tag{8.69}$$

where the reduced coupling parameters are, $\alpha = JS\pi\rho_F$ and $\beta = V\pi\rho_F$. In the presence of the spin scattering channel, $\alpha \neq 0$, the poles have energies lower than the energy gap, i.e. signify the existence of subgap excitations. On the other hand, if only the scattering potential were present, $\alpha = 0$, then the pole energies condensate at the gap edge, i.e. the subgap states disappear. This is in accordance with the Anderson theorem. Furthermore, each of the two solutions, $E^\pm$ are $2l+1$ degenerate. Hence the energy spectrum consists of $2l+1$ states above the gap and $2l+1$ states below the gap. The physical states have been sketched in Fig. 8.3.

8.4   Summary

In this section, we introduced two models to describe impurity spins. The first is the Kondo model, which is a spin-spin interaction between the conduction electron spin, $\boldsymbol{s}$ and the impurity electron, $\boldsymbol{S}$, written as $J\boldsymbol{s}\cdot\boldsymbol{S}$. The simplest approximation is to think of the impurity spin as classical and fixed vector acting as a background. This reduces the interaction Hamiltonian to a quadratic spin-dependent electron-electron, allowing to solve the energy eigenspectrum exactly. The model is referred to as the Shiba model.

   We used this model to show the appearance of discrete energy bound states within the energy gap. The energies of the states are obtained from the poles of the scattering T-matrix, which shows that there exists one hole-like excitation with energy below the Fermi energy, and one electron-like excitation with energy above the Fermi energy. Both have degeneracy $2l+1$. The origin of the appearance of those states can be traced back to the Anderson model, as the $J\boldsymbol{s}\cdot\boldsymbol{S}$ interaction breaks time-reversal when the electron spin is flipped while maintaining the impurity spin fixed. This is unlike the potential scattering, which does not break time-reversal, and does not lead to subgap states, as was showed. We thus conclude that the appearance of subgap states is the signature of the presence of impurities with magnetic moment.

   Nevertheless, the classical spin model is insufficient to properly capture the dynamics of the impurity state, that is the impurity spin flip or valence occupation. We introduced the Anderson model for a quantum impurity with an s-wave character.

In this model the quantum impurity interacts with the conduction electrons via a hopping interaction: the conduction electrons can tunnel from the conduction band onto the impurity site, and vice versa. This interaction makes the impurity state a scattering resonance with a finite decay lifetime.

In the next chapter, we build on that model by further including orbital degeneracy, and embed it in a superconductor. We will show that the quantum impurity model does lead to YSR states whose degeneracy confirms the classical YSR model. We will use the model to study the YSR energy spectrum in two limits: with finite energy gap and vanishing on-site Coulomb interaction, and in the infinite energy gap and finite Coulomb interaction. The latter limit is useful because the large energy gap limit effectively integrates out the conduction electron, and leaves the subgap states as the only dynamical states of the system.

Chapter 9

Quantum Theory of orbitally-degenerate impurity states in superconductors

Several recent advancements are driving research to better understand the physics of impurities in superconductors. Recently, scanning tunneling microscopy experiments detected for the first time the orbital splitting of Yu-Shiba-Rusinov (YSR) subgap states induced by Mn [276] and Cr [275] impurities in superconducting Pb. A rich spatial structure was observed, reminiscent of the orbital structure of p- and d-atomic orbitals.

Another advancement is the realization that defect centers such as impurities might be responsible for noise and decoherence of quantum bits based on super-conducting devices. It was claimed that the fluctuation of the magnetic moment of various impurities may be the source of intrinsic magnetic flux noise in Superconducting QUantum Interference Devices (SQUIDs) and other superconductor-based qubits [298]. Several defect centers were considered as sources of noise, including dangling bonds [299], interface states [300], adsorbed molecules [301], and molecular oxygen [302, 303].

Furthermore, the development of the superconducting ion chip [277] showed that superconducting devices are a sensitive platform for optical spectroscopy and manipulation of neutral ions [278, 279] including Rydberg states with large radial quantum number n,[280, 281].

All these developments motivate the study of the superconducting proximity effect

on general atomic and molecular states. Usually, these studies are done by taking the impurity to be a classical spin, the so called Shiba model [272]. This shows that the magnetic moment of the impurity leads to the formation of Cooper-pair states inside the superconducting gap, the so called Yu-Shiba-Rusinov (YSR) states [273, 271, 272]. Under the classical spin approximation the orbital structure of the YSR states is solely related to the conduction electron orbital states of the superconductor [273]. In other words, the classical spin approximation ignores the native orbital structure of the isolated impurity.

In the current chapter we develop a quantum theory of orbitally-degenerate YSR states. Section 9.1 describes our model, which is based on the Anderson model for a spherically-symmetric hydrogenic impurity hybridized with a conventional (s-wave) superconductor. Section 9.2 describes exact solutions of this model for the case of zero Coulomb repulsion ($U = 0$) and general orbital quantum numbers n, l, m. Quite interestingly, this solution demonstrates that with a proper choice of exchange energy J it is possible to exactly map the YSR energy levels of the classical spin Shiba model into the YSR levels resulting from the $U = 0$ Anderson model. Section 9.3 describes exact solutions of our model in the case of infinite superconducting energy gap, $\Delta \to \infty$, and arbitrary on-site Coulomb repulsion U. We present detailed solutions for three kinds of impurities: s-wave, p-wave, and mixed s and p. These cases demonstrate qualitative differences from $U = 0$ in that the Bogoliubov picture breaks down and additional energy level splittings appear due to $U > 0$. We use angular momentum as the organizing principle and the Young tableaux formalism to categorize the various eigenstates. We adapt the spectroscopic notation to keep track of the symmetries and of the electron content of the YSR states. This notation facilitates the study of electric and magnetic transitions between YSR states, and in Section 9.4 we discuss the optical selection rules that apply to YSR states, and we display specific examples of transitions between the vacuum, the ground state and other YSR states.

9.1 Orbitally-degenerate Anderson model

We consider a hydrogenic impurity hybridized with a conventional s-wave BCS superconductor. The model Hamiltonian consists of three contributions,

$$\mathcal{H} = \mathcal{H}_{\text{imp}} + \mathcal{H}_{\text{BCS}} + \mathcal{H}_{\text{hyb}}, \tag{9.1}$$

with the impurity Hamiltonian

$$\mathcal{H}_{\mathrm{imp}} = \sum_{nlm\sigma} \xi_{nl} N_{nlm\sigma} + \sum_{n,n'} \frac{U_{nn'}}{2} N_n \left(N_{n'} - \delta_{nn'} \right), \tag{9.2}$$

generalizing the Anderson model to include electronic states with $l \geq 0$. Here, $N_{nlm\sigma} = d^{\dagger}_{nlm\sigma} d_{nlm\sigma}$ is the number operator, and $d^{\dagger}_{nlm\sigma}$ ($d_{nlm\sigma}$) is a creation (annihilation) operator for atomic state with unperturbed energy ξ_{nl}, radial quantum number $n = 1, 2, \cdots$, orbital angular momentum $l = 0, 1, \cdots, n-1$, azimuthal magnetic quantum number $m = -l, \cdots, l$, and spin $\sigma = \pm 1/2$. The operator $N_n = \sum_{lm\sigma} N_{nlm\sigma}$ counts the number of electrons in one energy shell, and the Coulomb on-site repulsion energy $U_{nn'}$ represents the energy required to allows for both $n = n'$ and $n \neq n'$ interactions.[304]

In the spherical wave basis, the BCS superconductor and the hybridization parts of the Hamiltonian have the form,

$$\mathcal{H}_{\mathrm{BCS}} = \sum_{k,l,m,\sigma} \left\{ \xi_k c^{\dagger}_{klm\sigma} c_{klm\sigma} - \Delta\sigma(-1)^m c^{\dagger}_{klm\sigma} c^{\dagger}_{kl-m-\sigma} + h.c \right\}$$
$$\mathcal{H}_{\mathrm{hyb}} = \sum_{kl'm'\sigma'} \sum_{nlm\sigma} \langle nlm\sigma | V | kl'm'\sigma' \rangle \; c^{\dagger}_{kl'm'\sigma'} d_{nlm\sigma} + h.c. \tag{9.3}$$

The operator $c^{\dagger}_{klm\sigma}$ ($c_{klm\sigma}$) creates (annihilates) a conduction electron of momentum k and energy $\xi_k = \epsilon_k - E_F$, with $\epsilon_k = \hbar^2 k^2 / 2m^*$ where m^* is the effective electron mass. The atomic electrons hybridize with conduction electrons through a spherically symmetry impurity potential, $V(r)$ breaking translational symmetry and leading to the overlap amplitude,[305, 306]

$$\langle nlm\sigma | V | kl'm'\sigma' \rangle = \delta_{\sigma\sigma'} \delta_{mm'} \delta_{ll'} \; V_{knl} \tag{9.4}$$

where V_{knl},

$$V_{knl} = \sqrt{\frac{2}{R}} k \int dr r^2 V(r) R_{nl}(r) j_l(kr), \tag{9.5}$$

with $j_l(kr)$ the spherical Bessel functions of the first kind, and $R_{nl}(r)$ the radial part of hydrogenic impurity wave functions, and the V_{knl} parameters are real. The resulting hybridization potential takes the form,

$$\mathcal{H}_{\mathrm{hyb}} = \sum_k \sum_{nlm\sigma} V_{knl} c^{\dagger}_{klm\sigma} d_{nlm\sigma} + h.c. \tag{9.6}$$

9.2 Quantum YSR states: Exact solution for $U = 0$

When $U = 0$, our model is a quadratic form of creation and destruction operators. Therefore, it can be diagonalized exactly by a canonical (Bogoliubov-like) transformation. Here we obtain the Green's function for the impurity, and explicitly calculate the energies and spectral weights of the subgap states.

Subsequently, we use the equation of motion as an alternative to the Bogoliubov to calculate the quasiparticle operators. This will show the nature of each subgap excitation, and explicitly show that as a result of the hybridization, the eigenstates are mixtures of conduction electron and impurity electrons.

9.2.1 Spectral functions and subgap energies

The Heisenberg equations of motion for the impurity and conduction electron operators read

$$\dot{d}_{nlm\sigma}(t) = -\frac{i\xi_{nl}}{\hbar}d_{nlm\sigma}(t) - \frac{i}{\hbar}\sum_k V^*_{knl}c_{klm\sigma}(t),$$

$$\dot{c}_{klm\sigma}(t) = -\frac{i\xi_k}{\hbar}c_{klm\sigma}(t) + 2\sigma(-1)^m\frac{i\Delta}{\hbar}c^\dagger_{kl-m-\sigma}(t) - \sum_n \frac{iV_{knl}}{\hbar}d_{nlm\sigma}(t).$$

$$(9.7)$$

By taking the Hermitian conjugate, and $\sigma \to -\sigma$, $m \to -m$, we obtain,

$$\dot{d}^\dagger_{nl-m-\sigma}(t) = \frac{i\xi_{nl}}{\hbar}d^\dagger_{nl-m-\sigma}(t) + \frac{i}{\hbar}\sum_k V_{knl}c^\dagger_{kl-m-\sigma}(t),$$

$$\dot{c}^\dagger_{kl-m-\sigma}(t) = \frac{i\xi_k}{\hbar}c^\dagger_{kl-m-\sigma}(t) + 2\sigma(-1)^m\frac{i\Delta^*}{\hbar}c_{klm\sigma}(t) + \sum_n \frac{iV^*_{knl}}{\hbar}d^\dagger_{nl-m-\sigma}(t).$$

$$(9.8)$$

The energy and spectral weights of physical states are obtained through the imaginary part of the retarded normal Green's function. Here we will assume the energy shell n to be fixed. For the impurity, the retarded normal Green's function is,

$$G^R_{nlm\sigma}(t) = -i\theta(t)\left\langle\left\{d_{nlm\sigma}(t), d^\dagger_{nlm\sigma}(0)\right\}\right\rangle,$$

$$(9.9)$$

with its time derivative,

$$\dot{G}^R_{nlm\sigma}(t) = -i\delta(t)\left\langle\left\{d_{nlm\sigma}(0), d^\dagger_{nlm\sigma}(0)\right\}\right\rangle - i\theta(t)\left\langle\left\{\dot{d}_{nlm\sigma}(t), d^\dagger_{nlm\sigma}(0)\right\}\right\rangle.$$

$$(9.10)$$

For the first term we use $\{d(0), d^\dagger(0)\} = 1$; for the second we plug Eq. (9.7). Because the Hamiltonian mixes the impurity electron with the conduction electron, as well as the time-reversed conduction electron through the BCS interaction, the EOM procedure will involve the following Green's functions,

$$F^R_{k,nlm\sigma}(t) = -i\theta(t)\left\langle\left\{c_{klm\sigma}(t), d^\dagger_{nlm\sigma}(0)\right\}\right\rangle,$$
$$\overline{G}^R_{nlm\sigma}(t) = -i\theta(t)\left\langle\left\{d^\dagger_{nl-m-\sigma}(t), d^\dagger_{nlm\sigma}(0)\right\}\right\rangle, \tag{9.11}$$
$$\overline{F}^R_{k,nlm\sigma}(t) = -i\theta(t)\left\langle\left\{c^\dagger_{kl-m-\sigma}(t), d^\dagger_{nlm\sigma}(0)\right\}\right\rangle.$$

The Green's functions F, $\overline{F}$ give the amount of mixing between the conduction and the impurity electrons. The $\overline{G}$ Green's function tell us about the proximity effect. That is, the ability of the impurity electrons to form pairs between electrons that are time-reversed of each other.

The EOM procedure leads to the closed system of equations,

$$\dot{G}^R_{nlm\sigma}(t) = -i\delta(t) - \frac{i\xi_{nl}}{\hbar}G^R_{nlm\sigma}(t) - \frac{i}{\hbar}\sum_k V^*_{knl}F^R_{k,nlm\sigma}(t),$$
$$\dot{\overline{G}}^R_{nlm\sigma}(t) = \frac{i\xi_{nl}}{\hbar}\overline{G}^R_{nlm\sigma}(t) + \frac{i}{\hbar}\sum_k V_{knl}\overline{F}^R_{k,nlm\sigma}(t), \tag{9.12}$$

and,

$$\dot{F}^R_{k,nlm\sigma}(t) = -\frac{i\xi_k}{\hbar}F^R_{k,nlm\sigma}(t) - \frac{iV_{knl}}{\hbar}G^R_{nlm\sigma}(t) + 2\sigma(-1)^m\frac{i\Delta}{\hbar}\overline{F}^R_{k,nlm\sigma}(t),$$
$$\dot{\overline{F}}^R_{k,nlm\sigma}(t) = \frac{i\xi_k}{\hbar}\overline{F}^R_{k,nlm\sigma}(t) + \frac{iV^*_{knl}}{\hbar}\overline{G}^R_{nlm\sigma}(t). + 2\sigma(-1)^m\frac{i\Delta^*}{\hbar}F^R_{k,nlm\sigma}(t) \tag{9.13}$$

The system is best solved in Fourier space, by first solving for $F^R_{k\sigma}(\omega)$ and $\overline{F}^R_{k\sigma}(\omega)$ through the equations,

$$(\hbar\omega + i\eta - \xi_k)F^R_{k,nlm\sigma}(\omega + i\eta) = V_{knl}G^R_{nlm\sigma}(\omega + i\eta) - 2\sigma(-1)^m\Delta\overline{F}^R_{k,nlm\sigma}(\omega + i\eta),$$
$$(\hbar\omega + i\eta + \xi_k)\overline{F}^R_{k,nlm\sigma}(\omega + i\eta) = -V^*_{knl}\overline{G}^R_{nlm\sigma}(\omega + i\eta) - 2\sigma\Delta^*F^R_{k,nlm\sigma}(\omega + i\eta).$$
$$\tag{9.14}$$

In order to avoid the poles $\hbar\omega = \pm\xi_k$, we analytically continue to complex frequencies $\omega \to \omega + i\eta$. Multiplying the first equation by $\hbar\omega + \xi_k$ and make use of the second equation. At the same time, we multiply the second equation by $\hbar\omega - \xi_k$, and

$$\Sigma_{nl}(\omega) = \quad \longrightarrow \otimes \text{ -- -} \blacktriangleright \text{ - -} \otimes \longrightarrow$$

with labels V_{knl}, V_{knl}^* above and $nlm\sigma$, $nlm\sigma$ below.

$$\Lambda_{nl}(\omega) = \quad \longrightarrow \otimes \Longrightarrow \blacktriangleleft \otimes \longleftarrow$$

with labels V_{knl}, V_{knl} above and $nlm\sigma$, $nl-m\text{ -- }\sigma$ below.
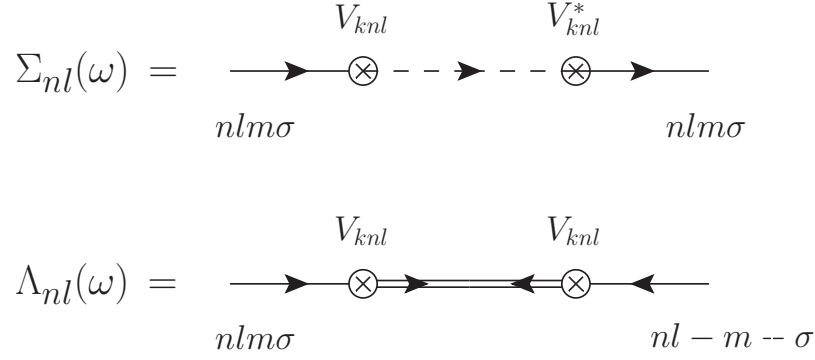
Figure 9.1: Feynman diagrams of processes giving rise to the impurity level self-energy $\Sigma_{nl}(\omega)$ (top), and SC proximity pairing potential $\Lambda_{nl}(\omega)$ (bottom). The dashed and double lines represent the conduction electron normal Green's functions, $-i\theta(t)\langle 0| c_{klm\sigma}(t)c_{klm\sigma}^{\dagger}(0)|0\rangle$, and anomalous Green's function $-i\theta(t)\langle 0| c_{klm\sigma}(t)c_{kl-m-\sigma}(0)|0\rangle$, respectively, as calculated in Sec. 7.2

make use of the first equation. In this way, we find the solutions,

$$
\begin{aligned}
F^R_{k,nlm\sigma}(\omega+i\eta) =& \frac{V_{knl}(\hbar\omega+i\eta+\xi_k)}{(\hbar\omega+i\eta)^2 - E_k^2}G^R_{nlm\sigma}(\omega+i\eta) \\
& + 2\sigma(-1)^m \frac{V_{knl}^*\Delta}{(\hbar\omega+i\eta)^2 - E_k^2}\overline{G}^R_{nlm\sigma}(\omega+i\eta), \\
\overline{F}^R_{k,nlm\sigma}(\omega+i\eta) =& -\frac{V_{knl}^*(\hbar\omega+i\eta-\xi_k)}{(\hbar\omega+i\eta)^2 - E_k^2}\overline{G}^R_{nlm\sigma}(\omega+i\eta) \\
& - 2\sigma(-1)^m \frac{V_{knl}\Delta^*}{(\hbar\omega+i\eta)^2 - E_k^2}G^R_{nlm\sigma}(\omega+i\eta).
\end{aligned}
\tag{9.15}
$$

where $E_k^2 = \xi_k^2 + |\Delta|^2$. Now that we have these functions, the following sums are expressed as,

$$
\begin{aligned}
\sum_k V_{knl}^* F^R_{k,nlm\sigma}(\omega+i\eta) =& G^R_\sigma(\omega)\Sigma_{nl}(\omega+i\eta) \\
& + 2\sigma(-1)^m \overline{G}^R_{nlm\sigma}(\omega+i\eta)\Lambda_{nl}(\omega+i\eta), \\
-\sum_k V_{knl} \overline{F}^R_{k,nlm\sigma}(\omega+i\eta) =& -\Sigma_{nl}^*(-\omega+i\eta)\overline{G}^R_{nlm\sigma}(\omega+i\eta) \\
& + 2\sigma(-1)^m \Lambda_{nl}^*(\omega+i\eta)G^R_{nlm\sigma}(\omega+i\eta).
\end{aligned}
\tag{9.16}
$$

with the impurity self energies, and the proximity pairing potentials,

$$\Sigma_{nl}(\omega) = \sum_k \frac{|V_{knl}|^2(\hbar\omega + \xi_k)}{(\hbar\omega)^2 - E_k^2},$$

$$\Lambda_{nl}(\omega) = \sum_k \frac{V_{knl}^* V_{knl}^* \Delta}{(\hbar\omega)^2 - E_k^2}, \tag{9.17}$$

In Fig. 9.1, we show that Feynman diagrams that generate the self-energy and proximity pairing potential at the second order in perturbation theory, mediated by the electrons Green's functions in the superconducting state [286]. Now we turn to the equation for $G_{nlm\sigma}^R(\omega)$ and $\overline{G}_{nlm\sigma}^R(\omega)$,

$$(\hbar\omega + i\eta - \xi_{nl})\, G_{nlm\sigma}^R(\omega + i\eta) = \hbar + \sum_k V_{knl}^* F_{k,nlm\sigma}^R(\omega + i\eta)$$

$$(\hbar\omega + i\eta + \xi_{nl})\, \overline{G}_{nlm\sigma}^R(\omega + i\eta) = -\sum_k V_{knl} \overline{F}_{k,nlm\sigma}^R(\omega + i\eta). \tag{9.18}$$

which, using the sum over the F and $\overline{F}$ functions above, take the form,

$$(\hbar\omega + i\eta - \xi_{nl} - \Sigma_{nl}(\omega + i\eta))\, G_{nlm\sigma}^R(\omega) = \hbar + 2\sigma(-1)^m \overline{G}_{nlm\sigma}^R(\omega)\Lambda_{nl}(\omega)$$

$$(\hbar\omega + i\eta + \xi_{nl} + \Sigma_{nl}^*(-\omega + i\eta))\, \overline{G}_{nlm\sigma}^R(\omega + i\eta) = 2\sigma(-1)^m \Lambda_{nl}^*(\omega + i\eta)\overline{G}_{n\sigma}^R(\omega + i\eta). \tag{9.19}$$

This system has the solution,

$$G_{nlm\sigma}^R(\omega + i\eta) = \hbar \frac{\hbar\omega + i\eta + \xi_{nl} + \Sigma_{nl}(-\omega)}{Q_{nl}(\omega + i\eta)}, \tag{9.20}$$

where

$$Q_{nl}(\omega + i\eta) = (\hbar\omega - \xi_{nl} - \Sigma_{nl}(\omega + i\eta))(\hbar\omega + \xi_{nl} + \Sigma_{nl}^*(-\omega + i\eta)) - |\Lambda_{nl}(\omega + i\eta)|^2. \tag{9.21}$$

The energies of the physical states are at the poles of Eq. (9.21), which are given by the real roots of the equation, $Q_{nl}(\omega + i\eta) = 0$. For each n, l, there are $2l + 1$ such equations, and each is a function of ω^2. Therefore, for each n,l we get two subgap energy levels, one at $+E_{nl}$ and the other at $-E_{nl}$. Each level has a $(2l + 1)$-fold degeneracy, making a total of $2(2l + 1)$ subgap bound states. This is as many states as was found in the Shiba model for a classical spin.
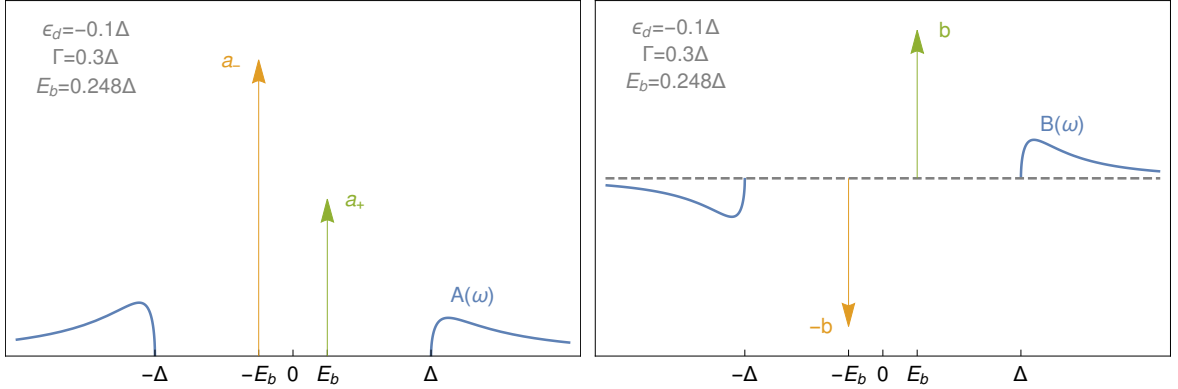
Figure 9.2: Plots of the normal (left) and anomalous (right) spectral functions for a quantum impurity.

In order to calculate the exact energy poles, it is necessary to evaluate the self energy and proximity potentials. We analytically continue the frequency into the complex plane, $\omega \to \omega + i\eta$, with a positive $\eta \to 0^+$ because the Green's function is a retarded Green's function. We find,

$$\Sigma_{nl}(\omega + i\eta) = -\sum_{k} \frac{|V_{knl}|^2 (\hbar\omega + \xi_k)}{\xi_k^2 + |\Delta|^2 - (\hbar\omega + i\eta)^2} \approx \begin{cases} -\frac{\hbar\omega}{\sqrt{|\Delta|^2 - (\hbar\omega)^2}}\Gamma_{nl} & |\Delta| > \hbar\omega \\ -i\frac{|\hbar\omega|}{\sqrt{(\hbar\omega)^2 - |\Delta|^2}}\Gamma_{nl} & |\Delta| < \hbar\omega \end{cases}$$

$$(9.22)$$

where the decay rate Γ_{nl} expresses the rate of decay of an impurity electron into the conduction electron sea. It is expressed as,

$$\Gamma_{nl} = \pi \rho_F \left\langle |V_{knl}|^2 \right\rangle_{\Omega} \Big|_{\epsilon_k = E_F}, \qquad (9.23)$$

where the average is taken over all momenta states with magnitude $\epsilon_k = E_F$. Furthermore, the proximity pairing potential is found as,

$$\Lambda_{nl}(\omega + i\eta) = -(-1)^m \sum_{k} \frac{|V_{knl}|^2 \Delta}{\xi_k^2 + |\Delta|^2 - (\hbar\omega + i\eta)^2} \approx (-1)^m \begin{cases} -\frac{\Delta}{\sqrt{|\Delta|^2 - (\hbar\omega)^2}}\Gamma_{nl} & |\Delta| > \hbar\omega \\ -i\frac{\Delta \, \text{sign}(\omega)}{\sqrt{(\hbar\omega)^2 - |\Delta|^2}}\Gamma_{nl} & |\Delta| < \hbar\omega \end{cases}$$

$$(9.24)$$

The poles of the Green's function are given by the root equation $Q(\omega + i\eta) = 0$, which

takes the form,

$$(\hbar\omega)^2 \left(1 + 2\frac{\Gamma_{nl}}{\sqrt{\Delta^2 - (\hbar\omega)^2}}\right) = \xi_{nl}^2 + \Gamma_{nl}^2 \qquad |\hbar\omega| < \Delta \tag{9.25a}$$

$$(\hbar\omega - \xi_{nl})^2 + \Gamma_{nl}^2 = 0 \qquad \Delta < |\hbar\omega| \tag{9.25b}$$

Thus, for each ξ_{nl} the impurity Green's function only has two poles that are within the gap, each appearing with multiplicity $2l + 1$. Those are the YSR states. The equation Eq. (9.25b) never has real roots.

The YSR energy level structure emerging from the roots of Eq. (9.26a) turns out to be identical to the one obtained by the classical spin Shiba model, see Eq. (8.69). The only difference is the presence of ξ_{nl} in Eq. (9.25a). If for each n, l we associate a different classical spin impurity interacting with the conduction electrons via $J_{nl} \sum_{k\sigma,k'\sigma',m} c^\dagger \boldsymbol{\sigma} c \cdot \boldsymbol{S}_{nl}$, then we are able to find a suitable J_{nl} that reproduces the roots of Eq. (9.25a) exactly. This leads to an important conclusion: That the YSR energy levels of the classical spin Shiba model may be mapped exactly into the YSR levels of the U=0 Anderson model. We emphasize that this mapping is not obtained from a canonical transformation such as Schrieffer-Wolff [297]– it is just a formal parametrization of the parameter J_{nl} in terms of ξ_{nl}, Γ_{nl}, and Δ.

The spectral functions for the impurity are given by $\mathcal{A}_{nlm\sigma}(\omega) = -\text{Im}\{G_{nlm\sigma}^R(\omega + i\eta)\}/\pi$, and the anomalous by $\mathcal{B}_{nlm\sigma}(\omega) = -\text{Im}\{\overline{G}_{nlm\sigma}^R(\omega + i\eta)\}/\pi$. We get

$$\mathcal{A}_{nlm\sigma}(\omega) = A_{nl}(\hbar\omega)\Theta(|\hbar\omega| - \Delta) + a_+\delta(\hbar\omega - E_b) + a_-\delta(\hbar\omega + E_b),$$
$$\mathcal{B}_{nlm\sigma}(\omega) = 2\sigma\left\{B_{nl}(\hbar\omega)\Theta(|\hbar\omega| - \Delta) + b\left[\delta(\hbar\omega - E_b) - \delta(\hbar\omega + E_b)\right]\right\} \tag{9.26}$$

where

$$a_\pm = \hbar\frac{\Delta^2 - E_b^2}{2}\frac{(\xi_{nl} \pm E_b)^2 + \Gamma_{nl}^2}{(\xi_{nl}^2 + \Gamma_{nl}^2)(2\Delta^2 - E_b^2) - E_b^4}$$

$$A_{nl}(x) = \hbar\frac{\Gamma_{nl}|x|\sqrt{x^2 - \Delta^2}}{\pi}\frac{(x + \xi_{nl})^2 + \Gamma_{nl}^2}{(x^2 - \Delta^2)[(x^2 + \xi_{nl}^2 + \Gamma_{nl}^2)^2 - 4x^2\xi_{nl}^2] + 4\Gamma_{nl}^2\Delta^2 x^2}$$

$$b = \hbar\frac{\Gamma_{nl}\Delta E_b\sqrt{\Delta^2 - E_b^2}}{(\xi_{nl}^2 + \Gamma_{nl}^2)(2\Delta^2 - E_b^2) - E_b^4}$$

$$B_{nl}(x) = -\hbar\frac{\Gamma_{nl}\Delta \text{sign}(x)\sqrt{x^2 - \Delta^2}}{\pi}\frac{x^2 - \xi_{nl}^2 - \Gamma_{nl}^2}{(x^2 - \Delta^2)[(x^2 + \xi_{nl}^2 + \Gamma_{nl}^2)^2 - 4x^2\xi_{nl}^2] + 4x^2\Delta^2\Gamma_{nl}^2}$$

$$\tag{9.27}$$
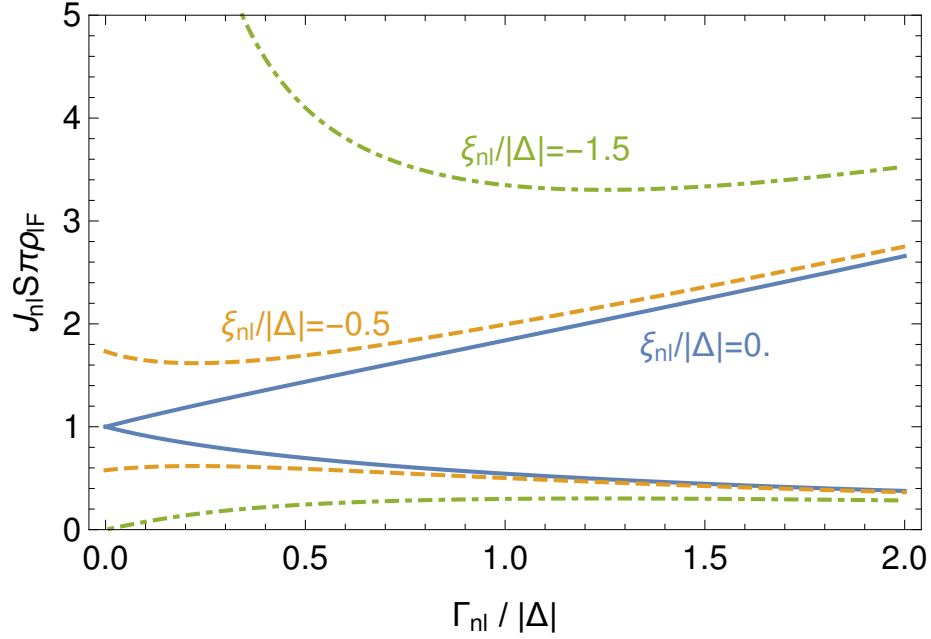
Figure 9.3: The two solutions α (solid and dashed) as a function of Γ_{nl} for which the classical and quantum $U = 0$ YSR energy spectra are equivalent, for three values of ξ_{nl}.

The quantum YSR energies are the solutions of Eq. (9.25a), while the energies of the classical YSR states are, Eq. (8.69), $\pm\Delta(1 - \alpha_{nl}^2)/(1 + \alpha_{nl}^2)$, where $\alpha_{nl} = J_{nl}S\pi\rho_{lF}$, where ρ_{lF} is the density at the Fermi level of conduction electrons in the l orbital state. We now show that the two are equivalent in the sense that there always exists a set of parameters $\{\xi_{nl}, \Gamma_{nl}, \alpha\}$, for which the two solutions are equal. This set of parameters is found by plugging the classical energies E_b^c into the equation for the quantum YSR states, and we obtain,

$$\Delta^2 \left(\frac{1 - \alpha_{nl}^2}{1 + \alpha_{nl}^2}\right)^2 \left[1 + \frac{1 + \alpha_{nl}^2}{\alpha_{nl}}\frac{\Gamma_{nl}}{\Delta}\right] = \xi_{nl}^2 + \Gamma_{nl}^2. \tag{9.28}$$

This equation always has two real solutions, $\alpha > 0$, which we plotted in Fig. 9.3 as a function of Γ_{nl} for various bare impurity levels ξ_{nl}. This is not a formal canonical transformation equivalence in the sense of Schrieffer-Wolff, but it is a proof that the energy levels of the Shiba's classical model can be reproduced by the $U = 0$ quantum model as long as we choose a suitable set of parameters ξ_{nl}/Δ and Γ_{nl}/Δ.

9.2.2 Bogoliubov transformation

In this section, we diagonalize the $U = 0$ Anderson+BCS model exactly with a Bogoliubov canonical transformation. In order for that, we go back to the system of Heisenberg equations of motion, Eqs. (9.7) and (9.8), written in Fourier space. The EOM for the impurity electron,

$$
\begin{aligned}
(\hbar\omega - \xi_{nl})\, d_{nlm\sigma}(\omega) &= \sum_k V^*_{knl} c_{klm\sigma}(\omega) \\
(\hbar\omega + \xi_{nl})\, d^\dagger_{nl-m-\sigma}(-\omega) &= -\sum_k V_{knl} c^\dagger_{kl-m-\sigma}(-\omega)
\end{aligned}
\tag{9.29}
$$

and that for the conduction electrons,

$$
\begin{aligned}
(\hbar\omega - \xi_k)\, c_{klm\sigma}(\omega) &= -2\sigma(-1)^m \Delta c^\dagger_{kl-m-\sigma}(-\omega) + \sum_n V_{knl} d_{nlm\sigma}(\omega) \\
(\hbar\omega + \xi_k)\, c^\dagger_{kl-m-\sigma}(-\omega) &= -2\sigma(-1)^m \Delta c_{klm\sigma}(\omega) - \sum_n V^*_{knl} d^\dagger_{nl-m-\sigma}(-\omega).
\end{aligned}
\tag{9.30}
$$

We limit ourselves to the case of a fixed energy shell n. We multiply the top equation by $\hbar\omega + \xi_k$ and make use of the bottom equation. This procedure leads to the equation

$$
\left[(\hbar\omega)^2 - E_k^2\right] c_{klm\sigma}(\omega) = d_{nlm\sigma}(\omega) V_{knl} (\hbar\omega + \xi_k) + 2\sigma(-1)^m d^\dagger_{nl-m-\sigma}(-\omega) V^*_{knl} \Delta,
\tag{9.31}
$$

whose solution is,

$$
\begin{aligned}
c_{klm\sigma}(\omega) = &\sum_\alpha \mathcal{K}^\alpha_{klm\sigma} \delta\left(\hbar\omega - \alpha E_k\right) \\
&+ d_{nlm\sigma}(\omega)\mathcal{P}\frac{V_{knl}(\hbar\omega + \xi_k)}{(\hbar\omega)^2 - E_k^2} + 2\sigma(-1)^m d^\dagger_{nl-m-\sigma}(-\omega)\mathcal{P}\frac{V^*_{k,nl-m}\Delta}{(\hbar\omega)^2 - E_k^2}
\end{aligned}
\tag{9.32}
$$

The fractions are understood to be Cauchy principal parts. The index $\alpha = \pm$ refers to the two solutions $\hbar\omega = \pm E_k$. The time-reversal symmetry imposes a redundancy among the $\mathcal{K}^\alpha_{klm\sigma}$ operators, expressed through the relation,

$$
\left(\mathcal{K}^{-\alpha}_{kl-m-\sigma}\right)^\dagger = -2\sigma(-1)^m \frac{\alpha E_k - \xi_k}{\Delta}\mathcal{K}^\alpha_{klm\sigma}
\tag{9.33}
$$

Plugging the $c_{klm\sigma}(\omega)$ solution into the equations Eq. (9.29) for the impurity equations, and ignoring the terms relating to the conduction electrons, we obtain the

equations,

$$[\hbar\omega - \xi_{nl} - \Sigma_{nl}(\omega)] d_{nlm\sigma}(\omega) = 2\sigma(-1)^m d^\dagger_{nl-m-\sigma}(-\omega)\Lambda_{nl}(\omega)$$

$$+ \sum_{k\alpha} V^*_{knl}\mathcal{K}^\alpha_{klm\sigma}\delta(\hbar\omega - \alpha E_k)$$

$$[\hbar\omega + \xi_{nl} + \Sigma_{nl}(-\omega)] d^\dagger_{nl-m-\sigma}(-\omega) = 2\sigma(-1)^m d_{nlm\sigma}(\omega)\Lambda^*_{nl}(\omega)$$

$$+ 2\sigma(-1)^m \sum_{k\alpha} V_{knl}\frac{\alpha E_k - \xi_k}{\Delta}\mathcal{K}^\alpha_{klm\sigma}\delta(\hbar\omega - \alpha E_k)$$

$$(9.34)$$

Again, multiplying the top equation by $\hbar\omega + \xi_{nl} + \Sigma_{nl}(-\omega)$ and making use of the bottom equation, we can put the solution into the form, $Q_{nl}(\omega)d_{nlm\sigma}(\omega) = 0 + \{\mathcal{K}^\alpha_k\}'s$, whose formal solution is of the form,

$$d_{nlm\sigma}(\omega) = \mathcal{K}_{nlm\sigma}(\omega)\delta[Q_{nl}(\omega)]$$

$$+ \sum_\alpha \mathcal{P}\sum_k \left\{ \left[\frac{\alpha E_k - \xi_k}{\Delta}\frac{V_{knl}\Lambda_{nl}(\alpha E_k)}{Q_{nl}(\alpha E_k)} + \frac{V^*_{km}(\alpha E_k + \xi_{nl} + \Sigma_{nl}(-\alpha E_k))}{Q_{nl}(\alpha E_k)}\right] \right.$$

$$\left. \mathcal{K}^\alpha_{klm\sigma}\delta(\hbar\omega - \alpha E_k) \right\}$$

$$(9.35)$$

With the function $Q_{nl}(\omega) \equiv [\hbar\omega - \xi_{nl} - \Sigma_{nl}(\omega)][\hbar\omega + \xi_{nl} + \Sigma_{nl}(-\omega)] - |\Lambda^2_{nl}(\omega)|^2$. For the calculation of the retarded Green's function, the function $Q(\omega)$ acquired an imaginary part as a result of the analytical continuation $\omega \to \omega + i0^+$, which is only possible because the retarded Green's function has definite time-ordering $t > 0$.

On the contrary, the real time impurity operator, $d_{nlm\sigma}(t)$, does not have a time-ordering, as it is valid for *all* times. It is therefore impossible to analytically continue into complex frequencies. The result is that the self-energy and proximity potentials $\Sigma_{nl}(\omega)$ and $\Lambda_{nl}(\omega)$ are both strictly real, and so is $Q_{nl}(\omega)$. As a consequence, the poles of the Dirac delta $\delta[Q_{nl}(\omega)]$ are at $[\hbar\omega - \Sigma_{nl}(\omega)]^2 = \xi^2_{nl} + |\Lambda_{nl}(\omega)|^2$, equivalent to

$$(\hbar\omega)^2\left(1 + 2\frac{\Gamma_{nl}}{\sqrt{\Delta^2 - (\hbar\omega)^2}}\right) = \xi^2_{nl} + \Gamma^2_{nl}. \qquad (9.36)$$

This equation is the same as Eq. (9.25a), the one for the location of the poles of the Green's function. As argued then, this equation gives $2l + 1$ degenerate energies,

symmetric with respect to the Fermi level, that is half of the spectrum is electron like (above the Fermi level), and half is hole like (below the Fermi level). We express the result for the impurity operator as,

$$d_{nlm\sigma}(\omega) = \sum_\alpha \mathcal{D}^\alpha_{nlm\sigma} \delta\left(\hbar\omega - \alpha E_{bm}\right) + \sum_\alpha \mathcal{P} \sum_k [...]\mathcal{K}^\alpha_{km\sigma}\delta\left(\hbar\omega - \alpha E_k\right), \qquad (9.37)$$

where $\alpha = \pm$. The two operators $\mathcal{D}^\pm$ are redundant. The redundancy can be found by taking the time-reversed impurity operator as obtained from the solution $d_{nlm\sigma}(\omega)$ and from the top equation in the system Eq. (9.34). Equating the two allows to find the relation,

$$\left(\mathcal{D}^{-\alpha}_{nl-m-\sigma}\right)^\dagger = 2\sigma(-1)^m \frac{E^\alpha_b - \xi_{nl} - \Sigma_{nl}(E^\alpha_b)}{\Lambda_{nl}(E^\alpha_b)}\mathcal{D}^\alpha_{nlm\sigma}. \qquad (9.38)$$

We eliminate the $\mathcal{D}^-$ in favor of $\mathcal{D}^+$. Furthermore, we define new operators $\gamma_{nlm\sigma}$ by making the rescaling $\mathcal{D}^+_{nlm\sigma} = 2\pi\hbar u\gamma_{nlm\sigma}$ so that we find,

$$\begin{aligned} d_{nlm\sigma}(t = 0) =& u\gamma_{nlm\sigma} - 2\sigma(-1)^m v\gamma^\dagger_{nl-m-\sigma} \\ &+ \sum_k \left[u_k\gamma_{km\sigma} - 2\sigma(-1)^m v_k\gamma^\dagger_{k-m-\sigma}\right] \end{aligned} \qquad (9.39)$$

with the definition,

$$v = \frac{E_b - \xi_{nl} - \Sigma_{nl}(E_b)}{\Lambda_{nl}(E_b)}u^*. \qquad (9.40)$$

Imposing canonical commutation relations among the $\gamma_{nlm\sigma}$, $\gamma_{km\sigma}$ operators leads to the normalization condition of the amplitudes,

$$|u|^2 + |v|^2 + \sum_k \left[|u_k|^2 + |v_k|^2\right] = 1. \qquad (9.41)$$

In solving for the operators, we found two kinds of quasiparticles; the impurity-like quasiparticle created by $\gamma^\dagger_{nlm\sigma}$ and the conduction electron-like quasiparticle, created by $\gamma^\dagger_{klm\sigma}$. We found that the impurity electron operator, $d^\dagger_{nlm\sigma}$ is a linear combination of both. Formally inverting will show that an "impurity" quasiparticle, $\gamma^\dagger_{nlm\sigma}$, is a mixture of conduction and impurity electrons, similarly, a conduction electron will be a mixture of impurity and conduction electrons. This is a manifestation of the hybridization coupling between the impurity and the conduction electron sea.

9.3 Quantum YSR states in the superconducting atomic limit (Large Δ)

We now describe a formal procedure to integrate out the conduction electrons in the $\Delta \to \infty$ limit. The procedure will provide us with an effective Hamiltonian for the impurity degrees of freedom. As such, this allows to obtain the impurity-like quasiparticles, in terms of coefficients u, v that include effects of conduction electrons.

The complete impurity–superconductor Hamiltonian includes all physical processes involving electrons with energies above and below the gap, Δ. By integrating out the above-gap energy electrons, we obtain an effective model that encapsulates the essential proximity effect on the atomic states. The regime of validity of such a model is generally referred to as the *superconducting atomic limit*,[307, 308, 295, 309]. Our method relies on eliminating the conduction electron operators the Heisenberg equation of motion for the impurity electron operators $d_\sigma(t)$. In the limit $\Delta \to \infty$ this method yields an exact solution of the Anderson+BCS model for arbitrary values of U.

By writing the Heisenberg equation of motion for a conduction electron, $\dot{c}_{klm\sigma}(t)$, based on the complete generalized Anderson Hamiltonian, Eq. (9.1), and Fourier transforming to frequency ω, we get

$$
\begin{aligned}
\left[(\hbar\omega)^2 - E_k^2\right] c_{klm\sigma}(\omega) = \sum_n \Big[& (\hbar\omega + \xi_k)\, V_{knl}\, d_{nlm\sigma}(\omega) \\
& + 2\sigma\Delta V_{knl}^*\, d_{nlm\sigma}^\dagger(-\omega) \Big],
\end{aligned}
\tag{9.42}
$$

with the conduction electron energies $\xi_k = \hbar^2 k^2/2m^* - E_F$ and the BCS quasiparticle energies $E_k^2 = \xi_k^2 + |\Delta|^2$. In the limit where $\hbar\omega \ll \Delta$, the processes with above-gap energies freeze out and lead to a linearized equation for the operators $c_{klm\sigma}(\omega)$ in terms of the impurity operators $d_{nlm\sigma}(\omega)$. An inverse-Fourier transform gives the solution,

$$
\begin{aligned}
c_{klm\sigma}(t) = -\sum_n \Big[& \frac{\xi_k}{E_k^2} V_{knl} d_{nlm\sigma}(t) \\
& + 2\sigma \frac{\Delta}{E_k^2} V_{knl}^* d_{nl-m-\sigma}^\dagger(t) \Big].
\end{aligned}
\tag{9.43}
$$

Upon inserting this solution into $\mathcal{H}_{\text{hyb}}$ and $\mathcal{H}_{\text{BCS}}$, leads to the superconducting atom
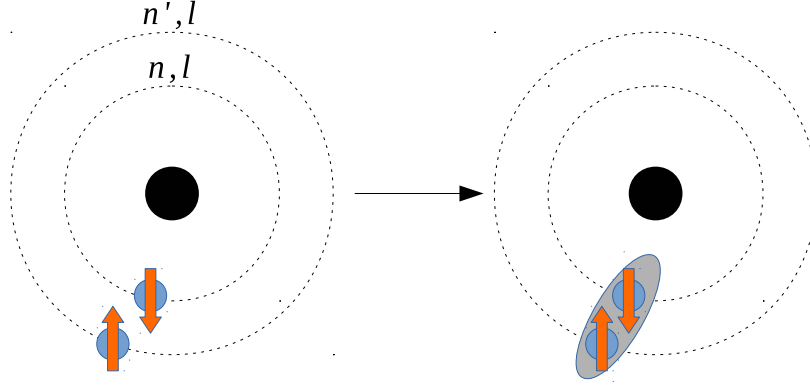
Figure 9.4: Sketch of the superconducting atomic limit, where two electrons undergo pair binding reminiscent to Cooper pair binding.

Hamiltonian

$$\mathcal{H}_{\text{eff}} = \mathcal{H}'_{\text{imp}} + \mathcal{H}_{\text{prox}}, \tag{9.44}$$

where $\mathcal{H}'_{\text{imp}}$ is the impurity potential with renormalized energy levels, and $\mathcal{H}_{\text{prox}}$ accounts for the proximity effect on the impurity,

$$
\begin{aligned}
\mathcal{H}'_{\text{imp}} &= \mathcal{H}_{\text{imp}} + \sum_{n'nlm\sigma} \Sigma_{nl,n'l}\, d^{\dagger}_{nlm\sigma} d_{n'lm\sigma} \\
\mathcal{H}_{\text{prox}} &= - \sum_{n'nlm\sigma} \sigma(-1)^m \tilde{\Delta}_{nl,n'l} d^{\dagger}_{nlm\sigma} d^{\dagger}_{n'l-m-\sigma} + h.c,
\end{aligned}
\tag{9.45}
$$

where,

$$\tilde{\Delta}_{nl,n'l} = \sum_{\boldsymbol{k}} \frac{\Delta}{E_k^2} V^*_{knl} V^*_{kn'l}, \tag{9.46a}$$

$$\Sigma_{nl,n'l} = \sum_{\boldsymbol{k}} \frac{\xi_k}{E_k^2} V_{knl} V^*_{kn'l}, \tag{9.46b}$$

are the induced pairing potential and the impurity self-energy, respectively. Note that the induced pairing Eq. (9.46a) does not bind impurity electrons that have different orbital angular momentum. This is a consequence of our assumption of spherically symmetric impurity potential $V(r)$.

The process of integrating out the conduction electrons led to a model of an atom whose electrons undergo Cooper-pair binding. The proximity Hamiltonian $\mathcal{H}_{\text{prox}}$, Eq. (9.45) induces pair-binding of an impurity electron in state m, σ with an electron

in state $-m, -\sigma$. A sketch of the superconducting atomic limit is represented in Fig. 9.4. The induced pairing $\tilde{\Delta}_{nl,n'l}$ can be expressed as follows,

$$
\begin{aligned}
\tilde{\Delta}_{nl,n'l} &= \sum_{\boldsymbol{k}} \frac{\Delta}{E_k^2} V_{knl}^* V_{kn'l}^* \\
&= \int_{-\hbar\omega_c}^{\hbar\omega_c} d\xi_k \rho(\xi_k) \frac{\Delta}{E_k^2} \langle V_{knl}^* V_{kn'l}^* \rangle (\xi_k) \\
&\simeq 2\rho_{lF} \langle V_{knl}^* V_{kn'l}^* \rangle \int_0^{\hbar\omega_c} d\xi_k \frac{\Delta}{\xi_k^2 + \Delta^2} \\
&= 2\rho_{lF} \langle V_{knl}^* V_{kn'l}^* \rangle \tan^{-1}\left(\frac{\hbar\omega_c}{|\Delta|}\right) \frac{\Delta}{|\Delta|}.
\end{aligned}
\tag{9.47}
$$

For most conventional superconductors we have $\hbar\omega_c \simeq 30|\Delta|$ [282]. In this regime, the induced pairing is well approximated by,

$$
\tilde{\Delta}_{nl,n'l} = \pi\rho_{lF} \langle V_{knl}^* V_{kn'l}^* \rangle \frac{\Delta}{|\Delta|},
\tag{9.48}
$$

loosing all dependence on the energy gap. In the specific case where the pairing takes place between two electrons on the same shell, $n = n'$, the induced pairing becomes the decay width,

$$
\tilde{\Delta}_{nl,nl} = \pi\rho_{lF} \langle V_{knl} \rangle \frac{\Delta}{|\Delta|} = \Gamma_{nl} \frac{\Delta}{|\Delta|}.
\tag{9.49}
$$

From now on we take the energy gap to be real, $\Delta = |\Delta|$. Hence, the effective Hamiltonian takes the form,

$$
\begin{aligned}
\mathcal{H}_{\text{imp}} &= \sum_{nlm\sigma} (\xi_{nl} + \Sigma_{nl,nl}) \, d_{nlm\sigma}^\dagger d_{nlm\sigma} \\
\mathcal{H}_{\text{prox}} &= -\sum_{nlm\sigma} \sigma(-1)^m \Gamma_{nl} d_{nlm\sigma}^\dagger d_{nl-m-\sigma}^\dagger + h.c.
\end{aligned}
\tag{9.50}
$$

Note that the functions $\tilde{\Delta}_{nl,nl}$ and $\Sigma_{nl,nl}$ are related to the proximity pairing and self-energy functions introduced in Sec. 9.2,

$$
\tilde{\Delta}_{nl,nl} = \Lambda_{nl}(\omega = 0), \quad \Sigma_{nl,nl} = \Sigma_{nl}(\omega = 0).
\tag{9.51}
$$

9.3.1 Bogoliubov transformation of the limit with $U = 0$

We restrict our attention to the case of impurity electrons in a single n, l shell. Because of this simplification, we remove the nl subscript from the impurity electron operator $d_{m\sigma}$.

The Hamiltonian can be diagonalized through a Bogoliubov transformation. We present a technique to perform the Bogoliubov transformation, that relies on the Heisenberg equation of motion (EOM) for the impurity operators, and writing the equation in Fourier space, we find,

$$(\hbar\omega - \xi_{nl})d_{m\sigma}(\omega) = -2\sigma(-1)^m \Gamma_{nl} d^\dagger_{-m-\sigma}(-\omega). \tag{9.52}$$

By further writing the equation for the operator $d^\dagger_{-m-\sigma}(-\omega)$, we can find the equation,

$$\left[(\hbar\omega)^2 - E_{nl}^2\right] d_{m\sigma}(\omega) = 0. \tag{9.53}$$

where $E_{nl} = \sqrt{\xi_{nl} + |\Gamma_{nl}|^2}$. Using the property that the solution of an equation of the form $xf(x) = 0$ must have the form of a Dirac delta function, $f(x) \propto \delta(x)$, the solution to the above equation generally takes the form $d_{m\sigma}(\omega) = K^+_{m\sigma}\delta(\hbar\omega - E_{nl}) + K^-_{m\sigma}\delta(\hbar\omega + E_{nl})$, with two operators $K^\pm_{m\sigma}$ that are undetermined for now. The EOM, Eq. (9.52), relates the operators $d_{m\sigma}$ and $d^\dagger_{-m-\sigma}$, which translates into the relation

$$K^-_{m\sigma} = 2\sigma(-1)^m \frac{E_{nl} - \xi_{nl}}{\Gamma_{nl}}(K^+_{-m-\sigma})^\dagger. \tag{9.54}$$

This relation shows that K^- and K^+ are related to each other, and we decide to eliminate K^-. The real time solution for $d_{m\sigma}(t)$ is obtained by inverse Fourier transforming $d_{m\sigma}(\omega)$. At $t = 0$, we get the impurity operator $d_{m\sigma} \equiv d_{m\sigma}(t = 0)$,

$$d_{m\sigma} = \frac{1}{2\pi\hbar}\left\{K^+_{m\sigma} + 2\sigma(-1)^m \frac{E_{nl} - \xi_{nl}}{\Gamma_{nl}}(K^+_{-m-\sigma})^\dagger\right\}. \tag{9.55}$$

The d impurity operators satisfy the Dirac algebra, $\{d_{m\sigma}, d^\dagger_{m'\sigma'}\} = \delta_{mm'}\delta_{\sigma\sigma'}$, but the $K^+_{m\sigma}$ operators, however, do not. Instead the physical Bogoliubov operators $\gamma_{m\sigma}$ are defined through the normalization $K^+_{m\sigma}/2\pi\hbar = u\gamma_{m\sigma}$ by imposing that they satisfy the algebra $\{\gamma_{m\sigma}, \gamma^\dagger_{m'\sigma'}\} = \delta_{mm'}\delta_{\sigma\sigma'}$. This leads to

$$d_{m\sigma} = u\,\gamma_{m\sigma} + 2\sigma(-1)^m v\,\gamma^\dagger_{-m-\sigma}. \tag{9.56}$$

Energy	State	Degeneracy	Parity
$E_{GS} + 2E_{nl}$	$\gamma_{m'\sigma'}^{\dagger}\gamma_{m\sigma}^{\dagger}|GS\rangle$	$\begin{pmatrix} 2(2l+1) \\ 2 \end{pmatrix}$	Even
$E_{GS} + E_{nl}$	$\gamma_{m\sigma}^{\dagger}|GS\rangle$	$\begin{pmatrix} 2(2l+1) \\ 1 \end{pmatrix}$	Odd
E_{GS}	$|GS\rangle$	$\begin{pmatrix} 2(2l+1) \\ 0 \end{pmatrix}$	Even
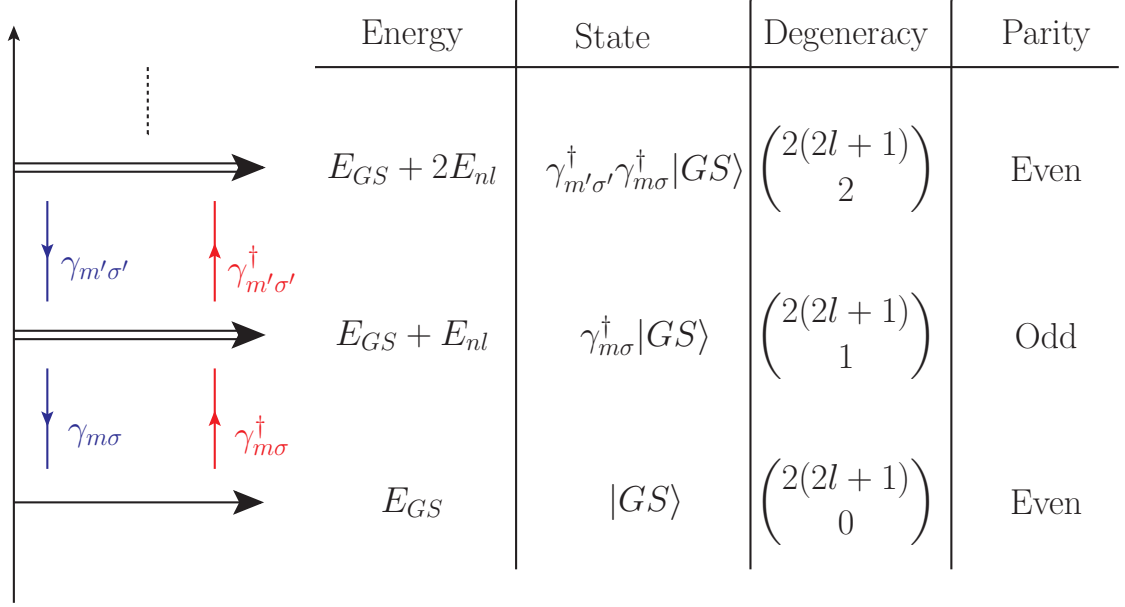
Figure 9.5: Energy and eigenstate structure of the impurity in the superconducting atomic limit and at $U = 0$. The energy column collects the energies of the Hamiltonian eigenstates, which are related by adding or removing quasiparticle energies, which are the poles of the Green's function. The degeneracy refers to the number of states at a given energy, and the parity refers to whether the number of electrons in the state is even or odd.

with the amplitudes,

$$u^2 = \frac{1}{2}\left(1 + \frac{\xi_{nl}}{E_{nl}}\right), \quad v^2 = \frac{1}{2}\left(1 - \frac{\xi_{nl}}{E_{nl}}\right) \tag{9.57}$$

Inverting Eq. (9.56) gives,

$$\gamma_{m\sigma} = u d_{m\sigma} - 2\sigma(-1)^m v d_{-m-\sigma}^{\dagger}. \tag{9.58}$$

This relation represents the Bogoliubov transformation for impurity operators that have orbital degeneracy at $U = 0$. The effect of $\gamma_{m\sigma}$ is to annihilate an electron in state $|m\sigma\rangle$ with probability u^2, or to create an electron in state $|-m-\sigma\rangle$ with probability v^2. Plugging this solution back into the effective Hamiltonian, $\mathcal{H}_{\text{eff}}$ leads to the diagonalized form,

$$\mathcal{H}_{\text{eff}}^{nl} = \sum_{m\sigma}\left\{E_{nl}\gamma_{m\sigma}^{\dagger}\gamma_{m\sigma} + \frac{1}{2}\left(\xi_{nl} - E_{nl}\right)\right\} \tag{9.59}$$

The ground state, is the specific state which contains no quasiparticle, i.e. $\gamma_{m\sigma}|GS\rangle = 0$ for all m, σ. The solution to this constraint is

$$|GS\rangle = \prod_{m=-l}^{l} \prod_{\sigma=\pm 1/2} \gamma_{m\sigma} |0\rangle. \tag{9.60}$$

First excited states can then be obtained by adding one quasiparticle excitation, $\gamma_{m\sigma}^{\dagger}|GS\rangle$. Because of the orbital degeneracy, there are $2(2l+1)$ first excited states. Since the effect of the Bogoliubov operators is to create or annihilate an electron, as shown by Eq. (9.58), the first excited states contain an odd number of electrons. Further excited states are obtained by consecutively adding quasiparticles by acting with $\gamma_{m\sigma}^{\dagger}$.

From this structure, the energy spectrum is readily obtained from the Hamiltonian. The ground state energy is $E_{GS} = \langle \text{GS}| \mathcal{H}_{\text{eff}}^{nl} |\text{GS}\rangle$

$$E_{\text{GS}} = \sum_{m\sigma} \frac{1}{2} (\xi_{nl} - E_{nl}) = (2l+1)(\xi_{nl} - E_{nl}) \tag{9.61}$$

The energy of the nth excited state is therefore $E_{\text{GS}} + nE_{nl}$. The spectrum is sketched in Fig. 9.5. This picture unveils the difference between the Bogoliubov transformation approach and the Green's function approach. Indeed, the poles of the Green's functions correspond to the physical quasiparticle energies, but they do not correspond to the energies of the actual impurity states.

This point can be made more explicitly by considering the retarded Green's function,

$$G_{m\sigma,m'\sigma'}^{R}(t) = -i\theta(t) \left\langle \left\{ d_{m\sigma}(t), d_{m'\sigma'}^{\dagger}(0) \right\} \right\rangle, \tag{9.62}$$

which through spectral decomposition can be calculated to be,

$$
\begin{aligned}
G_{m\sigma,m'\sigma'}^{R}(\omega) =\ & \hbar\delta_{mm'}\delta_{\sigma\sigma'} \\
& \times \sum_{\alpha,\beta} \frac{e^{-\beta E_{\alpha}}}{\mathcal{Z}} \left[\frac{|\langle\beta| d_{m\sigma}^{\dagger}(0) |\alpha\rangle|^2}{\hbar\omega - (E_{\beta} - E_{\alpha}) + i\eta} \right. \\
& \left. + \frac{|\langle\beta| d_{m\sigma}(0) |\alpha\rangle|^2}{\hbar\omega + E_{\beta} - E_{\alpha} + i\eta} \right].
\end{aligned}
\tag{9.63}
$$

In the zero-temperature limit, the state $|\alpha\rangle = |GS\rangle$ is the ground state, and we obtain the spectral function

$$
\begin{aligned}
A(\omega) = \ \hbar \sum_{m\sigma} \sum_{\beta} \Bigg[& |\langle\beta| d_{m\sigma}^{\dagger}(0) |GS\rangle|^2 \delta\left(\hbar\omega - (E_\beta - E_{GS})\right) \\
& + |\langle\beta| d_{m\sigma}(0) |GS\rangle|^2 \delta\left(\hbar\omega + E_\beta - E_{GS}\right) \Bigg].
\end{aligned}
\tag{9.64}
$$

It is clear here that the physical energies of the spectral weight, given by the poles of the Delta functions, correspond to adding and removing one electron with probabilities $|\langle\beta| d_{m\sigma}^{\dagger}(0) |GS\rangle|^2$ and $|\langle\beta| d_{m\sigma}(0) |GS\rangle|^2$.

9.3.2 Quick introduction to Young tableaux

We use symmetries as the organizing principles for all YSR states, in particular, we will use the formalism of Young tableaux [310] to work out the various representations and their dimensions.

Yound tableaux provide a systematic way to organize tensors according to their symmetries. To begin with, a vector $|\psi\rangle$ is a one-index tensor with vector components represented as ψ_α where α labels each component of the vector, to which we associate the box $\boxed{\alpha}$.

A tensor product between two vectors, $|\psi\rangle \otimes |\phi\rangle$, is a two-index tensor with each component labeled by two numbers α, β respectively labeling the two vector components, ψ_α, ϕ_β. The tensor product is represented as $\boxed{\alpha} \otimes \boxed{\beta}$.

The tensor components, $\psi_\alpha \phi_\beta$, can be traded for the symmetrized or antisymmetrized linear combinations, $\psi_\alpha \phi_\beta = \psi_{(\alpha}\phi_{\beta)} + \psi_{[\alpha}\phi_{\beta]}$, where

$$
\begin{aligned}
\psi_{(\alpha}\phi_{\beta)} &\equiv \frac{1}{2}\left(\psi_\alpha \phi_\beta + \psi_\beta \phi_\alpha\right), \\
\psi_{[\alpha}\phi_{\beta]} &\equiv \frac{1}{2}\left(\psi_\alpha \phi_\beta - \psi_\beta \phi_\alpha\right).
\end{aligned}
\tag{9.65}
$$

If the vectors $|\psi\rangle, |\phi\rangle$ are N-dimensional vectors, the indices $\alpha, \beta = 1, \cdots, N$, and the number of components of the two index tensor is N^2. The dimension of the symmetrized tensor $\psi_{(\alpha}\phi_{\beta)}$ is $N(N+1)/2$ and that of the antisymmetrized tensor $\psi_{[\alpha}\phi_{\beta]}$ is $N(N-1)/2$ The symmetrization and antisymmetrization procedure is represented

using the boxes as follows,

$$\boxed{\alpha} \otimes \boxed{\beta} = \boxed{\alpha\,|\,\beta} \oplus \boxed{\begin{array}{c}\alpha\\\beta\end{array}} \tag{9.66}$$

By convention, a horizontal tableau, such as $\boxed{\,|\,}$ is purely symmetric, and a vertical tableaux $\boxed{\begin{array}{c}\\\end{array}}$ is purely antisymmetric. The symmetry of a general tensor is associated tableau that look something like,

$$\tag{9.67}$$

A tableau like the one above is a mixed symmetry tableau, which is cannot be expressed purely in terms of symmetric or antisymmetric tensors.

A legal tableau is one where the number of boxes in each row is lower or equal to the number of boxes in the row above, and the number of rows cannot be larger than the dimension of the vector space. According to this rule, we can build larger tensors by multiplying tableaux and writing down all possible legal tableaux, e.g.

$$\boxed{\,|\,} \otimes \boxed{} = \boxed{\,|\,\,|\,} \oplus \boxed{} \tag{9.68}$$

For simplicity we have dropped the labeling of each box, but we must remember that each box does represent an index of the tensor. The index within each box is non-increasing going to the right, and must be strictly decreasing going down. The dimension of a tableau is found by calculating the number of different ways to write a tableaux given the number of values each box can take. The rules for the dimensionality of a tableau are given by calculating the ratio whose numerator and denominator are given as follows:

1. Numerator: fill the top left box with the dimension of one index, N. Fill in the rest of the tableau, increasing by one in each box to the right, and decreasing by one for each box down. Take the product of all the numbers.

2. Denominator: fill each box with one plus the number of boxes to the right plus the number of boxes down. Take the product of all the numbers.

For example, we find

$$
\begin{aligned}
d\left(\square\square\right) &= \frac{N(N+1)}{2}, \\
d\left(\begin{array}{c}\square\\\square\end{array}\right) &= \frac{N(N-1)}{2}, \\
d\left(\begin{array}{cc}\square&\square\\\square\end{array}\right) &= \frac{N(N+1)(N-1)}{3\cdot1\cdot1} = \frac{N(N^2-1)}{3}.
\end{aligned}
\tag{9.69}
$$

According to the rules for a legal tableau, a three-index tensor is represented as,

$$
\begin{aligned}
\square\otimes\square\otimes\square &= \left(\square\square\oplus\begin{array}{c}\square\\\square\end{array}\right)\otimes\square \\
&= \underbrace{\square\square\otimes\square}_{} \oplus \underbrace{\begin{array}{c}\square\\\square\end{array}\otimes\square}_{} \\
&= \square\square\square \oplus \begin{array}{cc}\square&\square\\\square\end{array} \oplus \begin{array}{cc}\square&\square\\\square\end{array} \oplus \begin{array}{c}\square\\\square\\\square\end{array}
\end{aligned}
\tag{9.70}
$$

The dimensions of the tensors are,

$$
\begin{aligned}
d\left(\square\otimes\square\otimes\square\right) &= d\left(\square\square\square\right) \oplus 2\cdot d\left(\begin{array}{cc}\square&\square\\\square\end{array}\right) \oplus d\left(\begin{array}{c}\square\\\square\\\square\end{array}\right) \\
N^3 &= \frac{N(N+1)(N+2)}{6} + 2\cdot\frac{N(N-1)(N+1)}{3} + \frac{N(N-1)(N-2)}{6}.
\end{aligned}
\tag{9.71}
$$

In the following, we are going to look at the representations of YSR states made out of different number of electrons that can be either s-wave or p-wave. In order for that, we will have to use Young tableaux that represent the coupling of orbital quantum numbers or spin quantum numbers. It will be convenient to define the following notation:

- An empty box, $\square$, stands for a spin representation,

- A dotted box, $\boxed{\bullet}$, stands for an s-wave orbital wave function,

- A circled box, $\boxed{\circ}$, stands for an p-wave orbital wave function,

- A crossed box, $\boxed{\times}$, stands for a mixed s-p orbital wave function.

	box	Dimension	J^2	states
spin	☐	$\underline{\mathbf{2}}$	$\frac{1}{2}$	$\{|\uparrow\rangle,|\downarrow\rangle\}$
orbital s-wave	⊡	$\underline{\mathbf{1}}$	$\mathbf{0}$	$\{|l=0\rangle\}$
orbital p-wave	⊡	$\underline{\mathbf{3}}$	$\mathbf{1}$	$\{|l=1,\ m\rangle\}$
mixed s- or p-wave	⊠	$\underline{\mathbf{4}}$	$\mathbf{0}\oplus\mathbf{1}$	$\{|l=0\rangle,\ \ |l=1,\ m\rangle\}$

Table 9.1: Definition of the notation.

In addition to the rules for creating tableaux above mentioned, we add the rule that ⊡ must always be above and to the left of ⊡. For example $\begin{smallmatrix}●&○\\○&\end{smallmatrix}$ is legal, but $\begin{smallmatrix}○&●\\○&\end{smallmatrix}$ is not. The dimension of a tableau is represented by underlined bold, and the angular momentum representation (eigenvalue of J^2) by simple bold. A summary of the notation is shown in Tab. 9.1.

As a concrete example, we present the explicit wave functions for a two-electron state. The spin degrees of freedom are understood via the tensor product of two spin-1/2 particle, represented in terms of Young tableaux as,

$$\square \otimes \square = \square\square \oplus \begin{smallmatrix}\square\\\square\end{smallmatrix} \tag{9.72}$$

The first term $\square\square$ is the symmetric spin wave function, that is

$$\square\square = \begin{cases} |\uparrow\uparrow\rangle \\ \frac{1}{\sqrt{2}}\left(|\uparrow\downarrow\rangle+|\downarrow\uparrow\rangle\right) \\ |\downarrow\downarrow\rangle \end{cases} \ . \tag{9.73}$$

while the second term is the antisymmetric wave function,

$$\begin{smallmatrix}\square\\\square\end{smallmatrix} = \frac{1}{\sqrt{2}}\left(|\uparrow\downarrow\rangle-|\downarrow\uparrow\rangle\right). \tag{9.74}$$

The dimension of the YSR state basis is the number of ways to pick N electrons out of all the possibilities of electron states. If the electron has orbital angular momentum l and spin $s = 1/2$, then the electron degeneracy is $2(2l + 1)$. The number of ways to pick N electrons out of $2(2l + 1)$ possibilities is given by the binomial factor, and

$$d_N = \binom{2(2l + 1)}{N}, \tag{9.75}$$

The dimension of the basis is the sum,

$$\sum_{N=0}^{2(2l+1)} d_N = \sum_{N=0}^{2(2l+1)} \binom{2(2l + 1)}{N} = 2^{4l+2}, \tag{9.76}$$

where we used the binomial expansion,

$$(x + y)^n = \sum_{k=0}^{n} \binom{n}{k} x^k y^{n-k}, \tag{9.77}$$

with $x = y = 1$.

9.3.3   YSR states from s-wave impurity

The effective Hamiltonian satisfies the same symmetries as the total Hamiltonian. In particular, BCS pairing being s-wave and the hybridization assumed spherically symmetric, the model conserves total orbital and spin angular momentum, $\boldsymbol{L}$, $\boldsymbol{S}$, as well as the total angular momentum $\boldsymbol{J} = \boldsymbol{L} + \boldsymbol{S}$. In addition, it also conserves the Casimir operators of each transformations, i.e. $\boldsymbol{L}^2$, $\boldsymbol{S}^2$ and $\boldsymbol{J}^2$. Therefore, it is convenient to represent states using the spectroscopic notation $^{2S+1}\boldsymbol{L}_J^N$. The superscript N specifies the number of electrons in the state, which is convenient to keep track of since the energy eigenspectrum contains states with a different number of electrons.

In this section we will calculate the YSR energy levels and eigenstates associated to the s-wave impurity. We will do this by exact diagonalization of the effective Hamiltonian, Eq. (9.45). We emphasize that this result is exact in the $\Delta \to \infty$ limit, when the impurity proximity potential $\tilde{\Delta}_{nl}$ becomes equal to the impurity hybridization linewidth Γ_{nl}.

The degeneracy of s-electrons ($l = 0$) is $2(2l + 1) = 2$, for the two spins $|\uparrow\rangle, |\downarrow\rangle$. This means that electron bound states can be made of 0, 1, or 2 electrons, and the

number of possible YSR states is $2^2 = 4$.

In the case where only s-electron are available, the Hamiltonian takes the concise form $\mathcal{H}_{\text{eff}} = \mathcal{H}'_{\text{imp}} + \mathcal{H}_{\text{prox}}$, with

$$\mathcal{H}'_{\text{imp}} = \mathcal{H}_{\text{imp}} + \Sigma_{ns} \sum_{m\sigma} N_{ns\sigma}$$

$$\mathcal{H}_{\text{prox}} = -\Gamma_{ns} \, d^\dagger_{ns\uparrow} d^\dagger_{ns\downarrow} + h.c. \tag{9.78}$$

The proximity potential breaks particle number by two units, therefore, we can separate the energy spectrum into those states that contain an even number of electrons and an odd number of electrons (in other words, the Hamiltonian Eq. (9.78) commutes with the number-parity operator).

Even-parity eigenstates

The even-parity eigenstates refer to the states that contain an even number of electrons. Because of the degeneracy of s-electrons, the even-parity eigenstates can contain either 0 electrons (vacuum state) or two electrons. The dimension of the basis is given by the number of ways to pick 0 or two electrons out of a set of 2 electrons, that is

$$d_{\text{even}} = \binom{2}{0} + \binom{2}{2} = 1 + 1 = 2. \tag{9.79}$$

The possible two-electron spin wave functions are,

$$
\begin{aligned}
\text{Tableaux:} \quad & \square \otimes \square = \boxed{} \oplus \begin{array}{c}\square\\\square\end{array} \\
\text{Dimensions:} \quad & \mathbf{\underline{2}} \otimes \mathbf{\underline{2}} = \mathbf{\underline{3}} \oplus \mathbf{\underline{1}} \\
\text{Representation:} \quad & \frac{1}{2} \otimes \frac{1}{2} = \mathbf{1} \oplus \mathbf{0}
\end{aligned}
\tag{9.80}
$$

The possible orbital wave functions are found similarly by,

$$
\begin{aligned}
\text{Tableaux:} \quad & \boxed{\bullet} \otimes \boxed{\bullet} = \boxed{\bullet\,\bullet} \oplus \begin{array}{c}\boxed{\bullet}\\\boxed{\bullet}\end{array} \\
\text{Dimensions:} \quad & \mathbf{\underline{1}} \otimes \mathbf{\underline{1}} = \mathbf{\underline{1}} \\
\text{Representation:} \quad & \mathbf{0} \otimes \mathbf{0} = \mathbf{0}
\end{aligned}
\tag{9.81}
$$

The tableau $\begin{array}{|c|}\hline \bullet \\ \hline \bullet \\ \hline\end{array}$ has been deleted because the number of rows is larger than the dimension of a box. This is because there exists only one s-orbital spatial wave function, given by the spherical harmonics Y_0^0, and it is not possible to form an antisymmetric wave function with only one wave function.

Since the two-electron pair must be antisymmetric under electron interchange, it is necessary that the spatial wave function multiplies the antisymmetric spin wave function. Thus, the YSR state representation is,

$$\boxed{\bullet}\,\boxed{\bullet} \otimes \begin{array}{|c|}\hline \\ \hline \\ \hline\end{array} = {}^1\mathbf{S}_0 \tag{9.82}$$

The vector form of the two electron state is,

$$\left|\,{}^1\mathbf{S}_0\right\rangle = \frac{1}{\sqrt{2}}\,|l=0\rangle\,(|\uparrow\rangle_1\,|\downarrow\rangle_2 - |\downarrow\rangle_1\,|\uparrow\rangle_2) = d_{ns\uparrow}^\dagger d_{ns\downarrow}^\dagger\,|0\rangle \equiv |\uparrow\downarrow\rangle \tag{9.83}$$

The 0-electron state is the vacuum state that also belongs to the ${}^1\mathbf{S}_0$ representation.

The even-number basis set consists of the two states $\{|0\rangle,\ |\uparrow\downarrow\rangle\}$. The proximity potential has the effect of mixing those two states:

$$\begin{aligned}
\mathcal{H}_{\text{prox}}\,|\uparrow\downarrow\rangle &= -\Gamma_{ns}\left(d_{ns\uparrow}^\dagger d_{ns\downarrow}^\dagger + d_{ns\downarrow}d_{ns\uparrow}\right) d_{ns\uparrow}^\dagger d_{ns\downarrow}^\dagger\,|0\rangle = -\Gamma_{ns}^*\,|0\rangle\,, \\
\mathcal{H}_{\text{prox}}\,|0\rangle &= -\Gamma_{ns}\left(d_{ns\uparrow}^\dagger d_{ns\downarrow}^\dagger + d_{ns\downarrow}d_{ns\uparrow}\right)|0\rangle = -\Gamma_{ns}d_{ns\uparrow}^\dagger d_{ns\downarrow}^\dagger\,|0\rangle\,.
\end{aligned} \tag{9.84}$$

Hence the Hamiltonian of the even-number subspace is found to have the form,

$$H = \begin{pmatrix} 2\xi_{ns} + 2\Sigma_{ns} & -\Gamma_{ns} \\ -\Gamma_{ns} & 2\xi_{ns} + 2\Sigma_{ns} \end{pmatrix} \begin{array}{l} |0\rangle \\ |\uparrow\downarrow\rangle \end{array} \tag{9.85}$$

Odd-parity eigenstates

For YSR states that contain an odd number of electron, we can only pick one electron, thus the dimension of the basis is,

$$d_{\text{odd}} = \begin{pmatrix} 2 \\ 1 \end{pmatrix} = 2. \tag{9.86}$$

The spin and orbital wave functions are respectively, ☐ and ●, and the overall wave function is that of a single s-wave electron,

$$\boxed{\bullet} \otimes \boxed{} = {}^2\mathbf{S}_{1/2} \tag{9.87}$$

The single-electron basis set is made of the up and down spins,

$$\left| {}^2\mathbf{S}_{1/2} \right\rangle = \begin{cases} |l=0\rangle\, |\uparrow\rangle \equiv d^\dagger_{ns\uparrow}\, |0\rangle \\ |l=0\rangle\, |\downarrow\rangle \equiv d^\dagger_{ns\downarrow}\, |0\rangle \end{cases} \tag{9.88}$$

and their response to the proximity potential is as follows,

$$\mathcal{H}_{\text{prox}}\, |\uparrow\rangle = -\Gamma_{ns}\left(d^\dagger_{ns\uparrow}d^\dagger_{ns\downarrow} + d_{ns\downarrow}d_{ns\uparrow} \right) d^\dagger_{ns\uparrow}\, |0\rangle = 0. \tag{9.89}$$

Similarly, we find that $\mathcal{H}_{\text{prox}}\, |\downarrow\rangle = 0$. That is to say the energy spectrum of single electron states is,

$$\left(\mathcal{H}'_{\text{imp}} + \mathcal{H}_{\text{prox}} \right) |\uparrow\rangle = \left(\xi_{ns} + \Sigma_{ns} \right) |\uparrow\rangle, \tag{9.90}$$

And similarly for the $|\downarrow\rangle$ state, thus in matrix representation,

$$H = \begin{pmatrix} \xi_{ns} + \Sigma_{ns} & 0 \\ 0 & \xi_{ns} + \Sigma_{ns} \end{pmatrix} \begin{matrix} |\uparrow\rangle \\ |\downarrow\rangle \end{matrix} \tag{9.91}$$

9.3.4 YSR states from p-wave impurity

The next situation is that of an atom where only p-electrons are available to pair. That is, in this section we reduce the complete effective Hamiltonian to the subset that includes only p electrons,

$$\begin{aligned} \mathcal{H}'_{\text{imp}} &= \mathcal{H}_{\text{imp}} + \Sigma_{np}\sum_{m\sigma} d^\dagger_{npm\sigma}d_{npm\sigma} \\ \mathcal{H}_{\text{prox}} &= -\Gamma_{np}\sum_{m\sigma}\sigma(-1)^m d^\dagger_{npm\sigma}d^\dagger_{np-m-\sigma} + h.c. \end{aligned} \tag{9.92}$$

Unlike the s-electron case, it is possible to form non-trivial states with an odd number of electrons. We use the same argument to count the dimension of the basis as in the case of s-electron. The degeneracy of one p-electron is $2(2l+1) = 6$. The total

number of YSR states is thus obtained as

$$d = d_{\text{even}} + d_{\text{odd}} = \sum_{k=0}^{6} \binom{6}{k} = 2^6 = 64. \tag{9.93}$$

Even-parity eigenstates

The number of even-numbered YSR states is,

$$d_{\text{even}} = \binom{6}{0} + \binom{6}{2} + \binom{6}{4} + \binom{6}{6} = 1 + 15 + 15 + 1 = 32, \tag{9.94}$$

The even-parity sector includes the empty state $|0\rangle$, the 2- 4- and 6-electron states. The wave functions can be obtained as follows. The 2-electrons states are obtained by adding two electrons into the vacuum; The 4-electron states are obtained by removing two electrons from the maximally occupied state, $|F\rangle = \prod_{m,\sigma} d^\dagger_{m\sigma}|0>$, which is also a singlet. In this way we find that the vacuum has the same symmetry as the maximally filled state, and the doubly-occupied state has the same symmetries as the quadruptly-occupied state.

The spin symmetries of the doubly occupied state are,

$$\square \otimes \square = \underbrace{\boxed{}}_{1} \oplus \underbrace{\boxed{\begin{array}{c}\\\end{array}}}_{0}. \tag{9.95}$$

The orbital symmetries of the doubly occupied state are,

$$\boxed{\circ} \otimes \boxed{\circ} = \underbrace{\boxed{\circ\,\circ}}_{S \oplus D} \oplus \underbrace{\boxed{\begin{array}{c}\circ\\\circ\end{array}}}_{P}. \tag{9.96}$$

In this way, the symmetry of two-electron state is found in the $\boldsymbol{L} \otimes \boldsymbol{S}$ space as,

$$\left(1 \otimes \frac{1}{2}\right) \otimes \left(1 \otimes \frac{1}{2}\right) = \underbrace{\boxed{\circ\,\circ} \otimes \boxed{\begin{array}{c}\\\end{array}}}_{{}^1\boldsymbol{S}_0 \oplus {}^1\boldsymbol{D}_2} \oplus \underbrace{\boxed{\begin{array}{c}\circ\\\circ\end{array}} \otimes \boxed{}}_{{}^3\boldsymbol{P}_0 \oplus {}^3\boldsymbol{P}_1 \oplus {}^3\boldsymbol{P}_2} \tag{9.97}$$

$$= {}^1\boldsymbol{S}_0 \oplus {}^1\boldsymbol{D}_2 \oplus {}^3\boldsymbol{P}_0 \oplus {}^3\boldsymbol{P}_1 \oplus {}^3\boldsymbol{P}_2$$

The 4-electron states have exactly the same symmetries. In particular, the $|{}^1\boldsymbol{S}_0^2\rangle$

Cooper-pair is written as

$$\begin{aligned}
\left|{}^1\boldsymbol{S}_0^2\right\rangle &= |\boldsymbol{L}=0, M_L=0\rangle \, |\boldsymbol{S}=0, M_S=0\rangle \\
&= \frac{1}{\sqrt{3}} \left(d_{1\uparrow}^\dagger d_{-1\downarrow}^\dagger + d_{-1\uparrow}^\dagger d_{1\downarrow}^\dagger - d_{0\uparrow}^\dagger d_{0\downarrow}^\dagger \right) |0\rangle .
\end{aligned} \tag{9.98}$$

From there, it follows that the Hamiltonian takes the block-diagonal form,

$$\mathcal{H}_{\text{eff}}^{\text{even}} = \begin{pmatrix} \mathcal{H}_{\text{eff}}({}^1\boldsymbol{S}_0) & 0 & 0 \\ 0 & \mathcal{H}_{\text{eff}}({}^1\boldsymbol{D}_2) & 0 \\ 0 & 0 & \ddots \end{pmatrix}, \tag{9.99}$$

where the singlet sector is given by,

$$\mathcal{H}_{\text{eff}}({}^1\boldsymbol{S}_0) = \begin{pmatrix} 0 & \sqrt{3}\Gamma_{np} & 0 & 0 \\ \sqrt{3}\Gamma_{np} & 2\xi_{np}+U & -2\Gamma_{np} & 0 \\ 0 & -2\Gamma_{np} & 4\xi_{np}+6U & \sqrt{3}\Gamma_{np} \\ 0 & 0 & \sqrt{3}\Gamma_{np} & 6\xi_{np}+15U \end{pmatrix} \begin{matrix} |0\rangle \\ |{}^1S_0^2\rangle \\ |{}^1S_0^4\rangle \\ |F\rangle \end{matrix}, \tag{9.100}$$

and the D blocks only contain a $J=2$ component,

$$\mathcal{H}_{\text{eff}}({}^1\boldsymbol{D}_2) = \begin{pmatrix} 2\xi_{np}+U & \Gamma_{np} \\ \Gamma_{np} & 4\xi_{np}+6U \end{pmatrix} \begin{matrix} |{}^1D_2^2\rangle \\ |{}^1D_2^4\rangle \end{matrix}. \tag{9.101}$$

and the P block contains $J=0,1,2$ components as,

$$\mathcal{H}_{\text{eff}}({}^3\boldsymbol{P}_0) = \begin{pmatrix} 2\xi_{np}+U & \Gamma_{np} \\ \Gamma_{np} & 4\xi_{np}+6U \end{pmatrix} \begin{matrix} |{}^3P_0^2\rangle \\ |{}^3P_0^4\rangle \end{matrix}, \tag{9.102}$$

$$\mathcal{H}_{\text{eff}}({}^3\boldsymbol{P}_1) = \begin{pmatrix} 2\xi_{np}+U & -\Gamma_{np} \\ -\Gamma_{np} & 4\xi_{np}+6U \end{pmatrix} \begin{matrix} |{}^3P_1^2\rangle \\ |{}^3P_1^4\rangle \end{matrix}, \tag{9.103}$$

$$\mathcal{H}_{\text{eff}}({}^3\boldsymbol{P}_2) = \begin{pmatrix} 2\xi_{np}+U & \Gamma_{np} \\ \Gamma_{np} & 4\xi_{np}+6U \end{pmatrix} \begin{matrix} |{}^3P_2^2\rangle \\ |{}^3P_2^4\rangle \end{matrix}. \tag{9.104}$$
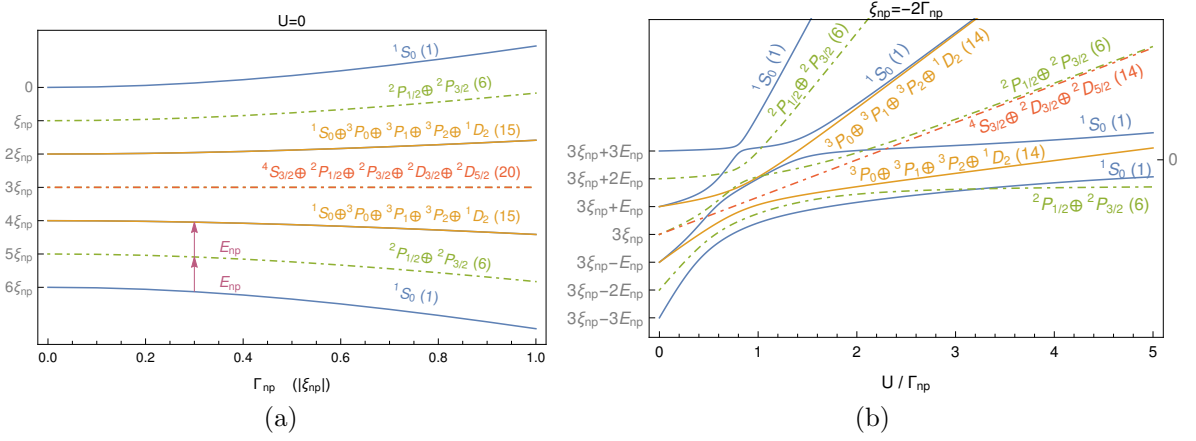
Figure 9.6: YSR energy spectrum as a function of induced pairing, Γ_{np} without Coulomb interaction (left), and as a function of Coulomb interaction (right).

Odd-parity eigenstates

The multiplicity of odd-numbered states is

$$d_{\text{odd}} = \binom{6}{1} + \binom{6}{3} + \binom{6}{5} = 6 + 20 + 6 = 32, \tag{9.105}$$

and contain 1- 3- and 5-electron states. The one-electron states are obtained by adding one electron to the vacuum state, and the 5-electron states are obtained by removing one electron from $|F\rangle$. The symmetry of 3-electron states contains mixed spin-orbital symmetries which requires the use of Young tableaux.

Therefore, the one- and five-particle symmetries are given by $\mathbf{1} \otimes \mathbf{1/2} = {}^2\boldsymbol{P}_{1/2} \oplus {}^2\boldsymbol{P}_{3/2}$. The three-particle representations are given by the direct product,

$$\begin{aligned}(\mathbf{1} \otimes \mathbf{1/2}) \otimes (\mathbf{1} \otimes \mathbf{1/2}) \otimes (\mathbf{1} \otimes \mathbf{1/2}) = \\ (\mathbf{1} \otimes \mathbf{1} \otimes \mathbf{1}) \otimes (\mathbf{1/2} \otimes \mathbf{1/2} \otimes \mathbf{1/2}).\end{aligned} \tag{9.106}$$

The spin and orbital parts are represented by the following Young tableaux:

$$\square \otimes \square \otimes \square = \boxed{} \oplus \diagup\!\!\!\!\square \oplus \square\!\!\square \oplus \square\!\!\square, \tag{9.107}$$
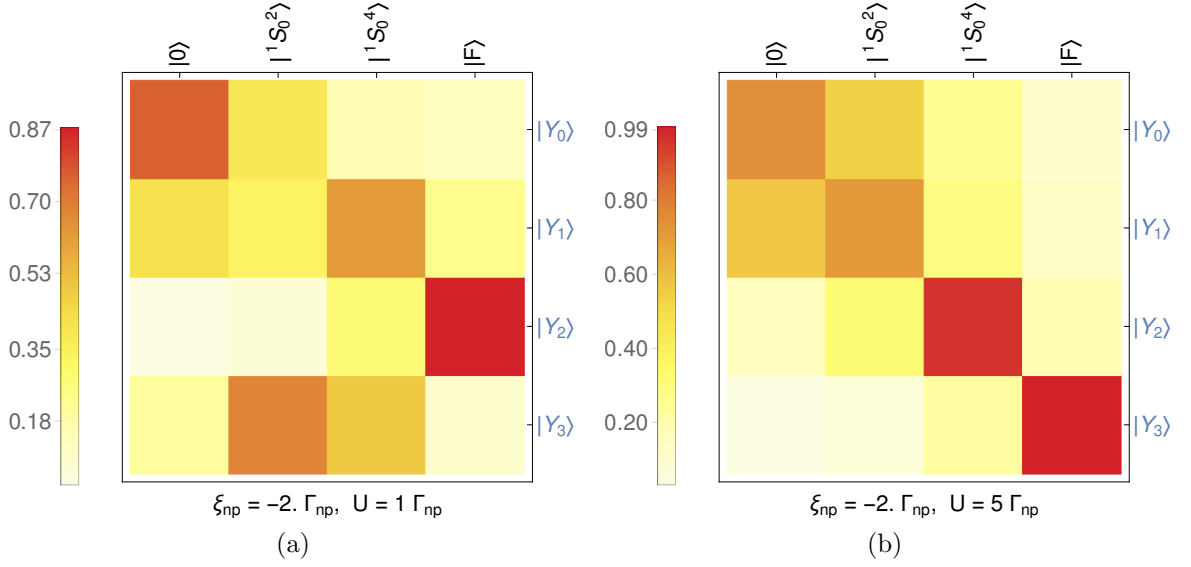
Figure 9.7: Representation of the components of the eigenstates of the multiplet $^1S_0$, at low U (left) and high U (right). In the low U regime all states in the multiplet are mixed, whereas at large U, the heavier eigenstates are predominantly the full state, $|F\rangle$. The eigenvectors are labeled $|Y_{0,1,2,3}\rangle$ in order of increasing eigenvalue.

where the completely antisymmetric tableaux is removed because it has more boxes than the number of spin degrees of freedom. For the Cooper-pair like states to be fermionic it is necessary to combine the totally symmetric orbital angular momentum parts with the totally antisymmetric spin angular momentum and vice versa. In contrast, the mixed orbital symmetry must combine with the mixed spin symmetry. Thus, we get the following,

$$
\left(\mathbf{1} \otimes \mathbf{1} \otimes \mathbf{1}\right) \otimes \left(\mathbf{1/2} \otimes \mathbf{1/2} \otimes \mathbf{1/2}\right)
$$

$$
= \; \ytableau \otimes \ytableau \; \oplus \; \ytableau \otimes \ytableau \tag{9.108}
$$

$$
= \; {}^4\boldsymbol{S}_{3/2} \oplus \left({}^2\boldsymbol{P}_{1/2} \oplus \; {}^2\boldsymbol{P}_{3/2} \oplus \; {}^2\boldsymbol{D}_{3/2} \oplus \; {}^2\boldsymbol{D}_{5/2}\right),
$$

where we used,

$$
\ytableau = \mathbf{1} \oplus \mathbf{2}
$$

$$
\ytableau = \mathbf{1/2} \tag{9.109}
$$

The S representation has maximum spin configuration $s = 3/2$, it is thus impossible to add anymore electrons while keeping the orbital symmetry $l = 0$. It is also not possible to remove two electrons from that state, because then we would obtain a one-electron state, but it is not possible to have a one-electron state with $s = j = 3/2$. Similarly, the D representation has maximal orbital symmetry $l = 2$, which means it is impossible to add or remove electrons while keeping the spin symmetry $s = 1/2$. As a result, neither those configurations form Cooper pairs,

$$
\begin{aligned}
\mathcal{H}_{\text{eff}} \left| {}^4 S_{3/2}^3 \right\rangle &= (3\xi_{np} + 3U) \left| {}^4 S_{3/2}^3 \right\rangle \\
\mathcal{H}_{\text{eff}} \left| {}^2 D_{3/2}^3 \right\rangle &= (3\xi_{np} + 3U) \left| {}^2 D_{3/2}^3 \right\rangle \\
\mathcal{H}_{\text{eff}} \left| {}^2 D_{5/2}^3 \right\rangle &= (3\xi_{np} + 3U) \left| {}^2 D_{5/2}^3 \right\rangle
\end{aligned}
\tag{9.110}
$$

whereas the P sector splits into two $J = 1/2, 3/2$ components,

$$
\mathcal{H}_{\text{eff}}({}^2 P_{1/2}) =
$$
$$
\begin{pmatrix}
\xi_{np} & \sqrt{2}\Gamma_{np} & 0 \\
\sqrt{2}\Gamma_{np} & 3\xi_{np} + 3U & \sqrt{2}\Gamma_{np} \\
0 & \sqrt{2}\Gamma_{np} & 5\xi_{np} + 10U
\end{pmatrix}
\begin{array}{l}
\left| {}^2 P_{1/2}^1 \right\rangle \\
\left| {}^2 P_{1/2}^3 \right\rangle \\
\left| {}^2 P_{1/2}^5 \right\rangle,
\end{array}
\tag{9.111}
$$

and

$$
\mathcal{H}_{\text{eff}}({}^2 P_{3/2}) =
$$
$$
\begin{pmatrix}
\xi_{np} & \sqrt{2}\Gamma_{np} & 0 \\
\sqrt{2}\Gamma_{np} & 3\xi_{np} + 3U & \sqrt{2}\Gamma_{np} \\
0 & \sqrt{2}\Gamma_{np} & 5\xi_{np} + 10U
\end{pmatrix}
\begin{array}{l}
\left| {}^2 P_{3/2}^1 \right\rangle \\
\left| {}^2 P_{3/2}^3 \right\rangle \\
\left| {}^2 P_{3/2}^5 \right\rangle,
\end{array}
\tag{9.112}
$$

The complete energy spectrum for a np-impurity is shown in Fig. 9.6a. This plot also shows the multiplicity of all states, as calculated from the dimensions of each representation. In Fig. 9.6b, we display the effect of the Coulomb interaction on the energy spectrum. We notice two effects; the energy levels all increase; some representations split.

A graphical representation of the effect of the Coulomb interaction on the energy eigenstates is shown in Fig. 9.7, which shows the amplitude of the mixing angles between the ${}^1 S_0$ YSR energy eigenstates and basis vectors $\{|0\rangle, |{}^1 S_0^2\rangle |{}^1 S_0^4\rangle, |F\rangle\}$. Figure 9.7b shows that the singlet singlet sector splits into blocks with increasing Coulomb interaction, with the largest energy eigenstate mixing mostly with the maximally
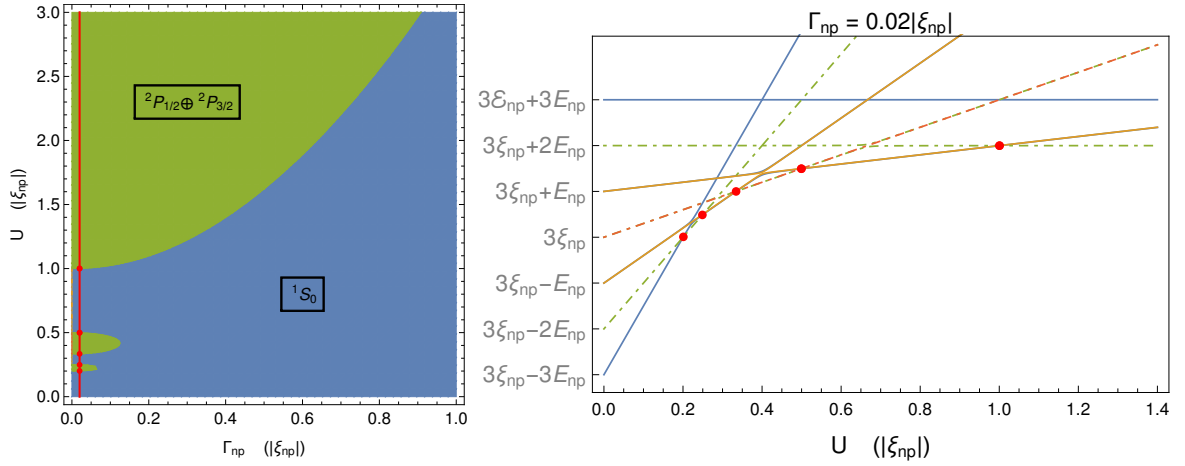
Figure 9.8: The left plot represents the phase space for the ground state. We see islands of different symmetries. Those are due to the dependence of each state on the Coulomb energy, which leads to even-odd state crossings, as shown on the right plot.

occupied state $|F\rangle$, the next-to-heaviest mixes mostly with the quadruply occupied state $|{}^1\boldsymbol{S}_0^4\rangle$, while the $\{|0\rangle, |{}^1\boldsymbol{S}_0^2\rangle\}$ sector remains strongly mixed.

At large $U \gg \Gamma_{np}$ the effective Hamiltonian also splits into blocks, leading to the four energy levels,

$$
\begin{aligned}
E_{0,1} &\simeq \xi_{np} + \frac{U}{2} \pm \sqrt{\left(\xi_{np} + \frac{U}{2}\right)^2 + 3\Gamma_{np}^2}, \\
E_2 &\simeq 4\xi_{np} + 6U, \\
E_3 &\simeq 6\xi_{np} + 15U.
\end{aligned}
\tag{9.113}
$$

We note that the ${}^1S_0$ sector splits from the ${}^3P \oplus {}^1D$ sector. This is due to the fact that since the ${}^3P \oplus {}^1D$ sector contains mixing with 2- and 4-electron states only, its energy levels can rise at much as $\sim 6U$, while the ${}^1S_0$ level can rise as much as $\sim 15U$.

The Coulomb interaction also leads to a level crossing between the lowest ${}^1S_0$ level and the ${}^2P_{1/2} \oplus {}^2P_{3/2}$ lowest level which goes as $\sim \xi_{np}$ at large U. Thus, a quantum phase transition from singlet to mutliplet ground state happens at $U > U_c$ where

$$
\frac{U_c}{|\xi_{np}|} \simeq 1 + 3\frac{\Gamma_{np}^2}{|\xi_{np}|^2}.
\tag{9.114}
$$

The complete ground state phase space as a function of Γ_{np} and U is shown in Fig. 9.8.

The left plot shows the ground state symmetry. We note the islands of odd parity within a singlet dominated region. This is due to the fact that states with different symmetries have a different behavior as a function of the Coulomb interaction as a result of the number of electrons they contain. This leads to level crossings between eigenstates of different symmetries, as is displayed on the right plot of Fig. 9.8, with parameters along the red line of the plot.

9.3.5 YSR states from impurity with mixed s- and p-character

So far, we have analyzed the situation where the outer shell electrons have definite $l = 0, 1$. The more realistic situation is that the outer shell contains a combination of electrons with different orbital angular momentum. Consequently, it is important to generalize the above discussion to a Hamiltonian including mixed angular momenta. Consider the Hamiltonian, $\mathcal{H}_{\text{eff}} = \mathcal{H}_{\text{imp}} + \mathcal{H}_{\text{prox}}$, where

$$\mathcal{H}_{\text{imp}} = \xi_{ns} \sum_\sigma N_{ns\sigma} + \xi_{np} \sum_{m\sigma} N_{npm\sigma} + \frac{U_{nn}}{2} N_n \left(N_n - 1 \right), \tag{9.115}$$

and

$$\mathcal{H}_{\text{prox}} = -\Gamma_{ns} \sum_\sigma d_{ns\sigma}^\dagger d_{ns-\sigma}^\dagger - \Gamma_{np} \sum_{m\sigma} \sigma(-1)^m d_{npm\sigma}^\dagger d_{np-m-\sigma}^\dagger + h.c., \tag{9.116}$$

Note that the proximity Hamiltonian does not contain mixed orbital terms because of the assumption of a spherically symmetric hybridization potential. Relaxing this assumption would lead the hybridization potential to break angular momentum conservation and mixed orbital pairing.

The energy spectrum will be described in the $U = 0$ and large Δ limit. Using the Bogoliubov transformation, shows that there are two kinds of quasiparticle energies s-type, $E_{ns} = \sqrt{\xi_{ns}^2 + \Gamma_{ns}^2}$ and one p-type, $E_{np} = \sqrt{\xi_{np}^2 + \Gamma_{np}^2}$. They combine to form the Hamiltonian

$$\begin{aligned}
\mathcal{H} =& E_{np} \sum_{m,\sigma} \gamma_{npm\sigma}^\dagger \gamma_{npm\sigma} + E_{ns} \sum_\sigma \gamma_{ns\sigma}^\dagger \gamma_{ns\sigma} \\
& + \left(\xi_{ns} - E_{ns} \right) + 3 \left(\xi_{np} - E_{np} \right).
\end{aligned} \tag{9.117}$$

The second line represents the ground state of the p-type quasiparticle and of the s-type quasiparticle. The spectrum is thus obtained by adding onto the ground state
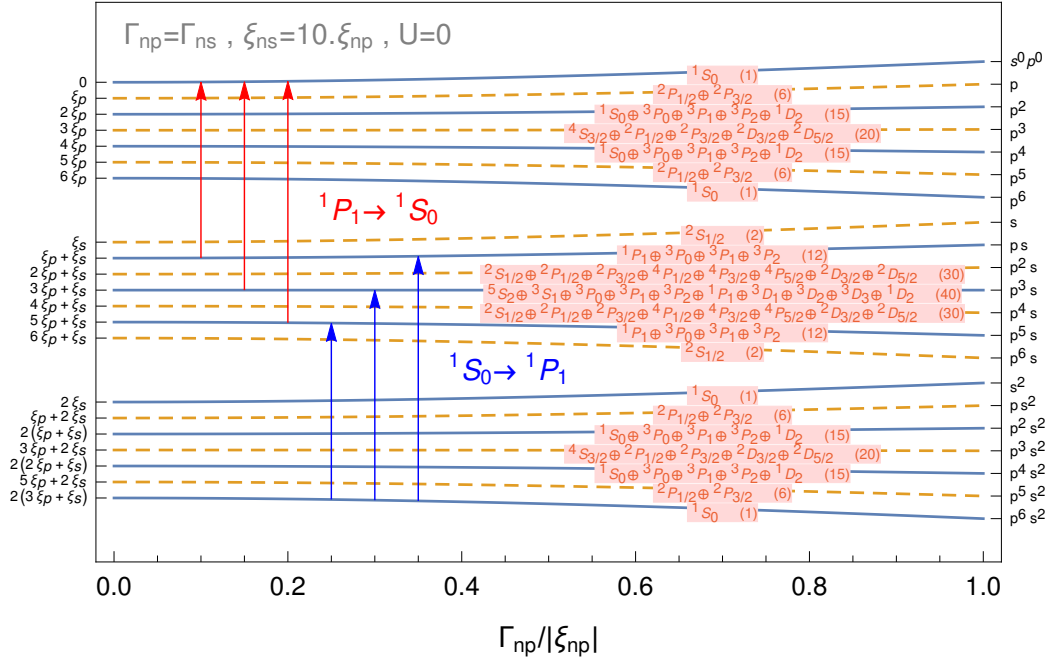
Figure 9.9: Complete set of mixed s and p orbital energies. The solid (dashed) lines represent YSR states with an even (odd) number of electrons. The red arrows represent all one-photon transitions that connect to the vacuum, while the blue arrows are all one-photon transitions that connect the ground state to excited states. The pink labels represent the symmetries of all energy levels, and with the number in parenthesis the associated degeneracy, out of a total of 256 states. On the right-hand side, we enumerated the s and p parities of each line.

energies successive quasiparticle energies according to the Pauli exclusion principle. The spectrum is displayed in Fig. 9.9.

Here we are going to count the dimension of the basis of YSR states. The number of one-electron states is $2(2 \cdot 0 + 1) + 2(2 \cdot 1 + 1) = 8$ since the electron can be either in the $l = 0$ or $l = 1$ states. Therefore, the total number of states is,

$$d = \sum_{k}^{8} \binom{8}{k} = 2^8 = 256 \tag{9.118}$$

The complete set of mixed orbital energy eigenstates has been plotted in 9.9. It has been solved on the grounds of the Bogoliubov transformation. That is, the ground state energy is the one that contains no quasiparticle, $E_{GS} = (\mathcal{E}_{ns} - E_{ns}) + 3(\xi_{np} - E_{np})$, and excited state energies are obtained by subsequently adding either s-quasiparticles or p-quasiparticle energies, E_{ns} or E_{np}. Since a quasiparticle operator

Orbital	Tableaux	Dimension	$\boldsymbol{L}$
$l \otimes l'$	$\boxed{\times\,\times}$	$\underline{\mathbf{10}} = (4 \times 5)/2$	$\boldsymbol{S} \oplus \boldsymbol{S} \oplus \boldsymbol{P} \oplus \boldsymbol{D}$
$s \otimes s$	$\boxed{\bullet\,\bullet}$	$\underline{\mathbf{1}} = (1 \times 2)/2$	$\boldsymbol{S}$
$p \otimes p$	$\boxed{\circ\,\circ}$	$\underline{\mathbf{6}} = (3 \times 4)/2$	$\boldsymbol{S} \oplus \boldsymbol{D}$
$s \otimes p$	$\boxed{\bullet\,\circ}$	$\underline{\mathbf{3}} = (1 \times 3)$	$\boldsymbol{P}$

(a) Symmetric wave functions

Orbital	Tableaux	Dimension	$\boldsymbol{L}$
$l \otimes l'$	$\begin{array}{c}\boxed{\times}\\\boxed{\times}\end{array}$	$\underline{\mathbf{6}} = (4 \times 3)/2$	$\boldsymbol{P} \oplus \boldsymbol{P}$
$p \otimes p$	$\begin{array}{c}\boxed{\circ}\\\boxed{\circ}\end{array}$	$\underline{\mathbf{3}} = (3 \times 2)/2$	$\boldsymbol{P}$
$s \otimes p$	$\begin{array}{c}\boxed{\bullet}\\\boxed{\circ}\end{array}$	$\underline{\mathbf{3}} = (1 \times 3)$	$\boldsymbol{P}$

(b) Antisymmetric wave functions

Table 9.2: Set of all mixed orbital wave functions for two quasiparticles.

has the effect of adding or removing one electron, we can add quasiparticle energies onto the ground state until the maximally filled state has been reached.

We now give a summary of the symmetry of the mixed s and p states. As noted in the previous subsections, the maximally occupied state must be singlet, that has the same symmetry as the $U = 0$ ground state. Adding a quasiparticle to the ground state leads to a state that has the same symmetry as a state where one quasihole has been added to the fully occupied state. As a consequence, the state obtained by adding one s-quasiparticle and 3 p-quasiparticle to the vacuum must coincide with the state where one s-qasihole and 3 p-quasiholes have been removed from the maximally occupied state. This implies that the energy levels are symmetric with respect to the sp^3 state (particle-hole symmetry).

2-quasiparticle states

The total number of YSR states that contain 2-quasiparticle are,

$$\begin{pmatrix} 8 \\ 2 \end{pmatrix} = 28. \tag{9.119}$$

Turning onto the orbital wave function, it can be represented using mixed orbital notation $\boxed{\times}$:

$$\text{Young tableaux:} \quad \boxed{\times} \otimes \boxed{\times} = \boxed{\times\ \times} \oplus \boxed{\begin{array}{c} \times \\ \times \end{array}} \tag{9.120}$$

$$\text{Dimensions:} \quad \underline{\textbf{4}} \otimes \underline{\textbf{4}} = \underline{\textbf{10}} \oplus \underline{\textbf{6}}$$

Among the symmetric wave functions, we find the configuration where either two quasiparticles are s-wave, or two p-wave, or one s- and one p-wave. Among the antisymmetric wave functions, we find the configuration where both quasiparticles are p-wave, and the configuration where one is s-wave and one is p-wave. A summary of all 2-quasiparticle mixed orbital wave functions is found in Tables 9.2a and 9.2b.

The total wave functions for the YSR states are the tensor products of the orbital and spin wave functions, in a way that is antisymmetric under electron interchange. The overall wave function is described in the following way,

$$\boxed{\times\ \times} \otimes \boxed{\begin{array}{c} \ \\ \ \end{array}} \oplus \boxed{\begin{array}{c} \times \\ \times \end{array}} \otimes \boxed{\ \ } = (\underline{\textbf{10}} \otimes \underline{\textbf{1}}) \oplus (\underline{\textbf{6}} \otimes \underline{\textbf{3}}) = \underline{\textbf{28}} = \begin{pmatrix} 8 \\ 2 \end{pmatrix}. \tag{9.121}$$

In terms of spectroscopic notation, the content of each two-quasiparticle YSR state is summarized as,

$$\boxed{\times\ \times} \otimes \boxed{\begin{array}{c} \ \\ \ \end{array}} = \underline{\textbf{10}} \otimes \underline{\textbf{1}} = \begin{cases} {}^1\boldsymbol{S}_0 \\ {}^1\boldsymbol{S}_0 \oplus {}^1\boldsymbol{D}_2 \\ {}^1\boldsymbol{P}_1 \end{cases} \tag{9.122}$$

$$\boxed{\begin{array}{c} \times \\ \times \end{array}} \otimes \boxed{\ \ } = \underline{\textbf{6}} \otimes \underline{\textbf{3}} = \begin{cases} {}^3\boldsymbol{P}_2 \oplus {}^3\boldsymbol{P}_1 \oplus {}^3\boldsymbol{P}_0 \\ {}^3\boldsymbol{P}_2 \oplus {}^3\boldsymbol{P}_1 \oplus {}^3\boldsymbol{P}_0 \end{cases}$$

In an analogous fashion we can find the symmetry of the other states. All symmetries are shown in Fig. 9.9.

9.4 Optical selection rules for YSR states

The previous section showed that the availability of impurity electrons in orbitals $l = 0, 1$ leads to YSR states that have non-trivial orbital, spin and total angular momentum symmetries. Electrons that can be in more than one orbital are able to absorb or emit one photon while transiting to a state with different orbital quantum numbers. Here, we are going to see the impact of those transitions on the response of YSR states to optical stimulation.

These selection rules are also relevant for electric dipole noise, i.e., if two states are connected by the electric dipole operator, then the impurity will emit noise at the frequency equal to the difference in energy between the two states.

Orbital selection rule

The Hamiltonian for the coupling of a multi-electron impurity to the electromagnetic field is $H = \sum_i^N (\boldsymbol{p}_i - e\boldsymbol{A}_i)^2/2m + U$, where $\boldsymbol{p}_i$ is the canonical momentum of electron i and $\boldsymbol{A}_i = \boldsymbol{A}(\boldsymbol{r}_i)$ is the vector potential of the photon at the location of the i-th electron. The presence of the electromagnetic field leads to the dipole interaction $\sum_i \boldsymbol{p}_i \cdot \boldsymbol{A}_i$, which is responsible for the absorption or emission of a photon by the electron. Under this process, the impurity's quantum numbers $\{S, L, J, m_J\}$ change to $\{S', L', J', m'_{J'}\}$, with a transition matrix element,

$$\left\langle {}^{2S+1}L_J, m_J \middle| \boldsymbol{p}_i \middle| {}^{2S'+1}L'_{J'}, m_{J'} \right\rangle. \tag{9.123}$$

Because $\sum_i \boldsymbol{p}_i$ transforms as a vector $({}^1\boldsymbol{P}_1)$ under spatial and spin rotations, the Wigner-Eckart theorem constrains the possible values for ${}^{2S'+1}L'_{J'}$ to,

$$ {}^1\boldsymbol{P}_1 \otimes {}^{2S+1}\boldsymbol{L}_J = \sum_{S',L',J'} {}^{2S'+1}\boldsymbol{L}'_{J'}. \tag{9.124}$$

Therefore, after applying the rules for addition of angular momentum we arrive at the following selection rules,

$$\begin{aligned} &L' - L = \pm 1, \\ &J' - J = 0, \pm 1 \quad (J = 0 \to J' = 0 \text{ forbidden}), \\ &S' - S = 0. \end{aligned} \tag{9.125}$$

Parity selection rule

It is convenient to keep track of the content of the YSR states with the notation $s^a p^b$ where a and b are the number of electrons in each orbital. A YSR state can be in four parity configurations: even-even, odd-odd, even-odd and odd-even, referring to the parities of a and b. Optical transitions connect $s \leftrightarrow p$, which combined with the fact that $a + b$ must be conserved because dipole interactions conserve particle number, we arrive at the rules

$$s^a p^b \xrightarrow[\text{one photon}]{} s^{a \pm 1} p^{b \mp 1}. \tag{9.126}$$

Unlike the dipole interaction, the induced proximity potential breaks particle number by 2, and because the proximity potential does not mix s- with p-orbitals, the proximity effect mixes YSR states with different number of electrons but with the same parity. Thus a YSR state is the following mixture,

$$|Y\rangle = \left|s^a p^b\right\rangle + \left|s^{a \pm 2} p^b\right\rangle + \left|s^a p^{b \pm 2}\right\rangle + \cdots \tag{9.127}$$

Since every state in this series can undergo a transition according to Eq. (9.126), we deduce the parity selection rule that applies to YSR states

$$\text{even a} - \text{even b} \xrightarrow[\text{one photon}]{} \text{odd a} - \text{odd b},$$
$$\text{odd a} - \text{even b} \xrightarrow[\text{one photon}]{} \text{even a} - \text{odd b}, \tag{9.128}$$

The set of all mixed orbital YSR eigenstates is shown in Fig. 9.9, where the parity of each state is noted on the right hand side, in addition to the symmetries of each. This helps us apply the above rules to identify allowed transitions. The total number of allowed transitions is very large, so here we focus on two sets of transitions: the ones with the vacuum state (which is the highest energy state) as a final state and the ones with the ground state as initial state. Both the vacuum and ground states have even-even parity and are pure singlets, $^1 S_0$, thus the possible transitions must involve,

$$\text{even} - \text{even} \longleftrightarrow \text{odd} - \text{odd}$$
$$^1 S_0 \longleftrightarrow {}^1 P_1. \tag{9.129}$$

As pictured in Fig. 9.9, only three transitions satisfy those rules for both the vacuum

and ground state. What is remarkable is that, although inactive in a normal state of the atom, under the proximity effect the vacuum state becomes optically active.

Recent experiments have used Superconducting QUantum Devices to serve as magnetic traps for Rydberg atoms above the surface. An impurity above the superconducting surface can interact with Cooper pairs via electron tunneling. Thus, although the effect will be weaker, we expect YSR states to appear on the Rydberg atoms akin to impurities within the bulk. This experimental setup allows to precisely control and manipulate quantum information stored in the Rydberg atoms via laser excitations [280, 281]. Our results show that extra optical channels open up as a result of the proximity effect, thus offering new avenues to manipulate quantum information stored in YSR states.

9.5   Summary

In summary, tunneling of electrons between impurity and conduction electron orbitals generates Cooper-pairing at the impurity site, imprinting the BCS pairing behavior on the hydrogenic impurity states.

We showed that the spectrum is separated into odd and even parity eigenstates. The eigenstates that get "dressed" by the SC are called YSR states. For an orbitally-degenerate impurity they form generalized Cooper-pairs containing mixtures of $1, 3, 5, \ldots$ (odd-parity) or $2, 4, 6, \ldots$ (even-parity) electrons. In contrast, some other eigenstates remain unpaired, i.e., they never get "dressed" by the SC.

Although the proximity pairing potential is invariant under rotations, the ability of many-electron states to form a variety of total spin and orbital angular momentum states implies that YSR states have a high degree of mixture between different single particle l-orbitals. We illustrated this idea by considering in detail the cases of s, p, and s+p wave impurities.

This observation has important implications for the response of YSR states under electric and magnetic excitations. Indeed, the existence of bound state as mixtures of s- and p- electrons implies the existence of YSR one-photon dipole transitions.

This shows that impurities in superconductors can act as a source of electric and magnetic noise, at frequencies equal to the differences between their discrete YSR and unpaired levels.

Chapter 10

Conclusions

The recent progress in superconducting quantum devices that enable the manipulation and storage of quantum information, such as Superconducting QUantum Interference Devices (SQUIDs) [270], Xmons, [269] and superconducting atom chips [277, 280, 281], motivates the need to better understand the impact of noise due to impurities in these devices.

According to Anderson's theorem, impurities with spin interacting with the superconductor lead to the appearance of bound states within the superconducting energy gap, called Yu-Shiba-Rusinov (YSR) states. Motivated by recent experiments that resolved the spatial structure of impurities embedded in superconductors that unveiled YSR states with orbital character, we developed a quantum theory of orbitally degenerate impurity YSR states based on a generalization of the Anderson model for a quantum s-wave impurity.

Our method relies on a combination of equation of motion, Bogoliubov canonical transformation, and effective Hamiltonian techniques to resolve the nature of the YSR states. The eigenspectrum has been exactly calculated in two extreme limits: (I) that of no on-site electron-electron Coulomb repulsion and finite energy gap, and (II) that of large superconducting energy gap and finite on-site Coulomb repulsion U. We find that the impurity electron's orbital degeneracy induces YSR states that are composed of more than pairs of electrons and that have non-trivial orbital quantum numbers, i.e. that are Cooper-triplets, quadruplets, etc. In particular, we resolve the energy eigenspectrum for YSR states arising from impurities with an s- and p-wave character, and obtain eigenstates that are in $\boldsymbol{S}$, $\boldsymbol{P}$, and $\boldsymbol{D}$ configurations of total orbital angular momentum. We organize the eigenstates according to their orbital, spin, and total angular momentum symmetries, thus we argue that our results captures the essence

of any physical situation with finite energy gap and Coulomb interaction. The only limitation of our approach is that it does not account for the Kondo effect. In essence our model is only valid in the regime $\Delta > 3k_B T_K$, when Cooper-pair formation wins the competition against the formation of the Kondo many-body state.

The fact that we found YSR states that have non-trivial orbital character opens the possibility to consider their optical excitation. Based on the optical selection rules for single-electron transitions, we are able to predict the existence of optical transitions among YSR states and enumerate the selection rules that apply. The non-trivial response of YSR states to electric and magnetic stimulation implies (from the fluctuation dissipation theorem) that they will accordingly contribute to electric and magnetic noise. Moreover, this discovery allows us to entertain the idea of manipulating the information stored in YSR states via optical excitations, most notably, in the context of superconducting atom chips where atomic states have been trapped in SQUID circuit-generated magnetic fields and manipulated via laser excitations.

Bibliography

[1] G. Aad et al., Phys.Lett. **B716**, 1 (2012).

[2] S. Chatrchyan et al., Phys.Lett. **B716**, 30 (2012).

[3] F. Englert and R. Brout, Phys. Rev. Lett. **13**, 321 (1964).

[4] P. W. Higgs, Phys. Rev. Lett. **13**, 508 (1964).

[5] G. S. Guralnik, C. R. Hagen, and T. W. B. Kibble, Phys. Rev. Lett. **13**, 585 (1964).

[6] M. Goldhaber, L. Grodzins, and A. W. Sunyar, Phys. Rev. **109**, 1015 (1958).

[7] A. Strumia and F. Vissani, (2006).

[8] R. Mohapatra et al., Rept.Prog.Phys. **70**, 1757 (2007).

[9] A. de Gouvea, page 197 (2004).

[10] M. Gonzalez-Garcia and Y. Nir, Rev.Mod.Phys. **75**, 345 (2003).

[11] F. Capozzi et al., Phys.Rev. **D89**, 093018 (2014).

[12] G. Fogli et al., Phys.Rev. **D86**, 013012 (2012).

[13] M. Gonzalez-Garcia, M. Maltoni, J. Salvado, and T. Schwetz, JHEP **1212**, 123 (2012).

[14] D. Forero, M. Tortola, and J. Valle, Phys.Rev. **D86**, 073012 (2012).

[15] P. Minkowski, Physics Letters B **67**, 421 (1977).

[16] T. Yanagida, Progress of Theoretical Physics **64**, 1103 (1980).

[17] R. N. Mohapatra and G. Senjanović, Phys. Rev. Lett. **44**, 912 (1980).

[18] J. Schechter and J. W. F. Valle, Phys. Rev. D **22**, 2227 (1980).

[19] H. Klapdor-Kleingrothaus and I. Krivosheina, Mod.Phys.Lett. **A21**, 1547 (2006).

[20] A. Bakalyarov, A. Y. Balysh, S. Belyaev, V. Lebedev, and S. Zhukov, Phys.Part.Nucl.Lett. **2**, 77 (2005).

[21] A. Gando et al., Phys.Rev.Lett. **110**, 062502 (2013).

[22] M. Auger et al., Phys.Rev.Lett. **109**, 032505 (2012).

[23] A. Garfagnini, (2014).

[24] D. Palioselitis, J.Phys.Conf.Ser. **606**, 012006 (2015).

[25] N. Cabibbo, Phys. Rev. Lett. **10**, 531 (1963).

[26] M. Kobayashi and T. Maskawa, Progress of Theoretical Physics **49**, 652 (1973).

[27] J. H. Christenson, J. W. Cronin, V. L. Fitch, and R. Turlay, Phys. Rev. Lett. **13**, 138 (1964).

[28] H. Burkhardt et al., Phys. Lett. **B206**, 169 (1988).

[29] V. Fanti et al., Phys. Lett. **B465**, 335 (1999).

[30] M. Pospelov and A. Ritz, Annals Phys. **318**, 119 (2005).

[31] Z. Maki, M. Nakagawa, and S. Sakata, Prog.Theor.Phys. **28**, 870 (1962).

[32] G. Branco, R. G. Felipe, and F. Joaquim, Rev.Mod.Phys. **84**, 515 (2012).

[33] L. Accardo et al., Phys. Rev. Lett. **113**, 121101 (2014).

[34] M. Aguilar et al., Phys. Rev. Lett. **113**, 121102 (2014).

[35] M. Aguilar et al., Phys. Rev. Lett. **110**, 141102 (2013).

[36] S. Weinberg, *Cosmology*, Oxford University Press, Oxford, first edition, 2008.

[37] G. Steigman, International Journal of Modern Physics E **15**, 1 (2006).

[38] C. Patrignani et al., Chin. Phys. **C40**, 100001 (2016).

[39] Planck Collaboration et al., A&A **594**, A13 (2016).

[40] A. Sakharov, Pisma Zh.Eksp.Teor.Fiz. **5**, 32 (1967).

[41] M.-C. Chen, TASI 2006 Lectures on Leptogenesis, in *Proceedings of Theoretical Advanced Study Institute in Elementary Particle Physics : Exploring New Frontiers Using Colliders and Neutrinos (TASI 2006): Boulder, Colorado, June 4-30, 2006*, pages 123–176, 2007.

[42] J. M. Cline, Baryogenesis, in *Les Houches Summer School - Session 86: Particle Physics and Cosmology: The Fabric of Spacetime Les Houches, France, July 31-August 25, 2006*, 2006.

[43] C. Jarlskog, Phys. Rev. Lett. **55**, 1039 (1985).

[44] C. Jarlskog, Z. Phys. **C29**, 491 (1985).

[45] M. Fukugita and T. Yanagida, Phys.Lett. **B174**, 45 (1986).

[46] M. Drewes, B. Garbrecht, D. Gueter, and J. Klaric, (2016).

[47] M. Drewes and S. Eijima, Physics Letters B **763**, 72 (2016).

[48] P. Hernndez, M. Kekic, J. Lpez-Pavn, J. Racker, and J. Salvado, JHEP **08**, 157 (2016).

[49] T. Asaka, S. Eijima, and H. Ishida, Phys. Lett. **B762**, 371 (2016).

[50] V. C. Rubin, W. K. Ford, Jr., and N. Thonnard, apj **238**, 471 (1980).

[51] K. G. Begeman, A. H. Broeils, and R. H. Sanders, Monthly Notices of the Royal Astronomical Society **249**, 523 (1991).

[52] E. Corbelli and P. Salucci, Monthly Notices of the Royal Astronomical Society **311**, 441 (2000).

[53] R. Massey, T. Kitching, and J. Richard, Reports on Progress in Physics **73**, 086901 (2010).

[54] A. Fattahi et al., Monthly Notices of the Royal Astronomical Society **457**, 844 (2016).

[55] M. Vogelsberger et al., Nature **509**, 177 (2014).

[56] V. Springel et al., Mon. Not. Roy. Astron. Soc. **391**, 1685 (2008).

[57] R. Essig et al., (2013).

[58] J. Alexander et al., Dark Sectors 2016 Workshop: Community Report, 2016.

[59] E. W. Kolb and S. Wolfram, Nucl.Phys. **B172**, 224 (1980).

[60] E. W. Kolb and M. S. Turner, Front.Phys. **69**, 1 (1990).

[61] F. Schwabl, *Statistical mechanics*, Springer, Berlin, second edition, 2006.

[62] J. Ehlers, *General Relativity and Kinetic Theory*, in *General Relativity and Cosmol- ogy, Proc. of the international school of physics Enrico Fermi*, Course XLVII, ed. B. K. Sachs, Academic Press, New York, 1971.

[63] S. Weinberg, *Gravitation and Cosmology, Principles and Applications of the general theory of relativity*, Wiley, 1972.

[64] W. Buchmuller and M. Plumacher, Int.J.Mod.Phys. **A15**, 5047 (2000).

[65] F. Hahn-Woernle, M. Plumacher, and Y. Wong, JCAP **0908**, 028 (2009).

[66] W. Buchmuller, P. Di Bari, and M. Plumacher, Annals Phys. **315**, 305 (2005).

[67] W. Buchmuller, R. Peccei, and T. Yanagida, Ann.Rev.Nucl.Part.Sci. **55**, 311 (2005).

[68] P. Langacker, Phys. Rept. **72**, 185 (1981).

[69] J. A. Harvey, E. W. Kolb, D. B. Reiss, and S. Wolfram, Nucl. Phys. **B201**, 16 (1982).

[70] S. Dodelson, *Modern Cosmology*, Academic Press, Massachusetts, 2003.

[71] W. H. Kinney, (2009).

[72] S. P. Martin, (1997), [Adv. Ser. Direct. High Energy Phys.18,1(1998)].

[73] A. G. Cohen, D. B. Kaplan, and A. E. Nelson, Phys. Lett. **B245**, 561 (1990).

[74] A. G. Cohen, D. B. Kaplan, and A. E. Nelson, Nucl. Phys. **B349**, 727 (1991).

[75] S. L. Adler, (2004).

[76] C. Burgess and G. Moore, *The Standard Model, a Primer*, Cambridge University Press, Cambridge, first edition, 2007.

[77] D. S. M. Peskin, *An Introduction to Quantum Field Theory*, Westview Press, 1995.

[78] S. L. Adler and W. A. Bardeen, Phys. Rev. **182**, 1517 (1969).

[79] J. S. Bell and R. Jackiw, Nuovo Cim. **A60**, 47 (1969).

[80] S. L. Adler, C. G. Callan, D. J. Gross, and R. Jackiw, Phys. Rev. D **6**, 2982 (1972).

[81] A. A. Belavin, A. M. Polyakov, A. S. Schwartz, and Yu. S. Tyupkin, Phys. Lett. **B59**, 85 (1975).

[82] R. V, *Classical Theory of Gauge Fields*, Princeton University Press, Princeton, 1999.

[83] S. M. A., *ITEP Lectures on Particle Physics and Field Theory*, World Scientific, Singapore, 1999.

[84] C. S., *Aspects of Symmetry*, Cambridge University Press, Cambridge, 1988.

[85] F. R. Klinkhamer and N. Manton, Phys.Rev. **D30**, 2212 (1984).

[86] P. B. Arnold and L. D. McLerran, Phys.Rev. **D36**, 581 (1987).

[87] P. B. Arnold, D. Son, and L. G. Yaffe, Phys. Rev. **D55**, 6264 (1997).

[88] D. Bodeker, Phys. Lett. **B426**, 351 (1998).

[89] D. Bodeker, Nucl. Phys. **B559**, 502 (1999).

[90] S. Davidson, E. Nardi, and Y. Nir, Phys.Rept. **466**, 105 (2008).

[91] J. A. Harvey and M. S. Turner, Phys.Rev. **D42**, 3344 (1990).

[92] I. I. Bigi and A. Sanda, Camb.Monogr.Part.Phys.Nucl.Phys.Cosmol. **9**, 1 (2000).

[93] M. Doi, T. Kotani, and E. Takasugi, Prog.Theor.Phys.Suppl. **83**, 1 (1985).

[94] R. Cutkosky, J.Math.Phys. **1**, 429 (1960).

[95] A. Strumia, page 655 (2006).

[96] R. Barbieri, P. Creminelli, A. Strumia, and N. Tetradis, Nucl.Phys. **B575**, 61 (2000).

[97] A. Abada, S. Davidson, F.-X. Josse-Michaux, M. Losada, and A. Riotto, JCAP **0604**, 004 (2006).

[98] E. Nardi, Y. Nir, E. Roulet, and J. Racker, JHEP **0601**, 164 (2006).

[99] T. Endoh, T. Morozumi, and Z.-h. Xiong, Prog.Theor.Phys. **111**, 123 (2004).

[100] A. Pilaftsis, Phys.Rev.Lett. **95**, 081602 (2005).

[101] P. S. B. Dev, P. Millington, A. Pilaftsis, and D. Teresi, (2014).

[102] M. Yu. Khlopov and A. D. Linde, Phys. Lett. **138B**, 265 (1984).

[103] J. R. Ellis, J. E. Kim, and D. V. Nanopoulos, Phys. Lett. **145B**, 181 (1984).

[104] V. S. Rychkov and A. Strumia, Phys. Rev. **D75**, 075011 (2007).

[105] K. Kohri, T. Moroi, and A. Yotsuyanagi, Phys. Rev. **D73**, 123511 (2006).

[106] A. Pilaftsis and T. E. Underwood, Nucl.Phys. **B692**, 303 (2004).

[107] A. Pilaftsis and T. E. Underwood, Phys.Rev. **D72**, 113001 (2005).

[108] D. V. Nanopoulos and S. Weinberg, Phys.Rev. **D20**, 2484 (1979).

[109] A. Bhattacharya, R. Gandhi, and S. Mukhopadhyay, Phys.Rev. **D89**, 116014 (2014).

[110] S. Profumo, M. J. Ramsey-Musolf, and G. Shaughnessy, JHEP **0708**, 010 (2007).

[111] A. Ahriche, Phys.Rev. **D75**, 083522 (2007).

[112] A. Biswas and D. Majumdar, Pramana **80**, 539 (2013).

[113] L. Covi, E. Roulet, and F. Vissani, Phys.Lett. **B384**, 169 (1996).

[114] E. Roulet, L. Covi, and F. Vissani, Phys.Lett. **B424**, 101 (1998).

[115] W. Buchmuller and M. Plumacher, Phys.Lett. **B431**, 354 (1998).

[116] A. Pilaftsis, Phys.Rev. **D56**, 5431 (1997).

[117] E. I. Gates and K. L. Kowalski, Phys.Rev. **D37**, 938 (1988).

[118] A. Denner, H. Eck, O. Hahn, and J. Kublbeck, Phys.Lett. **B291**, 278 (1992).

[119] A. Denner, H. Eck, O. Hahn, and J. Kublbeck, Nucl.Phys. **B387**, 467 (1992).

[120] J. Casas and A. Ibarra, Nucl.Phys. **B618**, 171 (2001).

[121] P. Ade et al., (2013).

[122] M. Moresco, L. Verde, L. Pozzetti, R. Jimenez, and A. Cimatti, JCAP **1207**, 053 (2012).

[123] J.-Q. Xia et al., JCAP **1206**, 010 (2012).

[124] E. Giusarma, R. de Putter, S. Ho, and O. Mena, Phys.Rev. **D88**, 063515 (2013).

[125] S. Davidson and A. Ibarra, Phys.Lett. **B535**, 25 (2002).

[126] I. Ginzburg, (1995).

[127] K. Melnikov and V. Serbo, Nucl.Phys. **B483**, 67 (1997).

[128] G. Giudice, A. Notari, M. Raidal, A. Riotto, and A. Strumia, Nucl.Phys. **B685**, 89 (2004).

[129] D. Aristizabal Sierra, M. Tortola, J. Valle, and A. Vicente, (2014).

[130] M. Plumacher, Z.Phys. **C74**, 549 (1997).

[131] C. Kiessig and M. Plumacher, JCAP **1207**, 014 (2012).

[132] B. Garbrecht and M. J. Ramsey-Musolf, Nucl.Phys. **B882**, 145 (2014).

[133] A. Pilaftsis and D. Teresi, Nucl.Phys. **B874**, 594 (2013).

[134] M. Beneke, B. Garbrecht, C. Fidler, M. Herranen, and P. Schwaller, Nucl.Phys. **B843**, 177 (2011).

[135] C. Kiessig and M. Plumacher, JCAP **1209**, 012 (2012).

[136] T. Frossard, M. Garny, A. Hohenegger, A. Kartavtsev, and D. Mitrouskas, Phys.Rev. **D87**, 085009 (2013).

[137] C. P. Kiessig, M. Plumacher, and M. H. Thoma, Phys.Rev. **D82**, 036007 (2010).

[138] M. D'Onofrio, K. Rummukainen, and A. Tranberg, (2014).

[139] G. Aad et al., Phys.Rev.Lett. **112**, 201802 (2014).

[140] A. Abada et al., JHEP **0609**, 010 (2006).

[141] E. Nardi, J. Racker, and E. Roulet, JHEP **0709**, 090 (2007).

[142] A. Pilaftsis, Phys.Rev. **D78**, 013008 (2008).

[143] A. Coc, J.-P. Uzan, and E. Vangioni, (2014).

[144] A. Kusenko, Phys.Rept. **481**, 1 (2009).

[145] K. Petraki and A. Kusenko, Phys.Rev. **D77**, 065014 (2008).

[146] M. Raidal et al., Eur.Phys.J. **C57**, 13 (2008).

[147] J. Engel, M. J. Ramsey-Musolf, and U. van Kolck, Prog.Part.Nucl.Phys. **71**, 21 (2013).

[148] A. de Gouvea and P. Vogel, Prog.Part.Nucl.Phys. **71**, 75 (2013).

[149] O. Gedalia and G. Perez, (2010).

[150] T. Asaka and M. Shaposhnikov, Phys.Lett. **B620**, 17 (2005).

[151] T. Asaka, S. Blanchet, and M. Shaposhnikov, Phys.Lett. **B631**, 151 (2005).

[152] B. Pontecorvo, Sov.Phys.JETP **26**, 984 (1968).

[153] S. Weinberg, Phys.Rev.Lett. **43**, 1566 (1979).

[154] E. K. Akhmedov, V. Rubakov, and A. Y. Smirnov, Phys.Rev.Lett. **81**, 1359 (1998).

[155] A. de Gouvea, Phys.Rev. **D72**, 033005 (2005).

[156] S. Weinberg, Phys.Rev. **D22**, 1694 (1980).

[157] H. Weldon and A. Zee, Nucl.Phys. **B173**, 269 (1980).

[158] W. Buchmuller and D. Wyler, Nucl.Phys. **B268**, 621 (1986).

[159] K. Babu and C. N. Leung, Nucl.Phys. **B619**, 667 (2001).

[160] A. de Gouvea and J. Jenkins, Phys.Rev. **D77**, 013008 (2008).

[161] F. Bonnet, D. Hernandez, T. Ota, and W. Winter, JHEP **0910**, 076 (2009).

[162] B. Grzadkowski, M. Iskrzynski, M. Misiak, and J. Rosiek, JHEP **1010**, 085 (2010).

[163] F. del Aguila, A. Aparici, S. Bhattacharya, A. Santamaria, and J. Wudka, JHEP **1206**, 146 (2012).

[164] P. W. Angel, N. L. Rodd, and R. R. Volkas, Phys.Rev. **D87**, 073007 (2013).

[165] K. Babu and R. Mohapatra, Phys.Rev.Lett. **109**, 091803 (2012).

[166] K. Babu and R. Mohapatra, Phys.Rev. **D86**, 035018 (2012).

[167] G. Chalons and F. Domingo, Phys.Rev. **D89**, 034004 (2014).

[168] L. Lehman, Phys.Rev. **D90**, 125023 (2014).

[169] J. Preskill, Annals Phys. **210**, 323 (1991).

[170] B. Batell, S. Jung, and C. E. Wagner, JHEP **1312**, 075 (2013).

[171] B. Holdom, Phys.Lett. **B166**, 196 (1986).

[172] R. Foot and X.-G. He, Phys.Lett. **B267**, 509 (1991).

[173] R. Foot, H. Lew, and R. Volkas, Phys.Lett. **B272**, 67 (1991).

[174] M. Pospelov, A. Ritz, and M. B. Voloshin, Phys.Lett. **B662**, 53 (2008).

[175] B. Batell, M. Pospelov, and A. Ritz, Phys.Rev. **D80**, 095024 (2009).

[176] R. N. Mohapatra and J. W. F. Valle, Phys. Rev. **D34**, 1642 (1986).

[177] R. N. Mohapatra, Phys. Rev. Lett. **56**, 561 (1986).

[178] M. Gonzalez-Garcia and J. Valle, Phys.Lett. **B216**, 360 (1989).

[179] S. Fraser, E. Ma, and O. Popov, Phys.Lett. **B737**, 280 (2014).

[180] M. Brooks et al., Phys.Rev.Lett. **83**, 1521 (1999).

[181] J. Adam et al., Phys.Rev.Lett. **110**, 201801 (2013).

[182] F. Renga, (2014).

[183] T. Cheng and L.-F. Li, Phys.Rev.Lett. **38**, 381 (1977).

[184] J. Bjorken, K. D. Lane, and S. Weinberg, Phys.Rev. **D16**, 1474 (1977).

[185] E. Ma and A. Pramudita, Phys.Rev. **D24**, 1410 (1981).

[186] A. Ilakovac and A. Pilaftsis, Nucl.Phys. **B437**, 491 (1995).

[187] B. Grinstein, (2015).

[188] J. Vergados, Phys.Rept. **133**, 1 (1986).

[189] T. Kosmas, G. Leontaris, and J. Vergados, Prog.Part.Nucl.Phys. **33**, 397 (1994).

[190] S. Weinberg and G. Feinberg, Phys.Rev.Lett. **3**, 111 (1959).

[191] T. Donnelly and J. Walecka, Ann.Rev.Nucl.Part.Sci. **25**, 329 (1975).

[192] W. H. Bertl et al., Eur.Phys.J. **C47**, 337 (2006).

[193] H. Natori, Nucl.Phys.Proc.Suppl. **248-250**, 52 (2014).

[194] R. K. Kutschke, (2011).

[195] A. Lusiani, PoS **KAON**, 054 (2008).

[196] A. Pich, NATO Sci.Ser.B **363**, 173 (1997).

[197] B. Aubert et al., Phys. Rev. Lett. **105**, 051602 (2010).

[198] C. Dib, J. C. Helo, M. Hirsch, S. Kovalenko, and I. Schmidt, Phys.Rev. **D85**, 011301 (2012).

[199] A. Abada, A. Teixeira, A. Vicente, and C. Weiland, JHEP **1402**, 091 (2014).

[200] F. Bergsma et al., Phys.Lett. **B166**, 473 (1986).

[201] B. Schwingenheuer, Annalen Phys. **525**, 269 (2013).

[202] P. Bhupal Dev, S. Goswami, M. Mitra, and W. Rodejohann, Phys.Rev. **D88**, 091301 (2013).

[203] J. Schechter and J. W. F. Valle, Phys. Rev. D **25**, 2951 (1982).

[204] P. Bamert, C. Burgess, and R. Mohapatra, Nucl.Phys. **B438**, 3 (1995).

[205] A. Faessler, M. Gonzalez, S. Kovalenko, and F. Simkovic, (2014).

[206] T. Aoyama, M. Hayakawa, T. Kinoshita, and M. Nio, Phys. Rev. Lett. **109**, 111807 (2012).

[207] H. Davoudiasl, H.-S. Lee, and W. J. Marciano, Phys.Rev. **D86**, 095009 (2012).

[208] B. C. Odom, D. Hanneke, B. D'Urso, and G. Gabrielse, Phys.Rev.Lett. **97**, 030801 (2006).

[209] G. Bennett et al., Phys.Rev. **D73**, 072003 (2006).

[210] M. Ablikim et al., (2017).

[211] A. Czarnecki and W. J. Marciano, Phys.Rev. **D64**, 013014 (2001).

[212] M. Pospelov, Phys.Rev. **D80**, 095002 (2009).

[213] P. Fayet, Phys.Rev. **D75**, 115017 (2007).

[214] S. Gninenko and N. Krasnikov, Phys.Lett. **B513**, 119 (2001).

[215] J. Lees et al., Phys.Rev.Lett. **113**, 201801 (2014).

[216] E. Goudzovski, (2014).

[217] B. Batell, P. deNiverville, D. McKeen, M. Pospelov, and A. Ritz, Phys.Rev. **D90**, 115014 (2014).

[218] B. Batell, R. Essig, and Z. Surujon, Phys.Rev.Lett. **113**, 171802 (2014).

[219] Y. Kahn, G. Krnjaic, J. Thaler, and M. Toups, (2014).

[220] W. Altmannshofer, S. Gori, M. Pospelov, and I. Yavin, Phys.Rev.Lett. **113**, 091801 (2014).

[221] W. Altmannshofer, S. Gori, M. Pospelov, and I. Yavin, Phys.Rev. **D89**, 095033 (2014).

[222] L. I. Schiff, Phys. Rev. **132**, 2194 (1963).

[223] J. Baron et al., Science **343**, 269 (2014).

[224] D. Ng and J. N. Ng, Mod.Phys.Lett. **A11**, 211 (1996).

[225] J. P. Archambault, A. Czarnecki, and M. Pospelov, Phys.Rev. **D70**, 073006 (2004).

[226] A. de Gouvea and S. Gopalakrishna, Phys.Rev. **D72**, 093008 (2005).

[227] C. Bird, R. V. Kowalewski, and M. Pospelov, Mod.Phys.Lett. **A21**, 457 (2006).

[228] D. O'Connell, M. J. Ramsey-Musolf, and M. B. Wise, Phys.Rev. **D75**, 037701 (2007).

[229] V. Barger, P. Langacker, M. McCaskey, M. J. Ramsey-Musolf, and G. Shaughnessy, Phys.Rev. **D77**, 035005 (2008).

[230] R. Sato, S. Shirai, and T. T. Yanagida, Phys.Lett. **B704**, 490 (2011).

[231] P. J. Fox, D. Tucker-Smith, and N. Weiner, JHEP **1106**, 127 (2011).

[232] I. Low, J. Lykken, and G. Shaughnessy, Phys.Rev. **D84**, 035027 (2011).

[233] D. McKeen, M. Pospelov, and A. Ritz, Phys.Rev. **D86**, 113004 (2012).

[234] H. Gharibnejad and A. Derevianko, Phys.Rev. **D91**, 035007 (2015).

[235] H. Davoudiasl, H.-S. Lee, and W. J. Marciano, Phys.Rev. **D85**, 115019 (2012).

[236] P. Gambino and M. Misiak, Nucl.Phys. **B611**, 338 (2001).

[237] J. Lees et al., Phys.Rev. **D86**, 052012 (2012).

[238] P. Batra, B. A. Dobrescu, and D. Spivak, J.Math.Phys. **47**, 082301 (2006).

[239] B. A. Dobrescu and C. Frugiuele, Phys.Rev.Lett. **113**, 061801 (2014).

[240] Y. Nir and D. J. Silverman, Phys.Rev. **D42**, 1477 (1990).

[241] P. Langacker and M. Plumacher, Phys.Rev. **D62**, 013006 (2000).

[242] M. S. Carena, A. Daleo, B. A. Dobrescu, and T. M. Tait, Phys.Rev. **D70**, 093009 (2004).

[243] E. Salvioni, A. Strumia, G. Villadoro, and F. Zwirner, JHEP **1003**, 010 (2010).

[244] A. Crivellin, G. DAmbrosio, and J. Heeck, Phys.Rev. **D91**, 075006 (2015).

[245] V. Baluni, Phys.Rev. **D19**, 2227 (1979).

[246] R. Crewther, P. Di Vecchia, G. Veneziano, and E. Witten, Phys.Lett. **B88**, 123 (1979).

[247] M. Pospelov and A. Ritz, Phys.Rev. **D63**, 073015 (2001).

[248] M. Pospelov and A. Ritz, Phys.Rev.Lett. **83**, 2526 (1999).

[249] C. Baker et al., Phys.Rev.Lett. **97**, 131801 (2006).

[250] W. Griffith et al., Phys.Rev.Lett. **102**, 101601 (2009).

[251] B. Graner, Y. Chen, E. G. Lindahl, and B. R. Heckel, Phys. Rev. Lett. **116**, 161601 (2016).

[252] M. Pospelov and A. Ritz, Annals Phys. **318**, 119 (2005).

[253] S. Ban, J. Dobaczewski, J. Engel, and A. Shukla, Phys.Rev. **C82**, 015501 (2010).

[254] P. Fileviez Perez and M. B. Wise, Phys.Rev. **D82**, 011901 (2010).

[255] S. Dodelson and L. M. Widrow, Phys.Rev.Lett. **72**, 17 (1994).

[256] J. McDonald, Phys.Rev.Lett. **88**, 091304 (2002).

[257] F. Piazza and M. Pospelov, Phys.Rev. **D82**, 043533 (2010).

[258] W. Meissner and R. Ochsenfeld, Naturwissenschaften **21**, 787 (1933).

[259] H. K. Onnes, Commun. Phys. Lab. Univ. Leiden. **12**, 120 (1911).

[260] F. London and H. London, Physica **2**, 341 (1935).

[261] F. London and H. London, Proceedings of the Royal Society of London A: Mathematical, Physical and Engineering Sciences **149**, 71 (1935).

[262] F. London, Phys. Rev. **74**, 562 (1948).

[263] V. Ginzburg and L. Landau, Zh. Eksp. Teor. Fiz. **20**, 1064 (1950).

[264] S. Weinberg, Progress of Theoretical Physics Supplement **86**, 43 (1986).

[265] J. Bardeen, Phys. Rev. **97**, 1724 (1955).

[266] L. N. Cooper, Phys. Rev. **104**, 1189 (1956).

[267] J. Bardeen, L. N. Cooper, and J. R. Schrieffer, Phys. Rev. **108**, 1175 (1957).

[268] J. Clarke and F. K. Wilhelm, Nature **453**, 1031 (2008).

[269] R. Barends et al., Nature .

[270] S. Boixo et al., Nature .

[271] L. Yu, Acta Physica Sinica **21**, 75 (1965).

[272] H. Shiba, Progress of Theoretical Physics **40**, 435 (1968).

[273] A. Rusinov, JETP **29**, 1101 (1969).

[274] T. Lanting et al., Phys. Rev. B **89**, 014503 (2014).

[275] D.-J. Choi et al., **8** (2016).

[276] M. Ruby, Y. Peng, F. von Oppen, B. W. Heinrich, and K. J. Franke, Phys. Rev. Lett. **117**, 186801 (2016).

[277] T. Nirrengarten et al., Phys. Rev. Lett. **97**, 1 (2006).

[278] J. Verdú et al., Phys. Rev. Lett. **103**, 1 (2009).

[279] S. Bernon et al., Nat. Commun. **4**, 2380 (2013).

[280] C. Hermann-Avigliano et al., Phys. Rev. A - At. Mol. Opt. Phys. **90**, 1 (2014).

[281] M. A. Beck et al., Appl. Phys. Lett. **109**, 092602 (2016).

[282] Tinkham, *Introduction to Superconductivity*, Dover Publications, second edition, 1996.

[283] M. Ashcroft, *Solid State Physics*, Holt, Rinehart and Winston, 1976.

[284] A. L. Fetter and J. D. Walecka, *Quantum Theory of Many-Particle Systems*, McGraw-Hill Book Company, New York, 1971.

[285] H. Fröhlich, Phys. Rev. **79**, 845 (1950).

[286] Parks, *Superconductivity, Vol. 1*, Marcel Dekker, 1969.

[287] A. A. A., *Fundamentals of the Theory of Metals*, Elsevier Science Publishers, 1988.

[288] K. C., *Quantum Theory of Solids*, John Wiley & Sons, 1964.

[289] P. Anderson, Journal of Physics and Chemistry of Solids **11**, 26 (1959).

[290] A. Abrikosov and L. Gor'kov, Soy. Phys. JETP **35**, 10901098 (1959).

[291] G. D. Mahan, *Many-Particle Physics*, Kluwer Academic/Plenum Publishers, New York, 3 edition, 2000.

[292] P. W. Anderson, Phys. Rev. **124**, 41 (1961).

[293] J. R. A, *Feynman Diagram Techniques in Condensed Matter Physics*, Cambridge University Press, 2013.

[294] J. Kondo, Progress of Theoretical Physics **32**, 37 (1964).

[295] J. Bauer, A. Oguri, and A. C. Hewson, Journal of Physics: Condensed Matter **19**, 486211 (2007).

[296] J. R. Schrieffer and P. A. Wolff, Phys. Rev. **149**, 491 (1966).

[297] M. M. Salomaa, Phys. Rev. B **37**, 9312 (1988).

[298] J. A. Schreier et al., Phys. Rev. B **77**, 180502 (2008).

[299] R. de Sousa, Phys. Rev. B **76**, 245306 (2007).

[300] S. Choi, D.-H. Lee, S. G. Louie, and J. Clarke, Phys. Rev. Lett. **103**, 197001 (2009).

[301] D. Lee, J. L. DuBois, and V. Lordi, Phys. Rev. Lett. **112**, 017001 (2014).

[302] H. Wang et al., Phys. Rev. Lett. **115**, 077002 (2015).

[303] P. Kumar et al., Phys. Rev. Applied **6**, 041001 (2016).

[304] J. Bauer, J. I. Pascual, and K. J. Franke, Phys. Rev. B **87**, 075125 (2013).

[305] K. Hanzawa, K. Yosida, and K. Yamada, Progress of Theoretical Physics **77**, 1116 (1987).

[306] H. Q. Lin and J. E. Hirsch, Phys. Rev. B **37**, 1864 (1988).

[307] I. Affleck, J.-S. Caux, and A. M. Zagoskin, Phys. Rev. B **62**, 1433 (2000).

[308] A. V. Rozhkov and D. P. Arovas, Phys. Rev. B **62**, 6687 (2000).

[309] T. Meng, S. Florens, and P. Simon, Phys. Rev. B **79**, 224521 (2009).

[310] H. F. Jones, *Groups, Representations and Physics*, Taylor and Francis Group, New York, second edition, 1998.